TOPOLOGICAL PHASES OF MATTER WITH DISORDER AND QUASIPERIODICITY

by

YIXING FU

A dissertation submitted to the

School of Graduate Studies

Rutgers, The State University of New Jersey

In partial fulfillment of the requirements

For the degree of

Doctor of Philosophy

Graduate Program in Physics and Astronomy

Written under the direction of

Jedediah H. Pixley

and approved by

_____

_____

_____

_____

_____

New Brunswick, New Jersey

January, 2022

ABSTRACT OF THE DISSERTATION

Topological phases of matter with disorder and quasiperiodicity

By Yixing Fu

Dissertation Director:

Jedediah H. Pixley

The topological materials have been theoretically and experimentally studied intensively in the past decades. The topological properties' robustness against distortion makes them a natural playground to explore novel phase transitions. In this thesis, we focus on topological insulators and semimetals to study the phase transitions driven by disorder and quasiperiodicity. The main focus of this thesis is on the non-perturbative effects that demand the application of state-of-the-art numerical methods.

We first consider models of semimetals under quasiperiodic modulation. We show that the non-perturbative incommensurate effect can drive semimetals through a quantum phase transition into a diffusive phase. Such phase transition will be referred to as the "magic-angle" effect, which will be interpreted to be central behind the magic-angle twisted bilayer graphene. The phase transition is shown to present universally in many models of semimetals. Meanwhile, the transitions have different characters based on the symmetry, in a way analogous to but fundamentally different from the 10-fold classification of Anderson transition.

On top of quasiperiodicity, we study the effect of adding disorder to models of "magic-angle" semimetals. For both the experimentally realized twisted bilayer graphenes

and the simpler models that emulate the same universal physics, we analyze a special type of disorder that is native to the physics of quasiperiodicity - the inhomogeneity of the modulation. Such disorder effects correspond to the varying twist angle in twisted bilayer graphene which has significant experimental relevance.

We then naturally generalize the considerations of semimetal to a 2D topological insulator. The topological mass intertwines with the strength of quasiperiodicity to create a fascinatingly rich phase diagram with interesting eigenstate criticality. In such criticality, we captured topological flat bands, which are of interest because of the potential to host strongly correlated topological phases.

Lastly, we study the effect of disorder in the 3D topological insulator. We revisit the question of the stability of the semimetal line as a phase boundary between topological insulator phases. Because of the rare-region effect that is strictly non-perturbative, we find the semimetal line is destabilized which prevents the occurrence of a quantum critical point.

Acknowledgements

First, I thank my advisor Jed Pixley who has introduced me to such a fascinating field of research. When I first stepped into condensed matter physics and was wondering where to go, Jed's guidance helped me quickly learn and become a productive researcher. Whenever the projects fall into some struggle, Jed's insights and optimism lead us to overcome the difficulties. Jed also gave me plenty of opportunities to present our works and to collaborate with many scientists. These experiences help me grow both as a physicist and as a person in general.

Thank all of my collaborators. On the theory side, I was lucky to work with Yang-zhi Chou, Shiang Fang, David Huse, Elio Konig, Sankar Das Sarma, Justin Wilson, all of whom are knowledgeable and insightful; and I am also honored to join forces with Xiaoran Liu, Fandi Wen and Liang Wu from Jak Chakhalian's group to work on projects closely tied to experiments, and with Minning Zhu and Chung-Tse Michael Wu on microwave resonators. From them, I learned tremendously not only about science, but about everything big or small – as small as the choice of suitable colors when making figures, or the optimal time to submit a paper to arXiv. Working with them has been productive and filled with fun. And I must thank them for bearing with my regular procrastination.

Next, I want to thank all the fellow graduate students I met at Rutgers: Jay Cushing, Victor Drouin-Touchette, Wenbo Ge, Zengle Huang, Hanzhi Jiang, Ahsan Khan, Ghanashyam Khanal, Wan Lin, Shang Ren, Yicheng Tang, Nicodemus Varnava, Ruoquan Wang, Wenbo Wang, Fangdi Wen, Angkun Wu, Xianghan Xu, Mai Ye, Jinjing Yi, Aidan Zabolo, Bingnan Zhang, Zhenyuan Zhang, and it is surely not an exhaustive list. The discussion with them always helped me refresh my passion for physics and brought lots of joy.

I also need to thank Minda Deng, Tian Kang, Wenxiong Li, Zhu-xi Luo, Yinchuan Lyu, Hao-yu Sun, Di Xu, Ziqi Yan, and many friends I met along my journey to physics before I joined Rutgers, as well as Xinhao Li, Haozhe Pang, Shumo Wang, Daheng Yang, Hanyu Zhang, Yuzhou Zhang, and many of my old friends who have always challenged me to think, to learn and to reason. They let me know I am not alone on the journey of intellectual pursuit, and provide me with a pleasant amount of peer pressure to move forward.

I thank my family for making me as I am today. My grandparents and parents fostered me to be curious about the world, encouraged me to ask questions, and taught me to find the answers. They are also always supportive of my decisions – without which I would not have come to the US to study physics, not to mention the prolonged indulgence of working on my doctoral research.

The research work presented here spanning the past four years has also witnessed my encounter with Jia Guo. In four years I studied the many phase transitions of topological phases of matter; and meanwhile, I went through a sequence of phase transitions with Jia until I can include "my wife" in the *dedication* of this thesis. I am grateful for her patience and support during the countless hours I scratch my head with little progress. Her adamant love is undoubtedly a cornerstone of my work.

Dedication

To my parents for their continued support, and my wife for her love.

Table of Contents

List of Tables

List of Figures

Chapter 1

Introduction

The abundant topological phases of matter have been of great interest in condensed matter physics. Since the discovery of integer and fractional quantum Hall effects [8, 9], a variety of topological invariants have been studied in the context of some condensed matter systems, leading to the discovery of many materials or platforms featuring the topological properties. There are gapped systems carrying various topological invariants such as the Chern number [10], the $\mathbb{Z}_2$ invariants [11, 12] and the higher-order topological invariants [13], to name a few. Recent years have also seen a surge of interest in gapless systems such as Dirac and Weyl topological semimetals[14, 15] that carries topological monopole charges. Those topological properties are robust against deformation. Such robustness has brought great prediction power to the field of condensed matter physics, as the topological properties initially defined for idealized, clean systems remain unchanged with high precision in a real-world, dirty system.

Such robustness, in turn, makes the process of destroying topological properties a fascinating ground for a large set of questions to be answered – because of the robustness, the breakdowns of topological properties are not a trivial deviation from ideal states, but often phase transitions driven by non-perturbative effects. Pertaining to the transitions, there are questions that are both of theoretical interest and experimental relevance. For example, adding random disorder to a condensed matter system is well known to induce Anderson localization[16]. In the case of adding disorder to a topological phase of matter, questions arise naturally – does localization still exist? Does topology hold up until localization happens? Are there any new phases of matter in between? The question becomes even more interesting for gapless topological phases, where even small disorder or other perturbation could push the system to a new phase;

and perturbations under certain conditions can allow the phase to remain stable until a more dramatic breakdown.

The main content of this dissertation will be exploring various situations "off" the simpler topological phases, either by incorporating random disorder or quasiperiodic modulation (to be explained soon).

To study condensed matter systems with either disorder or quasiperiodicity (or both), it is often necessary to apply many numerical methods, especially when non-perturbative effects become important. In addition, the lack of translational symmetry, the statistical nature of the disorder, and the complicated phase diagrams demand the numerical computation to be very large in scale. Hence, picking suitable observables with appropriate algorithms becomes vital to research in this field. In light of the importance of numerical computation, Chapter 2 explains in some detail the computational approaches shared in the chapters to follow.

Equipped with the numerical methods, in Chapter 3, we investigate various models to reveal the common 'magic-angle' effect in semimetals driven by an increasing quasiperiodic modulation. This chapter is based on [7] and its supplemental materials. Next, in Chapter 4 (based on [17]) we characterize the effects of disorder on magic-angle semimetals including the experimentally motivated twisted bilayer graphene case and our much simplified toy model from Chapter 3. Chapter 5 (based on [18]) moves on to focus on one model of magic-angle semimetals under chiral symmetry to study the transition in more detail. The chiral model also involves a curious commensurate limit that is equivalent to higher order TI[13]. In Chapter 6 (based on [12] and its supplement material), we shift gear from semimetallic models to 2D topological insulators, where we dive into the rich phase space with intriguing eigenstate criticality and topological flat bands driven by what is analogous to the magic-angle semimetals from previous chapters. Finally, in Chapter 7, the non-perturbative rare-region effects take a central role, as we investigate the fate of a 3D topological insulator and its semimetallic phase boundary under random disorder. Besides the work presented in this thesis, we have utilized the same numerical methods to study several problems in closer connection to experiments, including studies of anomalous Hall effect in $SrRuO_3$[19] and

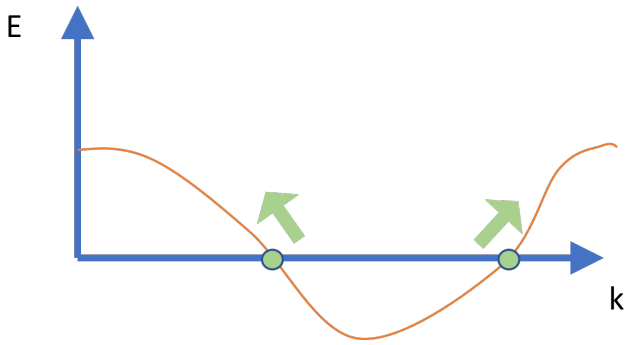

Figure 1.1: Schematics of arbitrary 1D band structure that must have 0, 1, or 2 points at a Fermi level. When there are 2 crossing points, the two crossings must be one right-moving and one left-moving. Figure adapted from Ref. [1]

$Eu_2Ir_2O_7$[20].

In the rest of this chapter, I will provide an overview of topological phases of matter (Section 1.1) that sets the stage for the study in all following chapters. Then Section 1.2 explains quasiperiodicity and disorder that we add to the topological models to drive phase transitions of interest.

1.1 Topological phases of matter

Topological phases are quantum phases defined with topological invariants, whose value does not change with adiabatic deformation. Such topological invariants can often relate to robust and quantized macroscopic quantities such as Hall conductivity in topological insulators.

In this section, I will briefly review the topological phases of matters involved in this dissertation.

1.1.1 Semimetals

Topological semimetals are characterized by isolated band touching points (the nodes) in the Brillouin zone. The two neighboring bands are exactly degenerate at the nodes. The topology of semimetals lies behind such degeneracy.

Because Hamiltonians are always Hermitian, the most general two-band Hamiltonian $H(\vec{p})$ can be written as

$$H(\vec{p}) = a(\vec{p}) + \vec{b}(\vec{p}) \cdot \vec{\sigma} \tag{1.1}$$

Where σ_i are the Pauli matrices

$$\sigma_x = \begin{bmatrix} 0 & 1 \\ 1 & 0 \end{bmatrix}, \sigma_y = \begin{bmatrix} 0 & -i \\ i & 0 \end{bmatrix}, \sigma_z = \begin{bmatrix} 1 & 0 \\ 0 & -1 \end{bmatrix}. \tag{1.2}$$

The points $\vec{p}_*$ in the Brillouin zone where $H(\vec{p}_*)$ is degenerate must have $\vec{b}(\vec{p}_*) = 0$. Hence, assuming $a(\vec{p})$ varies much slower than $b(\vec{p})$ in the vicinity of $\vec{p}_*$[1], the two-band Hamiltonian in the vicinity of $\vec{p}_*$ can be expanded into

$$H(\vec{p}) = \epsilon_0 \pm v_F(\vec{p} - \vec{p}_*) \cdot \vec{\sigma} \tag{1.3}$$

where ϵ_0 is a constant. Such Hamiltonian takes the form of the Weyl equation, and hence the name Weyl semimetals. The sign before v_F is the chirality of the node, which is analogous to the chirality of massless relativistic Weyl fermions. This analogy makes Weyl semimetals an interesting playground to study phenomena expected for fundamental particles in a condensed matter setting.

Most importantly, the existence of such degenerate points has a topological origin. The degeneracy requires $\vec{b}(\vec{p}) = 0$, corresponding to the intersection of 3 surfaces $b_i(\vec{p}) = 0$ where $i = x, y, z$. As momentum takes value in the Brillouin zone which is periodic, each of the three surfaces is closed. Intuitively, the intersection between two surfaces is a closed curve or empty, where each of the two cases is robust against some deformation. The curve can then intersect with the other surface which will always be an even number of points. If we assume those surfaces are all orientable, then the number of intersections into and out of the surface is the same. These are the Weyl nodes with positive and negative chiralities. Only when two Weyl nodes with opposite chirality annihilate each other can we eliminate them. We skip a mathematically rigorous derivation (that is connected to the Nielson-Ninomiya theorem[22]), but heuristically the nodes do not

[1] The contribution of $a(\vec{p})$ can be significant near $\vec{p}_*$, which lead to the so-called type-II semimetals[14, 21] which is out of the scope here.

rely upon the specific form of function $b_i(\vec{p})$ and allow deformation – hence the Weyl nodes are considered topological.

A simple model that features the above described Weyl semimetal is

$$\hat{H}_{SOC} = \sum_{\vec{r},\mu} \frac{it}{2} c^{\dagger}_{\vec{r}} \sigma_{\mu} c_{\vec{r}+\hat{\mu}} \tag{1.4}$$

where t is the hopping strength, c and $c^{\dagger}$ are creation and annihilation operators. Subscripts μ runs over directions x, y, z, and $\hat{\mu}$ are the unit vectors along direction μ. This two-band model corresponds to a cubic lattice with perfect spin-orbit coupling. The spin-orbit coupling breaks the general degeneracy of the two bands, while leaving 8 Weyl nodes at $(\frac{\pi}{2} \pm \frac{\pi}{2}, \frac{\pi}{2} \pm \frac{\pi}{2}, \frac{\pi}{2} \pm \frac{\pi}{2})$. The dispersion relation is

$$E(\vec{k}) = \pm t \sqrt{\sum_{\mu} \sin^2_{\mu}(k_{\mu})} \tag{1.5}$$

where the sign correspond to the valence band (below $E_f = 0$) and conduction band (above $E_f = 0$). Although this model is purely theoretical, the low energy physics captures what is seen in TaAs, NbAs, and so on [23].

There exist a natural extension of the idea of semimetal to 1D. We may consider a Hamiltonian with power-law dispersion [24] defined in momentum space:

$$\hat{H}_{LRH} = -t \sum_{k} \mathrm{sgn}[\cos(k)] |\cos(k)|^{\sigma} c^{\dagger}_{k} c_{k}. \tag{1.6}$$

for some arbitrary σ. This model's density of states vanishes as a power-law, as is in the case of 3D semimetals. The part of the band above $E_f = 0$ is the conduction band, which touches with the valence band below $E_f = 0$ at the semimetallic node. The crossing has a chirality given by the sign of the slope of the dispersion. The nodes, similar to the 3D case, appear in pairs with opposite chirality and can only be eliminated if the nodes of opposite chirality annihilate (see Fig. 1.1 for a schematic drawing). The model is named the long-range hopping (LRH) model because, in real space, the model includes a hopping term between any two lattice sites. The LRH model can be experimentally realized as 1D arrays of trapped ions with long-range interactions whose quasiparticles can resemble the dispersion of Eq. 1.6[25]. This model will be studied in Chapter. 3 as one of the examples exhibiting the universal magic angle physics.

In the case of two dimensions, discrete symmetry plays a more important role. Similar to the 3D case, the degenerate point can only show up at the intersection of three equations of the form $f_i(\vec{p}) = 0$, but now $\vec{p}$ is only two dimensional. Each of the three equations corresponds to a closed curve, then the generic intersection between two curves is isolated points. Tuning those isolated points to exist on the third curve demands a specific form of the functions $f_i(\vec{p})$, and would fail with small deformations. However, in models with suitable reflection or time-reversal symmetry, or when there is no spin-orbit coupling, the diagonal term (σ_z term) on the Hamiltonian is forbidden – then we can find the node that can withstand the deformation at the intersection between $f_x(\vec{p}) = 0$ and $f_y(\vec{p}) = 0$.

The first case leads to a 2D square lattice model that is a clear analogy to the 3D SOC model described above in Eqn.1.4 where the only difference is that μ only runs over x, y. The latter case, with no spin-orbit coupling, correspond to graphene, one of the most known semimetal. It is also the one that is easiest to produce, that can be prepared through exfoliating graphite[26]. Graphene, as a thin sheet of carbon atoms, can be modeled by a honeycomb lattice with only nearest-neighbor hopping terms, forming a two-band model that does not correspond to a spin degree of freedom. For graphene, the band crossing occurs at precisely the half-filling where the Fermi level naturally sits. Hence, its low-energy physics well resembles the Dirac equation.

Importantly, various types of semimetals across 1D to 3D share universal properties. Near $E_f = 0$, the density of states is $\rho(E) \sim |E|^{d/\sigma-1}$ for the 1D LRH model, and $\rho(E) \sim |E|^{d-1}$ for the other models where d is the dimension. Such power-law scaling of $\rho(E)$ is a universal signature of semimetals. These models set the stage for Chapter 3 and 5 where we add quasiperiodicity to observe universal behavior dubbed "magic-angle semimetals". Semimetals can also be found in other models, such as the phase boundary between topological insulators – this will be seen in Chapter 6 and Chapter 7.

1.1.2 Topological insulators

Topological insulators (TI) are gapped topological phases that the band structure is topologically distinct from trivial. The classic two-dimensional examples of TI include

quantum spin Hall insulators[11, 12]. These models were first constructed theoretically as an analogy of the quantum Hall effect that does not require a broken time-reversal symmetry.

The model of the 2D topological insulator that we will consider in this thesis is the Bernevig-Hughes-Zhang (BHZ) model [12], which is a four-band effective Hamiltonian for HgTe quantum wells. The four-band Hamiltonian can be separated into two 2×2 blocks of Chern insulators (called either a half-BHZ model or a Qi-Wu-Zhang model[27]). For one of the two blocks, the Hamiltonian is

$$h(\vec{k}) = \sin(k_x)\sigma_x + \sin(k_y)\sigma_y + [(M-2) - \cos(k_x) - \cos(k_y)]\sigma_z \tag{1.7}$$

and the other block is $-h(\vec{k})^*$. The half-BHZ model effective Hamiltonian has the form of $\vec{d}(\vec{k}) \cdot \vec{\sigma}$, whose eigenstates can be represented on a Bloch sphere. Hence for each band, there is a mapping from $\vec{k}$ (that lives on the 2D torus of Brillouin zone) to the eigenstate on the Bloch sphere (that is a 2D sphere). On such a mapping, the Chern number can be defined as a topological invariant that counts the times that the mapping wraps around the Bloch sphere. The surface of $\vec{d}(\vec{k})$ is plotted in Fig. 1.2. It is a two-lobes surface where one of them is oriented outward, and the other is oriented inward. When the origin is inside one of the lobes, we can continuously shrink the other lobe without the surface passing through the origin. Such deformation turns the surface into a sphere that is identical with or opposite in orientation to the Bloch sphere, and hence the Chern number of the cases are ± 1.

Such topological distinction can only change when bands are deformed significant enough that they touch each other. Hence, on the spatial boundary of the topological insulators which is the interface between the topologically nontrivial phase (inside the TI) and the topologically trivial phase (outside the TI), there are always edge states that connect the gapped bulk bands. The existence of such a robust edge state is one of the prominent signatures of TI. In the case of the half-BHZ model, the Chern number corresponds to a quantized Hall conductivity $\sigma_{xy} = Ce^2/h$. For the full BHZ model, the two blocks have opposite Hall conductivity but with the same amplitude. Such phenomenon is called the quantum spin Hall effect and was observed in HgTe/CdTe

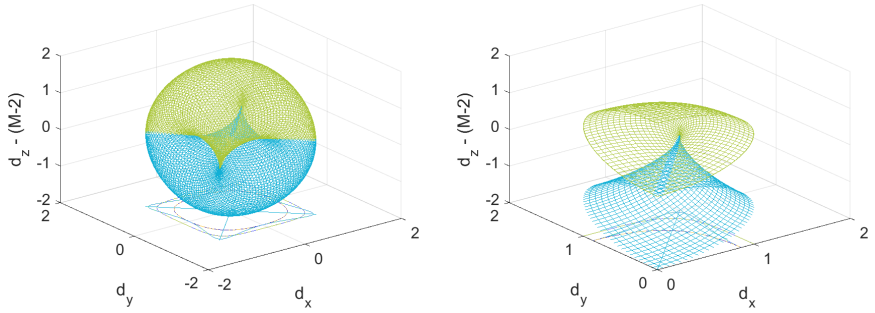

Figure 1.2: The surface of $\vec{d}(\vec{k})$ for the (half) BHZ model. The right panel is showing a view of a quarter ($d_x, d_y > 0$) of the left panel. Colors correspond to the orientation of the normal vector where green is inward and blue is outward. The surface of $\vec{d}(\vec{k})$ can wrap around the Bloch sphere if and only if the origin is in one of the two lobes. When $0 < M < 2$ ($2 < M < 4$), the origin is in the lower (upper) lobe and hence Chern number is $C = -1$ ($C = 1$). Otherwise, there is no wrapping and Chern number is 0.

quantum wells [28] as predicted. Other models with similar topological phases include the Kane-Mele model[11] that is based on graphene. It may see a natural realization in exfoliated jacutingaite crystals[29, 30]. However, the BHZ model is most convenient for our study because it is described on a square lattice, and at the phase boundaries it reduces to the SOC model of semimetals that we have discussed. The BHZ model will be the focus of Chapter 6 where we add quasiperiodicity to the model.

The 3D generalization of 2D topological insulators were first developed to describe Bi_2Se_3, Bi_2Te_3, and Sb_2Te_3[31]. In 3D, the Chern number is no longer possible to define and the topology is now represented by a $\mathbb{Z}_2$ invariant. The surface state of the 3D TI is a Dirac cone and has been observed with angle-resolved photoemission spectroscopy (ARPES)[32, 33]. By doping the TI, it is possible to bring it from the TI phase to a trivial insulating phase (hereafter NI, as short for normal insulator). Such a phase boundary is a semimetal line. As TI is stable against disorders[34, 35], the tuning of 3D TI has been considered a promising path towards realizing Weyl semimetals. In Chapter 7 we will dive into the stability of such TI-WSM-NI transition in the presence of disorder.

Apart from the 2D and 3D TI models that are nowadays considered more "classical" in the field of topological insulators, there are new findings of topology that require crystalline symmetries. Among them is the so-called higher-order topological insulator

[13]. In Higher-order topological insulators, the edge states are gapped, and there are corner excitations that carry half-integer charges. In Chapter 5 we briefly touch upon the commensurate limit of the 2D chiral semimetal model that manifests as a higher-order topological insulator.

1.2 Perturbing the topological models

The above discussion is all based on ideal lattices, focusing on the properties that allow for some distortion of the model. Now we discuss two types of disordering that we will add to the topological phases of matter as the extra axis we explore on the phase diagrams.

1.2.1 Random disorder

Real experiments can never be free from random disorder, making it an important theoretical topic to study. One common way to model random disorder is to add a static potential that is sampled from the same distribution to each lattice site. Such a random potential models the generic fluctuation seen in experiments.

For relatively strong disorder (usually comparable to the strength of the hopping terms), increasing disorder strength induces Anderson localization transition[16, 36, 37]. The localization happens as the random potential creates out-of-phase reflections of plane waves, resulting in destructive interference such that the eigenstates become exponentially localized as

$$|\psi(\vec{r})|^2 \sim \exp(-|\vec{r} - \vec{r}_0|/\xi) \tag{1.8}$$

where ξ is the called localization length. The localization length ξ characterizes the spatial size that the eigenstates have a significant probability. As a phase transition, a scaling theory can be formulated to describe the transition[36]. On the localized side of the Anderson transition the localization length features

$$\xi \propto (E_c - E)^{-\nu} \tag{1.9}$$

where E_c is the critical point of some parameter E, and ν is the scaling exponent. As E approaches E_c, the localization length ξ approaches infinity. On the delocalized

side, the localization length is no longer defined; but the DC conductivity σ can be considered. When scaling with system size L at zero-temperature (or in another word, at a diverging time-scale $\tau \to \infty$), we have

$$\sigma \propto (E - E_c)^s \tag{1.10}$$

where $s = \nu(d-2)$ to characterize the transition. When the temperature T is finite or energy resolution ε is finite, the time-scale is finite and scales as $\tau \sim 1/T$ or $\tau \sim 1/\varepsilon$. Assuming a dynamical scaling $\tau \sim \xi^z$, we have [38, 39]

$$\sigma(\tau) \propto \tau^{-s/z\nu} f[\tau^{1/z\nu}(E - E_c)] \tag{1.11}$$

where f is some universal function. Such an expression is useful for both experiments and numerical calculation where a finite temperature or a finite energy resolution is inevitable. The conductivity and the localization length are observables used in calculations in this thesis to probe the Anderson transition.

The critical behavior of Anderson transition can be classified based on the symmetries of the disordered systems. Such a 10-fold classification was introduced by Altland and Zirnbauer[40] (and hence called AZ classification) to extend the 3 Wigner-Dyson classes[41, 42]. The classification is based on time-reversal symmetry (T), particle-hole symmetry (P) and chiral symmetry (C). For T (or P) symmetry, the value of T^2 (P^2) is either ± 1 or the symmetry is absence. Each of the 9 combinations of the scenarios for T^2 and P^2 dictates the existence of C symmetry, except for the case where both T and P symmetries are absent and C symmetry can either be present or absent.

The three combinations with P and C both absent are the 3 Wigner-Dyson classes that arise from the Gaussian unitary ensemble (GUE, generic random matrices without any symmetry), the Gaussian orthogonal ensemble (GOE, real symmetric matrices) and the Gaussian sympletic ensemble (GSE, Hermitian quaternionic matrices) in random matrix theory [41]. Adding chiral symmetry, there are 3 chiral classes in analogy to the 3 Wigner-Dyson classes[43, 44]. The last 4 classes, to exhaust the 10 possible combinations, appear in the context of superconducting systems[40] and are not involved in the scope of this thesis. By the 10 AZ classification, the critical behavior on any

dimension can be exhaustively studied. For 3D cases, the Anderson transition exists for all symmetry classes; but in 2D, it is known that all but one (the GOE) classes feature Anderson transition, whereas the GOE class is localized for any disorder. See Ref. [37] for a thorough review. In any of the cases, the topological phases always complicate the scenarios and invite for more detailed studies.

Apart from the Anderson transition, another important feature of random disorder occurs even for very small amplitude of disorder: the rare-region effects. The rare-region are the statistically rare, localized and non-perturbative configurations that can significantly alter the phase transitions.

Here we illustrate the scenario of a rare region with a simple example. Consider an identical independent Gaussian distributed potential at each lattice point. One site with a potential 3 times the standard deviation lower than the average can happen, albeit as rare as 1% of times. Meanwhile, it is highly likely its neighbors will not be as extreme as itself. Then we have a very deep and localized potential well. Such potential well can host a localized bound state. Such bounded states are called rare events because they are statistically rare, with an exponentially small average density of states forming the Lifshitz tail[16, 45]. Despite being statistically rare, these states can be extremely important because they are non-perturbative, and can dramatically change the behavior where the density of states was zero.

The existence of rare regions may cause insulating gaps to close earlier than predicted by perturbation theory. Also, in the case of semimetals, the small but non-zero density of states induced by the rare-regions can immediately destroy the $\rho(E)\ |E|^{\alpha}$ scaling of a semimetal. Numerical studies have shown the SM is destroyed by an arbitrarily small random disorder [46].

On the other hand, when topology comes into play, we would expect the topological insulator or topological semimetal phase to be able to resist some deviation from the clean model. Combining the competing effects of rare-regions and topology gives rise to puzzling questions of whether the topological phase hold and what is the resulting phase diagram. This will be the main question of Chapter 7. We will consider a Dirac semimetal phase boundary predicted by perturbation theory between TI and NI phases,

and examine whether disorder destabilizes the SM phase. The stability of such an SM phase has been assumed previously by both theorists[34, 35] and experimentalists, leading to the expectation to find Weyl semimetal by doping topological insulators to tune topological mass from TI to NI[47]. The study in Chapter 7 will help resolve the observation of a large critical regime in the experiment [47] by providing a phase diagram featuring a destabilized SM for any small W.

1.2.2 Quasiperiodicity

Quasiperiodicity (QP) describes a system that is not periodic in any given period but follows a set of repetition rules. One simple form of such quasiperiodicity can be constructed through the incommensurability between the underlying lattice and a secondary lattice as a modulation. For example, consider 1D chain of particles that are located at $r = an$, where we set the lattice constant $a = 1$ for convenience. Then the Hamiltonian

$$H = -J(\sum_r c^\dagger_{r+1}c_r + c^\dagger_r c_{r+1}) + W\sum_r \cos(Qr)c^\dagger_r c_r \tag{1.12}$$

where $Q \in 2\pi\mathbb{Q}$ and W represents the strength of quasiperiodicity. The Hamiltonian is quasiperiodic, as there is strictly no common multiples between the periodicity of the underlying lattice (from the hopping part) and the modulation (the potential part). The model is the well-studied Aubry-Andre-Harper model (AAH model)[48, 49]. In the quasiperiodic limit, increasing W can drive the system through Anderson localization at $W = 2J$, which can be shown through duality arguments [48]. Notice that in finite size systems quasiperiodicity can be approximated with $Q = 2\pi\frac{a_{n+m}}{a_n}$ where a_n is a sequence such that $\lim_{a\to\infty}\frac{a_{n+m}}{a_n} \in \mathbb{Q}$. For any system size L it is sufficient to choose a fraction with $a_n = L$. A convenient choice we will use frequently in this work is $a_n = F_n$, where F_n is the Fibonacci sequence. With a rational approximation of the irrational Q, the Anderson transition turns into a smooth crossover that sharpens at large system size limit.

The idea of adding modulation to induce quasiperiodicity on an existing lattice can be generalized to other dimensions and other models. In particular, we can add the

potential term

$$V(\vec{r}) = W \sum_{\mu=x,y,...} \cos(Qr_\mu) \tag{1.13}$$

to any of the tight-binding models we consider. In Chapter 3 and 6 we shall discuss in detail the quasiperiodicity driven transition, similar to the transition described above for the AAH model. Besides adding the modulation as a potential term, the modulation can also be added through the hopping term, by substituting $t \to t(\vec{r})$ where $t(\vec{r})$ is incommensurate with the underlying lattice. We will show in Chapter 5 that such a chiral modulation features the same universal transition as the potential-term modulation; meanwhile, the chiral modulation demonstrates unique behavior because of its additional chiral symmetry. Such difference between symmetry classes is analogous to the classification of Anderson transitions driven by the random disorder. However, the symmetry classification of the QP modulation is clearly different from the AZ classification as we will show in Chapter 5 and 6.

Such modulations are not only of theoretical interest but can be experimentally realized. In cold atom experiments, applying standing waves of laser with incommensurate wavelength to create quasiperiodic modulation on the atom array [50, 51] is common. Other approaches such as programmable potential in quantum simulator[52], engineered spatial modulation in metamaterials[53] can all realize quasiperiodicity. The experimental accessibility makes the theoretical discussion in Chapter 3,5 and 6 feasible experimental proposals.

Another form of quasiperiodicity that has drawn much attention in recent years is the incommensurate limit of moirè superlattice systems. This is especially relevant in the case of graphene. When two copies of graphenes are stacked and twisted by a small angle, the overall system will have a much larger supercell repeating itself, spanning many unit cells. When the angle is incommensurate, the supercell has an infinite size in a way similar to the quasiperiodic modulation. At finite size, the incommensurate effect can also be approximated through angles that maximize the superlattice.

Described above is the so-called twisted bilayer graphene (TBG) that has been one of the hottest topics since they were found to host superconductivity [54] or correlated

insulator [55] at a small twist angle. The theoretical description of magic-angle TBG has not been fully understood; but noticing the importance of the quasiperiodicity, we provide a perspective connecting the TBG with the more theoretically tractable models of quasiperiodic semimetals that can help understand the incommensurate effect behind magic angle TBG. In Chapter 3 we highlight that the universal physics is tied to the quasiperiodicity, and hence the TBG has the same universal physics as the simpler SM models.

It is worth noticing that the quasicrystals are also quasiperiodic systems. Quasicrystals are materials that do not have translational symmetry but often show rotational symmetry.[56]. Such quasicrystal systems follow tiling patterns such as Penrose tiling and Fibonacci quasicrystals[57, 58]. As long as the rules of tiling continue infinitely, the structure never repeats itself (and hence no translational symmetry exists) but is in close proximity to periodicity. Recently, there has also been interest in exploring topological phases in the context of quasicrystals[59, 60, 61]. Those quasicrystals from aperiodic tiling demonstrate certain similarities with the quasiperiodic modulation that we focus on in this thesis, and it is shown for the specific case of Fibonacci tiling and AAH model that aperiodic tiling is equivalent to modulation induced quasiperiodicity [62].

One important advantage of modulation or twist based quasiperiodicity over the quasicrystals from tiling is the ability to control the strength of the quasiperiodicity. The tunable QP strength enables us to study the phase transitions driven by quasiperiodicity. For the quasiperiodic systems from twisting stacked layers, the inter-layer coupling naturally tunes the strength of quasiperiodicity. Similarly for the case of modulation, the amplitude of QP modulation can be explicitly controlled.

1.2.3 Similarities and differences between quasiperiodicity and disorder

As we have mentioned above, the QP and random disorder have many analogous behaviors. They both represent ergodic traversals of phase space when we consider the ensemble average of all realizations. Both of them can induce Anderson transition. The

transitions in both of the cases depend on symmetry. In perturbation theory, they often yield very similar renormalizations.

However, it is very important to realize many fundamental differences. Firstly, only the random disorder can host rare-region effect; while even for strong quasiperiodicity that drives the system across the Anderson transition, there is no role for rare region effect. The QP modulation is always analytic and can be understood as a highly correlated disorder that forbids the existence of rare regions. On the other hand, an arbitrarily small amplitude of *random* disorder that is spatially not correlated can create rare regions. An exemplifying consequence of such a difference can be seen on 2D semimetals. 2D SM is destroyed by random disorder immediately because of the rare regions, but allows for a SM to metal transition with a QP modulation.

Secondly, the 10-fold AZ classification of disordered systems[40] does not hold for quasiperiodic systems. This is shown clearly in chapter 5 where the chiral symmetry on the magic-angle semimetal induces unique phase transition; and in chapter 6 where the transition out of the topological insulator phase has no counterpart in the AZ symmetry classes.

Chapter 2

Methods

Thoroughly studying quasiperiodic and random systems is challenging because of the non-perturbative behaviors. For many cases, the phase transitions and criticality can only be accurately probed through numerical calculations of lattice models at large system sizes and a huge amount of realization of randomness. Meanwhile, varying the amplitude of random disorder or quasiperiodicity also induces changes of spectra that are usually so obvious compared to the more subtle non-perturbative effects such as the rare-region effects, making the latter difficult to be clearly resolved. Consequently, the proper choice and optimization of numerical approaches are vital to all of our studies in this thesis. Hence, we spend the current chapter discussing the algorithms we use and the observables that are enabled by those algorithms.

2.1 KPM method

Most of the projects discussed in this work apply the Kernel Polynomial Method (KPM)[4]. KPM is a class of algorithms that expand the operator expression of any spectral quantity into Chebyshev polynomials. The Chebyshev polynomial expansion provides fast convergence and numerical stability on most quantities. In addition, KPM provides a consistent way to suppress the Gibbs phenomenon, the oscillation that occurs when approximating non-analytic function with a finite approximation of polynomial series.

Computationally, the expansion of KPM transforms the computationally expensive multiplication of operators into the trace of operator products with building blocks in the form of $T_n(H)$ and a few other operators. Then, the stochastic trace evaluation [4, 63] (to be discussed in detail below) allows the calculation to solely consist of

matrix-vector multiplication, which can be optimally organized based on the recurrence definition of Chebyshev polynomials.

Aside from the computational advantages, the energy resolution ϵ of the calculated observable is proportional to $1/N_C$ where N_C is the finite cutoff of expansion order. Such cutoff provides a consistent way to probe energy scaling, allowing us to conveniently calculate the observables as a function of ϵ.

2.1.1 The expansion

KPM method always starts with decomposing an observable with one or multiple sets of Chebyshev polynomials as bases. Then all the coefficients $\mu_{n,m,...}$ (will be dubbed as moments) are all linear combinations of words composed from Chebyshev polynomials of Hamiltonian, delta function, and other operators. For example, one observable heavily used in this thesis is the density of states (DOS) defined as

$$\rho(E_f) = \frac{1}{N_H}\left[\!\!\left[\sum_n \delta(E_f - E_n) \right]\!\!\right] \tag{2.1}$$

where the index n runs through all eigenstates of a given basis and assumes an ascending ordering on the eigenvalues. $N_H = N_{int}L^d$ is the total degree of freedom of the lattice model, with N_{int} being the number of bands at each lattice site, L the linear size of the lattice, and d the spatial dimension. For example, the 2D BHZ model we consider in Chapter. 6 has $d = 2$, $N_{int} = 2$; the 3D TI model (Chapter 7) has $d = 3$, $N_{int} = 4$. For more realistic models, we may have N_{int} as the sum of bands of all atoms. This convention (slightly deviating from how the density of states is usually defined) conveniently fixes the integral of $\rho(E_f)$ over all Fermi energy to 1. The square bracket $[\![...]\!]$ represents averaging across all random realizations. Such averaging is assumed for most of the thesis unless otherwise specified. The density of states observable in Eq. 2.1 can be expanded into

$$\rho(\tilde{E}_f) = \left[\!\!\left[\frac{1}{\pi\sqrt{(1-\tilde{E}_f)^2}} \sum_n \delta_{n,0}\mu_n T_n(\tilde{E}_f) \right]\!\!\right] \tag{2.2}$$

where we have a tilde on top of E_f because necessary normalization is always needed. Similar normalization is always needed whenever a Chebyshev polynomial expansion

is involved. T_n is the Chebyshev polynomial of the first kind. The exact transformation involves summing n from 0 to ∞, but convergence is guaranteed with Chebyshev polynomials for a finite cut of to $m < N_C$, and with the help of the kernel (to be explained soon) the convergence can be accelerated significantly and to preserve desired properties. The only part depending on specific models is μ_n, calculated as

$$\mu_m = \operatorname{Tr} T_m(\tilde{H}) \tag{2.3}$$

where T_n is now understood as Chebyshev polynomial of operators. Because any Hamiltonian commutes with itself, there is no ambiguity in the definition and hence we will not emphasize the difference between the scalar and operator polynomials. Through such expansion, we have converted the calculation of $\rho(E_f)$ into the calculation of a sequence of μ_m that are all traces of $T_m(\tilde{h})$; and the original function $\rho(E_f)$ is only a Chebyshev linear transformation from μ_m.

Another example used extensively in this thesis is the calculation of conductivity. In general, any order of linear or nonlinear conductivity can be formulated into the expectation of some combination of words composed by Hamiltonian, velocity operators (v_ν where ν is for direction), and some Green's function (whose choice depends on the gauge used for calculation)[64, 65, 66, 67]. Those expectations can then be expressed as linear transformations (that can include Chebyshev transformations, integrals and some finite summations) of moments $\mu_{m,n,\ldots}$ that consists of words of $T_n(\tilde{H})$ and velocity operators v_ν.

For the calculation in this work, we consider observables from the linear response theory (the calculation of DC conductivity and optical conductivity for example). For DC conductivity, the conductivity tensor defined through the Kubo formula [64] is

$$\sigma_{\alpha\beta} = \frac{2e^2\hbar}{L^2}\int f_{E_f}(\epsilon)d\epsilon \operatorname{Im}\operatorname{Tr}\left[\!\!\left[v_\alpha \frac{dG^-}{d\epsilon} v_\beta \delta(\epsilon - H)\right]\!\!\right] \tag{2.4}$$

where $f(E) = [e^{\beta(E-E_f)} + 1]^{-1}$ is the Fermi function at inverse temperate β and Fermi energy E_f, v_α is the velocity operator, G^- is the retarded Green function, and $[\![\cdots]\!]$ denotes an average over samples (realization of disorders) and boundary condition. The velocity operator is constructed in the so-called length gauge, which is most convenient when working with a tight-binding model defined in real space.

The moments needed for the calculation are

$$\mu_{mn}^{\alpha\beta} = \mathrm{Tr}\left[T_n(\tilde{H})v_\alpha T_m(\tilde{H})v_\beta T_n(\tilde{H})\right] \tag{2.5}$$

that does not depend on energy.

For DC conductivity, the observable can be assembled from the moments as

$$\tilde{\sigma}_{\alpha\beta} = \frac{4e^2\hbar}{\pi N_H}\frac{4}{\Delta E^2}\int d\epsilon \frac{f_{E_f}(\epsilon)}{(1-\epsilon^2)^2}\sum_{m,n}\Gamma_{nm}(\epsilon)\,\mathrm{Tr}\left[\hat{\mu}_{nm}^{\alpha\beta}\right] \tag{2.6}$$

where Fermi energy is encoded in function f_{E_f}, and ΔE is the total bandwidth of the spectrum. $\Gamma_{nm}(E)$ are a set of functions explicitly constructed from Chebyshev polynomials independent of models. See Ref. [64] for details. With the expansion, we have split the calculation of the conductivity into two parts: the first part is the calculation of traces of operator products and the second part does not involve operator operations at all.

Such KPM expansions have two important advantages. Firstly, the usage of the Chebyshev polynomial ensures numerical stability and convergence. Secondly, the computationally expensive part (the trace of operators products) is agnostic of Fermi energy. Hence the expansion enables easy access to the entire spectrum of the observables as a function of E_f and temperature at minimal extra computational cost than a fixed E_f and temperature.

When computing longitudinal DC conductivity at zero temperature, there exist a further simplification of the expansion that is found in the appendix of Ref. [64]

$$\sigma_{xx} = \frac{4e^2\hbar}{\pi N_H}\sum_{m,n\le m}\mu_{nm}^{\alpha\alpha}T_n(E_f)T_m(E_f) \tag{2.7}$$

This expression avoids the need to save all intermediate states in the calculation, and hence significantly reduces the memory cost. Of course, it forfeits the benefit of calculating all E_f and temperature altogether.

Additionally, the recurrence definition of Chebyshev polynomial significantly accelerates the calculation. The operator product $T_n(H)$ can be calculated based on $T_{n-1}(H)$ and $T_{n-2}(H)$ with only one extra application of matrix-vector multiplication.

Hence, when calculating all of the N_C moments, the computational cost is asymptotically the same as the cost of calculating $T_{N_C}(H)$ itself. Consequently, the amortized computational cost for each moment is reduced to $1/NC$.

2.1.2 The kernels

The expansion above is only a reorganization of calculation. Even with all the gains in efficiency, computationally we can only reach some finite cutoff N_c for the expansion. When the computed observable is a function of a parameter E, the finite cutoff will always broaden the ideal $\delta(E - E_0)$ to some finite profile. In the case of taking a naive hard-cutoff for N_C, the profile is significantly oscillatory, causing the Gibbs phenomenon. Such oscillation is not physical and degrades the calculated results.

To suppress such oscillation, a trick central to KPM is the usage of kernels. The kernels counter the Gibbs oscillation by damping the cutoff of expansion order into a soft fade-away. For a kernel function g_n that monotonically decrease with n from $g_0 = 1$ to $g_{N_c} = 0$, we define

$$\tilde{\mu}_{n_1,n_2,\ldots} = \mu_{n_1,n_2,\ldots} g_{n_1} g_{n_2} \cdots \tag{2.8}$$

and $\tilde{\mu}$ will be used in place of μ for all consequent calculations. The hard cutoff can be considered as a Dirichlet kernel where $g_n = 1$ for all $n < N_C$. Any damping that is strictly decreasing reduces the Gibbs oscillation. Moreover, the freedom of choosing g_n allow us to pick the smoothing that either optimizes the distance from ideal series summation or satisfies certain constraint desirable for physical quantities.

One of the most used kernels in KPM calculations is the Jackson kernel

$$g_n^J = \frac{(N - n + 1)\cos\frac{\pi n}{N+1} + \sin\frac{\pi n}{N+1}\cot\frac{\pi}{N+1}}{N + 1} \tag{2.9}$$

The Jackson kernel guarantees the result to be positive without non-Hamiltonian operators, which is desired in the calculation of the density of states. The kernel is also proved to turn delta-functions $\delta(E - E_0)$ into the narrowest possible near-Gaussian peak in the sense of minimizing the second moment $\langle E^2 \rangle$ to be π/N_C when E_0 is near 0. It is worth noting that the near-Gaussian behavior is only valid for E very close to

E_0; and for E away from E_0, the tail of the broadened peak turns into

$$f^J(E, N_C) \sim 1/N_C^3 \tag{2.10}$$

while the dependency in E does not yield a simple expression.

Another choice of the kernels is the Lorentz kernel

$$g_n^L = \frac{\sinh[\lambda(1 - n/N_C)]}{\sinh(\lambda)} \tag{2.11}$$

that preserves the analytical properties of Green's function and precisely broadens a delta function into a Lorentzian. An extra parameter λ is introduced to control the width of the peak, but the tail of the broadened profile of $\delta(E - E_0)$ will always read

$$f^L(E, N_C) \sim 1/N_C \tag{2.12}$$

When multiple Chebyshev expansion is involved (such as for conductivity that has two expansion over E), the effects of two kernels on the tails of broadened delta functions are applied multiplicatively. If the Jackson kernel is applied twice, the tail is $\sim 1/N_C^6$; if one Jackson kernel and one Lorentz kernel is used, the tail would be $\sim 1/N_C^4$.

The choice of kernel usually comes from two parts of considerations. Firstly, when analytical properties are important, we may want to choose Lorentzian. Similarly, when we need to consider some physical broadening (for example, a Drude peak that is a Lorentzian) with a similar width as the KPM introduced broadening, choosing Lorentz kernel may avoid the need for considering the convolution of Lorentzian with Gaussian which produces a more complicated Voigt profile. Otherwise, the Jackson kernel is preferred for faster convergence.

2.1.3 The stochastic trace

One final component of KPM is a stochastic estimator of the trace of operator products. For generic matrices of rank n, the best matrix-matrix multiplication takes $O(n^{2.3})$ and significant memory cost. Although better algorithms exist for sparse matrices like tight-binding Hamiltonians, matrix multiplication can quickly spoil the sparsity and diminish

the advantage of sparse algorithms when calculating $T_n(H)$. For the lattice size we work on, such computational cost is prohibitive even on modern computers.

To surmount the problem, computational physicists have been using the so-called stochastic trace[63, 68] that is the complex analogy of Hutchinson's estimator for real positive definite matrices [69]. The idea is to use the expectation value of the operator on a small set of N_R random vectors, $|\xi_{ri}\rangle$, to approximate the trace of the operator. Here r is the index for the random vectors and i runs over a given basis of the Hamiltonian. When the elements ξ_{ri} are independent random variables such that the random vectors satisfy normalization condition ($\langle\xi_r|\xi_r\rangle = 1$), then the trace of operator $\hat{\mathcal{B}}$ can be estimated with estimator Θ, defined as

$$\Theta = \frac{1}{N_R}\sum_{r=1}^{N_R}\langle\xi_r|\hat{\mathcal{B}}|\xi_r\rangle \tag{2.13}$$

The fluctuation of the estimator is

$$(\delta\Theta)^2 = \frac{1}{R}(\mathsf{Tr}(\mathcal{B}^2) + (\langle|\xi_{ri}|^4\rangle - 2)\sum_{j=0}^{D-1}\mathcal{B}_{jj}^2) \tag{2.14}$$

Usually the trace of operator $\hat{\mathcal{B}}$ and the square of it, $\hat{\mathcal{B}}^2$, are both $O(n)$. Hence the estimator's relative fluctuation $\delta\Theta/\Theta \sim O(1/\sqrt{n \times N_R})$. For a very large lattice size, the choice of N_R can therefore be small and does not add to asymptotic complexity. Also, the calculation now can be formulated to only include matrix-vector multiplication which takes only $O(n)$ time for matrices as sparse as tight-binding Hamiltonians and velocity operators. Thus, the time complexity of KPM for single-Chebyshev expansion is $O(n \times N_C \times N_R) \approx O(n \times N_C)$, which is $O(n)$ amortized for each moment. The memory cost is asymptotically the same as the cost to store the matrix itself.

For conductivity calculation, if we save all intermediate matrix-vector product results (that takes $O(n \times N_C \times N_R$, note that for conductivity N_R is significantly larger than that of DOS) the time complexity is $O(n \times N_C \times N_R$ as for DOS; or $O(n \times N_C^2 \times N_R)$ time and $O(n \times N_R)$ memory; or any combination in between, as long as the product of time complexity and memory cost is constant. For the special case of longitudinal DC conductivity at zero temperature, utilizing expansion in Eq. 2.7 helps keep memory cost at $O(n \times N_R)$ with time complexity $O(n \times N_C \times N_R)$, if we only need the observable

at very few Fermi levels. These are the best computational efficiency we can achieve for DOS and conductivity calculation.

The choice of random vector is not of great importance, but choosing complex ξ_{ri} that is Gaussian distributed achieves $|\xi_{ri}|^4 = 2$, providing a basis independence estimator fluctuation

$$(\delta\Theta)^2 = \frac{1}{R}(\mathsf{Tr}(\mathcal{B}^2)) \tag{2.15}$$

Otherwise, we may also choose $\xi_{ri} = e^{i\phi_{ri}}$ where $\phi_{ri} \in [0, 2\pi)$ to minimize $\delta\Theta$. However, recall that the operator $\mathcal{B}$ we consider are words of $T_n(H)$ that we will calculate iteratively and velocity operators. Choosing to minimize $\delta\Theta$ implicitly demands the existence of a mutual basis for all moments in the calculation. It is usually only possible for DOS calculation as only a Hamiltonian is involved. In practice, any randomized independent choice of ξ_{ri} can be used.

2.2 Lanczos

Lanczos method [70] is an efficient iterative method to compute a few (n_{ev}) eigenvalue and eigenvectors of a matrix. It allows a time complexity of $\tilde{O}(n/\sqrt{\varepsilon})$ and negligible extra spatial-complexity. Here ε is the allowed error for the iterative method and $\tilde{O}$ means the asymptotic complexity is only approximate[71]. More prominently, being an iterative method it is most efficient when the matrix is sparse – which is the case for most Hamiltonian H we consider.

When we need eigenstates in the interior of the spectrum of H (usually near a given E_f), we can transform the Hamiltonian so that the desired eigenstates have the largest magnitude. One universal approach is the shift-invert Lanczos method[72]. The first step of shift-invert Lanczos transforms the eigenproblem

$$H\psi_n = \lambda_n\psi_n \tag{2.16}$$

into

$$(H - \sigma I)^{-1}H\psi_n = \frac{\lambda_n}{\lambda_n - \sigma}\psi_n \tag{2.17}$$

where σ is the designated energy around which we look for eigenvalues. The extra

cost of the shift-invert Lanczos compared to the bare Lanczos is the need to construct $(H - \sigma I)^{-1}$.

Computing the inverse of a sparse matrix requires tremendous spatial and temporal cost and breaks all the benefits of the sparsity of the matrix; however, here we only need to express the action of the inverse matrix on vectors. Hence in most available implementations or wrappers of Lanczos method [72, 73], the inverse of matrix achieved through a Cholesky decomposition that takes $O(n^{3/2})$ time, close to $O(n^2)$ memory and results in only $O(n \log n)$ entries in the resulting factors[74], retaining the benefits of sparsity in the iteration part of the calculation. Nevertheless, the Cholesky decomposition step dominates the shift-invert Lanczos computation both in time and memory and is hard to parallelize for sparse matrices. Such restrictions typically limit our calculation capability to systems with $\sim 10^6$ sites. The benefit of the shift-invert approach is that the procedure has been well-developed in out-of-the-box packages. In addition, it guarantees good convergence for almost any Hermitian matrices and *always* captures the first n_{ev} eigenpairs.

An alternative approach is to convert the problem in Eq. 2.16 into

$$((H - \sigma I)^2 - \gamma)\psi_n = ((\lambda_n - \sigma)^2 - \gamma)\psi_n \tag{2.18}$$

where γ is a very large number. This method assumes exactly the same asymptotic complexity as the bare Lanczos and requires no extra memory, allowing the calculation on Hamiltonians with 10^7 sites or more and is much faster than shift-invert by orders of magnitude. However, this method does not warrant capturing the first n_{ev} eigenvalues near σ, especially in the presence of degeneracy (that happens a lot when we consider systems with quasiperiodicity) or when the spectrum is very dense (when the system has a finite density of states near σ)[46].

2.2.1 Wavefunction, IPR, and (generalized) multifractal analysis

Whenever a wave function $|\psi\rangle$ is calculated, we shall often look at the probability on any basis $|\psi_i|^2$ where i is some basis, usually real or momentum space. However, it is often very difficult and subjective to directly learn from probability or wavefunction itself. In

such a case, the conventional approach is to look for various summarizing quantities of the wavefunctions (and of course, there are newer approaches using machine learning to directly characterize wave functions, as we discuss later). The properties of the probability distribution of an eigenstate can be characterized by inverse participation ratio (IPR), or more generally, a multifractal analysis [75, 37].

We first define a "coarse grained" real-space wavefunction (ψ_b) with its resolution controlled by a binning size $b \geq 1$. The spatial region is divided into $(L/b)\times(L/b) = 1/\lambda$ boxes. We assign a position vector $\vec{X}_j$ to indicate the position of the jth box. The binned wavefunction is given by $\psi_b(\mathbf{X}_j) \equiv \sum'_{\mathbf{x}} \psi(\mathbf{x})$ where ψ is the original normalized wavefunction, and $\sum'_{\mathbf{x}}$ runs over the positions inside the jth box. Then, we define the real-space (generalized) inverse participation ratio (IPR) and multifractal exponent via

$$\mathcal{I}_R(E; q, \lambda) = \sum_{\mathbf{X}_j} |\psi_b(E, \mathbf{X}_j)|^{2q} \propto (\lambda)^{\tau_R(q)}\,, \tag{2.19}$$

where $\mathcal{I}_R(E, q, \lambda)$ is the qth real-space IPR with a coarse graining ratio λ, E is the energy of the wavefunction, and we use a subscript R to denote real space or K for momentum space (and will be referring to real space if not specified). Note that the sum in Eq. (5.7) is running over the positions of boxes ($\mathbf{X}'_j s$) rather than the full lattice points. The quantity $\tau_R(q)$ is the multifractal exponent associated with the qth IPR in real space, and $b = 1$ is the finest resolution in the IPR measure. The exponent $\tau_R(q)$ is extracted via varying values of b for $b \ll L$. To obtain $\tau_R(q)$ in the finite-size system, we vary the binning size b for a given L. The exponent $\tau_R(q)$ is known to be a self-averaging quantity in the studies of disordered free-fermion models [76]. In addition, $\tau_R(q = 0) = -d = -2$ (the trivial limit which corresponds to counting binning boxes) and $\tau_R(q = 1) = 0$ (normalization of the wavefunction) must hold for arbitrary wavefunctions. If we set $b = 1$ and $q = 2$, we arrive at the second IPR for studying spatial ergodicity/non-ergodicity in a wavefunction.

When determining phase transitions, we also define the multifractal exponent α_q which is employed for characterizing the localization properties – and $q = 0$ is chosen for easy converging and clear distinction between insulating and metallic phases. The α_0 can be computed via numerical Legendre transformation of $\tau(q)$. Alternatively, a

method by Chhabra and Jensen [77] is available to compute α_0 is available through the multifractal spectrum.

2.3 Machine learning

In several cases, calculating a phase diagram may need repetitive tasks that are difficult to iron out a clear mathematically expressed observable. The machine learning method can be helpful in such situations.

Machine learning is the overarching name for a class of methods where a non-specialized model can be used to perform a specific task when supplied with an abundance of data. The process of supplying data to the model is called "training", after which the model has "learned" to perform the tasks and can then be applied to new data sets. Many machine learning techniques have been applied to various aspects of physics (see [78, 79, 80] for some examples). One type of machine learning method, dubbed deep-learning, has seen the most development in the past decade and attracted attention in various fields.

Deep learning involves training neural network models inspired by the structure of the neural systems. A neural network model consists of a massive number of nonlinear functions and linear transformations, usually organized into several "layers," to replicate any task that distills information from raw data. Practically, such a combination can be tuned to fit any mapping. Hence, as long as a concrete definition of the task to be executed is available, we can use labeled data as an example to tune the neural network until it replicates the task. Such a process is called "training," and can be calculated efficiently using modern computers.

Such a procedure makes exploring phase boundaries efficient and relatively objective. In this thesis, Chapter 6 includes works using Convolutional Neural Networks (ConvNets) to classify wave function into localized or extended phases.

2.4 Discussion

The algorithm mentioned in previous sections, the latest computational hardware (CPU, GPU, and large memory devices), the infrastructure facilitating vastly parallel and distributed computation (OSG[81] is a great example), and the software making efficient computation more accessible to non-computer-experts (Julia[73], Keras[82]) together has made the exploration of the details of phase diagrams specific to thermodynamic limit feasible.

The easiness can help us discover or understand phenomena that are not obvious to intuition. For example, in Chapter 5 a scan in a two-parameter phase space lead me to draw a connection between the chiral model of SOC with quasiperiodicity and the higher-order topological insulators. In Chapter 6 the renormalization of topological mass and the existence of eigenstates criticality both come to our attention when plotting a scan of two-parameter phase space. The luxury of being able to code up in an hour, and use a handful of days to densely scan a large area of the phase diagram is the endowment of contemporary technology. Taking advantage of those state-of-the-art computational tools, we will present lots of details beyond the analytical methods and previous numerical efforts. Those results help us to extend the understanding of topological phases transitions with random disorder and/or quasiperiodicity in the thermodynamic limit.

2.5 Appendix: Additional details on the observables calculated using the KPM method

Density of States

As mentioned earlier, the density of state (Eq. 2.1) can be calculated through KPM. A few other observables closely related to DOS include the local density of states (LDOS) and typical density of states (TDOS). Local density of states is defined as

$$\rho_i(E_f) = \left[\!\!\left[\sum_n |\langle n|i\rangle|^2 \delta(E_f - E_n) \right]\!\!\right] \tag{2.20}$$

where i is for some basis, which is usually chosen to be real or momentum space. The arithmetic average of LDOS gives back the DOS in Eq. 2.1. If we take a geometric average instead, we arrive at the typical density of states

$$\rho_{typ}(E_f) = \frac{1}{N_H}\left[\!\!\left[\sum_{i}^{N_s} \log \rho_i(E_f) \right]\!\!\right] \tag{2.21}$$

where i randomly samples N_s states from the total N_H states. As is usual for geometric mean, the weight of outliers is significantly suppressed and hence it reflects the typical value of the distribution of $\rho_i(E_f)$. Being a typical measure, it usually suffices to randomly sample $N_s << N$ sites from the complete bases.

The DOS is directly measurable in condensed matter experiments through ARPES [83], and the LDOS (and hence TDOS) can be measured through STM [84]. Once DOS is known, many single-particle properties of the system can be calculated; and it provides some information of many-body physics that the system potentially can host. The TDOS provides information on transport, which helps determine localization-delocalization when compared with DOS.

For different systems, we often consider some quantities derived from the DOS that highlights the properties we are most interested in. For gapped phases, the size of energy gap Δ (or typical gap Δ_{typ}) – the range of E_f where there is no DOS (or TDOS) is often of great interest. The discrepancy between the energy gap and the typical gap can show the range of spectrum with dense but localized states. The gap size can also be useful for understanding the critical behavior near the gap-closing point, as scale invariance connects gap size (Δ) to length scale (ξ) by $\Delta \sim \xi^{-z}$. As length scale diverges at critical point W_c, we have $\Delta \sim \xi^{-z} \sim |W - W_c|^{\nu z}$. This is conveniently applied in Chapter 6.

Another quantity derived from the DOS of interest is the derivative of $\rho(E)$ near $E = 0$. In 2D semimetals for example, the derivative is related to the Dirac velocity v as $\rho'(0) \propto 1/v^2$. The Dirac cone velocity will be an important measure for magic-angle transition in the dissertation. Also, the derivative itself can help locate quantum critical points between semimetal and metallic phases or an avoided one. This will be discussed in Chapter 7.

Likewise, the derivative $\rho(0)'$ can either be calculated by fitting either the Lanczos

histogram or KPM curve. However, it can be conveniently calculated by analytically differentiating the Chebyshev polynomials used in KPM, yielding a better accuracy. In addition, depending on the chosen kernel in KPM, an expansion of the KPM broadening can often produce a convenient expression of derivatives of $\rho(E)$ involving N_c.

Transport properties

Transport properties are often important in studying metal-insulator transitions. We mainly calculate transport based on linear response theory.

When the directions α and β are perpendicular, the formula gives Hall conductivity σ_{xy}. Hall conductivity is quantized and serves as a good proxy for Chern number in topological systems. On the other hand, for parallel α and β such as σ_{xx}, it calculates longitudinal conductivity which is a direct measure distinguishing insulating and metallic phases.

Using the KPM method, assuming the availability of sufficient memory, the calculation of DC conductivity has the same asymptotic complexity as DOS; and even with limited memory, it is still significantly better than other methods to calculate conductivity (like the transfer matrix method). Such an advantage allows us to calculate conductivity for lattice models at very large system sizes.

The fluctuation in conductivity calculation

The situation is a bit more complicated for KPM when the computed quantity intrinsically hosts extreme long-tailed fluctuation. Naively, the fluctuation seems always small relative to the desired value (if we apply central limit theorem naively) and vanishes quickly by increasing lattice site number or increasing N_R for many applications – which is the source of efficiency of KPM. However, when calculating conductivity with a strong need for accuracy (most prominently in Chapter 7), the fluctuation of stochastic trace (and hence the fluctuation of KPM result) becomes important to discuss.

An important limitation of stochastic trace estimation in the context of KPM is often overlooked. When the trace of the expanded operators becomes very small or even, the assumption that backs the $O(1/\sqrt{n \times N_R})$ relative fluctuation breaks. To make things

worth, when $\mathrm{Tr}\,\mathcal{B}$ vanishes, $\mathrm{Tr}(\mathcal{B}^2)$ usually do not vanish. Such a situation happens a lot in the calculation of conductivity because the velocity operator is $v_x \propto [x, H]$ and any operator that can be written as commutator has zero traces. The terms in the form of $T_n(\hat{H})\hat{\sqsubseteq}T_m(\hat{H})\hat{\sqsubseteq}$ for example are 0 when $m-n$ is odd, and very small when m or n is large. In the case of small trace, the fluctuation is only constraint by $O(\sqrt{1/N_R})$, or even $O(\sqrt{n/N_R})$ if the trace does not scale with n. Consequently, $N_R >> n$ is needed for stochastic trace estimation to act better than exact trace – however, an exact trace can be calculated with $N_R = n$. In such a case, the KPM expansion is still useful, but stochastic trace is no longer as powerful.

Interestingly, however, the fluctuation itself can be taken as an observable when calculating conductivity. Take Eq.(1) from [64],

$$\sigma_{\alpha\beta}(\mu, T) = \frac{ie^2\hbar}{N_H}\int d\epsilon f(\epsilon)\mathsf{Tr}\left\langle v_\alpha \delta(\epsilon - H)v_\beta \frac{dG^+}{d\epsilon} - v_\alpha \frac{dG^+}{d\epsilon} v_\beta \delta(\epsilon - H)\right\rangle \tag{2.22}$$

Through the KPM expansion from Eq. 2.6, we have the KPM estimator for the random vector $|\psi_r\rangle$

$$\tilde{\sigma}^{(r)}_{\alpha\beta} = \frac{4e^2\hbar}{\pi N_H}\frac{4}{\Delta E^2}\int d\epsilon \frac{f(\epsilon)}{(1-\epsilon^2)^2}\sum_{m,n}\Gamma_{nm}(\epsilon)\langle\psi_r|\hat{\mu}^{\alpha\beta}_{nm}|\psi_r\rangle \tag{2.23}$$

where $\hat{\mu}^{\alpha\beta}_{nm} = \hat{v}_\alpha T_n H \hat{v}_\beta T_m H$ is the operator product for each moment. As mentioned earlier, KPM calculation takes the advantage of iterative calculation and hence $|\psi_r\rangle$ are always the same for the entire set of m, n. Also, all the calculations outside of the trace evaluation are linear. Thus, we can rewrite

$$\tilde{\sigma}^{(r)}_{\alpha\beta} = \left\langle \psi_r \left| \frac{4e^2\hbar}{\pi N_H}\frac{4}{\Delta E^2}\int d\epsilon \frac{f(\epsilon)}{(1-\epsilon^2)^2}\sum_{m,n}\Gamma_{nm}(\epsilon)\hat{\mu}^{\alpha\beta}_{nm}\right| \psi_r\right\rangle \tag{2.24}$$

The $\tilde{\sigma}^{(r)}_{\alpha\beta}$ is the estimated conductivity using each random vector; and the resulting KPM estimation, the average of all single random vector estimators is

$$\tilde{\sigma}_{\alpha\beta} = \frac{1}{R}\sum_{r=1}^{R}\left\langle \psi_r \left| \hat{\tilde{\sigma}}_{\alpha\beta}\right| \psi_r\right\rangle \tag{2.25}$$

where

$$\hat{\tilde{\sigma}}_{\alpha\beta} = \frac{ie^2\hbar}{N_H}\int d\epsilon f(\epsilon)\left[v_\alpha \delta(\epsilon - H)v_\beta \frac{dG^+}{d\epsilon} - v_\alpha \frac{dG^+}{d\epsilon} v_\beta \delta(\epsilon - H)\right] \tag{2.26}$$

is the KPM estimator operator of $\sigma_{\alpha\beta}$. By Eq. 2.15, we know

$$\frac{1}{R}\mathrm{Var}[\tilde{\sigma}^{(r)}_{\alpha\beta}] = (\delta\tilde{\sigma}_{\alpha\beta})^2 = \frac{1}{R}\,\mathrm{Tr}(\hat{\tilde{\sigma}}^2_{\alpha\beta}) \tag{2.27}$$

In another word, the fluctuation of the single random vector estimators equals to the expectation of the square of conductivity. The square of conductivity, in turn, can be understood as the (basis independent) conductivity fluctuation inside a lattice.

2.6 Appendix: Design of computational workflow

In general, the numerical computation we carry out can be separated into the following stages:

1. Define model
2. Creating operators (Hamiltonian and velocity operator) for the different random realizations
3. Calculate observable for each realization
4. Summarize the result

In order to efficiently utilize computational resources, there are two important considerations.

Firstly, we need to separate the technical details in optimizing the computation from the model define process where we think physics. In particular, the operator creation step can be very inefficient if naively coded; but a fully optimized program takes too much effort to compose and is hard to read. For this purpose, I developed a package *SuperLattice. jl* that aims to minimize the intellectual load to code different models. This part only involves the manipulation of the rules of creating operators (and does not actually create), hence running in negligible computational resources.

The operator creation (step 2) and observable computation (step 3) are the computationally intensive parts, that need tremendous replicates. For both of these two steps and especially for operator creation, the initialization time is significantly longer than the time for processing one set of operators. Moreover, they have very different resource demands. Step 2 is memory demanding (often requires $\sim 100GB$ or more) and not parallelizable inside a single sample; on the other hand, step 3 has a more elastic

demand for memory but can be extremely time-consuming, while it significantly benefits from GPU or multi-threading. Hence, it is beneficial to have dedicated processes that perform steps 2 and3.

However, each calculation of step 3 depends on the output of step 2 as input. A naive directed acyclic graph (DAG) organization of calculation would often leave either the process for step 2 or step 3 waiting. The situation is even worse as each instance of step 2 or 3 can vary up to 100 times in running time because of different parameter, or different configurations of computers. To efficiently utilize available computational resources, I implemented a bounded buffer utilizing the shared file system on clusters, or over HTTP for distributed grids to optimize the loose producer-consumer problem[85].

Chapter 3

The universality of magic-angle semimetals

3.1 Introduction

We start with a study of semimetals under quasiperiodic modulation that drives a quantum phase transition. The motivation of this work comes at the intersection between the theoretical interest of incommensurability physics and the experimental breakthrough surrounding twisted bilayer graphenes.

From a purely theoretical side, quasiperiodicity provides a curious manifestation of Anderson localization without randomness[86]. Such similarity inspired the study of quasiperiodic modulation on cases where random disorder is expected to induce phase transitions. In such cases, novel phase transitions arise that do not have a random-disorder counterpart. For example, Weyl semimetal in 3D is driven by quasiperiodic potential into a transition toward metallic phase well before the onset of Anderson localization [87]. The ability of quasiperiodic modulation to generate eigenstate phase transition that accompanies drastic change in spectrum invites plenty of intriguing theoretical questions, among which is the universality: how general is such a transition?

Such a question resonated just in time with the experimental breakthroughs. In the past decades, the engineering of band structures with non-trivial topological wave functions has achieved success in creating and controlling quantum phases in a variety of systems such as doped semiconductors [88, 89, 90, 91], ultracold atoms [92, 93], and metamaterials [94, 95]. In the last few years, the advance in twisted graphene heterostructores [55, 96, 54, 97], as well as other two-dimensional van der Waals heterostructures in general (i.e. "twistronics") further allowed new, strongly interacting, solid state systems can now also be engineered with a rather weakly correlated two-dimensional semimetal exemplified by graphene [98, 99, 100]. In these systems, as a

consequence of the quenched kinetic energy, correlations dominate the physics and exotic many-body states may form. This interpretation relies on the reduction of the electronic velocity and large increase of the density of states (DOS) which was shown in twisted bilayer graphene (TBG) theoretically [101, 2, 102, 103] and experimentally [104, 105, 106] prior to the more recent groundbreaking discoveries in Refs. [55, 54, 96]. Understanding the essential single-particle ingredients necessary to build emulators of TBG can help shed light on the strong coupling regime where consensus about the form of an effective low-energy description remains elusive [107, 108, 109, 110, 111, 112, 113]. Despite of the lack of full understanding of the physics of magic-angle twisted bilayer graphenes, the development of moirè pattern that spans a huge number of unitcells is understood to take a central role in the magic of TBG.

The finite moirè pattern, as we explained earlier in Chapter 1, can be thought of as a finite size approximation of quasiperiodicity. The quench of velocity is also exactly what marks the semimetal to metal transition in the 3D case in [87]. Hence, we attempt to draw a connection between the metallic phase theoretically found in quasiperiodic semimetals and the magic-angle twisted bilayer graphene.

This universality is the main theme of this chapter. We studied a variety of models of semimetal (i.e. have a node in the band structure) in different dimensions, with an incommensurate modulation. We will call those "magic-angle semimetals" as they generalize magic-angle TBG. A theory for twistronic emulators is developed by first distilling the basic physical phenomena that create correlated flat bands out of two-dimensional Dirac cones. Generically, *quasiperiodicity* that respects the symmetry protecting the Dirac nodes creates flat bands in nodal, semimetallic band structures in a universal fashion near a previously unnoticed single particle quantum phase transition (QPT)—what we call the "magic-angle" in analogy to TBG. At small angles in TBG, a single scattering wavevector accounts for the majority of the band flattening [2, 3] but misses any QPT. With quasiperiodicity, an infinite sequence of higher wavevectors (i.e., Brillouin zone downfoldings) further flatten the bands and culminate into a QPT. This band flattening occurs irrespective of the topology present, and in fact, many of the models we study have topology distinct from TBG [108]. We demonstrate strong

correlations by computing Wannier states within this series of bands; these lead to a Hubbard model with a quenched kinetic energy and relative to this, the interaction scale is increased dramatically. We therefore argue that the single particle quantum critical state is unstable towards the inclusion of interactions, which form a correlated insulator at half filling.

Crucially, our findings are independent of many of the system's details and, therefore, demonstrate the existence of a wide multitude of engineered, strongly-coupled quantum systems that we call *magic-angle semimetals*. To demonstrate this, we classify the family of these models with symmetry protected nodes (including chiral TBG at moderate twist angles) as well as introduce and solve a series of models; most of which can be straightforwardly realized with existing ultracold atom, trapped ion, and metamaterial experimental setups. Thus, the universaility we highlight in this chapter proposes a simple route to emulate the phenomena of magic-angle TBG in a wide variety of quantum many body systems [114, 100], including but not limited to cold-atomic, trapped ion, and metamaterial systems. As a particular example, we discuss how to observe this effect in an ultracold Fermi gas. We show that the magic-angle effect can be observed at experimentally relevant time scales and temperatures in interacting ultracold Fermi gases through measurements of wavepacket dynamics.

3.2 'Magic-angle semimetals'.

The whole class of magic-angle semimetal models are governed by Hamiltonians of the form

$$\hat{H} = \hat{T} + \hat{V} + \hat{U} \tag{3.1}$$

containing single particle hopping $\hat{T}$, a quasiperiodic modulation $\hat{V}$ (such as potential scattering or interlayer tunneling), and inter-particle interactions $\hat{U}$. The kinetic term $\hat{T}$ has isolated nodal points in the Brillouin zone where the DOS vanishes in a power-law fashion (i.e. semimetallic). The quasiperiodicity in $\hat{V}$ is encoded in an *angle* originating either from twisted bilayers or the projective construction of quasicrystals [115], and it is characterized by an amplitude W and an incommensurate modulation Q (or twist

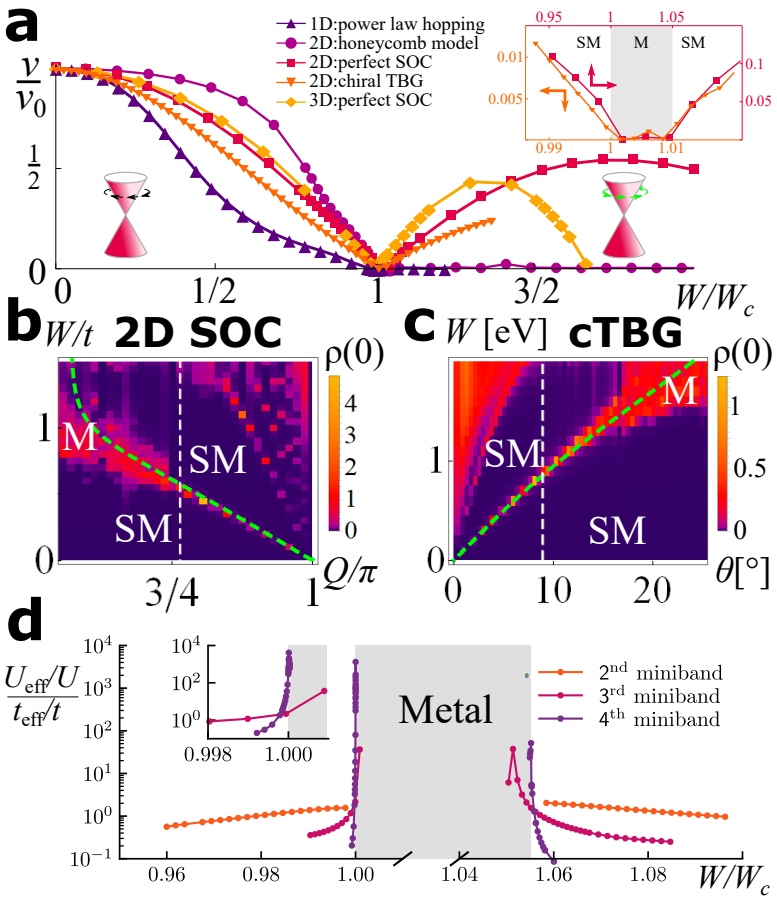

Figure 3.1: **Magic-angle transition.** A quasiperiodic potential or tunneling generically drives an eigenstate quantum phase transition from a semimetal (SM) to metal (M). **a**. For many models, the velocity at the Dirac node v decreases with the strength of the potential W until it reaches $v = 0$ at the transition, W_c; this is an indication of the flattening of the bands. In some cases an intermediate metallic phase (see inset) separates a reentrant semimetal with a reversed helicity (depicted by the Dirac cones). **b, c** We construct a phase diagram in terms of potential strength W (interlayer tunneling for cTBG) and quasiperiodic modulation Q (twist angle θ for cTBG) by computing the density of states at zero energy $\rho(0)$; analytical perturbative results [see Eq. (3.9), Section 3.8.1 and [2, 3]] are represented by the green dashed lines. Cuts along the dashed white lines are presented in Fig. 3.2**c**,**d**. Color bars represent $\rho(0)$ and with widths **b:** 5, and **c:** 1.25 and dark purple represents the value 0 on both. **d**. An infinite number of semimetal minibands form as the transition is approached; each has higher effective interaction than the last as we approach the transition. For 2D SOC, we construct exponentially localized Wannier states on the first four minibands (see Fig. 3.4) leading to a model with an effective, strongly renormalized Hubbard interaction $U_{\text{eff}}/t_{\text{eff}}$ in terms of the bare interaction U/t.

angle θ).

Generalizing the physics of the first magic angle of TBG to magic-angle semimetals results in the phenomena summarized by Fig. 3.1. First, increasing W quenches the kinetic energy, reducing the Dirac velocity v until it ultimately reaches zero at the single-particle quantum critical point (where the DOS becomes nonanalytic). The velocity vanishes in a universal manner characterized by critical exponents that are distinct in each dimension. Second, the DOS and wave functions display a transition from a ballistic semimetal to a metallic phase; this is a so-called 'unfreezing' transition in momentum space, which represents a non-standard form of delocalization [37]. For a subset of magic-angle semimetals [including Eqs. (3.2) and (3.3) below], the semimetal reenters at a second transition W_c' with a reversed sign of the helicity at each Dirac node [116]; for general Q (or θ), multiple semimetal-metal-semimetal transitions can appear as W is tuned, see Figs. 3.1**b**, **c**. Third, the quenched kinetic energy implies a divergence of the dimensionless interaction coupling constant, Fig. 3.1**d**, leading to exotic many-body states. Importantly, these effects occur generically under the necessary condition that the quasiperiodic modulation respects the symmetries which protect the semimetallic touching points (as discussed in Section 3.8.4).

3.2.1 Effective models.

A variety of effective models illustrate our proposal. Among them, we especially focus on two models: a 2D tight-binding Hamiltonian of "perfect" spin-orbit coupling (SOC) on a square lattice and a lattice model of TBG at moderate twist angles ($\theta \approx 9^\circ$) in the chiral limit (cTBG) that disallows interlayer tunneling between equivalent sublattices [3] (we fix the bare lattice spacing to unity and $\hbar = 1$). Nonetheless, our main conclusions also apply to TBG beyond the chiral limit for similar twist angles. (Here, we consider the chiral limit of TBG as it provides the clearest presentation of magic-angle criticality but such a transition can also be shown to persist in the full TBG model. This study will appear elsewhere.) The SOC model is given by a hopping

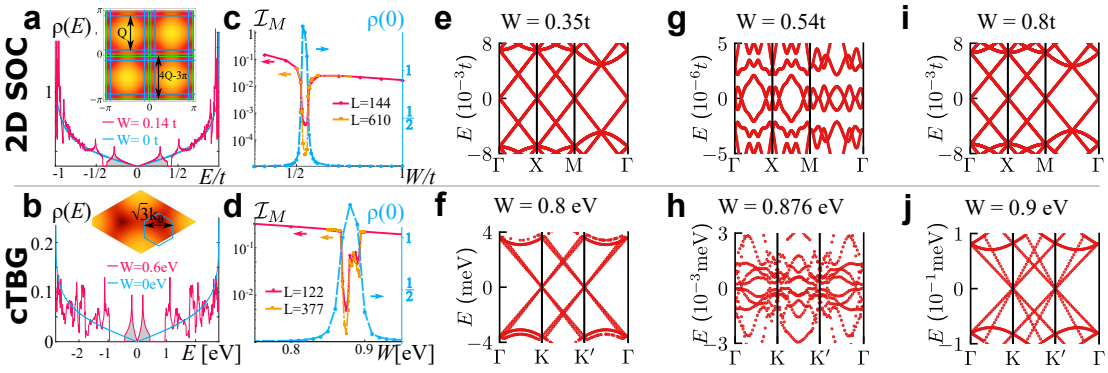

Figure 3.2: **Eigenstate transition as manifested in the single particle spectrum**. Panels **a,b**: DOS $\rho(E)$ in units of $(tL^2)^{-1}$ averaged over 300 realizations of phases ϕ_μ and random twisted boundary conditions. The gray shading represents the number of states in the first miniband and matches the area of the mini Brillouin zones around each Dirac point produced by the leading scattering vectors depicted in the inset of **a, b** (we chose a rhombic representation of the Brillouin zone of TBG such that $\mathbf{k} = k_1\mathbf{G}_1 + k_2\mathbf{G}_2$ for reciprocal lattice vectors $\mathbf{G}_{1,2}$ of graphene). Panels **c, d**: Cuts along the dashed white lines of the phase diagram in Fig. 3.1**b,c**, displaying $\rho(0)$ and $\mathcal{I}_M(q = 2, L)$ [Eq. (3.10)]. These illustrate sequences of semimetallic and metallic transitions concomitant with momentum space delocalization (see Fig. 3.3). Panels **e - j**: The twist dispersions illustrate the difference between semimetallic phases (**e,f,i,j**) and the metallic phase (**g,h**) as well as the remarkably reduced bandwidths (note the reduced scale). The 2D SOC (cTBG) data were obtained for $Q = 2\pi F_{n-2}/F_n$ ($\theta = 2\arcsin(\sqrt{3}F_{n-5}/[2F_n])$) at $L = 144$ ($L = 377$) and KPM expansion order $N_C = 2^{12}$ ($N_C = 2^{13}$) in the calculation of the DOS while $L = 233$ in panels **e - j**.

$\hat{T}_{\rm SOC} = t/2\sum_{\vec{r},\mu}(ic^\dagger_{\vec{r}}\sigma_\mu c_{\vec{r}+\hat{\mu}} + \text{h.c.})$ and a quasiperiodic potential

$$\hat{V}_{\rm SOC} = W\sum_{\vec{r},\mu=x,y}\cos(Qr_\mu + \phi_\mu)c^\dagger_{\vec{r}}c_{\vec{r}}, \tag{3.2}$$

where the σ_μ are Pauli matrices, $c_{\mathbf{r}}$ are two-component annihilation operators, t is the hopping strength, and ϕ_μ is the offset of the origin. The lattice model that captures the low-energy theory of cTBG at incommensurate twist angles contains $\hat{T}_{\rm cTBG}$ that describes nearest neighbor hopping (amplitude $t = 2.8\,\text{eV}$) on the honeycomb lattice. The interlayer tunneling in the chiral limit is given by

$$\hat{V}_{\rm cTBG} = W\sum_{\mathbf{r},\mu}\Bigg[\cos(\mathbf{q}_\mu\cdot\tfrac{\mathbf{r}+\mathbf{r}_\mu}{2} + \phi_\mu)c^\dagger_{1A\mathbf{r}_\mu}c_{2B\mathbf{r}} - \sum_{n=1}^{6}\tfrac{(-1)^n}{3\sqrt{3}}\sin(\mathbf{q}_\mu\cdot\tfrac{\mathbf{r}+\mathbf{r}_{\mu n}}{2} + \phi_\mu)c^\dagger_{1A\mathbf{r}_{\mu n}}c_{2B\mathbf{r}} + (A\leftrightarrow B)\Bigg] + \text{h.c.} \tag{3.3}$$

where $c_{lA/B\mathbf{r}}$ annihilates an electron on layer l, sublattice A/B, and position $\mathbf{r}$. The index $\mu = 1, 2, 3$ labels nearest neighbors such that $\mathbf{r}_1 - \mathbf{r} = (0, 1)$ $[\mathbf{q}_1 = k_\theta(0, -1)]$ with $\mathbf{r}_\mu - \mathbf{r}$ $[\mathbf{q}_\mu]$ being 120° rotations of the previous vector. The positions $\mathbf{r}_{\mu n} = \mathbf{r}_\mu + \mathbf{a}_n$ where $\mathbf{a}_1 = (\sqrt{3}/2, 3/2)$ and each subsequent $\mathbf{a}_n$ is a 60° rotation of the last (i.e. labeling nearest neighbors on the triangular Bravais lattice). Last, $|\mathbf{q}_\mu| = k_\theta = \frac{8\pi}{3\sqrt{3}} \sin(\theta/2)$ encodes the twist angle, and $\sum_\mu \phi_\mu = 0$ to satisfy C_6 symmetry. Typically the offsets ϕ_μ in either model are averaged over. The kinetic part $\hat{T}_{\text{SOC}}$ ($\hat{T}_{\text{cTBG}}$) has a momentum-space dispersion with four (two) Dirac nodes and a velocity $v_0 = t$ ($v_0 = 3t/2$), see Fig. 3.2**a** (3.2**b**) inset. Returning to Eq. (3.2), we see that Q replaces the role of the twist angle in Eq. (3.3); unless otherwise stated, we highlight incommensurate effects by taking $Q = 2\pi/\varphi^2$ ($\theta = 2\arcsin(\sqrt{3}/2\varphi^5) \approx 8.96°$) where φ is the golden ratio, and in numerical simulations we employ rational approximants $Q_n \equiv 2\pi F_{n-2}/F_n$ (k_θ is approximated using continued fractions) where the system size $L = F_n$ is given by the nth Fibonacci number [116]. Other values, in particular smaller $\pi - Q$ and θ, are discussed below. In the low-energy approximation this model is identical to the continuum model studied in Ref. [3] where exact flatbands are uncovered and explained; this makes this model ideal to study incommensurate effects on the lattice.

In addition to Eqs. (3.2) and (3.3) we have studied a multitude of other d-dimensional models in an incommensurate potential, including the π-flux model, the honeycomb model in 2D, a 3D variant of Eq. (3.2) (studied previously in Ref. [116]), and a 1D long range hopping model.

The Hamiltonian for the π-flux model has the same potential term in 2D. The hopping term is modified as follows

$$\hat{T}_\pi = -t \sum_{\vec{r},\mu=x,y} [c^\dagger_{\vec{r}} e^{iA_\mu(\vec{r})} c_{\vec{r}+\hat{\mu}} + \text{h.c.}], \tag{3.4}$$

where we choose the gauge with $A_x(\vec{r}) = \pi/2$ for all sites $\vec{r}$ on the square lattice, and $A_y(\vec{r}) = -(-1)^{r_x}\pi/2$. For the chosen gauge, periodic boundary conditions require the lattice size in x direction to be even.

The spinless honeycomb (HC) lattice model is given by a Hamiltonian of the form

$$\hat{T}_{\rm HC} = -t\sum_{\vec{r}_A,i}[c_A^\dagger(\vec{r}_A)c_B(\vec{r}_A+\vec{d}_i)+\text{h.c.}], \tag{3.5}$$

$$\hat{V}_{\rm HC} = W\sum_{\vec{r},\boldsymbol{\delta}_\mu}\cos(Q\vec{r}\cdot\boldsymbol{\delta}_\mu+\phi_\mu)c_{\vec{r}}^\dagger c_{\vec{r}}. \tag{3.6}$$

The sum over $\vec{r}_A$ is over one of the two sub-lattices, while $\vec{r}$ is over all points. The index i labels the three nearest neighbors of $\vec{r}_A$, and $\vec{d}_i$ is the vector from $\vec{r}_A$ to its nearest neighbor i. The vectors $\boldsymbol{\delta}_\mu$ are a choice of each particular model and for numerics we choose $\boldsymbol{\delta}_1=\vec{d}_1=(2/3)\hat{x}$ and $\boldsymbol{\delta}_2=\vec{d}_2=-(1/3)\hat{x}+(1/\sqrt{3})\hat{y}$.

The kinetic part of the Hamiltonian for the one dimensional model with power law dispersion [24] $E=-t\,\text{sign}(\cos k)|\cos k|^\sigma$ is given in momentum space as mentioned in Chapter 1:

$$\hat{T}_{1D}=-t\sum_k \text{sgn}[\cos(k)]|\cos(k)|^\sigma c_k^\dagger c_k.$$

We assume $\sigma<1$, this expression can be readily Fourier transformed to a tight binding model with long range hopping (LRH). This yields a hopping amplitude

$$t_{ij}\sim -2t[1-(-1)^{|i-j|}]\sin[\pi(|i-j|-\sigma)/2]\Gamma(1+\sigma)|i-j|^{-(1+\sigma)} \tag{3.7}$$

for $|i-j|\gg 1$ and $\Gamma(x)$ is the Gamma function. The potential is

$$\hat{V}_{1D}=W\sum_r\cos(Qr+\phi)c_r^\dagger c_r. \tag{3.8}$$

Note that in this 1D case, v is not a velocity .

Each of these models generates flat bands and magic-angle physics similar to TBG. Importantly, these semimetallic 2D Dirac points have been realized in cold atomic setups using either a honeycomb optical lattice [117, 118] or artificial gauge fields [119, 120, 121], whereas the 1D model we consider can be realized using trapped ions [122]. The 3D variant of Eq. (3.2) is theoretically possible to implement [123, 124, 125], but has not been experimentally realized yet. In each of these experimental setups, quasiperiodic potentials can then be realized, e.g. by additional lasers [51], programmable potentials [52], or a digital mirror device [126]. Alternative emulators of Dirac semimetals can also be realized in metamaterials, e.g. in topolectrical circuits [94] or in arrays of electromagnetic microwave resonators [53]. Quasiperiodicity can then be encoded through the spatial modulation of the electrical circuit elements.

3.3 Single-particle spectrum and velocity renormalization.

We first discuss the spectral characteristics of magic-angle semimetals probed through the DOS, defined as $\rho(E) = [\![1/N_H \sum_i \delta(E - E_i)]\!]$ where E_i is the ith eigenenergy and N_H is the size of the single particle Hilbert space. The double-bracket $[\![...]\!]$ represents average across all samples when relevant. At weak quasiperiodic modulation the semimetal is stable, i.e. $\rho(E)$ vanishes at zero energy with the same power law as in the limit of $W = 0$, while hard spectral gaps and van Hove singularities develop at finite energy. For Weyl and Dirac Hamiltonians the low-$|E|$ DOS obeys $\rho(E) \sim v^{-d}|E|^{d-1}$, and as W increases, the $(d-1)$st derivative of the DOS [$\rho^{(d-1)}(0) \propto 1/v^d$] increases, see Fig. 3.2**a**, **b** for the model in Eqs. (3.2) and (3.3), respectively. These weak coupling features may be understood at the level of perturbation theory.

We find that gaps appear at finite energy due to the hybridization around Dirac nodes a distance Q (or $\sqrt{3}k_\theta$) away in momentum space, see the insets in Fig. 3.2**a** and **b**, inset. For the SOC (cTBG) model, this process "carves out" a square (hexagon) around each Dirac cone which contains $2[(\pi - Q)L/2\pi]^2$ ($4[3\sqrt{3}k_\theta L/4\pi]^2$) states. For a given *incommensurate* Q or θ, there is an infinite sequence of relevant orders in perturbation theory that produce quasi-resonances and open up gaps near zero energy, forming minibands; this is in contrast to the *commensurate* case when this sequence is finite. For example, for 2D SOC and $Q = 2\pi/\varphi^2$, the infinite sequence is given by half the even Fibonacci numbers $F_{3n}/2$, which is the sequence $1, 4, 7, 72, 305, \ldots$ (see Section 3.8.3). In the incommensurate limit, near the magic-angle transition this sequence of gaps produces a corresponding sequence of minibands, shown in Fig. 3.1**d** for the second, third, and fourth. We explore the effect of this sequence of minibands using superlattices in Sec. 3.5.

Similar to TBG, the renormalization of the velocity in the 2D SOC model can be analytically determined using fourth-order perturbation theory (details in Section 3.8.1) [2]. In terms of the dimensionless coupling constant $\alpha = W/[2t\sin(Q)]$ for Eq. (3.2) this yields

$$\frac{v(W)}{v(0)} = \frac{1 - 2\alpha^2[1 - \cos(Q)] + \alpha^4 \frac{4 - 5\cos(Q) + 6\cos(2Q)}{\cos(Q)}}{1 + 4\alpha^2 + \alpha^4\{16 + [2 + 1/\cos(Q)]^2\}}. \tag{3.9}$$

The root of the numerator captures the first magic-angle transition line well when $Q > \pi/2$, see Fig. 1**b**, independently of whether Q is commensurate or incommensurate. To describe additional magic-angles, as observed in our numerical data in Fig. 3.1**b**,**c**, higher order perturbation theory is required. For reentrent semimetallic phases, Eq. (3.9) indicates the reversal of the Berry phase, consistent with the inversion of miniband states in 3D [116]. In each model we have considered for $d > 1$, we have found that the perturbative expression for the velocity (summarized in Table 3.1) has a magic-angle condition where the velocity vanishes.

As the magic-angle is approached, higher perturbative corrections become relevant. To go beyond perturbation theory, we compute the DOS using the numerically exact kernel polynomial method (KPM), on sufficiently large system sizes across a range of models of various dimensions. At a critical $\alpha = \alpha_c \sim 1$ the DOS becomes non-analytic and a metallic spectrum with finite $\rho(0)$ develops for $\alpha > \alpha_c$, see Fig. 3.2**c,d** (for cTBG $\alpha = \frac{W}{2t\sin(3k_\theta/4)}$). In particular, for $d > 1$ and fixed Q or θ, $\rho(E) \sim |W - W_c|^{-\beta}|E|^{d-1}$ implying the velocity $v(W) \sim |W - W_c|^{\beta/d}$. Surprisingly, we find $\beta \approx 2$ in each model investigated above 1D [116], indicating that this exponent is universal. In 1D this magic-angle effect also exists but is modified by the form of the dispersion such that $\rho(E) \sim |W - W_c|^{-\beta}|E|^{1/\sigma-1}$, and for the case $\sigma = 1/3$ we find $\beta = 4.0 \pm 0.8$.

This velocity renormalization is the manifestation of the aforementioned reconfiguration of the band structure and the appearence of a sequence of minibands. Of course, broken translational symmetry precludes a standard bandstructure of dispersive Bloch waves. In Fig. 3.2 **e-j** we therefore illustrate this reconfigured bandstructure, at a fixed rational approximant, in the form of the twist dispersion (obtained by exact diagonalization in the presence of twisted boundary conditions) along high symmetry lines for the models defined in Eqs. (3.2), (3.3). We performed the analogous analysis for a multitude of models and plotted the velocity $v(W)$ near the semimetallic touching points in Fig. 3.1**a**. The velocity $v(W)$ as determined by computing the twist dispersion agrees with the calculation of $\rho^{(d-1)}(0)$.

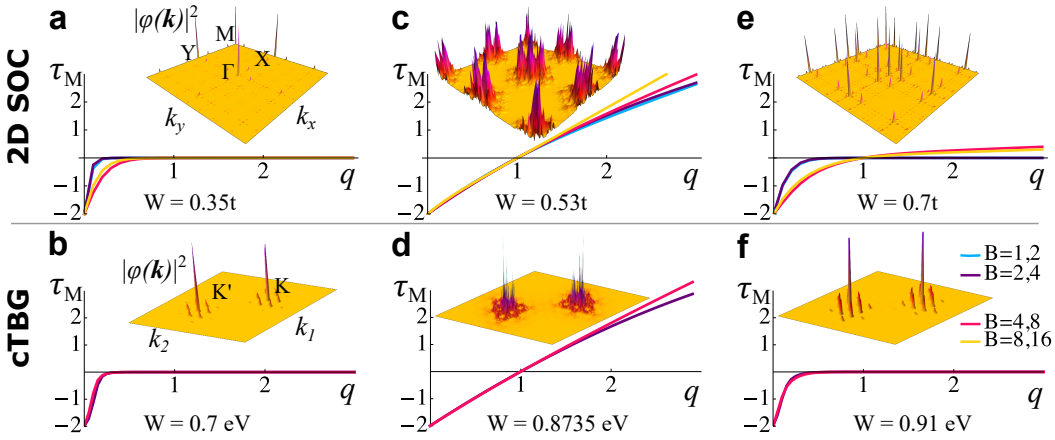

Figure 3.3: **Eigenstate transition as manifested in momentum space wave functions at the Dirac node energy $E = 0$.** Panels **a** - **f**: Wave function characteristics as described by the scaling exponent $\tau_M(q)$ averaged over 100 random phases and twisted boundary conditions. For $W < W_c$ and $W > W_c'$ the wave functions are ballistic [with a frozen $\tau_M(q)$] while for $W_c < W < W_c'$ they are critical in momentum space [$\tau_M(q)$ is weakly non-linear in q]. Inset of **a** - **f**: corresponding momentum space wavefunctions. The 2D SOC (cTBG) data were obtained for $Q = 2\pi F_{n-2}/F_n$ ($\theta = 2\arcsin(\sqrt{3}F_{n-5}/[2F_n])$) at $L = 144$ ($L = 377$).

3.4 Critical single-particle wave functions

Magic-angle semimetals are intimately linked to the physics of Anderson transitions in momentum space; this is captured by the eigenfunctions near the Dirac node energy, $E = 0$ [116].

We compute the low-energy wavefunctions using Lanczos for large L reaching up to $L = 377$ and 610 in the cTBG and SOC models, respectively. Qualitatively, we find that the structure of the wave functions in the semimetallic phase is stable and adiabatically connected to the ballistic $W = 0$ limit, with isolated ballistic spikes in momentum space, see Fig. 3.3**a**,**b**. In contrast, the form of the wave functions is completely different in the metallic state, see Fig. 3.3**c**,**d**, as it appears delocalized both in momentum and real space with non-trivial structure. Finally, in the reentrant semimetal, the wave functions are again ballistic, see Fig. 3.3**e**,**f**. Crucially, in all models that we studied, the positions of the transitions in the spectral properties of the DOS coincide with the transitions of the wave functions characteristics within numerical resolution, see Figs. 3.2**c**,**d**.

In order to quantify the eigenstate QPTs of the wave functions, we generalize the

multifractal wave function analysis [37] to momentum space. We define the inverse participation ratio of the energy eigenstates in momentum space [116] $\psi_E(\vec{k})$ at a given energy E

$$\mathcal{I}_M(q,L) = \sum_{\vec{k}} |\psi_E(\vec{k})|^{2q} \sim L^{-\tau_M(q)}. \tag{3.10}$$

We can now apply properties of the scaling exponent $\tau_M(q)$, typically used to analyze real space localization, to momentum space. It monotonically increases [obeying $\tau_M(0) = -d$ and $\tau_M(1) = 0$] and distinguishes delocalized wave functions [$\tau_M(q) = d(q-1)$] from exponentially localized peaks [$\tau_M(q>0) = 0$] and critical states with nonlinear "multifractal" $\tau_M(q)$. A variant of multifractal states, which are called "frozen," display $\tau_M(q > q_c) = 0$ for a given $q_c \in (0,1]$; their peak height is system size independent, as in standard localized states, but show multifractal correlations in their tails [37]. We employ the standard binning technique (varying the binning size B) to numerically extract the scaling exponents $\tau_M(q)$ in systems of a given finite size.

Focusing on $q = 2$, as shown in Fig. 3.2**c**, **d** for the SOC and cTBG models, respectively, the momentum space wavefunction at the Dirac node energy delocalizes upon crossing the magic-angle in the incommensurate limit. The momentum space delocalization can not occur in the commensurate case; Bloch's theorem ensures the existence of states with well defined (i.e. well localized) crystalline momenta. For example, consider Eq. (3.2) in the commensurate limit where $Q/2\pi = a/b$ (a and b are coprime integers). In this case, $\mathcal{I}_M(q,L)$ is bounded from below by $1/b^{d(q-1)}$ and hence $\tau_M(q) = 0$ in the thermodynamic limit $L/b \to \infty$ preventing momentum space delocalization. In contrast, we here numerically access the incommensurate limit using finite size scaling of rational approximants corresponding to $L = b \to \infty$.

The scaling analysis of $\mathcal{I}_M(q,L)$ at the energy of the Dirac node $E = 0$, presented in Figs. 3.3**a-f** for Eqs. (3.2) and (3.3), demonstrates three phases of distinct wavefunction structures in momentum space. A frozen spectrum $\tau_M(q)$ occurs in the two semimetal regimes. In sharp contrast, the function $\tau_M(q)$ unfreezes in the metallic phase with finite $\rho(0)$. Surprisingly, throughout the metallic phase the spectra appear to be weakly multifractal in both momentum and real space, we find for the

SOC model that $\tau_M(q) \approx 2(q-1) - 0.25q(q-1)$ and for the cTBG model we obtain $\tau_M(q) \approx 2(q-1) - 0.15q(q-1)$ (in the region $|q| < 1$ and within the limits of our numerical precision) in Fig. 3.3**c**,**d**, which are both *non-linear* in q. The observation of similar behavior in all models that we investigated corroborates the interpretation of the magic-angle phenomenon in the incommensurate limit as one of eigenstate quantum criticality and generalizes the quasiperiodic 3D Weyl semimetal-to-diffusive metal QPT [116] to arbitrary dimensions. In two dimensions we do not find any signatures of diffusion (consistent with the marginality of two dimensions [36, 86]) and in one dimension the semimetal transitions directly to an Anderson insulator. Lastly, when $d > 1$ and W is substantially larger than the magic-angle transition, all investigated models undergo Anderson localization in real space (e.g. at $W > 1.75t$ in the case of the 2D SOC model at $Q = 2\pi/\varphi^2$).

3.5 Commensurate superlattices and Hubbard models.

So far, our analysis regarded non-interacting magic-angle semimetals in the strict incommensurate limit. We now turn to the interparticle interaction term $\hat{U}$ in the Hamiltonian in Eq. (3.1) in commensurate superlattices. In order to illustrate how the appearance of flatbands enhances correlations, we construct a series of emergent Hubbard models near the magic-angle transition for Eq. (3.2) at $\phi_\mu = \pi/2$ supplemented by

$$\hat{U}_{SOC} = U \sum_{\mathbf{r}} n_{\mathbf{r},\uparrow} n_{\mathbf{r},\downarrow}, \tag{3.11}$$

with $n_{\mathbf{r}\sigma} = c^\dagger_{\mathbf{r}\sigma} c_{\mathbf{r}\sigma}$. In contrast to the previous discussion, we take commensurate approximations in order to build translationally invariant Hubbard models. In particular, we still use the rational approximants $Q_n = 2\pi F_{n-2}/F_n$, only now we take the size of the system $L = mF_n$ for some integer m, effectively taking the thermodynamic limit in L before the limit of quasiperiodicity $Q_n \to Q$. This is reminiscent of moiré lattices used to model TBG, and similarly, we can unambiguously define a supercell of size $\ell = F_n$ and isolate bands in k-space.

In particular, these bands are intimately related to the hierarchy of minibands derived with perturbation theory: when $\ell = F_{3a+b}$ for integers a and $b = 1, 2$, the gap for

the central band opens at order $F_{3a}/2$ in perturbation theory (for $\ell = F_{3a}$, the Dirac nodes gap at order $F_{3a}/2$ as discussed in Section 3.8.3). The series of superlattices indicated by ℓ correspond to the sequence of gap openings in Section 3.3 — making the notion precise — with (downfolded) Brillioun zones depicted in Fig. 3.4**b**. Near W_c, hard gaps open and the minibands form as illustrated in Fig. 3.4**a** for $\ell = 13, 55, 233$ (respectively, the 2nd, 3rd, and 4th minibands). We conjecture that all of these minibands (as $\ell \to \infty$) achieve gaps near W_c as evidenced by Fig. 4**a,c** in the incommensurate limit, indicating something akin to the singular continuous spectrum of the Aubry-André model at criticality [127]. Furthermore, the central band becomes flatter, as indicated by the reduction in bandwidth seen in Fig. 3.4**c** which we track until the dispersion loses its semimetallic character.

We exploit this miniband formation and the existence of hard gaps to build symmetric Wannier functions in the semimetallic regime, see Fig. 3.4**d**. To build the Hubbard models, we perform approximate joint diagonalization on the position operators ($\hat{x}_\mu$) projected (with projection operator P) onto a given band $\hat{X}_\mu^{\mathrm{MB}} \equiv P\hat{x}_\mu P$ in order to determine the Wannier states [128]. We have checked that not only are the computed Wannier states exponentially localized to numerical precision (Fig. 3.4**d**, inset), but that they are also symmetric. Therefore, the minibands formed from the SOC model and pictured in Fig. 3.4 are *not* topological [129], fragile [130, 131] or otherwise.

As a clear example, when $W = 0.5t$ and $(\ell, m) = (13, 8)$, we see a clear band around $E = 0$ in Fig. 3.4**a**, and we find Wannier centers in a well defined grid (Fig. 3.4**d**, main panel) corresponding to exponentially localized Wannier states (Figs. 3.4**d**, inset). The projected Hamiltonian has the approximate form of Eqs. (3.2) and (3.11) with a renormalized U_{eff}, t_{eff} and $W_{\mathrm{eff}} = 0$. With this approach, we can identify successive gaps leading up to the metallic transition from either side along with dramatic enhancements of interactions, which reach up to a massive $U_{\mathrm{eff}}/t_{\mathrm{eff}} \sim 4100U/t$ for the fourth miniband with supercell $\ell = 377$, as shown in Fig. 3.1**d**. This can also been shown analytically using a one step renormalization group calculation, which yields the divergence $U_{\mathrm{eff}}/t_{\mathrm{eff}} \sim U(1/\ell)^{d-1}Z^2/v \sim 1/|W - W_c|$, ($\sqrt{Z}$ is the wave function renormalization), as shown in detail in Section 3.8.2. Due to finite size, the apparent location of W_c can

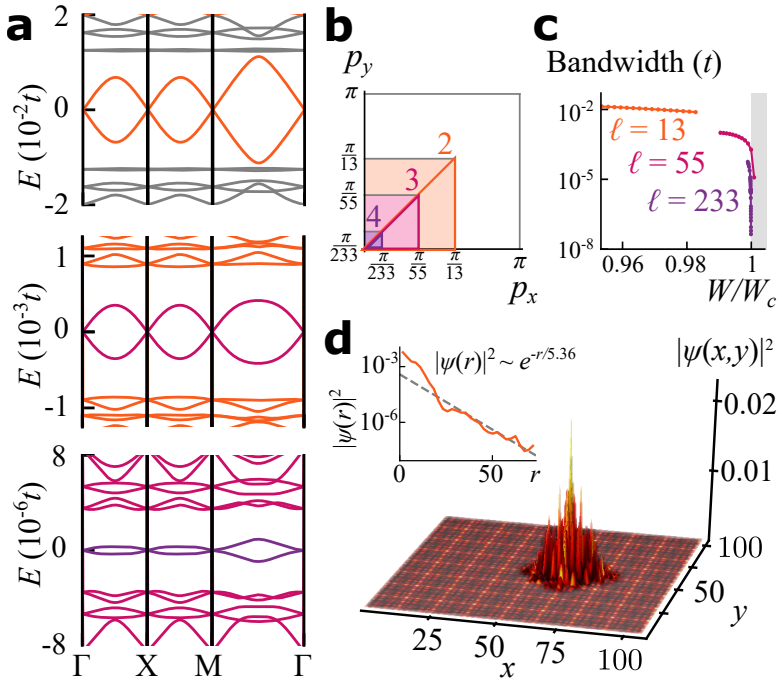

Figure 3.4: **Supercell analysis and Wannier functions.** The color coding matched across **a**–**c** (and Fig. 3.1**d**) indicates the 2nd (orange), 3rd (maroon), and 4th (purple) minibands. **a**. The dispersion of Eq. (3.2) in the mini-Brillouin zone for superlattices $(\ell, W) = (13, 0.5), (\ell, W) = (55, 0.5244), (\ell, W) = (233, 0.5244)$ (from top to bottom); this illustrates successive emergence of minibands (from top-to-bottom) as a consequence of consecutive downfoldings of the Brillouin zone. **b**. The corresponding mini-Brillouin zones (logarithmic scale). **c**. The dramatic reduction in bandwidth near the critical point for each miniband. **d**. For $(\ell, W) = (13, 0.5)$ and $L = 104$, computed Wannier function $\psi(x, y)$ that is sitting upon the local density of states $\rho_{\text{band}}(\mathbf{r}) = \sum_n |\langle \mathbf{r}|E_n\rangle|^2$ (shown as a density plot) for eigenstates of the (orange) band $|E_n\rangle$, on a 104×104 lattice. (Inset). The exponential localization of the Wannier state.

artificially shift, therefore in Fig. 3.1**d** we use $W_c = \tilde{W}_c \frac{\sin Q}{\sin Q_n}$ where $\tilde{W}_c$ is the transition point when $n \to \infty$.

Away from $E = 0$, nearly flat (semimetallic) bands can form well before the magic-angle transition with similarly large $U_{\text{eff}}/t_{\text{eff}}$, see Fig. 3.4**a**. In very close proximity to the transition, multi-orbital Hubbard models appear.

3.6 Experimental cold atomic realization

All sufficient ingredients for emulating magic-angle phenomenon are available in ultra-cold atomic gas and metamaterial [132, 53] experiments. In particular for ultra-cold atomic gases, to probe fermionic strong correlations, the atomic species ^{40}K and ^{6}Li are prime candidates; we estimate that the underlying lattice can be relatively shallow (around 8 lattice recoil energies), and need temperatures relative to the Fermi temperature (of the entire gas) $T/T_{\text{F}} \approx 0.25$ to ensure fermion population fills but does not exceed the first miniband. To see large correlations, trap sizes should accommodate at least roughly 30×30 optical lattice sites. In addition to any spectroscopic measurements that probe the density of states (e.g. radiofrequency spectroscopy [133]), we propose that the analysis of wavepacket dynamics is an indicator of magic-angle physics. In the absence of interactions, we numerically predict a non-monotonic spreading of the wave function for increasing W in the regime with multiple magic angles. We have also studied the interacting model in the hydrodynamic regime by using a generalization of the Boltzmann kinetic equation [134] . Its solution confirms the drastic decrease of the expansion velocity and a substantial enhancement of diffusive dynamics near the magic angle, see Fig. 3.5. The observation of these effects is possible within experimentally realistic observation time of $50t^{-1}$ ($\sim$10–100 ms). Moreover, our work demonstrates an experimental protocol for realizing strong correlations by first cooling the gas to quantum degeneracy and then applying a quasiperiodic potential to create flat bands without the need to cool the system in a Mott insulator phase or load the atoms into a flat band.

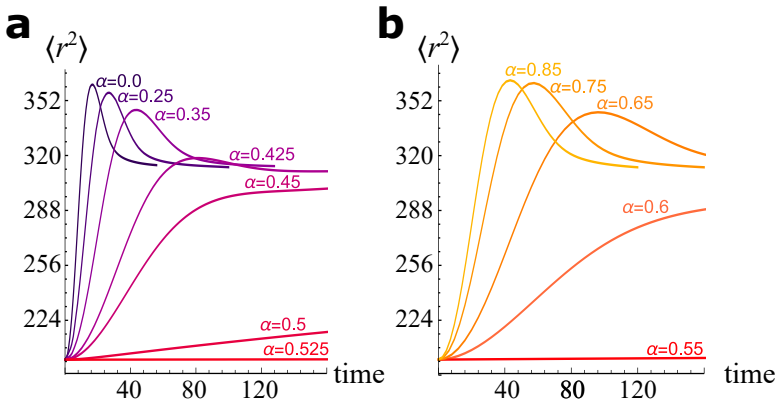

Figure 3.5: **Boltzmann wave packet spreading.** Spreading of the mean square radius $\langle r^2 \rangle = \sum_{\mathbf{r}} \mathbf{r}^2 \rho(\mathbf{r})$ of the particle density $\rho(\mathbf{r})$ as a function of time in units of the inverse hopping rate $1/t$ (panel **a**: $\alpha < \alpha_c$, panel **b**: $\alpha > \alpha_c$). Here, we consider the interacting 2D SOC model, Eqs. (3.2) and (3.11), and we employ Eq. (3.9) to incorporate the magic angle effect (occuring at $\alpha_c \approx 0.53$ in this approximation) into a semianalytical hydrodynamic treatment. The initial steady state at finite temperature is defined by a particle [energy] density $\rho(\mathbf{r}) = e^{-\mathbf{r}^2/[2\xi^2]}/\xi^2$ $[\rho_E(\mathbf{r}) = v_0 \left(1 + 3e^{-\mathbf{r}^2/\xi^2}\right)/\xi^3]$, with $v_0 \equiv v(\alpha = 0)$ is the bare velocity and we chose $\xi = 4$ for the initial spread of the density profile. The hydrodynamic equations were numerically solved in the presence of an onsite repulsion $U(\alpha = 0) = 0.025t$ and Umklapp scattering rate $1/\tau(\alpha = 0) = 0.0075t$.

3.7 Discussion

In summary, we introduced a class of magic-angle semimetals and demonstrated the general appearance of a single-particle quantum phase transition in the incommensurate limit at which, simultaneously, (i) the kinetic energy vanishes universally, (ii) a non-zero density of states appears at zero energy, and (iii) the wave functions display delocalization and multifractality in momentum space. In the presence of interactions we demonstrated that this eigenstate criticality leads to a strongly correlated Hubbard model by computing Wannier states on a superlattice. Lastly, we presented a detailed discussion of an experimental realization in cold atomic quantum emulators.

Regarding experimentally realized twisted graphene heterostructures at much smaller twist angles than we have considered here ($\theta \approx 1.1^\circ$), it has not been obvious whether incommensuration is an important ingredient [135]. Quasiperiodic effects rely upon weakly detuned processes at which the total transferred momentum wraps the Brillouin zone. In contrast, the momentum transfer induced by scattering off a small

angle superstructure is minute. Therefore—it is often concluded—both effects of incommensurability and intervalley scattering are negligible as processes in higher order perturbation theory. As our numerics demonstrate, this results in the suppression of the width of the metallic sliver in Fig. 3.1**b**, **c** that scales like $W_c' - W_c \sim \theta^3$, making observing such a metallic phase exceedingly difficult at small twist angles. Nonetheless, we expect Anderson delocalization in momentum space even at small twist angles. This is because this physics is dominated by rare resonances (as manifested in the locator expansion [136]) and controlled by α, while perturbative processes are parameterized by W/t and are therefore small. Furthermore, the contiguous phase boundary in Fig. 3.1**b**, **c** may imply that the physics of small angles directly connects to large, incommensurate twists [137, 138, 139]. However, within present day numerics, we cannot exclude that this boundary of eigenstate phase transitions terminates at a finite, small angle, which would imply the existence of a critical Anderson delocalization end point in Fig. 3.1**b,c**. The coexistence of finite DOS with other features of this phase at larger angles suggests that the phase extends to $\theta \to 0$ ($Q \to \pi$), but an end-point is appealing as it would establish a theoretical paradigm of quasiperiodic Anderson tricriticality. Any rational approximant or commensurate angle truncates the infinite sequence of resonances and minibands which leads to a rounding of the QPT (akin to finite size effects in usual transitions) and the absence of momentum space delocalization. The amplified interactions due to flat bands and an enhanced DOS occur for both incommensurate and commensurate cases as Fig. 3.1**d** demonstrates. This enhancement coupled with eigenstate quantum criticality in the incommensurate limit characterizes magic-angle semimetals, including twisted bilayer graphene at moderate twist angles.

3.8 Appendix: Details of the Analytical Results

Here we elaborate on several results on the models we study using analytical methods. The perturbation calculation qualitatively shows the renormalization of velocity that tells the existence of magic-angle transition. Renormalization interaction on the 2D SOC model exemplifies the relevance between the numerical single-particle result

to the question of interaction. The number theory result drops hints on the non-perturbative nature of the physics of incommensurability. Finally, we discuss the stability of semimetal at weak coupling to roughly scope the generality of the magic-angle transition. Most of the analytical arguments here hold only far away from the critical quasiperiodicity; but provide a qualitative understanding and pilots our detailed numerical study at the transition.

3.8.1 Perturbative calculation of velocity renormalization.

We present the perturbative calculation of velocity renormalization using the language of retarded Green's functions,

$$\hat{G}_0(E) = [E + i\eta - \hat{T}]^{-1}, \quad \hat{G}(E) = [E + i\eta - \hat{T} - \hat{V}]^{-1}, \tag{3.12a}$$

and are interested in diagonal components $G_{\vec{k},\vec{k}'}$ with $\vec{k} = \vec{k}'$, only (e.g. for the DOS we only need $\rho(E) = -(1/\pi)\mathrm{Im}\sum_{\vec{k}} \mathsf{Tr} G_{\vec{k},\vec{k}}(E)$). We define the self energy at momentum $\vec{k}$ by all diagrams which are $G_0(\vec{k}, E)$ irreducible and write

$$G_{\vec{k},\vec{k}}(E) = [G_0(\vec{k}, E)^{-1} - \Sigma(\vec{k}, E)]^{-1}. \tag{3.12b}$$

We expand about a given node $\vec{K}_i$ of the dispersion $T(\vec{K}_i + \vec{p}) \simeq T(\vec{K}_i) + h^{(\vec{K}_i)}(\vec{p})$ to leading order in $p \ll 1/a$. For models which satisfy the symmetry constraints exposed in the main text (see also Section 3.8.4) $\Sigma(\vec{K}_i + \vec{p}, E) = E\Sigma_E + h(\vec{p})\Sigma_p$ to leading order in E, p. Henceforth, we choose the energy offset such that $T(\vec{K}) = 0$. Then,

$$G_{\vec{k},\vec{k}}(E) = Z[E - (v/v_0)h(\vec{k})]^{-1} \quad \text{with } Z^{-1} = 1 - \Sigma_E \text{ and } v/v_0 = (1 + \Sigma_p)Z. \tag{3.13}$$

In this section we evaluate the self energy to leading and, for some models, next to leading order in powers of W and summarize them in Table 3.1. A discussion of infinite order perturbation theory can be found at the end of this note.

To illustrate the procedure we analyze the model of 2D perfect SOC for which the states at small $\vec{k}$ with Hamiltonian $H(\vec{k}) = t(\sin(k_x)\sigma_x + \sin(k_y)\sigma_y) \simeq t\vec{k} \cdot \boldsymbol{\sigma}$ are

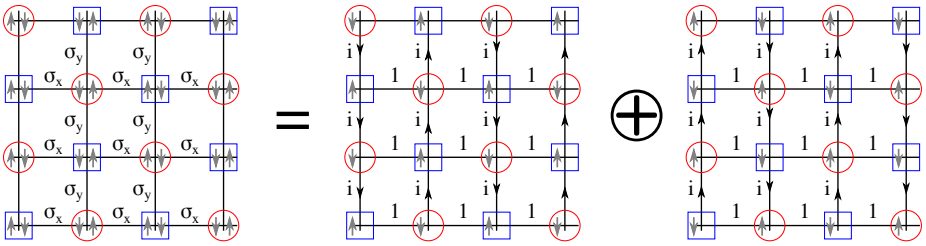

Figure 3.6: Graphic demonstration that the model of perfect SOC in 2D is a direct sum of two decoupled π flux models. The model of perfect SOC, on the left of the equality sign, is characterized by direction dependent hopping matrices. Using blue squares and red circles to depict the bipartition, hopping only connects $|\square,\uparrow\rangle$ with $|\circ,\downarrow\rangle$, and *separately* $|\square,\downarrow\rangle$ with $|\circ,\uparrow\rangle$. The hopping in y -direction is imaginary and directed (this results from the asymmetry of σ_y) and, in conclusion, leads to the inclusion of a flux π per plaquette. The onsite potential does note violate the described block-diagonalization.

connected to the states at $\vec{k} \pm Q\hat{e}_{x,y}$ and therefore to leading order perturbation theory

$$\Sigma^{(2)}(\vec{k}) = (W/2)^2 \sum_{\pm} \frac{1}{E - H(\vec{k} \pm Q\hat{e}_x)} + x \leftrightarrow y \simeq -E4\alpha^2 - t\vec{k}\cdot\boldsymbol{\sigma}(2\alpha^2(1-\cos(Q)) \tag{3.14}$$

For the next to leading order, all states at Manhatten distance $2Q$ from the origin are integrated out and we obtain

$$\begin{aligned}\Sigma^{(4)}(\vec{k}) \;\simeq\; & -\frac{E}{16}\left(\frac{W}{t}\right)^4 \left(4\cos(Q) + 10\cos(2Q) + 11\right)\csc^4(Q)\sec^2(Q)\big) \\ & + \left(\frac{W}{t}\right)^4 \frac{t\vec{k}\cdot\boldsymbol{\sigma}}{16}(4 - 5\cos(Q) + 6\cos(2Q))\csc(Q)^4\sec(Q)\end{aligned} \tag{3.15}$$

It turns out that the results obtained for the 2D model of perfect SOC directly apply to the π flux model. This is best graphically shown, see Figure 3.6: the model of 2D perfect SOC is a direct sum of two π-flux models which in the absence of interactions completely decouple. By consequence, all single particle results obtained for model of 2D perfect SOC also hold for the π-flux model.

model	Z^{-1}	v/v_0
2D SOC	$1+\left[\frac{W}{t\sin(Q)}\right]^2$	$Z\left(1-\frac{1-\cos(Q)}{2}\left[\frac{W}{t\sin(Q)}\right]^2\right)$
3D SOC	$1+\frac{3}{2}\left[\frac{W}{t\sin(Q)}\right]^2$	$Z\left(1-\frac{2-\cos(Q)}{2}\left[\frac{W}{t\sin(Q)}\right]^2\right)$
1D LRH	$1+2\left[\frac{W}{t\lvert\sin(Q)\rvert^\sigma}\right]^2$	Z
2D cTBG	$1+\frac{W^2}{t^2}\frac{\left[\cos\left(\frac{3k_\theta}{2}\right)+6+2\cos\left(\frac{3k_\theta}{4}\right)\right]}{12\sin^2\left(\frac{3k_\theta}{4}\right)}$	$Z\left(1-\frac{W^2}{t^2\sin^2\left(\frac{3k_\theta}{4}\right)}\frac{\left[2\cos\left(\frac{3k_\theta}{2}\right)-16\cos\left(\frac{3k_\theta}{4}\right)+4\cos\left(\frac{9k_\theta}{4}\right)+5\cos(3k_\theta)-49\right]}{72}\right)$
HC, $\boldsymbol{\delta}_\mu=\vec{d}_\mu$	$1+\frac{W^2}{t^2}\frac{3}{8\sin^2(3Q/4)}$	$Z\left(1-\frac{W^2}{t^2}\frac{1/4}{1+2\cos(Q/2)}\right)$
HC, $\boldsymbol{\delta}_\mu=O_{\pi/2}\vec{d}_\mu$	$1+\frac{W^2}{t^2}\frac{3[2+\cos(\sqrt{3}Q/2)]}{8\sin^2(3\sqrt{3}Q/4)}$	$Z\left(1+\frac{W^2}{t^2}\frac{5+4\cos(\sqrt{3}Q/2)}{4[1+\cos(\sqrt{3}Q/2)]^2}\right)$
HC, $\boldsymbol{\delta}_\mu=\vec{d}_{1,2}$	$1+\frac{W^2}{t^2}\frac{1}{4\sin^2(3Q/4)}$	$Z\left(1-\frac{W^2}{t^2}\frac{\begin{pmatrix}3[\cos(Q/2)-2\cos(Q)] & -\sqrt{3}[\cos(Q/2)+2\cos(Q)]\\ -\sqrt{3}[\cos(Q/2)+2\cos(Q)] & 5\cos(Q/2)-2\cos(Q)\end{pmatrix}}{48\sin(3Q/4)^2}\right)$

Table 3.1: Perturbative corrections to quasiparticle weight Z and velocity v/v_0 for a variety of magic angle models. Note that for the honeycomb model and $\boldsymbol{\delta}_\mu = \vec{d}_{1,2}$, the symmetry protection of nodes is lost. It implies a relocation of $K-$point node $\delta\vec{k} = W^2(1,-\sqrt{3})^T/[12t^2(1+2\cos(Q/2))$ and a distorted velocity matrix. For cTBG, the momentum dependent self-energy has the form $\Sigma_{\mathbf{p}}h(p_x,p_y)+\tilde{\Sigma}_{\mathbf{p}}h(p_y,-p_x)$ and we extract $v/v_0 = Z(1+\Sigma_{\mathbf{p}})$.

3.8.2 Renormalization of interactions

We present an analytical estimate of the renormalization of the interaction upon projection onto certain minibands and approaching the transition for the model of 2D SOC. Let the bare ($W = 0$) model in the continuum be written as ($\vec{K}_i$ are various Dirac/Weyl nodes, with linear $\vec{k} \cdot \vec{p}$ Hamiltonian $h^{(\vec{K}_i)}(\vec{p})$)

$$\begin{aligned} S = &\sum_{\vec{K}_i} \int^{1/a} (dp) \int d\tau \bar{c}^{(\vec{K}_i)}(\vec{p})[\partial_\tau + h^{(\vec{K}_i)}(\vec{p})]c^{(\vec{K}_i)}(\vec{p}) \\ &+ \sum_{\vec{K}_{1,2,3,4}} \int^{1/a} \prod_{j=1}^{4} (dp_j) \int d\tau (2\pi)^d g_{\{\vec{K}_i\}} \delta_{\vec{K}_1+\vec{K}_3-\vec{K}_2-\vec{K}_4} \delta(\vec{p}_1 + \vec{p}_3 - \vec{p}_2 - \vec{p}_4) \times \\ &\times \frac{[\bar{c}^{(\vec{K}_1)}(\vec{p}_1)c^{(\vec{K}_2)}(\vec{p}_2)][\bar{c}^{(\vec{K}_3)}(\vec{p}_3)c^{(\vec{K}_4)}(\vec{p}_4)]}{|\vec{p}_1 - \vec{p}_2|^\sigma}. \end{aligned} \tag{3.16}$$

The spectrum of $h^{(\vec{K}_i)}(\vec{p})$ has the form $v_0|\vec{p}|$ with bare value $v_0 \sim ta$ and, for contact interaction ($\sigma = 0$), $g_{\{\vec{K}_i\}} \sim Ua^d$, while for Coulomb interaction ($\sigma = d - 1$) $g_{\{\vec{K}_i\}} \propto \delta_{\vec{K}_1,\vec{K}_2}$. Perturbation theory indicates a dimensionless parameter

$$\frac{g_{\{\vec{K}_i\}}}{v_0/a^{d-1}} \sim \frac{U}{t} \quad \text{for} \quad \sigma = 0 \text{ (contact interaction)}, \tag{3.17}$$

$$\alpha = \frac{g_{\{\vec{K}_i\}}}{v_0} \quad \text{for} \quad \sigma = d - 1 \text{ (Coulomb interaction)}. \tag{3.18}$$

We now consider the effect of integrating out high energy states and projecting onto a miniband with effective Brillouin zone size $1/a'$. This leads to

$$\begin{aligned} S = &\sum_{\vec{K}_i} \int^{1/a'} (dp') \int d\tau \bar{c}_<^{(\vec{K}_i)}(\vec{p}')Z^{-1}[\partial_\tau + \frac{v}{v_0} h^{(\vec{K}_i)}(\vec{p}')]c_<^{(\vec{K}_i)}(\vec{p}') \\ &+ \sum_{\vec{K}_{1,2,3,4}} \int^{1/a'} \prod_{j=1}^{4} (dp'_j) \int d\tau (2\pi)^d g_{\{\vec{K}_i\}} \delta_{\vec{K}_1+\vec{K}_3-\vec{K}_2-\vec{K}_4} \delta(\vec{p}'_1 + \vec{p}'_3 - \vec{p}'_2 - \vec{p}'_4) \times \\ &\times \frac{[\bar{c}_<^{(\vec{K}_1)}(\vec{p}'_1)c_<^{(\vec{K}_2)}(\vec{p}'_2)][\bar{c}_<^{(\vec{K}_3)}(\vec{p}'_3)c_<^{(\vec{K}_4)}(\vec{p}'_4)]}{|\vec{p}'_1 - \vec{p}'_2|^\sigma}. \end{aligned} \tag{3.19}$$

The renormalizations Z and v/v_0 originate from scalar and matrix components of the self-energy and were calculated perturbatively above. We now first rescale $p' = \frac{a}{a'}p$ with $p \in (0, 1/a)$ and then define $c_<^{(\vec{K})}(a\vec{p}/a')Z^{-1/2}(a/a')^{d/2} = c^{(\vec{K})}(\vec{p})$. Under this rescaling, we restore the form of Eq. (3.16), including its UV cut-off $1/a$, but obtain the rescaling $v_0 \to va/a'$, $g \to g(a/a')^{d-\sigma}Z^2$. From this we obtain the final formula for

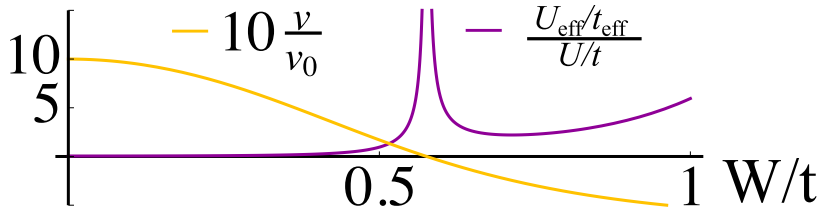

Figure 3.7: Divergence of contact interaction according to Eq. (3.21) for the model of 2D SOC. Here, the fourth order perturbative self energy was employed and we used $\gamma = 1/5$.

renormalization of the dimensionless coupling constant

$$\frac{U_{\rm eff}/t_{\rm eff}}{U/t} = \gamma \left(\frac{a}{a'}\right)^{d-1} \frac{Z^2}{v/v_0} \qquad \text{(contact interaction)}, \tag{3.20}$$

$$\frac{\alpha_{\rm ren.}}{\alpha_{\rm bare}} = \frac{Z^2}{v/v_0} \qquad \text{(Coulomb)}. \tag{3.21}$$

Here, γ is an unknown constant of order unity which depends on details of the cut-off of the linearized theory. Importantly, the integration reduces the bare contact interaction by a factor $(a/a')^{d-1}$, except in the closest vicinity of the magic angle where the vanishing velocity overtakes the reduction, see Figure 3.7.

3.8.3 Relationship to number theory.

In addition, we show the relationship of the sequence of relevant perturbative processes with certain well known sequences from number theory. Starting from the scattering process of order $l_1 = 1$ we want to determine the sequence $\{l_n\}_{n=1}^{\infty}$ for which the l_nth order momentum transfer carves out smaller minibands than the l_{n-1}th order. In formulae, this implies for the 2D model of perfect SOC of the main text and arbitrary incommensuration wavevector Q the condition $\sin^2(l_n Q) < \sin^2(l_{n-1} Q)$. We now concentrate on the specific case $Q = 2\pi/\phi^2 = \pi(3 - \sqrt{5})$. For this situation, the defining condition on the sequence of l_n is $\sin^2(\pi l_n \sqrt{5}) < \sin^2(\pi l_{n-1}\sqrt{5})$. The sequence $\{l_n\}_{n=1}^{\infty}$ for which $l_n\sqrt{5}$ successively approaches integers is the sequence of denominators of the leading rational approximants, i.e. the sequence of denominators of continued fraction convergents of $\sqrt{5}$ (OEIS ID A001076). This sequence is also half the value of the even fibonaccis $l_n = F_{3n}/2$.

This sequence also connects to the formation of minibands as found with the finite

size $Q_n = 2\pi F_{n-2}/F_n$. Intuitively, when F_n is even (n is a multiple of 3), then at order $F_n/2$, the Dirac nodes gap out, but then for F_{n+1} and F_{n+2} this perturbative gap must have moved to small but finite energy, forming the miniband. This motivates using Q_{3n+1} and Q_{3n+2} to study the effective model of successive minibands.

In fact, following theorem can be proven that connects this sequence to the order of perturbation theory where a gap is opened:

Theorem. *Let $n = 3m+r$ for $r = 0, 1, 2$, then the integer $g_n = F_{3m}/2$ is the smallest integer such that $g_n F_{n-2} \equiv \frac{F_n+\delta_n}{2} \mod F_n$ with integer $|\delta_{3m}| \leq 1$. In particular, $\delta_{3m} = 0$, $\delta_{3m+1} = (-1)^m$, and $\delta_{3m+2} = (-1)^{m+1}$.*

Therefore, the order of perturbation theory that opens up a gap nearest to $E = 0$ for $Q = 2\pi F_{3m+r-2}/F_{3m+r}$ for $r = 0, 1, 2$ is $F_{3m}/2$.

A crucial consequence of this analysis is that when $m \to \infty$ (which is the limit for Q being incommensurate), the complete formation of all gaps that approaches $E = 0$ requires infinite orders of perturbation theory. Hence the full effect of all the gap opening is only seen at a quantum criticality where all orders of perturbation theory become important. That is our magic-angle transition.

3.8.4 Generality of the magic-angle phenomenon - symmetry protection.

In this section we discuss the generality of our findings by highlighting the general condition for the appearance of the magic angle phenomenon, namely the stability of the semimetal at weak coupling.

We concentrate on nodes in the kinetic term $\hat{T}$ which are protected by a symmetry group G_T. For example, this analysis applies to each model we have considered in 2D as well as Dirac semimetals in 3D. Note that in general G_T is a subgroup of all symmetry operations of the kinetic term. Let U_{S_T} be the representation of $S_T \in G_T$ in the (e.g. spinorial) Hilbert space, then the symmetry of the Hamiltonian implies $T(\vec{k}) = U^\dagger_{S_T} T(S_T\vec{k}) U_{S_T}$. We concentrate on high symmetry points where $S_T\vec{K} = \vec{K}$, $\forall S_T \in G_T$. Then, a non-trivial representation implies degeneracy in view of $[T(\vec{K}), U_{S_T}] = 0$ $\forall S_T \in G_T$ (formally, two non-commuting U_{S_T} are needed). We further assume a

group G_V of spatial (point group) symmetries of the quasiperiodic background $\hat{V}$, such that

$$V(\vec{x}) = \sum_{S_V \in G_V} \tilde{U}_{S_V} W \tilde{U}_{S_V}^\dagger e^{iQ\vec{x}\cdot S_V \hat{e}_0} + h.c.. \tag{3.22}$$

Here now, $\tilde{U}_{S_V}$ is the representation of $S_V \in G_V$ and $\hat{e}_0$ is an arbitrary vector in $\mathbb{R}^d$.

In this section, we consider Eq. (3.12) formally to all orders in perturbation theory. The semimetallic behavior persists if a) $\Sigma(\vec{k})$ is hermitian and b) $T(\vec{k}) + \Sigma(\vec{k})$ has the same symmetry protected touching point as $T(\vec{k})$, i.e. if $\Sigma(\vec{k})$ respects the symmetries ensuring the semimetal. In view of the incommensuration, perfect resonance is formally absent to any order in perturbation theory and therefore, the decay rate $1/\tau \sim \sum_{\vec{k}'} |\mathbf{T}_{\vec{k},\vec{k}'}|^2 \delta(E_{\vec{k}} - E_{\vec{k}'})$ (more generally: the anti-hermitian part of the self-energy) vanishes ($\mathbf{T}_{\vec{k},\vec{k}'}$ denotes the T-matrix). Thus a) is fulfilled and $1/\tau \neq 0$ signals the breakdown of perturbation theory (spontaneous unitarity breaking). We can then show to all orders in perturbation theory that the semimetal is stable provided G_T is a subgroup of G_V.

We proceed to the proof of $\Sigma(\vec{k}) = U_{S_T}^\dagger \Sigma(S_T \vec{k}) U_{S_T}$ under the outlined assumptions. To get a feeling, we first consider second order perturbation theory.

$$\Sigma^{(2)}(\vec{k}) = \sum_{S_V \in G_V} \tilde{U}_{S_V} W \tilde{U}_{S_V}^\dagger [E^+ - T(\vec{k} + QS_V \hat{e}_0)]^{-1} \tilde{U}_{S_V} W^\dagger \tilde{U}_{S_V}^\dagger. \tag{3.23}$$

We compare to

$$\begin{aligned} U_{S_T}^\dagger \Sigma^{(2)}(S_T \vec{k}) U_{S_T} &= \sum_{S_V \in G_V} U_{S_T}^\dagger \tilde{U}_{S_V} W \tilde{U}_{S_V}^\dagger U_{S_T} [E^+ - U_{S_T}^\dagger T(S_T \vec{k} + QS_V \hat{e}_0) U_{S_T}]^{-1} \\ &\quad U_{S_T}^\dagger \tilde{U}_{S_V} W \tilde{U}_{S_V}^\dagger U_{S_T} \\ &= \sum_{S_V \in G_V} U_{S_T}^\dagger \tilde{U}_{S_V} W \tilde{U}_{S_V}^\dagger U_{S_T} [E^+ - T(\vec{k} + QS_T^{-1} S_V \hat{e}_0)]^{-1} \\ &\quad U_{S_T}^\dagger \tilde{U}_{S_V} W^\dagger \tilde{U}_{S_V}^\dagger U_{S_T} \end{aligned} \tag{3.24}$$

This expression is invariant provided the action of S_T onto G_V is a bijection of G_V onto itself $\forall S_T \in G_T$, i.e. $S_T S_V \in G_V$ $\forall S_V \in G_V$ and $S_T G_V = G_V$ as this allows to uniquely relable the summation index. Taking $S_V = \mathbf{1}$ implies that $S_T \in G_V$ and hence G_T is a subgroup of G_V. By consequence, the representation in the Hilbert space fulfills $\tilde{U}_{S_T^{-1} S_V} = U_{S_T}^\dagger \tilde{U}_{S_V}$ and $\Sigma^{(2)}(\vec{k})$ is invariant under the symmetries protecting the

semimetal. We now continue with the next order $\Sigma^{(4)}$, from there the generality of the statement becomes apparent,

$$\begin{aligned}\Sigma^{(4)}(\vec{k}) &= \sum_{S_V \in G_V} \sum_{\substack{S'_V \in G_V \\ S'_V \hat{e}_0 \neq -S_V \hat{e}_0}} \tilde{U}_{S_V} W \tilde{U}^{\dagger}_{S_V} [E^+ - T(\vec{k} + QS_V \hat{e}_0)]^{-1} \\ &\quad \tilde{U}_{S'_V} W \tilde{U}^{\dagger}_{S'_V} [E^+ - T(\vec{k} + QS_V \hat{e}_0 + QS'_V \hat{e}_0)]^{-1} \\ &\quad \tilde{U}_{S'_V} W^{\dagger} \tilde{U}^{\dagger}_{S'_V} [E^+ - T(\vec{k} + QS_V \hat{e}_0)]^{-1} \tilde{U}_{S_V} W^{\dagger} \tilde{U}^{\dagger}_{S_V}. \end{aligned} \tag{3.25}$$

The exclusion $S'_V \hat{e}_0 + S_V \hat{e}_0 \neq 0$ ensures the irreducibility with respect to $G_{\vec{k}}$. Again we can apply an S_T transformation and exploit the two conditions exposed above to relabel both S_V and S'_V. This implies the invariance of $\Sigma_{(4)}$. This procedure can be used to arbitrary order in perturbation theory.

Acknowledgements

A significant portion of this work should be attributed to my collaborators E.J.Konig, J.H.Wilson, YZ.Chou and J.H.Pixley. In particular, E. J. K., J. H. W., and J. H. P. designed the research, Y. F., E. J. K., J. H. W., YZ. C, and J. H. P. performed the research, and Y. F., E. J. K., J. H. W., YZ. C, and J. H. P. wrote the original paper. Y. F., E. J. K., and J. H. W. contributed equally. We also thank I. Bloch, P.-Y. Chang, P. Coleman, B. J. DeSalvo, M. Foster, Y. Komijani, G. Pagano, A. M. Rey, M. Schütt, I. Spielman, and D. Vanderbilt for useful discussions. We also thank S. Gopalakrishnan and D. Huse for collaborations on related work and for insightful discussions. We also note that, independent proposals to simulate twistronics in cold atoms appeared and were published in ref. [140, 141].

Chapter 4

Disordered magic-angle semimetals

4.1 Introduction

The previous chapter considered adding quasiperiodicity to lattice models. Hence, in order for the study to have any realistic significance, it is natural to study the effect of disorder – which part of the "magic-angle" physics we discuss is most robust against disorder?

Meanwhile, the same question is imperative in the research of twisted bilayer graphene. Although the ever evolving experiments has produced increasingly clean samples, inhomogeneity will never be gone. There can be random potential or magnetic disorder (that is inevitable from sample preparation and the exposure to the environment), for example. Any attempt to connect theory and experiment will need to answer the question of whether the predicted phenomena can withstand disorder, and how the predicted phenomena change as the system is less ideal.

In this chapter, we develop a theory for a special type of disorder that is native to quasiperiodic systems – the fluctuation of the "period" of quasiperiodic modulation. In the case of simple quasiperiodic potential, this correspond to the wave vector Q as we discussed in Chapter 3. In the context of twisted bilayer graphenes, it is the disorder of the local twist-angle fluctuations, which will be the main focus of this chapter.

In experimental samples of pristine twisted bilayer graphene, which are nominally free of impurities and defects, the main source of disorder is believed to arise from the unavoidable and uncontrollable non-uniformity of the twist angle across the sample. Such type of disorder arise in research activity in the physics of twisted bilayer graphene. To address this new physics of twist-angle disorder, we develop a real-space, microscopic

model of twisted bilayer graphene where the angle enters as a free parameter. Once we have a viable real-space model, we are able to study the effects of disorder on twisted bilayer graphene at the single-particle level. Not only does twisting two sheets of graphene create flat bands near the magic-angle ($\sim$ 1-1.1°), it also induces gaps that separate the miniband, which has Van Hove singularities in the density of states [104, 2, 102], from the rest of the spectra as seen in Fig. 4.1. These miniband insulating gaps arising from the single-particle band structure of the twisted system are simply the moiré superlattice band gaps due to the tunneling between the two graphene bands in the combined bilayer heterostructure. We are interested in how all of these single-particle, superlattice, miniband features are affected or even destroyed due to randomness in the twist angle. In particular, we focus on the size of single-particle energy gaps separating the miniband from the rest of the spectrum, the Van Hove peaks, the renormalized Dirac cone velocity near charge neutrality, and the minibandwidth. We find that the energy gaps and minibandwidth are strongly affected by disorder while the renormalized velocity remains virtually unchanged. In addition, following the universality argument of Chapter 3, we also studied the much simpler model of 2D SOC (the 2D lattice model with spin-orbit coupling) with quasiperiodic potential and find similar behavior.

This chapter is organized as follows: In Sec. 4.2 we discuss the experimental origin of the twist angle disorder we focus on. In Sec. 4.3 we build an approximate lattice model for twisted bilayer graphene and use it to introduce real-space disorder in the twist angle. In Sec. 4.4 we discuss the results of the numerical calculations, and in Sec. 4.6, we discuss our approximations and the implications of these results for ongoing experiments. In addition to the more realistic models, in Section 4.5 we analyze a simpler model with similar magic-angle phenomena using a deterministic quasiperiodic potential. Finally, we conclude in Sec. 4.7 with a summary of our results. Throughout, we take the lattice spacing between neighboring carbon atoms to be unity, which serves as our unit of length.

4.2 The disorders in graphene and twisted bilayer graphenes

The ability to isolate and characterize single sheets of graphene [142] has lead to a significant amount of control over van der Waals heterostructures [143]. This spectacular materials engineering feat has led not only to relatively clean, high mobility graphene samples, but also to the ability to place two coupled sheets of graphene on top of each other with a relative "twist" angle between them [104]. The introduction of the 'twist angle' as a new experimental parameter to tune the electronic properties of 'twisted' van der Waals heterostructures has led to a new paradigm in condensed matter systems where one can now study materials properties not only as a function of temperature, carrier density, magnetic field, gate voltage, applied pressure or strain, etc., but also as a function of the twist angle between the two layers controlling the electronic band structure in a radical manner, which is a completely new tool in the laboratory.

While these bilayers are clean and relatively disorder free, the twist angle can vary across samples, leading to a new source of disorder. Thus, even if the two starting monolayers are completely clean (i.e. no impurities or defects), the very fact of creating the twisted bilayer system introduces an inherent (and a new type of) disorder by virtue of local fluctuations in the twist angle throughout the macroscopic sample. This 'twist angle disorder', which has no analogy in usual condensed matter systems and has never before been studied in the literature, is thought to be the main disorder controlling the quality of the currently available twisted graphene systems.

In single-layer graphene, the most dominant effect of disorder near the Dirac point has been attributed to charge disorder (arising from unintentional quenched random charged impurities in the system) inducing "puddles" of unequal charge density that locally dope the Dirac cones [144]. This issue has been circumvented by using an all van der Waals device geometry, and the absence of any significant charge inhomogeneities in such ultra-clean samples has enabled the observation of exotic many-body states [145] akin to what has been seen in clean suspended graphene [146]. As a result, the current graphene sample quality is rather remarkable and for most practical purposes, both charge inhomogeneities as well as any extrinsic disorder due to vacancies or defects has

been greatly suppressed, if not almost eliminated except perhaps for experiments using very low ($< 10^{10}\,\mathrm{cm}^{-2}$) carrier densities.

With these capabilities, very clean samples of twisted bilayer graphene (TBG) near the magic-angle (where the nominal band structure becomes completely flat suppressing the Dirac velocity to zero) have recently been observed to develop insulating states at integer filling fractions of the moiré miniband near the Dirac points [55, 97]. Upon gating (i.e. doping) away from the insulating phases, nearby superconducting phases have been observed [54, 97, 147]. To achieve an accurate choice (to within $\sim 0.1°$) and rather small value of the twist angle ($\sim 1°$), the "tear and stack" mechanical approach places two sheets of graphene on top of each other with a great deal of precision in the twist angle [148]. Only after such a mechanical procedure of creating the twisted bilayer sample with a carefully chosen twist angle, the sample is transferred to the cryostat for electrical measurements. To study the electronic properties as a function of the twist angle, the whole procedure has to be repeated for a different sample with a different twist angle. In practice however, this procedure does not produce a single twist angle across the entire sample: Scanning tunneling microscopy has observed different twist angles across separate regions of the sample [104, 105, 149, 150, 151, 152, 153]. Moreover, signatures of the nonuniformity of the twist angle have also been observed in conductance measurements that have a strong dependence on where the leads are placed on the device [97]. In addition, two different samples with nominally identical twist angles typically manifest quite different electronic properties in transport and STM measurements, again reflecting that some inherent variations in the twist angle invariably exist in the system. Thus, in any given high-quality (i.e. low extrinsic impurity and defect concentration) sample the main source of disorder comes in the form of a *varying* twist angle across the sample. The nature of this variation is not unique: some samples have hard domain walls separating regimes with different twist angles, whereas some samples have a much smoother change in the twist across the sample [1]. Twist angle disorder is a radically new type of intrinsic disorder in condensed matter systems whose study is, quite apart from its singular importance in determining

[1] Private communication with Eva Andrei

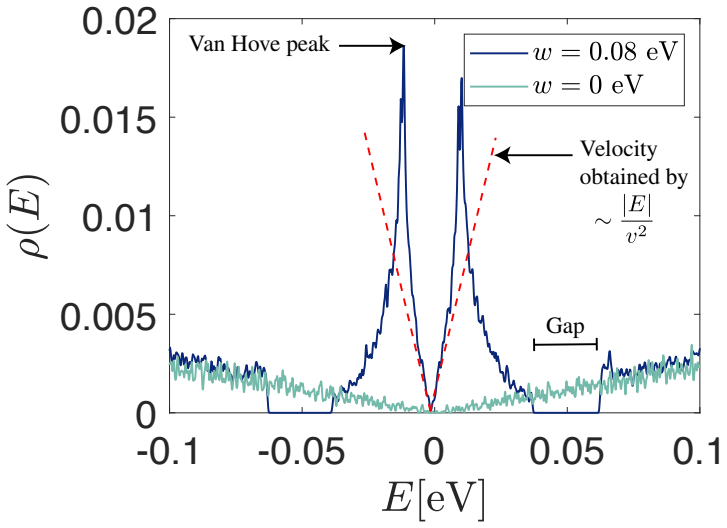

Figure 4.1: The density of states $\rho(E)$ as a function of energy E for the lattice model of twisted bilayer graphene at a twist angle $\theta = 1.05°$, a linear system size $L = 569$, a kernel polynomial method [4] expansion order $N_C = 2^{17}$, and a weak breaking in the interlayer tunneling between AA and AB sites ($w_0/w_1 = 0.75$, $w_1 = w$ where w_0 (w_1) is the strength of AA and BB (AB and BA) tunneling), which captures lattice relaxation effects [5, 6] and it opens a hard gap on both sides of the semimetal miniband. We note that at small angles, a single parameter controls the physics: $w/[2v_F k_D \sin(\theta/2)]$, so lowering the angle is equivalent to increasing w_1. Therefore, one can read the plots of smaller w_1 as at an angle larger than 1.05°. This density of states has a number of features relevant to the physics: Van Hove peaks, gaps, and the velocity (as determined by the scaling of the density of states). Dark (light) blue lines give the calculated density of states for finite (zero) values of the parameter w as shown in the inset of the figure.

the twisted graphene bilayer properties, of fundamental conceptual significance.

We focus on various features of the low energy density of states and the miniband structure to determine how the single-particle spectrum is modified as a result of randomness in the twist angle. We demonstrate that disorder smooths the non-analyticities in the density of states, fills in the band-gaps, broadens the minibandwidth, and smears out the Van Hove peaks. We compare this with the size of the gap isolating the low-energy miniband, the renormalized Dirac velocity, and the size of the minibandwidth. Surprisingly, we find that the Dirac cone velocity is remarkably robust to twist disorder, whereas other miniband characteristics are systematically broadened. The essential complete protection of the miniband Dirac velocity (at low energy, where the Dirac cone

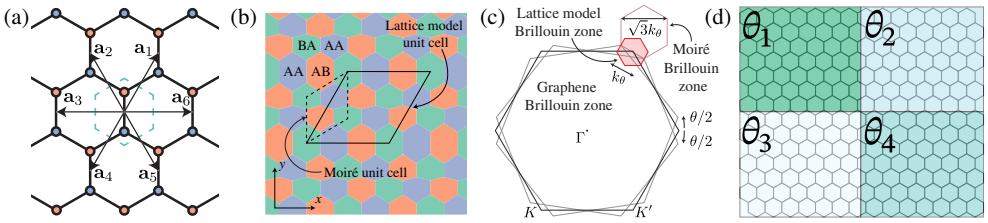

Figure 4.2: (a) A schematic of graphene and the notation we use for our model. The A (B) sublattice is represented by the blue (orange) lattice sites. The unit cell for the triangular lattice is shown by the dashed central hexagon. The lattice vectors are $\mathbf{a}_1 = (\sqrt{3}/2, 3/2)$ and $\mathbf{a}_2 = (-\sqrt{3}/2, 3/2)$, and we further define $\mathbf{a}_3 \equiv \mathbf{a}_2 - \mathbf{a}_1$, $\mathbf{a}_4 \equiv -\mathbf{a}_1$, $\mathbf{a}_5 \equiv -\mathbf{a}_2$, as well as $\mathbf{a}_6 \equiv -\mathbf{a}_3$. (b) A course-grained view of the tunneling between the layers calculated from $\mathcal{T}_0$ and $\mathcal{T}_1$ in Eq. (4.5) which defines the energy parameters w_0 and w_1; the color represents whether AA, AB, or BA hopping is dominant based on the chance for an electron on a site in layer 1 to hop onto sublattice A or B on layer 2, given by $P_X(\mathbf{r}) = |[\mathcal{T}_0(\mathbf{r})]_X|^2 + 6|[\mathcal{T}_1(\mathbf{r})]_X|^2$. Note that C_3 is broken and the moiré unit cell is larger than in real TBG. Both of these effects are relatively small. (c) Complementary to the real space picture, in momentum space the lattice Brillioun zone is effectively downfolded by a factor of three from the moiré Brillioun zone after unrotating the two graphene layers; this introduces small gaps in the band structure at these points. (d) In our model, the effect of the twist is entirely contained within interlayer coupling, so we model disorder by changing the continuous twist parameter θ within different regions of space. In this common example, we break up the system into four equal regions and pick a value of θ_j that are drawn from the box distribution $[(1 - W_R/2)\theta, (1 + W_R/2)\theta]$ with $\theta = 1.05°$.

approximation holds) in the twisted bilayer graphene (TBG) against the twist-angle disorder is a rather unexpected finding of our nonperturbative calculations, particularly since all other aspects of the miniband electronic structure are strongly affected by the twist-angle randomness.

4.3 Model and Approach

The numerical study of twist-angle disorder is difficult with the current models available in the literature. First, the usual continuum model is built as a hexagonal lattice in momentum-space [154, 2] where disorder enters the Hamiltonian in a highly non-local way. Second, current real-space models rely on both a uniform and commensurate twist angle [135, 155]. To circumvent this problem, we build a new real space model where the twist is built directly into the interlayer hopping in such a way that it can be continuously tuned, and can vary spatially while the model remains *local* in real

space. The model exactly reproduces the continuum model as written by Bistritzer and MacDonald [2] near the K and K' Dirac points in the Brillouin zone. The version of this model presented here preserves C_2T symmetry (i.e. the combined operation of a 180° rotation and a time reversal operation) and hence preserves the Dirac nodes. Further, it qualitatively preserves the spatial structure of AA and AB tunneling; however, it explicitly breaks C_3 symmetry. While there is no obstruction to building the model with C_3 symmetry (a version of which will appear in Chapter 3), real experiments introduce strain which also explicitly breaks C_3 [156], so we do not require this of our real space model. So, in some sense, our disorder model incorporates both the twist-angle disorder (in a controlled manner) and strain effects (in an uncontrolled manner through the explicit breaking of C_3 symmetry). The model (see Fig. 4.2) we primarily focus on is a lattice model that is an approximation of twisted bilayer graphene which captures the low energy limit of the continuum model [154, 2]. However, this particular ultra-violet (UV) completion of the continuum model does not respect the underlying C_3 symmetry of the microscopic lattice. As a result, the velocity does not strictly vanish at the magic angle but becomes very small due to the Dirac points not being pinned to high-symmetry points in the Brillouin zone and acquires an angular dependence relative to each Dirac point in momentum space. However, the band structure that results is still qualitatively similar, and so we expect that effects arising from this approximation are not relevant to understand the qualitative effects of disorder. In any case, it is unclear that a strict magic angle with vanishing velocity can ever be achieved in any laboratory samples, so our approximation of a finite, but very small, velocity should not be a practical problem in any sense.

To motivate the model, consider the continuum model written as in Ref. [2] around the K point

$$H_K = \begin{pmatrix} h_{\mathbf{k},\theta/2} & T(\mathbf{r}) \\ T^\dagger(\mathbf{r}) & h_{\mathbf{k},-\theta} \end{pmatrix}, \tag{4.1}$$

where $h_{\mathbf{k},\theta} = \frac{3t}{2}\mathbf{k} \cdot e^{-i\theta\sigma_z/2}\boldsymbol{\sigma}^* e^{i\theta\sigma_z/2}$, $T(\mathbf{r}) = \sum_{j=1}^{3} e^{-i(\mathbf{q}_j\cdot\mathbf{r}+\phi_j)}T_j$ and $T_j = w_0 + w_1(\sigma^+ e^{2\pi i(j-1)/3} + \sigma^- e^{-2\pi i(j-1)/3})$. We can "unrotate" this Hamiltonian by considering the $\mathbf{k}$ vectors to be the same and applying a unitary in pseudospin space (using

the properties of Dirac cones, one can replace the full angular momentum operator L_z with $\sigma_z/2$)

$$H'_K = \begin{pmatrix} h_{\mathbf{k},0} & e^{i\theta\sigma_z/4}T(\mathbf{r})e^{i\theta\sigma_z/4} \\ e^{-i\theta\sigma_z/4}T^\dagger(\mathbf{r})e^{-i\theta\sigma_z/4} & h_{\mathbf{k},0} \end{pmatrix}. \tag{4.2}$$

We can do a similar operation to the K' point. The interlayer tunnelings at the K and K' points differ, so it is important to have a function interpolate between the two while preserving symmetries C_2 and time-reversal and staying as local as possible. This can be done, and we can replace the Dirac cone $h_{\mathbf{k},0}$ with the Hamiltonian for graphene which in real space and second quantized notation is

$$H_0 = \sum_{\mathbf{r},\ell} t[c^\dagger_{\mathbf{r},\ell}\sigma_x c_{\mathbf{r},\ell} + \sum_{j=1}^{2}(c^\dagger_{\mathbf{r}+\mathbf{a}_j,\ell}\sigma^+ c_{\mathbf{r},\ell} + \text{h.c.})] \tag{4.3}$$

where $t = 2.8\,\text{eV}$ [157], $\mathbf{r}$ labels points on the triangular lattice, $c_{\mathbf{r},\ell} = (c_{\mathbf{r},A,\ell}, c_{\mathbf{r},B,\ell})^T$ is a vector of annihilation operators at triangular lattice site $\mathbf{r}$ and layer $\ell = 1, 2$ whose first and second components represent the A and B sublattices, respectively. The lattice vectors $\mathbf{a}_1$ and $\mathbf{a}_2$ are shown in Fig. 4.2(a) where the lattice site $\mathbf{r}$ is the central hexagon. The tunneling between layers in real space then becomes

$$\begin{aligned} H_{\text{TBG}} = H_0 + \sum_{\mathbf{r}} \left[c^\dagger_{\mathbf{r},2}\mathcal{T}_0(\mathbf{r})c_{\mathbf{r},1} + \text{h.c.}\right] \\ + \sum_{\mathbf{r}}\sum_{n=1}^{6} \left[(-1)^n c^\dagger_{\mathbf{r}+\mathbf{a}_n,2}\mathcal{T}_1(\mathbf{r}+\tfrac{1}{2}\mathbf{a}_n)c_{\mathbf{r},1} + \text{h.c.}\right]. \end{aligned} \tag{4.4}$$

The second line of of Eq. (4.4) represents interlayer hopping to the nearest neighbors on the triangular lattice, summed over all $\mathbf{a}_n$, as depicted in Fig. 4.2 (a), and the interlayer hopping matrices are given by

$$\begin{aligned} \mathcal{T}_0(\mathbf{r}) &= \sum_{j=1}^{3} \begin{pmatrix} w_0\cos(\mathbf{q}_j\cdot\mathbf{r} + \phi_j - \theta/2) & w_1\cos(\mathbf{q}_j\cdot\mathbf{r} - \frac{2\pi(j-1)}{3} + \phi_j) \\ w_1\cos(\mathbf{q}_j\cdot\mathbf{r} + \frac{2\pi(j-1)}{3} + \phi_j) & w_0\cos(\mathbf{q}_j\cdot\mathbf{r} + \phi_j + \theta/2) \end{pmatrix} \\ \mathcal{T}_1(\mathbf{r}) &= \frac{1}{3\sqrt{3}}\sum_{j=1}^{3} \begin{pmatrix} w_0\sin(\mathbf{q}_j\cdot\mathbf{r} + \phi_j - \theta/2) & w_1\sin(\mathbf{q}_j\cdot\mathbf{r} - \frac{2\pi(j-1)}{3} + \phi_j) \\ w_1\sin(\mathbf{q}_j\cdot\mathbf{r} + \frac{2\pi(j-1)}{3} + \phi_j) & w_0\sin(\mathbf{q}_j\cdot\mathbf{r} + \phi_j + \theta/2) \end{pmatrix}, \end{aligned} \tag{4.5}$$

where w_0 represents AA tunneling, w_1 is the AB tunneling (commonly, if we refer to w, we are referring to w_1 and a fixed w_0/w_1 ratio), θ is the twist angle, ϕ_j are random

phases which sum to zero and represent the center of rotation [2] , $q_1 = k_\theta(0, -1)$, $q_2 = k_\theta(\sqrt{3}/2, 1/2)$, and $q_3 = k_\theta(-\sqrt{3}/2, 1/2)$. The value of the twisted wavevector k_θ is given by $k_\theta = 2k_D \sin(\theta/2)$ where $k_D = 4\pi/(3\sqrt{3})$. The effect of varying w for a fixed twist angle $\theta = 1.05^\circ$ is shown in Fig. 4.3(a), which demonstrates the formation of a semimetal miniband and shrinking minibandwidth. We note that other parameter sets for the tight binding parameters are available [158] but do not affect any of the qualitative results presented here.

If we go to the crystal momentum basis and expand about the K point (with similar results at K'), we indeed obtain the continuum model [2] up to a unitary transformation as our construction dictated. Furthermore, if we compare the low-energy continuum model to the actual lattice model itself, we find remarkable agreement in the calculated density of states [defined in Eq. (4.6)] as shown in Fig. 4.3(b,c,d) for three representative sets of parameters.

Some comments are in order. First, while it reproduces the continuum model at the K (and K') point, this particular UV-completion explicitly breaks the C_3 symmetry present in the original model (this symmetry is just weakly broken near the K and K' points). To see this explicitly, we can consider the pattern of AA, AB, and BA tunnelings our model exhibits. This can be entirely determined by the form of $\mathcal{T}_0$ and $\mathcal{T}_1$ in Eq. (4.5): If an electron is on an A site on layer 1 and wants to hop to an A site on layer 2, then the sum of the squares of the hoppings give that $P_{AA}(\mathbf{r}) = |[\mathcal{T}_0(\mathbf{r})]_{AA}|^2 + 6|[\mathcal{T}_1(\mathbf{r})]_{AA}|^2$ (and similarly for $P_{AB}(\mathbf{r})$ and $P_{BA}(\mathbf{r})$). Comparing which term [$P_{AA}(\mathbf{r})$, $P_{AB}(\mathbf{r})$, or $P_{BA}(\mathbf{r})$] is largest gives us Fig. 4.2(b) where we can explicitly see how C_3 is broken for this model. As a result of this symmetry breaking, the Dirac points are not pinned to the high-symmetry points and are free to move around the Brillouin zone, yet since the model preserves the C_2T symmetry they do not gap out. Numerically, we find that the Van Hove peaks never fully merge [Fig. 4.3(d)] unlike the continuum model, and further, perturbation theory can be used at second order in the

[2]The phases always modify terms like $\mathbf{q}_j \cdot \mathbf{r} + \phi_j$, and in order to see how they represent a center of rotation, consider an $\mathbf{q}_j \cdot (\mathbf{r} - \mathbf{r}_0)$, then $\phi_j = -\mathbf{q}_j \cdot \mathbf{r}$ and $\sum_j \phi_j = 0$. In fact, for any $\phi_{1,2}$ we can determine an $\mathbf{r}_0$ that creates it.

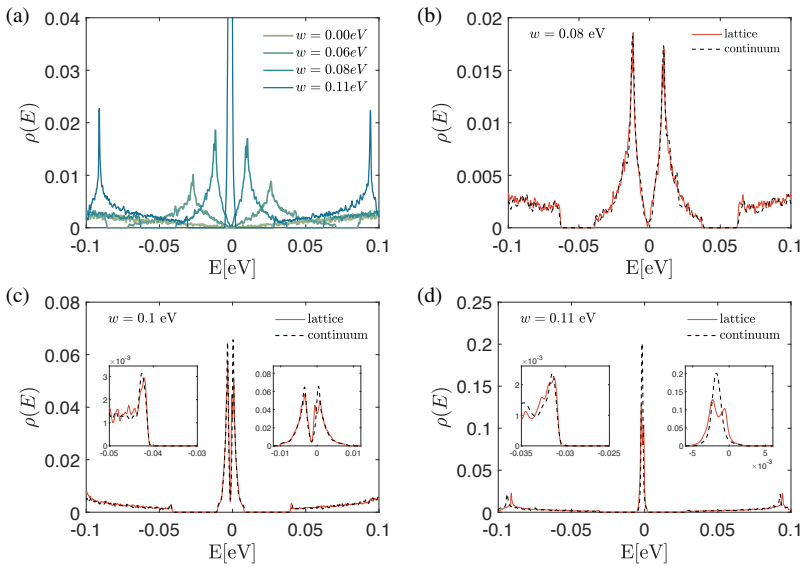

Figure 4.3: (a) The calculated density of states $\rho(E)$ for TBG without disorder as a function of energy E for various interlayer tunneling strengths $w = w_1$ (keeping $w_0/w_1 = 0.75$ where w_0 (w_1) denote the strength of AA and BB (AB and BA) tunneling) at a low twist angle of $\theta = 1.05^\circ$ close to the magic angle, a system size of $L = 569$ and a KPM expansion order of $N_C = 2^{17}$ in the lattice model. The calculated minibandwidth in the magic angle regime $w = 110\,\text{meV}$ is consistent with other studies of the continuum model and the KPM numerical resolution limits to the extent we can access the low-energy regime near charge neutrality. (b,c,d) Comparisons between our lattice model and the continuum theory near $E = 0$ and $\theta = 1.05^\circ$ for $w = 80$, $w = 100$ and $w = 110\,\text{meV}$ respectively, we find remarkable agreement. The insets show the details of the miniband. At $\theta = 1.05^\circ$ and $w = 100\,\text{meV}$, inset of (c), we see a splitting of the Van Hove peaks that is missing from the continuum model associated with additional zone folding in this model. This is seen clearly in the right inset; the left inset shows how the gap of the lattice model here and in the continuum model also match rather well. In (d) at the magic angle $\theta = 1.05^\circ$ and $w = 110\,\text{meV}$, we see that the Van Hove peaks never clearly merge as they do in the continuum model. Again, this is clearly seen in the right inset. The continuum model data here includes 338 bands and has $N_C = 2^{13}$ or 2^{14} whereas the lattice model has $L = 569$ and $N_C = 2^{17}$. Overall, the agreement with the continuum TBG model is quite excellent.

interlayer tunneling strength to see that the velocity never fully vanishes either. For ideal theoretical calculations this might pose a problem, however for our present study, disorder already breaks this C_3 symmetry. Furthermore, in the experimental samples strain from the substrate explicitly breaks the C_3 symmetry [156], which is a natural single-particle source for a nonvanishing velocity and further justifies the use of this model. Thus, the weak breaking of C_3 symmetry in our model is not a problem at all in understanding the physics of real twisted bilayer graphene systems. Second, while the model still has the spatial structure of AA, AB, and BA tunneling, it is slightly distorted, as seen in Fig. 4.2(b). Consequently, the usual TBG moiré unit cell is larger than the unit cell considered in this model. In fact, the mini-Brillioun zone is folded more than in actual TBG as seen in Fig. 4.2(c) (it is smaller by a factor of 3); the process of "unrotating" the two-layers puts the K points of each individual layer on top of each other in momentum space effectively downfolding the moiré Brillouin zone. It is then necessary to determine if this downfolding opens up any gaps, and while it does, these are small indirect gaps in the mini-Brillioun zone of TBG as seen near the Van Hove peaks in Fig. 4.3(c)(inset). Last, for the value of the clean twist angle we focus on here $\theta = 1.05^\circ$ we can emulate the effects of strain and lattice relaxation, similar to Ref. [3], by setting the ratio of AA to AB/BA tunneling to $w_0/w_1 = 0.75$ and $w_1 = w$ based on relaxed band structure calculations [5, 6]. This acknowledges the empirical fact that Bernal-stacked graphene is the energetically favored stacking arrangement in untwisted bilayer graphene. While varying the twist angle changes the ratio w_0/w_1 (as in Refs.[5, 6]), for simplicity we fix this ratio to take that of the clean twist angle ($w_0/w_1 = 0.75$) throughout.

We compare the lattice model with the continuum model in Fig. 4.3(b,c,d). We find good agreement between the two models over a rather broad energy range even beyond the low-energy miniband. In particular, we find that the TBG gap and Dirac velocity are well-produced by the lattice model, see the insets in Fig. 4.3(c,d) . However, a direct comparison at the magic angle condition ($w = 0.11$ eV and $\theta = 1.05^\circ$) reveals that the mini-bandwidth is slightly overestimated within the lattice model. We further notice that beyond the "magic-angle" (i.e. smaller angle θ at fixed w_1 or larger interlayer

tunneling w_1 at fixed $\theta = 1.05°$), the lack of symmetries leads to disagreement with the continuum model (not shown). As a result, we restrict ourselves to the regime where the dimensionless parameter $w_1/(k_\theta v_F)$ is below or at the "magic" value where the discrepancy between the continuum model and the effective lattice model is minimized. Here, we achieve this by focusing on fixing the clean twist angle to $\theta = 1.05°$ and limit the interlayer tunneling to $w \leq 0.11eV$. In this regime, our model captures the TBG electronic structure very well and should be a quantitatively reliable model. This is also the regime of current experimental interest.

These effective models are rather natural as most twist angles are not commensurate, and hence, a quasiperiodic incommensurate background potential should have effects very similar to the moiré potential induced by the twist angle. In fact, twisted bilayer graphene at a large twist angle ($\sim 30°$) has recently been used to form quasicrystals [159, 139], and renormalized but stable low-energy Dirac excitations have been observed [139], supporting the idea of an incommensurate quasiperiodic potential mimicking the twist-angle moiré superlattice. These simpler quasiperiodic models exhibit a similar magic-angle condition where the velocity of the Dirac cone vanishes continuously. In addition, the formation of minibands with large gaps and a strongly renormalized velocity that can be seen to clearly vanish without having to resort to very large system sizes as in the case of twisted bilayer graphene. Therefore, we supplement our calculations on twisted bilayer graphene with similar disorder calculations on a quasiperiodic "toy" model to determine how our choice to model twist disorder impacts our results (see Section 4.5). The two models produce similar results on disorder effects.

In the following, we model the effect of a non-uniform twist by breaking the system up into four equal sections, each having their own twist angle θ with sharp domains between them, as depicted in Fig. 4.2(d). We first choose random phases ϕ_j in the interlayer coupling (this reflects different centers of origin for the twist). In what follows, we take a uniform random phase in the TBG calculations as this seems to be the most physically sensible starting point provided the twist angle is not sufficiently small, which would induce significant lattice relaxation [5, 160, 6]. The θ in each patch is sampled from a box distribution around a central value $\theta \in [(1 - W_R/2)\theta_0, (1 + W_R/2)\theta_0]$ where

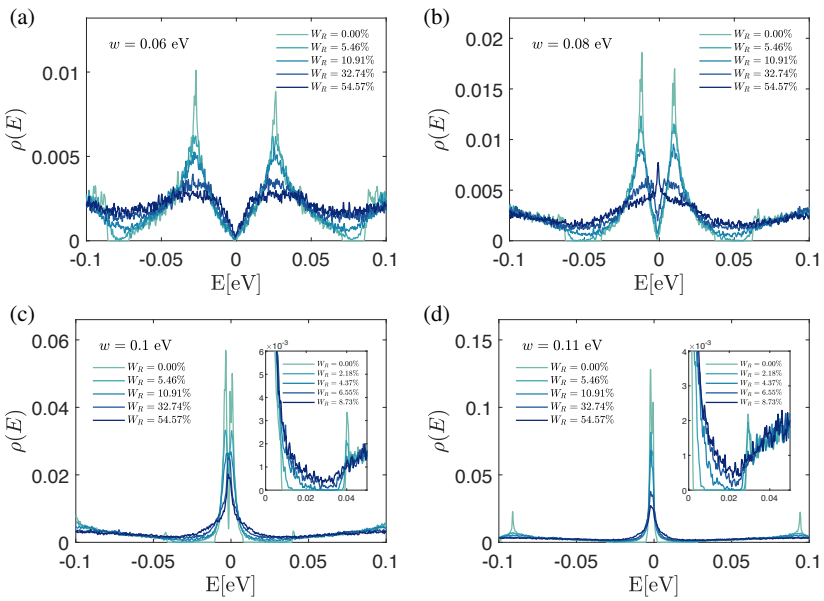

Figure 4.4: The effects of twist disorder on the low energy density of states. The density of states $\rho(E)$ as a function of energy E for a clean twist angle $\theta = 1.05°$, linear system size $L = 569$, and a KPM expansion order of $N_C = 2^{17}$ starting in the semimetal regime of the the TBG model (Top) as well as in the magic-angle regime (Bottom), for different twist-disorder strengths W_R (that characterizes the width of a box distribution $[(1 - W_R/2)\theta, (1 + W_R/2)\theta]$ with $\theta = 1.05°$ from which we sample the random twist angle in each patch). In each case the randomness smoothly fills in the gap while also smearing out the Van Hove peaks. The insets in the bottom two figures is a zoom in of the band gap that clearly fills in with increasing disorder.

we express W_R as a percentage and we fix $\theta_0 = 1.05°$. For twist angles that are small and near the "magic-angle," the moiré unit cell includes roughly 10,000 atoms in each layer. Numerically, we can reach on the order of 36-49 unit cells containing up to 500,000 atoms. This should suffice for our purpose of studying random twist angle disorder effects since the disorder is essentially local in nature. However, to confirm these disorder calculations we consider a related model in Section 4.5: a model which can numerically include an order of magnitude more unit cells. That model has the same features as TBG (the formation of a semimetal miniband and a vanishing velocity at a critical potential strength), confirming the picture presented here. It is gratifying that we get very similar results in the two models (Section 4.5), thus justifying our investigation of twist-angle TBG disorder.

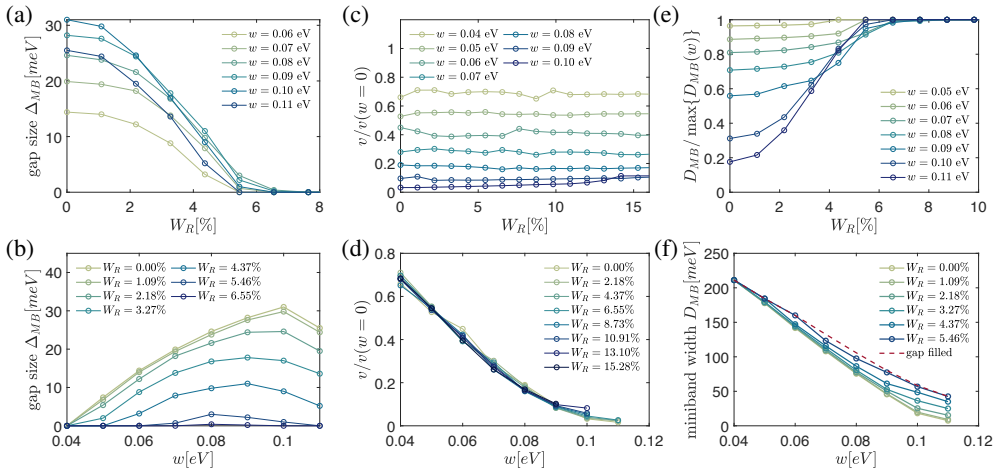

Figure 4.5: Summary of results on the miniband properties in the TBG model with a clean twist angle $\theta = 1.05°$ extracted from system sizes $L = 569$ and a KPM expansion order $N_C = 2^{17}$. (a,b) The estimated gap size Δ_{MB} as a function of disorder strength in the twist angle W_R and the interlayer tunnelings w (where $w = w_1$ and the ratio of AA and BB tunneling to AB and BA tunneling is $w_0/w_1 = 0.75$). (c,d) The velocity $v/v(w = 0)$ as calculated from the density of states as a function of disorder W_R remains approximately unchanged in the presence of disorder W_R (for each value of w). (e,f) The minibandwidth D_{MB} for interlayer tunneling w and disorder W_R. Note that for larger disorder strength ($W_R = 6\%$ or above) in (e) the bandwidth appears to plateau; this is just an artifact arising from disorder completely filling out the gap at this point. While the gap and bandwidth are strongly affected by disorder, the velocity remains unchanged. The red dashed line in (f) that sets the maximum that the minibandwidth can achieve, is determined from the gaps in (b).

We focus on the density of states (DOS), that is defined as

$$\rho(E) = \frac{1}{4L^2}\left[\sum_i \delta(E - E_i)\right] \tag{4.6}$$

where $[\dots]$ denotes an average over disorder, phases, and twists in the boundary condition. In what follows we average over 100 disorder samples. In order to reach large system sizes we use the kernel polynomial method (KPM) to compute the density of states through an expansion in terms of Chebyshev polynomials and we use the Jackson Kernel to filter out oscillations due to truncating this expansion to an order N_C [4]. In the following, we focus on a linear system of $L = 569$ and a KPM expansion order ranging from $N_C = 2^{13}$ up to 2^{17}. This should give us an essentially exact nonperturbative evaluation of the TBG DOS in the presence of twist disorder.

From the density of states we extract an estimate of the renormalized velocity of

the Dirac cones, using the scaling for two-dimensional Dirac cones with velocity v,

$$\rho(E) \sim \frac{1}{v^2}|E - E_D| \tag{4.7}$$

near the Dirac nodal energy E_D and we extract an estimate of v through a fit of the low-energy density of states. We mention that the Dirac cone approximation is only valid at low TBG energies well below the Van Hove singularities, and hence our extracted Dirac cone velocity applies only at low energies. Despite the expectation that disorder will induce a small but nonzero density of states at E_D, we can still use the scaling in Eq. (4.7) to provide an estimate of the renormalized velocity. To quantify the effect of disorder on the Van Hove peaks in the DOS we make a qualitative estimate of the "BCS superconducting transition temperature" from the DOS through

$$T_c \propto \exp\left(-\frac{1}{g\rho(E_{\mathrm{vH}})}\right) \tag{4.8}$$

where E_{vH} is the location of the Van Hove (vH) peak in energy, we take an electron-phonon coupling $g = 1$, and T_c is in units of eV for the TBG model. We stress that we by no means are claiming electron-phonon interaction is the origin of superconductivity in twisted bilayer graphene (although we do not rule out this possibility either). We are only using Eq. (4.8) as a qualitative measure of how disorder smears out the Van Hove peaks, which reduces the largest possible mean-field critical temperature in the miniband within BCS theory. One should think of the effective T_c in Eq. (4.8) as a measure of the effective nonperturbative coupling induced by the vH singularity, and Eq. (4.8) is a simple quantitative approximation to estimate the effect of twist angle disorder on the vH singularity expressed in units of energy (i.e. coupling strength). The fact that this formula coincides with the BCS formula for the superconducting transition temperature is a matter of convenience in this respect. Any other such formula should provide the same qualitative results although the quantitative details will depend on the specific form of the chosen formula.

4.4 Results

To begin, we first discuss the effects of a random twist angle in the effective TBG lattice model. Since the twist shows up explicitly in the interlayer tunneling term, randomness appears solely in this part of the Hamiltonian. However, interlayer tunneling either occurs between equivalent sites or nearest neighbors (on the triangular Bravais lattice) between the two layers. This is due to $\mathcal{T}_0$ and $\mathcal{T}_1$ terms in Eq. (4.4), and thus, randomness in the twist angle will induce contributions from both of these terms.

The miniband that is formed due to the twist can be characterized by the following independent and complementary quantities: (1) the size of the energy gaps (mostly at 'higher' energies at the miniband edges) separating it from the rest of the states, (2) the effective low-energy velocity of the Dirac cones in the minizone, (3) the minibandwidth, and (4) the size and shape of the Van Hove peaks (which are strongly enhanced due to the formation of the miniband itself before disorder is taken into account). These features are all summarized in Fig. 4.1.

First, as shown in Fig. 4.4, disorder destabilizes the integrity of the miniband that is created due to the twist. When the gaps first develop, they appear at energies $\sim v_{\mathrm{F}} k_{\mathrm{D}} \sin(\theta/2)$ and their size is perturbatively controlled by $w_1 = w$. As the figure shows, the gaps become soft due to averaging together different patches of random twist angles. We extract the miniband (MB) gap Δ_{MB} for various values of interlayer tunneling (w_1) and disorder strength, as shown in Fig. 4.5(a,b). Increasing the interlayer tunneling and approaching the magic-angle condition makes the semimetal miniband more pronounced and stable by increasing the size of the gap, which is maximal near $w = 0.1\,\mathrm{eV}$. Introducing finite disorder makes these gaps soft and the average band gap fills in monotonically with increasing disorder. Eventually, the gap is filled in completely, which we find occurs roughly for $W_R = 6\%$ of the clean twist angle, and there is no longer a clear separation between the miniband and the rest of the states. This effect is clearly visible in experiments, as the band insulating gap is destroyed (e.g. as seen in Ref. [97]). The sensitivity of the gap to disorder in the twist angle is rather intuitive, as the location of the gap is dictated by the scattering between the Dirac

nodes of equal chirality but different layers, and the energies that mix to open a gap are determined by θ, whereas the size of this gap is dictated by w. But the fact that the primary insulating gap at the full filling of the moiré miniband may be completely suppressed by a twist-angle disorder as small as just $< 10\%$ is non-obvious– naively on perturbative grounds one may expect a relative disorder of the order of unity (i.e. 100%) in order to completely suppress the gap. Clearly, the miniband insulator is very sensitive to twist-angle disorder, and this may be the reason why the measured gaps vary quite a bit from sample to sample even for nominally fixed twist angles.

Second, we discuss to the features of the miniband which presumably drive strong correlation effects, namely the renormalized Dirac cone velocity v [Fig. 4.5(c,d)] and the size of the minibandwidth D_{MB} [Fig. 4.5(e,f)]. Surprisingly, we find that the Dirac velocity is remarkably robust to disorder and while it is strongly suppressed for increasing w (as expected since this is an effective decrease of the twist angle), increasing disorder enough even to fill in the band gaps and suppress T_c completely is not sufficient to modify the effective velocity which maintains its clean value in a robust manner even in the highly disordered situation. As shown in Figs. 4.5(c,d), the effective velocity extracted from Eq. (4.7) does not renormalize until the disorder is very large; in particular, Fig. 4.4 demonstrates that the low-energy scaling of the DOS $\rho(E) \sim |E - E_D|$ remains robust for a range of disorder with an unmodified slope. Close to the magic-angle regime ($w \approx 0.11\,\mathrm{eV}$), the vanishing of the velocity is becoming rounded out; however to see this develop for a large disorder range is challenging as we are limited by the energy resolution needed and therefore we only present results for disorder strengths where the scaling in Eq. (4.7) is clearly visible. In any case, close to θ_{Magic}, the whole concept of a velocity becomes dubious as the TBG basically is a completely flatband system with essentially no energy regime available for the Dirac cone approximation to apply.

The minibandwidth D_{MB} is similarly substantially reduced as we approach the magic-angle regime, as shown in Figs. 4.5(e,f). However, disorder both fills in the band gaps [Figs. 4.5(a,b)] and also broadens the minibandwidth which we we are able to track provided the band gaps have not completely filled in [that we mark with a

red dashed line in Fig. 4.5(f)]. The effect of disorder on the minibandwidth is much stronger than the effect on the velocity, and we expect disorder may reduce the strength of correlations by broadening the size of the miniband. It will not, however, have a very large effect on the Dirac velocity for weak disorder. We believe that such effects of disorder strongly suppressing correlation effects in the system (by effectively broadening the minibandwidth) are already apparent in the experimental samples since the insulating gaps (i.e. the correlated insulator phase) at commensurate fractional filling of the miniband often do not show up in many samples, and when they do, the typical correlated insulating gap energies are often rather small and vary strongly from sample to sample.

While the gap and hence minibandwidth are strongly affected, disorder also has an effect on the finer features of the minibands. The effects of twist disorder on the Van Hove peaks are captured quantitatively in Fig. 4.6. Van Hove singularities in 2D have a logarithmic singularity and thus should diverge with system size $\rho(E_{\mathrm{vH}}) \sim \log L$. However, in our KPM calculations, we expect that the finite expansion order (N_C) produces a larger finite size effect than the system size. Therefore, we study the scaling of the Van Hove peaks with the KPM expansion order in Fig. 4.6(a). This clearly demonstrates that the 2D logarithmic vH singularity, manifesting the scaling $\rho(E_{\mathrm{vH}}) \sim \log N_C$ in the clean limit, becomes rounded out due to disorder and no longer diverges with increasing N_C. Interestingly, however, the location and separation of the Van Hove peaks is very insensitive to disorder as shown in Fig. 4.6(b). Despite the average location of the Van Hove peaks remaining fixed, disorder broadens them out as we show in Fig. 4.6(c) by computing the full width at half maximum (FWHM). Not only does this figure demonstrate that the FWHM of the vH peaks strongly decreases with increasing w it also shows that the effects of disorder on the vH peaks are much stronger for smaller w away from the magic-angle regime. This subtle effect of twist angle disorder on the vH peaks is rather non-obvious.

To study disorder effects on the Van Hove peaks in more detail we extract an estimate of the mean-field BCS superconducting transition temperature from Eq. (4.8) due to the DOS at the Van Hove peak energy. We show the effects of interlayer tunneling

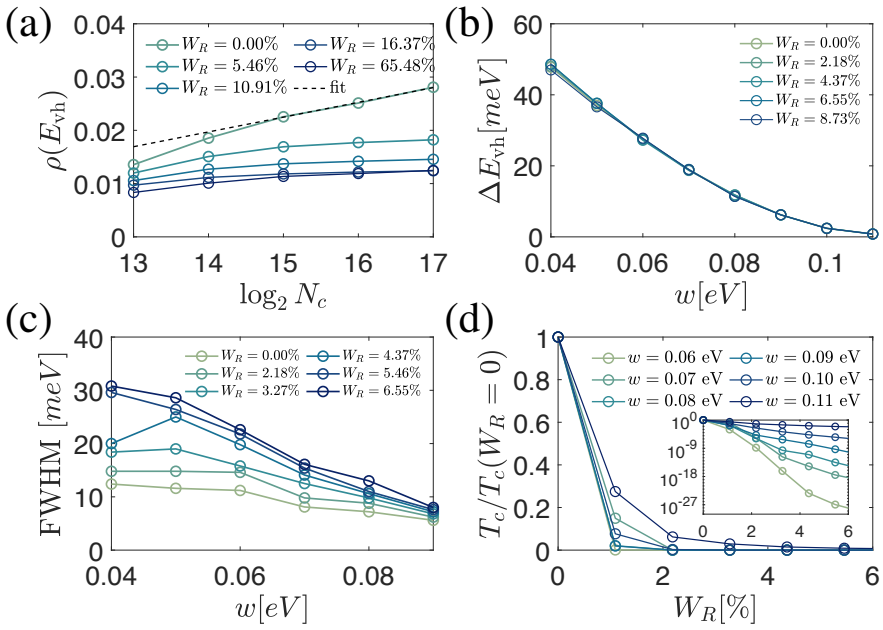

Figure 4.6: The effects of twist disorder on the properties of the Van Hove peaks for a clean twist angle $\theta = 1.05°$, a linear system size $L = 569$, and a varying KPM expansion order (N_C) in (a) whereas in (b,c,d) we use $N_C = 2^{17}$. (a) As we scale the Chebyshev expansion order, we see that the Van Hove peak is logarithmically divergent (with a fit shown as a black dashed line), but once we add disorder, it rounds out and saturates to a finite value. (b) The energy separation between Van Hove peaks remains stable as disorder increases even though we find (c) that the full-width half-max (FWHM) of the Van Hove peaks becomes broader as disorder increases. (d) The estimated BCS critical temperature or the effective coupling constant [see Eq. (4.8) in the main text] from the density of states at the Van Hove peak as disorder is tuned up for various values of w.

and disorder on T_c in Fig. 4.6(d). Since the Van Hove peaks are strongly affected by w, we normalize T_c by its value in the clean limit to compare our disordered results for each value of w. In the absence of randomness, shown in Fig. 4.3(a), as we increase w the minibandwidth shrinks, pushing the same number of states down to a lower energy scale, which in turn enhances the Van Hove peaks considerably. Upon introducing the twist disorder, T_c is suppressed, and this effect, rather unexpectedly, is most pronounced for weak interlayer tunneling strengths, whereas for w close to the magic-angle condition ($w = 0.11\,\text{eV}$ for $\theta \approx 1.05°$) we find T_c is not as strongly affected by weak disorder in comparison.

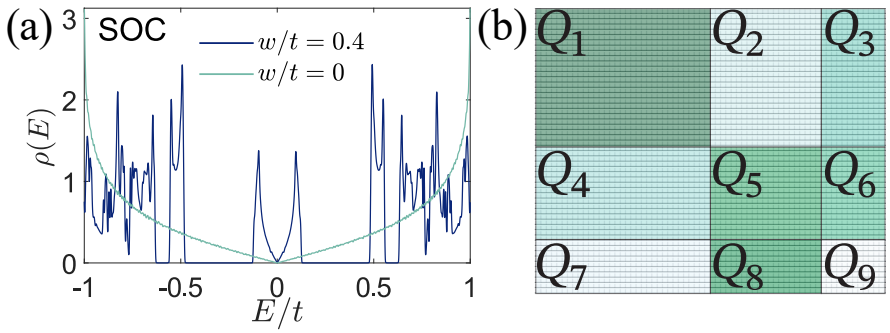

Figure 4.7: (a) The calculated density of states $\rho(E)$ as a function of energy E for the spin-orbit coupled model of Dirac points perturbed by a quasiperiodic potential, with a quasiperiodic wavevector $Q = 2\pi F_{n-2}/F_n$ with the system size $L = F_n = 144$ and a KPM expansion order $N_C = 2^{14}$. (b) A depiction of how we break up the SOC square lattice model into regions of different quasiperiodic wavevector Q_i (to simulate disorder), which are taken from a box distribution about a central value. We vary both the number of regions and the size of disorder in each region.

4.5 Spin-orbit coupling model

In addition to the lattice model of twisted bilayer graphene in previous sections, the second disordered TBG-like model we study is a two-dimensional tight-binding model with spin-orbit coupling (SOC) in the presence of a quasiperiodic potential, which is defined the same way as Chapter 3 as

$$H_{SOC} = \frac{1}{2} \sum_{\mathbf{r},\mu=x,y} (it\chi^\dagger_{\mathbf{r}}\sigma_\mu\chi_{\mathbf{r}+\hat{\mu}} + \text{h.c.}) + \sum_{\mathbf{r}} V(\mathbf{r})\chi^\dagger_{\mathbf{r}}\chi_{\mathbf{r}}. \tag{4.9}$$

where t is the hopping strength, the lattice spacing is set to unity, $\chi_{\mathbf{r}}$ denotes a two component spinor of annihilation operators, and σ_μ are the Pauli operators. We mimic the effect of a twist through a quasiperiodic potential

$$V(\mathbf{r}) = W \sum_{\mu=x,y} \cos(Qr_\mu + \phi_\mu), \tag{4.10}$$

of strength W, an incommensurate (or quasiperiodic) wave-vector Q, and ϕ_μ is a random phase sampled between 0 and 2π. We average over twisted boundary conditions to reduce the finite size effects. The goal of using this second model is to test the universality of the conclusions we reached in the main text using the TBG lattice model. Note that for the DOS computed in the SOC model we normalize the DOS in Eq. (4.6) by a factor of $2L^2$ as opposed to $4L^2$ to account for the smaller local Hilbert space.

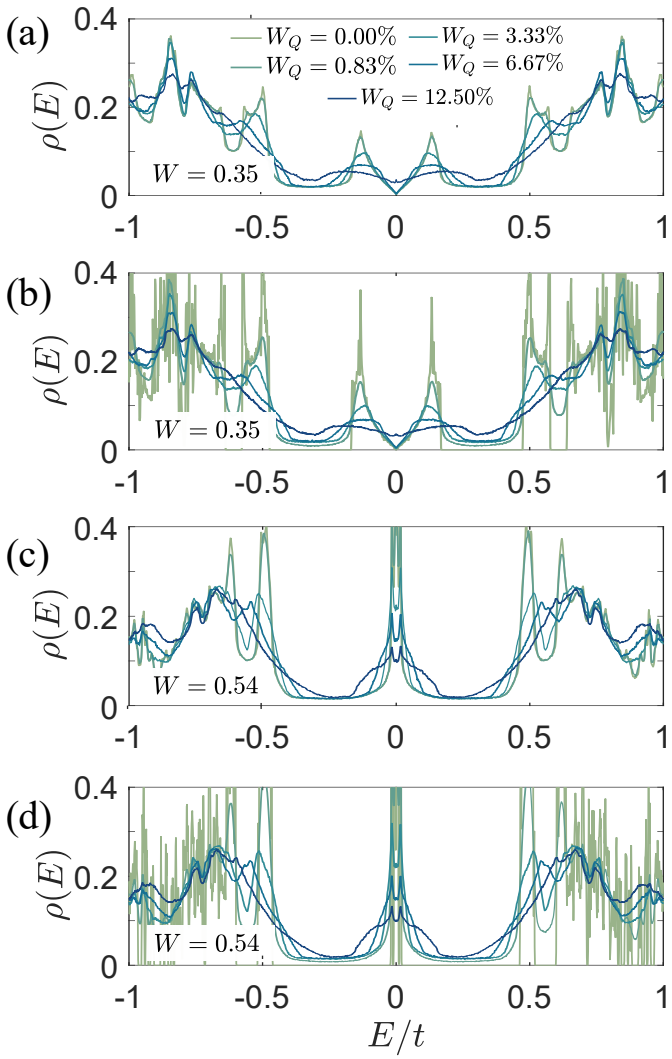

Figure 4.8: The disorder-free density of states $\rho(E)$ as a function of energy E obtained from a linear system size $L = 144$ and a KPM expansion order $N_C = 2^{14}$ starting in the semimetal regime of the model, comparing the case of a fixed random phase across the entire sample (b, d) and a different random phase in each patch (a, c) for different strengths of disorder in the wavevector and $n_P = 7$ randomly placed patches. Note that the random phase in each patch is disordered even for $W_Q = 0$.

The effect of the quasiperiodic potential on Dirac points is similar to twisting two layers of graphene [7]. As shown in Fig. 4.7(a) for a large enough value of W, a semimetal miniband forms with a renormalized velocity, sharp Van Hove peaks, and hard gaps separating it from the rest of the spectrum. Importantly, the SOC model has the great advantage that the formation of minibands, a hard gap, and flat bands are clearly visible on much smaller system sizes compared with the effective lattice model of TBG. Here, it is sufficient to consider system sizes of $L = 144$ or larger to see these effects, whereas in the TBG model the minimum number of sites required to form a clear miniband is at least a linear system size of $L = 300$.

In the calculations of the TBG model we broke the system into four squares of equal size, which was for simplicity of modeling while being able to correctly capture the formation of the miniband by keeping each patch sufficiently large. We now investigate the effects of making the size and shape of these regions random as well as increasing the number of random patches n_P, something that the computational demands of the lattice TBG model did not allow us to do. We divide the $L \times L$ lattice into $(n_P)^2$ domains, by cutting it through $n_P - 1$ vertical and $n_P - 1$ horizontal lines which are randomly located. Each domain i is given a quasiperiodic wavevector and phase $[Q(i), \phi_\mu(i)]$, as illustrated in Fig. 4.7 (b). We introduce randomness in Q in a similar way as in the main text, such that $Q(i) = Q_0 + \delta Q_i$ where $Q_0 = 2\pi F_{n-2}/F_n$, F_n is the nth Fibbonnaci number, and we take the system size $L = F_n$ so that Q_0 is a rational approximant to the irrational number $2\pi(2/[\sqrt{5}+1])^2$. In each domain (or patch) δQ_i is taken from a uniform distribution around Q_0, i.e. $Q(i) \in [(1 - W_Q)Q_0, (1 + W_Q)Q_0]$ and W_Q is expressed as a percent (similar to the random disorder W_R in the main text). For the results on the SOC model we average over 300 disorder samples.

In order to understand the role of taking a uniform phase [ϕ_j in Eq. (4.5)] in the TBG calculations we consider choosing the phase in each patch $\phi_\mu(i)$ in two distinct ways, which are: (A) One global phase $\phi_\mu(i) = \phi$, which is equivalent to our set up in the TBG model. (B) In each patch, the phases $\phi_\mu(i)$ are independently picked from a uniform distribution $[-\pi, \pi]$, which amounts to a disorder potential even for a fixed wavevector across the sample. Option (A) has no discontinuity in the phase across the

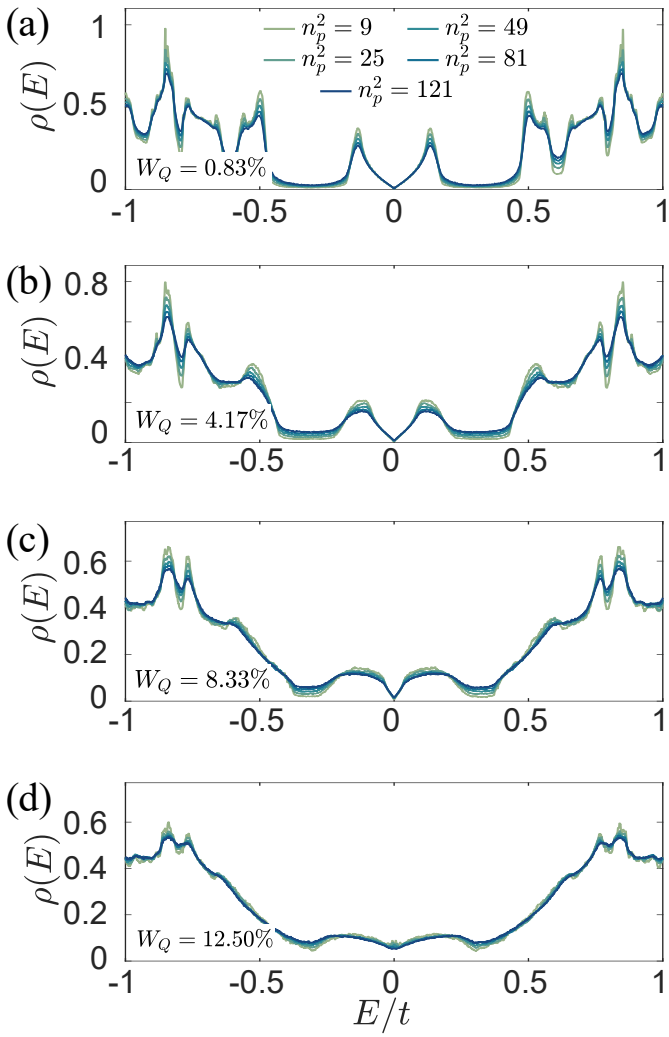

Figure 4.9: Density of states as a function of energy in the semimetallic regime of the SOC model focusing on the miniband at low energy using a linear system size $L = 144$ and a KPM expansion order $N_C = 2^{14}$. We focus on the effects of the different number of random patches used for various different disorder strengths in the quasiperiodic wavevector W_Q from $W = 0.35$. Here we are taking one global phase across the sample to isolate the effects of randomness in Q and choice of patches alone.

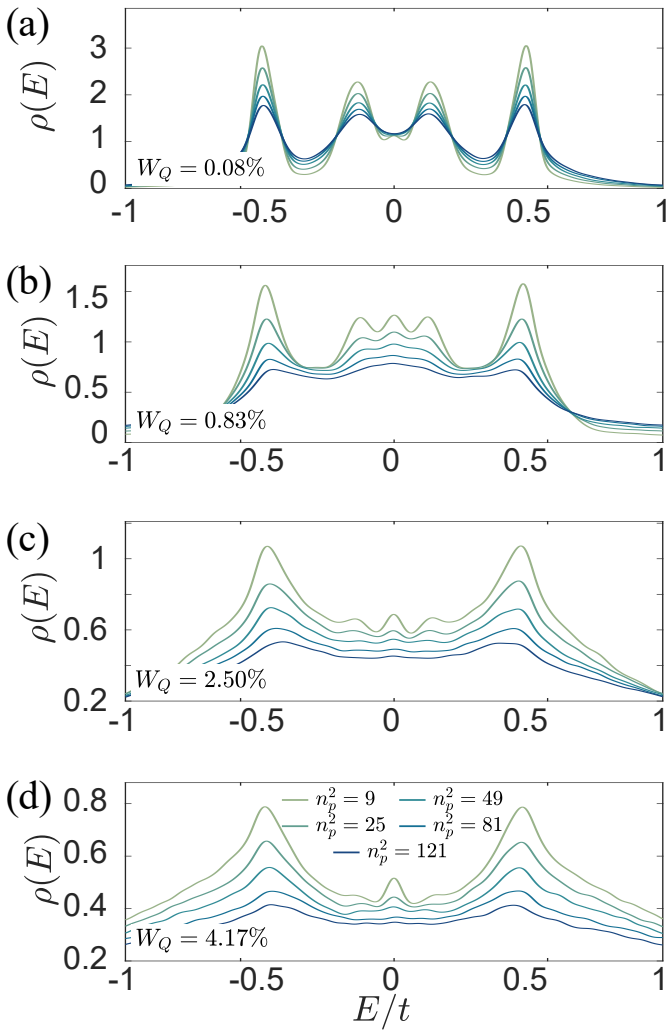

Figure 4.10: Density of states as a function of energy in the magic-angle regime ($W = 0.54$) of the SOC model focusing on the miniband at low energy with a linear system size $L = 144$ and a KPM expansion order $N_C = 2^{14}$. We are displaying the effects of different number of patches of a random wave vector across the sample.

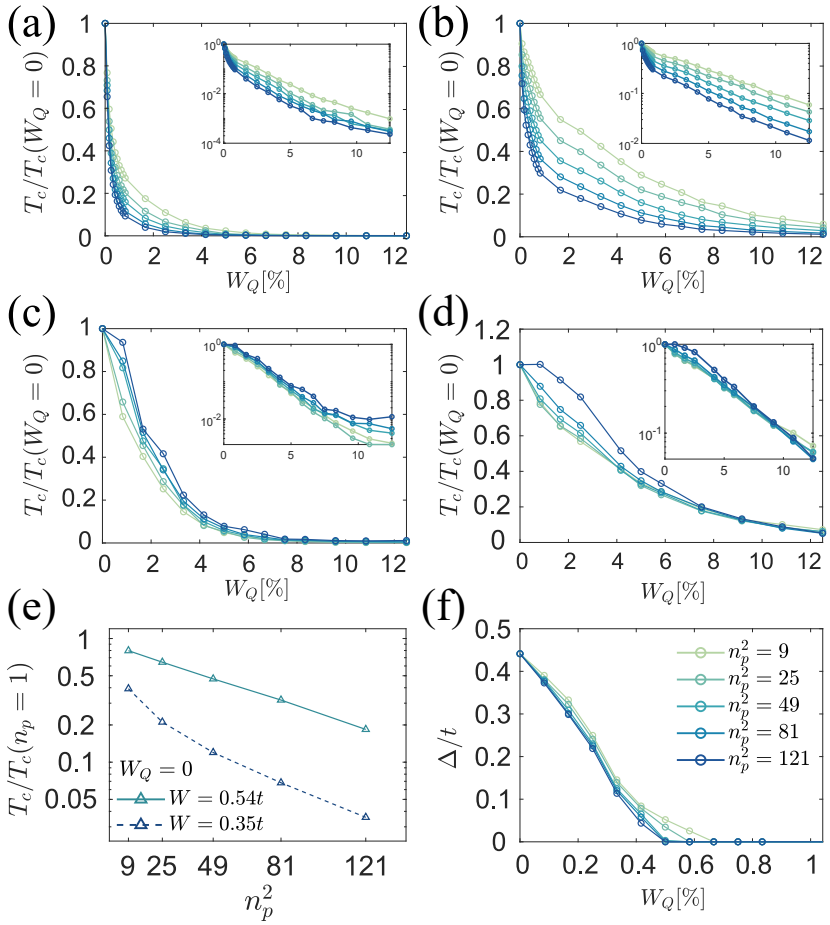

Figure 4.11: The estimated critical temperature (or effective coupling– see Eq. (4.8) in main text) from the Van Hove peaks in the DOS as a function of randomness in the twist vector comparing two choices for the random phase for different number of randomly placed patches. (a,b) One fixed phase, corresponding to a single rotation origin. (c,d) Random phases $\phi_\mu(i)$ in each block. The left panels are $W = 0.35$ in semimetal phase, while the right panels are $W = 0.54$ at the magic-angle. Random phases in each block produce very strong randomness in the model and smears out the Van Hove peaks more easily. (e) The critical temperature T_c with random phases $\phi_\mu(i)$ in each block but without randomness in Q, as function of number of patches n_p^2, and normalized by T_c with only one patch. (f) The gap size as function of randomness. Comparing to the suppression of T_c, the gap is filled in for $W_Q \approx 0.5\%$, which is much smaller than the critical W_Q ($\sim 10\%$) needed for Van Hove peaks to be smeared out. These results are obtained from data using a linear system size $L = 144$ and a KPM expansion order $N_C = 2^{14}$.

boundaries of each patch. Note that because of the variation in Q, even fixing $\phi_\mu(i) = \phi$ to be one global phase does not enforce a continuous boundary condition across patches. The most random choice we can make is through option (B), which means any phase can be chosen on each patch, with no restriction. In this case there is a sharp jump of the potential across all of the patches. In particular, when the number of domains approaches the number of sites, the quasiperiodic potential turns into random disorder potential. The "randomness" of option (B) is clearly the strongest and is not controlled by the parameter W_Q. This is demonstrated in Fig. 4.8, which shows that randomness in the phase smears out the fine features of the density of states and fills the gaps in more easily and is qualitatively similar to the case with a fixed phase. Thus, randomness in the phase is not essential to include to study disorder, and in the following we will mainly focus on keeping the phase fixed throughout the sample.

To understand the effects of a finite number of patches we present results in the semimetal ($W \approx 0.35t$) and magic-angle ($W \approx 0.54t$) regime of the SOC model (see Ref. [7]) in Figs. 4.9 and 4.10. A clear trend in all of the results is that increasing the patch number enhances the randomness, which effectively increases the strength of disorder. This is demonstrated in Fig. 4.11 by the gaps becoming soft for weaker disorder strength, as well as an increased rounding of the Van Hove peaks as we increase the number of random patches. Eventually, at large enough disorder in the wavevector, any remnant of the semimetal scaling regime is destroyed, as shown in Fig. 4.9. In the magic-angle regime as shown in Fig. 4.10, which has a small miniband and a large density of states at the Dirac node energy, we find that disorder systematically broadens the size of the minibandwidth while also smearing out the structure of the DOS at finite energy. Similarly, increasing the number of random patches effectively increases the strength of disorder.

We capture the effects of disorder on the Van Hove peaks through T_c [see Eq. (4.8) in the main text for the definition of T_c, which is simply an effective coupling constant inspired by the BCS theory], which is shown in Fig. 4.11 for wavevector disorder. We find that disorder reduces T_c monotonically, however when compared to the main insulating gap isolating the miniband we find that the Van Hove peaks are relatively

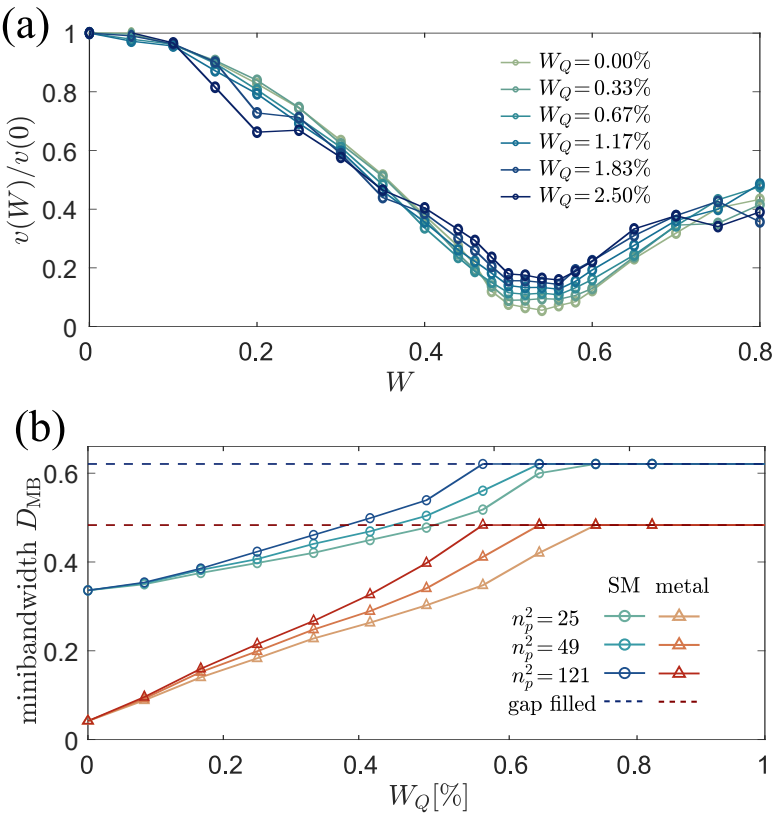

Figure 4.12: Effects of disorder on the renormalization of the velocity of the Dirac cone and the minibandwidth using a linear system size $L = 144$ and a KPM expansion order $N_C = 2^{14}$. (a) Effective velocity of the Dirac cone and how it is rounded out due to randomness in the wavevector. The finite velocity in the magic-angle regime for $W_Q = 0$ is just a finite size effect [7]. (b) Minibandwidth as a function of disorder in the quasiperiodic wavevector, which monotonically broadens for increasing disorder until the gap is filled in and the miniband is no longer separated from the rest of the band (marked as dashed lines). We include both $W = 0.35$ for semimetallic phase and $W = 0.54$ for the magic-angle regime. Note that we have set $t = 1$ here.

much more robust than the main miniband gap. This features is distinct from what we saw in the case of TBG in the lattice model (main text), where T_c was suppressed more strongly than the gap. Given this dichotomy, we believe that the lattice model should be trusted more in capturing the Van Hove physics of real TBG, and thus, T_c is likely to be suppressed more than the main insulating gap in the presence of TBG twist disorder.

We now turn to the effects of wavevector disorder on properties of the Dirac velocity and the minibandwidth, as shown in Fig. 4.12. The velocity that vanishes in the magic angle regime is rounded out and remains finite due to the finite disorder

strength. Away from the magic angle regime, the effects of disorder on the velocity remain weak. Moreover, the minibandwidth broadens with both increasing disorder strength and the number of patches until the gaps are completely filled. This is consistent with the behavior of the TBG model in the main text, namely that twist disorder weakly effects the velocity and increases the size of the minibandwidth, and the latter effects weakens the strength of correlations in the miniband. Thus, both models predict a universally robust disorder-resistant Dirac cone velocity at low energies and a considerable disorder-induced broadening of the minibandwidth, thus weakening the correlated insulator phase.

4.6 Discussion

First, we discuss our approximations in incorporating twist-angle disorder effects in the otherwise defect and impurity free clean twisted bilayer graphene. Using an effective model for twisted bilayer graphene we have theoretically investigated effects of twist angle disorder nonperturbatively by breaking the system into four separate equally sized squares each with a random twist angle around a mean value of $\theta_0 = 1.05^\circ$ close to the magic angle. To understand the effects of our choice of modeling twist disorder with four equal sized squares, in Section 4.5 we analyze a simpler model to determine the effects of this patching scheme. By breaking the system into randomly sized rectangles with each having a different twist value we show that our qualitative results are robust. Increasing the patch number as well as changing the size and shape introduces more randomness into the system and increases the effective disorder strength overall. Therefore, the amount of randomness in each sample is a function of both the random distribution and the number of patches. Here, we want to ensure that each patch has enough sites in it to host a well defined low-energy semimetallic miniband at the magic-angle regime ($w = 0.11$ eV and $\theta \approx 1.05^\circ$) and therefore have focused on 4 squares and total linear system size $L = 569$ (in terms of Bravais lattice sites). Increasing the number of squares or modifying the shape will only introduce more randomness into the system.

We have introduced an effective lattice model of twisted bilayer graphene that is

local, only requiring nearest neighbor (on the triangular Bravais lattice) interlayer hopping terms which already captures many of the features of the continuum model [154, 2], such as the miniband gaps, Van Hove peaks, as well as the velocity and minibandwidth renormalization. The model we have used maintains the C_2T symmetry but breaks the C_3 symmetry. As a result, the velocity and minibandwidth renormalization are affected in the magic-angle regime, which leads to a non-vanishing velocity and an overestimate of the minibandwidth. Moreover, the model also introduces fine structure into the Van Hove peaks that we attribute to additional zone folding that appears in the lattice model. Despite these shortcomings, this lattice model does capture the qualitative behavior of the low energy miniband very well while remaining local and easy to work with numerically. It is possible to construct an effective lattice model that preserves the C_3 symmetry and more accurately reproduces the continuum model in the magic-angle regime with a true vanishing velocity. However, this requires a more non-local interlayer hopping model keeping up to third nearest neighbor tunneling terms on the triangular lattice, which will appear in Ref. [7] (our conclusions change little using this more sophisticated model). In experiments on twisted bilayer graphene, the encapsulating substrate as well as other forms of disorder break the C_3 symmetry explicitly. Therefore, we do not expect that the weak breaking of this symmetry in our effective lattice model affects our conclusions on the qualitative experimental implications of disorder in the twist angle.

Now we briefly summarize our main findings. Our results clearly demonstrate that the low-energy scaling of the semimetal miniband $\rho(E) \sim v^{-2}|E - E_D|$ and the effective Dirac cone velocity (v) are remarkably robust to disorder in the twist angle. While this robustness slightly weakens in the magic-angle regime due to disorder eventually rounding out the velocity minimum, we find that v is essentially disorder independent for less then 15% of randomness in the twist angle. This result suggests that the semimetallic scaling near the magic-angle regime should be clearly visible in transport experiments that average over the whole sample. Indeed, our findings are consistent with the experimental observations on twisted bilayer graphene that have observed a robust "V-shaped" conductance minimum at charge neutrality [138, 97] that signifies

that the semimetallic low-energy scaling persists in spite of the inevitable presence of twist angle fluctuations in the sample. The existence of a low-energy Dirac cone is protected against twist angle disorder. It is interesting to note that twisted bilayer graphene samples that are "massaged" to remove bubbles that have formed in the "tear and stack" approach exhibit an insulating phase at charge neutrality [147]. Presumably, this procedure eliminates some of the twist disorder in the sample and, as a result, domains of twist angle that still possess the semimetallic density of states no longer contribute to the density of states near $E = 0$. Thus, the suppression of twist disorder comes with the price of a strong modification of the observed density of states at low energies.

On the other hand, the minibandwidth is much more strongly affected by disorder, and D_{MB} monotonically increases for increasing disorder strength until the gap is completely filled in and the integrity of the miniband is lost. Similarly, we have found that the insulating gap that separates the miniband from the rest of the states is completely filled in at weak disorder strengths ($\sim 6\%$ of the clean twist angle). This strong sensitivity of the single-particle gaps to twist disorder has been observed in Ref. [97] by placing leads at different places in the sample and finding very strong variations in the gap energies. We suspect that twist disorder will have an even stronger effect on the gaps at the correlated insulator filling fractions. In particular, the increase of the effective minibandwidth by twist disorder entails an effective lowering of the dimensionless correlation strength (i.e. the effective U/t value in the Hubbard-type models) since the Coulomb interaction energy (i.e. the effective U) should not be affected by the disorder whereas the minibandwidth (i.e. the typical t) increases. These combined results imply that disorder will reduce the strength of many-body correlations by increasing the bandwidth of the miniband but will not affect the flatness of the Dirac cones. This interesting subtle prediction of our nonperturbative theory may already have support in the existing experiments since many otherwise high-quality TBG samples (i.e. made from extreme high-mobility graphene sheets) often manifest correlated insulating phases that are very weak, and it is unclear why the correlated insulator phase at commensurate fractional fillings is not universally seen in all TBG samples

of nominally same quality at the same twist angle. We propose that the twist angle randomness is responsible for causing sample to sample variations in the TBG physics for the same average twist angles.

Last, the Van Hove peaks are a clear signature of the miniband in twisted bilayer graphene experiments [104, 161, 105, 149, 150, 151, 152, 153]. Our results demonstrate that the location of the Van Hove peaks of the miniband as well as their separation in energy, which is minimized in the magic-angle regime, are essentially unaffected by twist-angle disorder. Twist-angle randomness smears out the logarithmic Van Hove singularity without affecting their locations in energy. As a result, the density of states becomes an analytic function of energy and system size at the Van Hove peaks in the presence of twist-angle disorder. We have qualitatively assessed the impact of disorder on the mean-field BCS superconducting transition temperature in the miniband by considering a Fermi energy at a Van Hove peak. We have found that twist disorder strongly suppresses T_c [as it is defined in Eq. (4.8)]. If the superconductivity in twisted bilayer graphene is BCS like then our results suggest that samples with large amounts of disorder in the twist angle will likely not superconduct. This is again consistent with experimental observations where not all samples with similar twist angles manifest superconductivity, and we speculate that this nonuniversality is connected with the presence of variable twist-angle disorder in different samples.

4.7 Conclusion

In this work we construct an effective lattice model of twisted bilayer graphene which we use to study the effects of disorder in the twist angle within a nonperturbative essentially exact theory. We also investigate how our choice of modeling disorder affects our results through a detailed investigation of a related but simpler model in Section 4.5. It will be interesting in future work to incorporate larger and smoother domain walls between different twist angles than we have considered here. We demonstrate how randomness in the twist angle affects various properties of the low energy miniband through numerically exact calculations of the density of states using the kernel polynomial method. Remarkably, we show that the velocity of the Dirac cone is robust to

disorder, whereas the other features of the miniband are rather sensitive to randomness in the twist angle. Last, we also discuss how the implications of our theory might already been observed out in existing experimental data and have given guidance for how these disorder effects can be used to help understand the putative strongly correlated effects seen in experiments.

Acknowledgement

This work is done in collaboration with Justin H. Wilson, Jed Pixley and Sankar Das Sarma. We thank Shaffique Adam, Eva Andrei, Zhen Bi, Jason Ho, Philip Kim, Elio König, and Alex Thomson for useful discussions.

Chapter 5

Magic-angle semimetals with chiral symmetry

In chapter 3 we demonstrated the universality of magic-angle semimetals, and spelt out the conditions under which any Weyl / Dirac node can be driven towards a magic-angle transition. Despite of all the similarity across different models, there is clearly the question of how symmetry affect the eigenstate phase transition we described. An analogy that often helps when thinking about models with quasiperiodicity (QP) is the Anderson localization with disorder (but keep in mind that the case of QP strongly differ from the disordered case as no rare-region exist in QP). It is well understood that symmetries [40, 37] dictate the universality class of conventional Anderson localization transitions with disorder. In such classification, chiral symmetry play a vital role. In this chapter, we deep dive into the particular case of incorporating chiral symmetry to the 2D perfect spin-orbit coupling (SOC) model.

To retain chiral symmetry when adding quasiperiodicity, we apply the quasiperiodic modulation through the hopping terms of the base model instead of through potential. Using this model we will characterize the eigenstate phase transition that generates finite density of states in more detail through both spectral observable and multifractal analysis of the wavefunctions. Importantly, this study is a first step towards the task to classify various classes within the universal "magic-angle semimetals". We contribute to the understanding of how such an eigenstate phase transition (EPT) depends on the symmetries of the model, analogous to the story of conventional disorder-driven Anderson transitions. For the case of disorder, the impact of various symmetry classes has been well studied; but it has been unclear for the case of quasiperiodicity despite of the many similarities between disorder and quasiperiodicity. The lack of rare-regions, for example, definitively distinguishes the transition driven by quasiperiodicity from

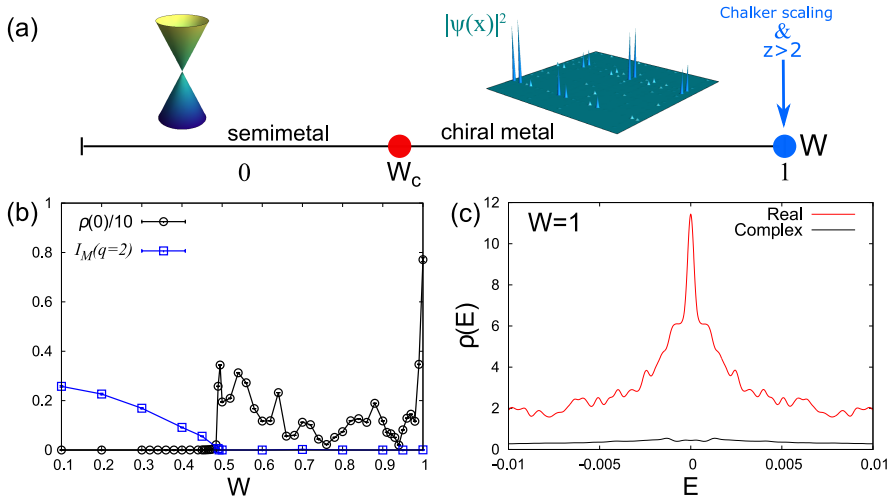

Figure 5.1: (a) Schematic phase diagram at the band center ($E = 0$) extracted from our work. In the semimetal phase the linearly dispersing Dirac cone is stable in the low-energy regime. In the chiral metal phase a band of hybridized zero modes qualitatively explain the sparse (yet still delocalized) structure of the wave functions at the band center. The point $W = 1$ is critical, with a diverging low-energy density of states, a dynamic exponent $z > 2$, and multifractal eigenstates that obey Chalker scaling. (b) The zero energy DOS $\rho(0)$ for a linear system size $L = 233$ and $N_C = 2^{14}$ and the momentum space inverse participation ratio $I_M(q = 2)$ at $E = 0$ with $Q = 2\pi F_{n-2}/L$ and $L = 144$ versus the hopping strength W on a linear scale. (c) The low-energy DOS $\rho(E)$ as a function of energy E for pure QP hopping ($W = 1$) for the case of real and complex hopping amplitudes for system sizes $L = 987$ and $L = 233$ respectively. For the real QP hopping amplitudes we find the zero energy density of states diverges, which is cut off by the finite KPM expansion order N_C, here we take $N_C = 2^{16}$.

those by random disorder.

In addition, the chiral symmetry introduces drastically more flat band at the magic-angle transition with curious connection to topological zero modes. The commensurate limit of the model also manifest intriguing example of higher-order topological insulators.

The rest of the chapter is organized as follows. In Sec. 5.1 we introduce the QP hopping model. In Sec. 5.2, we summarize the main observables of interest, while in Sec. 5.3 we present, in detail, our numerical and analytical results. We discuss the experimental aspects of realizing the theory in Sec. 5.4 and summarize our results and the remaining open questions in the conclusion, Sec. 5.5. The details of the numerical method has been discussed in Chapter 2 and will only be briefly mentioned here. In

Sec. 5.6 we analyze commensurate limits of the model that can be described as a higher-order topological insulator.

5.1 Model

The general form of the Hamiltonian that we focus on can be written as

$$\hat{H} = \hat{T}_0 + \hat{T}_{\mathrm{QP}}, \tag{5.1}$$

where $\hat{T}_0$ denotes a bare, translationally invariant hopping model and $\hat{T}_{QP}$ is the non-trival part of the model that has the QP structure. The model we consider is on the square lattice and the bare hopping model is given by

$$\hat{T}_0 = \sum_{\mathbf{r},\mu=x,y} it/2\psi^\dagger_{\mathbf{r}+\hat{\mu}}\sigma_\mu\psi_{\mathbf{r}} + \mathrm{H.c.}, \tag{5.2}$$

where t is the bare hopping amplitude between site $\mathbf{r}$ and $\mathbf{r}+\hat{\mu}$, $\sigma_{x,y}$ are the Pauli matrices, and $\psi_{\mathbf{r}}$ is a two-component spinor of annihilation operators. The dispersion relation for $\hat{T}_0$ is $E_0(\mathbf{k}) = \pm 2t\sqrt{\sin k_x^2 + \sin k_y^2}$, which contains four Dirac points at $(0,0),(0,\pi),(\pi,0)$, and (π,π), and a low-energy density of states (DOS) $\rho(E) \sim |E|$. Thus, this spinful model on the square lattice describes a two dimensional semimetal with linearly dispersing excitations. It is the 2D SOC model studied in the previous chapter. This model naturally captures the universal low-energy physics of two-dimensional semimetals and is convenient for performing both analytical as well as numerical calculations. It is important to realize that, on the single-particle level, the model in Eq. (5.2) describes the direct sum of two π-flux models (see Chapter 3 which are readily implemented using shaken optical lattices [119]. And indeed, much of our analysis and conclusions apply equally well for a single copy of pi-flux.

5.1.1 Quasiperiodic perturbation

The QP part of the Hamiltonian on the square lattice is given by

$$\hat{T}_{QP} = \sum_{\mathbf{r},\mu=x,y} iJ_\mu(\mathbf{r})\psi^\dagger_{\mathbf{r}+\hat{\mu}}\sigma_\mu\psi_{\mathbf{r}} + \mathrm{H.c.}, \tag{5.3}$$

where $J_\mu(\mathbf{r})$ is the QP hopping amplitude between site $\mathbf{r}$ and $\mathbf{r}+\hat{\mu}$. We construct the hopping matrix elements by considering a two-dimensional surface [e.g. $\cos(Qx)+\cos(Qy)$] with a quasiperiodic wavevector Q (i.e. incommensurate with the underlying lattice) that we evaluate at the mid-point of each bond on the lattice, this yields

$$J_\mu(\mathbf{r}) = W \sum_{\nu=x,y} \cos\left[Q\left(r_\nu + \hat{\mu}\cdot\hat{\nu}/2\right) + \phi_\nu\right], \tag{5.4}$$

where Q is an incommensurate wavevector, ϕ_x and ϕ_y are random phases sampled uniformly between $[0, 2\pi]$ that are the same at each site, and we have set the lattice spacing to unity. We take the linear system size to be given by a Fibonacci number $L = F_n$ and take a rational approximate for the QP wave vector $Q = Q_L \equiv 2\pi F_{n-2}/L$ (unless otherwise stated) such that as $n \to \infty$, $Q/2\pi \to 4/(\sqrt{5}+1)^2$.

In order to reach the pure QP hopping model with finite model parameters we find it convenient to parameterize the bare hopping to be given by

$$t = \sqrt{1-W^2}, \tag{5.5}$$

such that at $W = 0$, $\hat{H} \to \hat{T}_0$ and for $W = 1$, $\hat{H} \to \hat{T}_{QP}$. To test for the possibility of a divergence in the low-energy DOS it is ideal to start from a semimetal model where we know *a priori* there is (strictly speaking) zero DOS in the bare model, thus any potential finite or divergent DOS we find is strictly due to the QP hopping. In the following, the hats are dropped for operators when its meaning is unambiguous.

5.1.2 Commensurate limit and higher order topological insulator phases

In a commensurate limit, the model in Eq. (5.1) can realize a higher order topological phase. Higher order topological insulators have a gapped topological bulk as well as a gapped topological surface. This induces corner modes in two-dimensions and hinge modes in three-dimensions [162]. In particular, in the present model for $Q = \pi n/2$ for $n = 1, 3$ ($n = 2$) the hopping is commensurate with a sixteen (four) site unit cell and perfect nesting induces a gap at the Dirac nodes. As a result, the model realizes a higher-order topological insulator phase for a sufficiently strong W, which we describe in more detail in Sec. 5.6. We will sketch the results in this subsection.

As a concrete example, for $Q = \pi$ we analytically show that the model we consider is a quadrupole topological insulator [162, 13] (QTI). The hopping for $Q = \pi$ induces a two-sublattice unit cell. The Bloch Hamiltonian is then $h(\mathbf{k}) = W(\cos(k_x)\tau_x\sigma_0 - \sin(k_x)\tau_y\sigma_x - \cos(k_y)\tau_y\sigma_y - \sin(k_y)\tau_y\sigma_x) + E_0(\mathbf{k})\tau_z\sigma_0$, where σ, τ are Pauli matrices parametrizing an effective 4-dimensional Hilbert space, see Sec. 5.6. Interestingly, this Bloch Hamiltonian is equivalent to the QTI model in Ref. [162] without intracell coupling for $W > 0$, and as we demonstrate in Sec. 5.6 this phase has topological corner modes at zero energy that lie within the surface and bulk band gap.

More generally, in Sec. 5.3.1 and Sec. 5.6 we show similar higher-order topological insulator (HOTI) behavior also show up when $Q = 2\pi m/n$, where n is an even factor of L, and $\gcd(m, n) = 1$. These can be interpreted by considering a unit cell of n^2 sites. For larger n, there are fewer unit cells in our finite size calculation, making the HOTI character more challenging to observe. Interestingly, in a similar vein, recent work on twisted bilayer graphene predicts the existence of HOTI with large twist angles [163]. It is interesting to note that the quasiperiodic model we investigate here can be regarded as tuning away from a higher-order topological phase via an incommensurate flux.

5.2 Observables

We solve the Hamiltonian in Eq. (5.1) using a combination of numerically exact methods, mostly discussed in Chapter 2. To compute the DOS and wave packet dynamics we use the Chebyshev expansion techniques including the kernel polynomial method (KPM) [4, 164], which allows us to reach sufficiently large system sizes ($L = 987$ is the largest system size considered here). In addition, we obtain wavefunctions via Lanczos or exact diagonalization. In this section, we summarize the observables used in this chapter, with some extended discussion of the ones not heavily used in the rest of the dissertation.

5.2.1 The structure of eigenvalues

To study the transition out of the semimetal phase and the effect of strong QP hopping, we compute the average density of states (DOS) $\rho(E)$ averaged over random phases and twists. The KPM expands the DOS in terms of Chebyshev polynomials up to an order N_C, which together with system size L serves as the main finite size effects that we consider in the numerics. We use twisted boundary conditions by augmenting the hopping terms with a phase. We average over random twists and phases sampled uniformly between $[0, 2\pi]$ (for over 500 samples on each data point). In certain regimes of the model we use the power law scaling of the low-energy DOS

$$\rho(E) \sim |E|^{d/z-1} \tag{5.6}$$

to extract the dynamic exponent z.

The finite KPM expansion order leads to a broadening of the Dirac delta functions in the definition of the DOS [see Eq. (2.1)] into Gaussians with a width $\delta E = \pi D/N_C$ for a bandwidth D (this holds for the Jackson kernel [4] that we are using for all of the calculations presented here). Thus, we also use the scaling of $\rho(E = 0)$ with N_C, where Eq. (5.6) implies that $\rho(E = 0) \sim (N_C)^{1-d/z}$, to analyze the scaling of the low-energy density of states.

We also consider typical DOS (Eq. 2.21) to study the real-space localization properties of the model. In the thermodynamic limit, the typical density of states is non-zero in the extended phase and will go to zero in an Anderson insulating phase, which thus serves as a diagnostic for real-space localization.

5.2.2 The structure of eigenstates

We connect the physical properties of the model to its low-energy eigenstates by studying their structure in both real and momentum space. The semimetal phase is characterized by stable plane-wave states that are localized in momentum space. As shown in Refs. [87, 7], a unique feature of the "magic-angle" semimetal to metal transition is that it coincides with a delocalization of the momentum-space wavefunctions. This implies that the critical momentum-space wavefunctions are developing non-trivial structure

that we should be able to describe using methods to treat localization transitions in real space.

The properties of the probability distribution of an eigenstate can be characterized by a multifractal analysis [75, 37]. We "coarse grain" real-space wavefunction (ψ_b) with its resolution controlled by a binning size $b \geq 1$, and define inverse participatiion ratio (IPR, as elaborated in Chapter 2) on the coarse-grained wavefunction so that we have generalized IPR as a function of binning size b

$$\mathcal{I}_R(E; q, b, L) = \sum_{\mathbf{X}_j} |\psi_b(E, \mathbf{X}_j)|^{2q} \propto \left(\frac{b}{L}\right)^{\tau_R(q)}, \tag{5.7}$$

The dependency on b then allows extracting multifractal exponent $\tau_R(q)$. We take the conventional $b = 1$ and $q = 2$ for studying the second IPR as a proxy of spatial ergodicity/non-ergodicity in a wavefunction.

Moreover, the multifractal analysis is generalized to momentum-space wavefunctions and focus on the Dirac node energy $E = 0$ and therefore drop the energy label. Similar to our work in Ref. [7], we Fourier transform the zero energy wavefunction from real to momentum space $\phi(\mathbf{k}) = (1/L) \sum_{\mathbf{x}} e^{-i\mathbf{x}\cdot\mathbf{k}} \psi(E = 0, \mathbf{x})$. Then, we set up momentum-space boxes of size B and the binned wavefunction (ϕ_B) in momentum space. We note that the box size B in the momentum space determines the effective infrared scale while b in real space is related to the effective ultraviolet scale. The momentum-space IPR and multifractal exponent are given by

$$\mathcal{I}_M(q, B, N) = \sum_{\mathbf{K}_j} |\phi_B(\mathbf{K}_j)|^{2q} \propto \left(\frac{B}{N}\right)^{\tau_M(q)}, \tag{5.8}$$

where $\mathcal{I}_M(q, B, N)$ is the qth momentum-space IPR with a momentum binning size B, a linear size of the momentum grid $N = L$, and we use a subscript M to denote momentum space. Using this definition we can study localization transitions in momentum space by either fixing $q = 2$ (Ref. [87]) or in more detail by analyzing the behavior of the multifractal exponent $\tau_M(q)$ (Ref. [7]). $\tau_M(q)$ also obeys the conditions $\tau_M(q = 0) = -d = -2$ and $\tau_M(q = 1) = 0$.

The multifractal exponents $\tau_R(q)$ and $\tau_M(q)$ provide systematic ways of characterizing the properties of the wavefunction probability distributions in the in the real-

and momentum-space bases respectively. For a plane wave in real space, the spectrum is simply $\tau_R(q) = 2(q-1)$, i.e. a straight line. The corresponding momentum-space wavefunction generically contains a few of sharp peaks (due to a linear combination of the degenerate eigenstates) and is characterized by $\tau_M(q) = 0$ for $q \geq q_c$ where the termination value $q_c \geq 1$, indicates a "frozen" spectrum [37]. In the limit of a single peak, the spectrum is reduced to a localization spectrum with $q_c \to 0$. We will focus on an "unfreezing" transition in $\tau_M(q)$ which is related to the semimetal-metal transition.

Lastly, we test for Chalker scaling by defining a two-wavefunction correlation function as follows [165, 166, 167, 168]:

$$C(E) \equiv \sum_{\mathbf{x}} |\psi_{E_0}(\mathbf{x})|^2 |\psi_E(\mathbf{x})|^2, \tag{5.9}$$

where E_0 is a reference energy and ψ_E is the eigenstate with energy E. Note that the sum runs over all the positions and the internal degrees of freedom have been integrated over. We are interested in energies near the Dirac node so we set $E_0 = 0$. The two-wavefunction correlation $C(E)$ characterizes the degree of overlapping probability among two eigenstates separated by an energy E in a fixed realization. In particular, $C(E) \sim 0$ for localized states with $0 \leq E \ll \delta_l$ (δ_l is the mean level spacing in a localization volume). For states near a mobility edge, $C(E)$ shows nontrivial scaling in the energy separation [165, 166, 169, 167]. States that obey a power law scaling

$$C(E) \sim |E|^{-\mu} \tag{5.10}$$

with $\mu = [d - \tau_R(2)]/z > 0$ exhibit Chalker scaling. (Note that the exponent μ here has been generalized to the system with a low-energy power law DOS [168].) The existence of the power-law scaling potentially implies an enhancement of interactions [170, 171, 172, 173]. We adopt such a diagnostic to study the correlations among the low-energy states in the pure QP hopping limit.

5.2.3 Dynamics

We study transport properties of the model via wavepacket dynamics. We initialize a wave packet to be localized at a single site ($\mathbf{r}_0 = (0,0)$) in real space $\Psi_0(\mathbf{r}) =$

$\langle \mathbf{r}|\Psi_0\rangle = \delta_{\mathbf{r}_0,\mathbf{r}}$ with zero initial velocity (in this case, a spin up/down state suffices), then time evolve that state $|\Psi(t)\rangle = e^{-iHt}|\Psi_0\rangle$, which we evaluate using a Chebyshev expansion [164]. We compute the spread of the wavepacket

$$\langle \delta r(t)^2\rangle \equiv \langle \Psi(t)|[\hat{\mathbf{r}} - \mathbf{r}_0]^2|\Psi(t)\rangle \tag{5.11}$$

where $\hat{\mathbf{r}} = (\hat{x}, \hat{y}) = \sum_{\mathbf{r}}(x, y)|\mathbf{r}\rangle\langle\mathbf{r}|$ and $\mathbf{r} = (x, y)$. The initialized wave packet has weight across the spectrum of eigenstates and is not energy resolved. Therefore it will not be particularly sensitive to the semimetal to metal phase transition at $E = 0$. As a result any estimate we make will be averaged over all energy eigenstates. With this in mind, we use the scaling of wavepacket spreading at long times

$$\langle \delta r(t)^2\rangle \sim t^{2/\tilde{z}} \tag{5.12}$$

to extract an "average" estimate of of the dynamic exponent $\tilde{z}$ (and hence use a tilde) to distinguish this from our energy resolved DOS estimate of z in Eq. (5.6). We note here that the Chebyshev expansion order N_C does not lead to a broadening of levels; it instead dictates the final time that can be reached accurately. Here we track this by requiring the norm of the wavefunction be preserved for all times. In all the results presented here we choose N_C such that the wavepacket has enough time to spread out as far as possible ($= L/2$ in each direction due to periodic boundary conditions) so that the only finite-size effect in our data is due to system size and not N_C.

5.3 Results

While we study all energies and quasiperiodicity strengths, our principle consideration is the Dirac node energy ($E = 0$). At weak quasiperiodicity, we study the development of a non-zero DOS at the Dirac node, which coincides with a delocalization of the wavefunction in momentum space [87, 7]. At strong quasiperiodicity, we study the evolution of the low-energy eigenstates and wavepacket dynamics that contribute to a clear divergence in the low-energy DOS in the limit of pure QP hopping ($W = 1$).

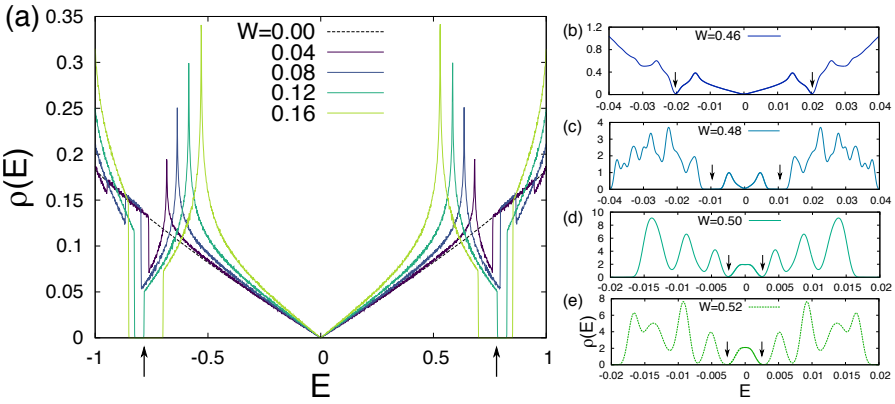

Figure 5.2: DOS versus E for $L = 233$ and $N_C = 2^{14}$ with different QP hopping strengths W. (a) Formation of the first miniband with increasing values of W (vertical black arrows marking the gap that separates this miniband from the rest of the states). (b)-(e) Formation of the second miniband and semimetal to metal transition (vertical black arrows mark the location of the gap to the second miniband). The second miniband is displayed as a thicker line for clarity. Note that the full bandwidth for $W = 0$ is $4\sqrt{2} \approx 5.7$ and all of these results are obtained for $Q = 2\pi \times 89/233$ with a critical value of W for this Q given by $W_c = 0.485 \pm 0.005$.

5.3.1 Transition out of the semimetal phase

Formation of the Miniband(s)

Introducing a weak QP hopping with Q close to π, creates dominant internode scattering that transfers momentum Q_L and mixes degenerate states of equivalent spin. This leads to the formation of hard gaps at finite energy that separates a semimetal miniband near $E = 0$ described by a DOS $\rho(E) \approx \rho'(0)|E|$ with the rest of the spectrum. We note that this defines the slope $\rho'(0)$ and formally we only focus on $\rho'(0^+)$. As W increases, higher-order processes gain importance, hybridize with lower-energy eigenstates, and, therefore, open additional smaller mini bands, see Fig. 5.2. Similar to what was reported in Refs. [87, 7] for semimetals in a QP potential, these minibands can be described perturbatively in the QP strength, and the states in the miniband can be counted by considering the number of states near the Dirac cones that cannot be mixed via a momentum transfer that is restricted to a size Q_L (or smaller for higher order perturbative processes). For $Q_L = 2\pi F_{n-2}/F_n$ we find that there $N_1 = 2(F_{n-3})^2$ states in the first miniband and $N_4 = 2(F_{n-6})^2$ states in the second miniband, which are generated by a momentum transfer of Q_L (from first order in perturbation theory)

and $4Q_L - 3\pi$ (from fourth order in perturbation), respectively. This matches our numerical results, which we compute using either exact diagonalization on small sizes or integrating the DOS over the energy window of the miniband. The formation of the first and second miniband is shown in Fig. 5.2 for a potential strength $W \approx 0.1$ and $W \approx 0.48$ respectively. The van Hove peaks in each miniband are conventional and we have checked that they diverge logarithmically in the thermodynamic limit (not shown). Interestingly, this is a similar result to what was found in Refs. [87, 7], thus the development of minibands at weak QP hopping is not distinct from those generated by a QP potential or from "twisting" two layers of graphene.

If we instead focus on a small Q_L (relative to π) then internode scattering is no longer the dominant effect and intranode scattering also plays a prominent role in the low-energy description. In this case, the hard gaps can be softened into pseudogaps or smeared out altogether. Nonetheless, we still find a semimetal to metal phase transition persists at small Q_L. For $Q_L \lesssim 2\pi F_{n-3}/F_n$ the location of semimetal-to-metal transition is roughly the same, as shown in Fig. 5.3.

Density of states and velocity renormalization

We first focus on the low-energy DOS at weak QP hopping strength. The semimetal is defined as having zero DOS at $E = 0$, and we find this is stable over a finite range of W (as shown in Figs. 5.1, 5.3, and 5.4). This can be seen clearly from the scaling of the zero-energy DOS with the KPM expansion order; in the semimetal regime $\rho(E) \sim |E|$ implies that $\rho(E = 0) \sim 1/N_C$ (see inset of Fig. 5.4) and we use this to locate the boundary of the semimetal phase. Note that this is completely different then the random model, where DOS is always non-zero due to the perturbative (marginal) relevance of disorder in two-dimensions [36, 174, 175].

As the QP hopping is increased the gaps approach $E = 0$, which "flattens" the semimetal miniband until a non-zero value of the DOS is generated after a critical QP hopping strength. For $Q_L = 2\pi F_{n-2}/F_n$ with $L = F_n$ we find that this occurs at $W_c = 0.485 \pm 0.005$ by studying the N_C dependence as shown in Fig. 5.4. After the transition we find a low-energy peak centered about $E = 0$ survives (which eventually

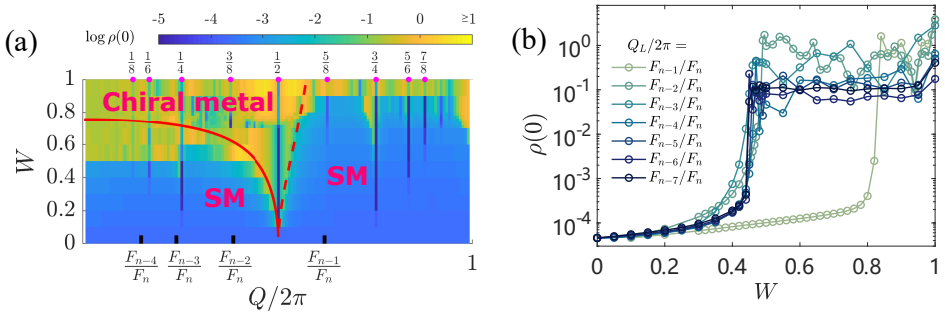

Figure 5.3: The dependence of the DOS at zero energy on the choice of the wavevector Q_L. (a) A phase diagram in the space of W and Q specifying the semimetallic regime (SM), the gapped higher order topological insulating phases (indicated by the sharp drops in DOS on vertical lines indicating rational Q labeled on top), and the chiral metal phase, where the color plot denotes the value of $\log \rho(0)$. Each data point is calculated for a system size $L = 144$ and KPM expansion order of $N_C = 2^{12}$. For these finite sizes, $\rho(0)$ around 10^{-3} corresponds to the SM phase, while larger DOS signals the metallic phase. The solid red curve shows the result of perturbation theory for the critical W_c, given by $v = 0$ in Eq. (5.13). For $Q > \pi$ the estimate of W_c from Eq. (5.13) becomes imaginary, we plot the magnitude of this as a dashed red curve. (b) The $Q_L/(2\pi) = F_{n-m}/F_n$ cuts (marked by the black ticks in top panel) with system sizes $L = 144$, and $N_C = 2^{14}$. We see the transition persists for very small Q_L. Note that the finite value of $\rho(0)$ in the semimetal regime is just a finite-size effect and the transition appears when this rises over several orders of magnitude, see Fig. 5.4.

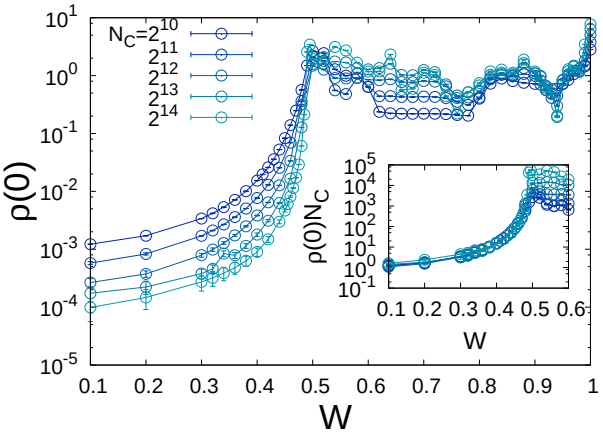

Figure 5.4: The zero-energy DOS $\rho(0)$ as a function of W for various KPM expansion orders N_C and a system size of $L = 233$. In the semimetal regime $\rho(0)$ goes to zero for increasing N_C like $\rho(0) \sim 1/N_C$, which allows us to identify a sharp semimetal to metal transition at $W_c = 0.485 \pm 0.005$. (Inset) The N_C independence of $\rho(0)N_C$ allows us to identify the semimetal phase boundary and demonstrates the robustness of the semimetal phase to quasiperiodicity. This data for $N_C = 2^{14}$ on a linear scale is shown in Fig. 5.1(b).

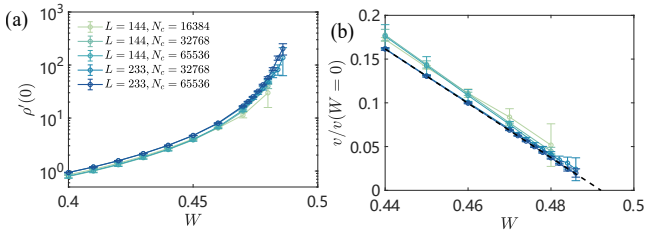

Figure 5.5: The effective Dirac cone velocity extracted from the scaling of the low-energy DOS $\rho(E) \sim \rho'(0)|E|$ [formally we compute $\rho'(0^+)$]. (a) The slope $\rho'(0)$ vs W for various combination of N_c and L. We find that $\rho'(0)$ rises steeply, strongly suggesting a divergence and a non-analytic DOS at the transition. We extract $\rho'(0)$ from a fit to the scaling of the low-energy DDOS $\rho(E) \sim \rho'(0)|E|$. (b) Velocity $v = 1/\sqrt{\rho'(0)}$. The dashed line shows the linear fit of highest N_c and L we have. The linear scaling of $\rho'(0)^{-0.5}$ indicates $\rho'(E=0) \sim (W_c - W)^{-2}$, and predicts critical point $W 0.485 \pm 0.005$ that is consistent with our other analysis.

develops structure at larger QP hopping strength), see Fig. 5.2. We find that all of the states that make up the second (smaller) miniband $= 2(F_{n-6})^2$ for $Q_L/2\pi = F_{n-2}/L$ and $L = F_n$ in the semimetal phase become mixed in the metallic phase and are all *contained* in the peak about zero energy in Fig. 5.2 for $W = 0.50$ and 0.52. This behavior only holds for the chiral model and does not necessarily occur for the case of a QP potential [7]. The location of the transition W_c is not universal and depends on the model details.

We find that the semimetal miniband is well described by $\rho(E) \approx \rho'(0)|E|$, with no change to the power law in energy as the quantum phase transition is approached. The Fermi velocity of the Dirac cone v is related to the DOS via $\rho'(0) \propto 1/v^2$. As the transition is approached from the semimetal side we find $\rho'(0)$ diverges like $\rho'(0) \sim (W_c - W)^{-\beta}$, with $\beta = 2 \pm 0.2$, see Fig. 5.5. This signals that the DOS develops non-analytic behavior at the semimetal-to-metal transition. As a result the velocity of the Dirac cone goes to zero like $v \sim (W_c - W)$. It is very interesting to compare this result with what we found in Ref. [7] for the case of a QP potential, which yielded $\beta = 1.8 \pm 0.4$, which suggests (rather remarkably) that this exponent seems to be independent of the symmetry class.

The suppression of the velocity for $0 < Q < \pi$ can also be captured analytically using perturbation theory in the QP hopping strength, borrowing techniques originally

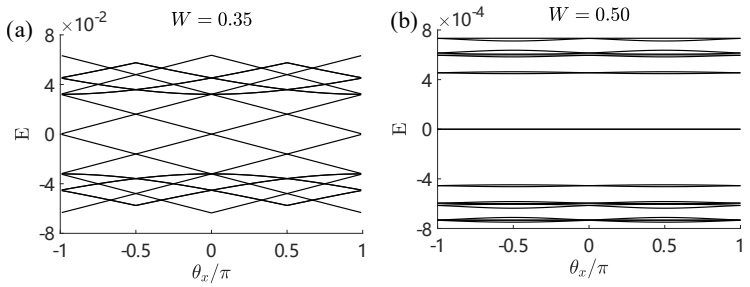

Figure 5.6: The twist dispersion in the semimetal phase (a) and in the chiral metal (b), i.e. low-energy eigenvalues (E) as a function of a twist (θ_x) in the boundary condition along the x-direction obtained by diagonalizing an $L = 89$ sample. (a) For $W = 0.35$ in the semimetal phase with clear Dirac points at $(0, 0)$ and $(\pi, 0)$. (b) Focusing on $W = 0.50$ that is right after the semimetal to metal transition. We see the low-energy minibandwidth for $W = 0.5$ has been substantially renormalized, the band in the center of the spectrum has a bandwidth that has been renormalized by a factor $\sim 10^{-8}$ from its unperturbed value, which is an even stronger effect then has been seen previously [7].

applied to twisted bilayer graphene [2, 7]. Using this framework and going to second order in the QP hopping strength we find

$$\frac{v}{2t} = \frac{1 - \frac{W^2}{4t^2}[1 + 2\sec(Q/2)]}{1 + \frac{W^2}{4t^2}\sec(Q/2)^2}. \tag{5.13}$$

This yields a vanishing velocity, i.e. a magic-angle condition $v = 0$, for $W = W_c^{(\mathrm{v})} \equiv 2/\sqrt{5 + 2\sec(Q/2)}$ which we compare to the numerical calculation of the DOS at zero energy in Fig. 5.3(a). In the regime near $Q = \pi$, where the W_c is small and perturbation theory is controlled, both methods agree well.

These results strongly suggest that the semimetal-to-metal transition generates flat bands due to the vanishing velocity. To clearly demonstrate the presence of flat bands, we study how the low-energy eigenvalues evolve as a function of the twist in the boundary condition. To twist the boundaries we apply a gauge transformation that is equivalent to replacing the hopping terms $t + J_\mu(\mathbf{r}) \to e^{i\theta_\mu/L}[t + J_\mu(\mathbf{r})]$ for a twist θ_μ in the μ direction. We use this as a measure of the low-energy dispersion in the mini (twist) Brillouin zone of size $(2\pi/L)$. This is mathematically equivalent of tiling an infinite system with supercells of size $L \times L$ and finding the corresponding band structure (much akin to tiling graphene with moiré unit cells). As shown in Fig. 5.6(a), we clearly see the presence of the Dirac cones at $(0, 0)$ and $(\pi, 0)$ for weak QP hopping. These bands become incredibly flat in the metallic phase, as shown in Fig. 5.6(b), which confirms

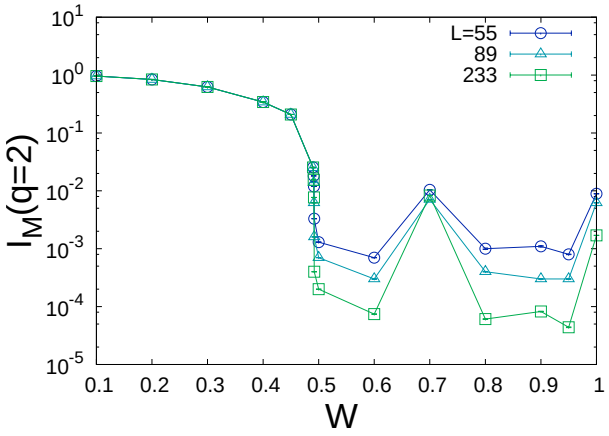

Figure 5.7: The $q = 2$ inverse participation ratio in momentum space $\mathcal{I}_M(q = 2)$ as a function of W for various system sizes L. In the semimetal regime the momentum-space IPR is L-independent and becomes L-dependent in the chiral metal phase due to the wavefunction delocalizing in momentum space. At $W = 0.7$, the momentum-space wavefunctions are still delocalized (see Fig. 5.9) even though the IPR data seems to be only weakly depending on the sizes. All the statistical errorbars in this plot are smaller than the symbols.

both the qualitative expectation from the perturbative analysis and our approach of extracting the velocity from the scaling of the density of states. The flattening effect is substantial in the chiral model and suppresses the minibandwidth orders of magnitude more from the magic-angle transition driven by a quasiperiodic potential [7]. Interestingly, incredibly flat bands have also been seen in the so-called chiral model of twisted bilayer graphene [3], and we find a similar effect here in this much simpler model that also possess a chiral symmetry. Thus, we conclude that the particle-hole symmetry leads to a significant enhancement of miniband renormalization effects.

Wavefunction delocalization in momentum space

We now connect the structure of the eigenvalues that we have probed through the DOS with the structure of the wavefunction. A complementary way to understand the transition is to study how the zero-energy plane-wave eigenstates are perturbed by the QP hopping. For the case of two-dimensional/three-dimensional Dirac/Weyl cones subject to a QP scalar potential it has been shown that the generation of a non-zero DOS coincides with a momentum-space delocalization transition [87, 7], which can be seen in the momentum-space IPR ($\mathcal{I}_M$) for $q = 2$. Similar results for the current model

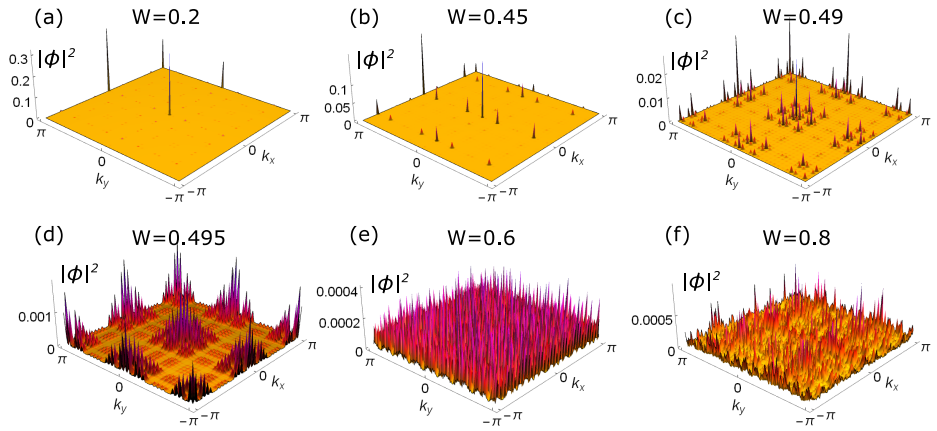

Figure 5.8: Probability distributions of zero energy wavefunctions in momentum space with $L = 144$ and different values of W. (a)-(b): The wavefunctions contain well-defined ballistic peaks at $(k_x, k_y) = (0, 0)$, $(0, \pi)$, $(\pi, 0)$, and (π, π). A few of satellite peaks can be seen in (b) while the major ballistic peaks are still well resolved from the figures. (c): The wavefunction is close to the critical point; The ballistic peaks can still be resolved. Meanwhile, the satellite peaks start to form regions instead of a few well-separated points. (d)-(f): The ballistic peaks are no longer sharply defined due to the hybridization with the satellite peaks which arise from scattering off QP potentials. In (f), the momentum-space wavefunction looks very much like a conventional delocalized state. The critical value is close to $W = 0.49$.

are shown in Figs. 5.1(b) and 5.7. In the absence of the QP hopping, the wavefunction at zero energy is composed of the Fourier modes at the Dirac points $(k_x, k_y) = (0, 0)$, $(0, \pi)$, $(\pi, 0)$, and (π, π). Generically, the zero-energy states are linear combinations of these four plane waves. Therefore, the probability distributions (integrating over the internal degrees of freedom) of the momentum-space wavefunction contains four peaks, which we call "ballistic peaks." If we now translate the multifractal nomenclature to the present problem, we see that these ballistic peaks give rise to a frozen wavefunction. We note that the momentum-space wavefunction here has peaks at the Dirac points regardless of the QP potential (as long as it is weak). On the other hand, the real-space frozen wavefunctions, as realized in the the random vector potential Dirac model [176, 177], have peaks randomly distributed depending on the disorder realization.

To support the argument of perturbing stable ballistic peaks, we plot the momentum-space wavefunctions in Fig. 5.8. In Fig. 5.8 (a), the momentum-space wavefunction is essentially composed of the four ballistic peaks. Generically, the QP hopping decreases the ballistic peaks via "hopping" in momentum space and generates other satellite

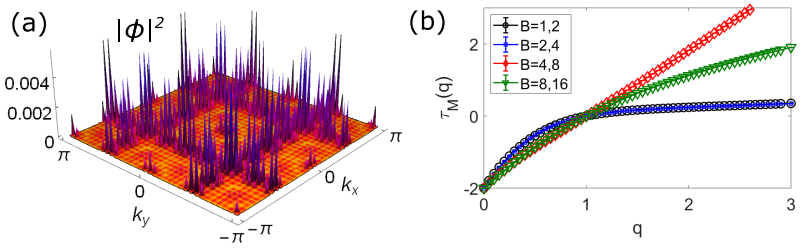

Figure 5.9: Zero-energy momentum-space wavefunction with $W = 0.7$. (a) The probability distribution. The wavefunction is made of sparse peaks and is still delocalized in momentum space. (b) The multifractal spectra $\tau_M(q)$. Each data is averaged over 100 realizations. For smaller binning sizes ($B = 1, 2$ and $B = 2, 4$), the $\tau_M(q)$ show strongly multifractal (but still unfreezing) behavior. Note that $\tau_M(q = 2)$ is not zero for all the binning sizes.

peaks which arise due to the coupling of the QP wavevectors $(\pm Q_L, 0)$ and $(0, \pm Q_L)$. Those satellite peaks have weights related to the order of scattering off of the QP hopping. While there are infinitely many such peaks in the thermodynamic limit, the wave function is weighted subextensively among them (akin to how a localized state dies off exponentially from a central localized site). In finite system sizes and sufficiently weak W, only a finite number (smaller than L^2) of satellite peaks dominate, as shown in Fig. 5.8 (b). For $W < 0.49$, where $W = 0.49$ is close to the critical point, the ballistic peaks remain sharply defined even in the presence of the satellite peaks, and this structure can be captured perturbatively. The weight of the wavefunction on the satellite peaks increases when driving W to a larger value, similar to a localized wavefunction as we approach a delocalization transition. For $W > 0.49$, the ballistic peaks hybridize with extensively many satellite peaks, the wavefunction is "delocalized" in momentum space, as displayed in Figs. 5.8 (d), (e), and (f). Throughout this transition, the wave function is delocalized in real space; however, it acquires a definitive structure that we explain qualitatively in terms of topological zero modes in Sec. 5.3.1. This state is delocalized in both real- and momentum- space, in contrast to the wavefunctions with $W < 0.49$ which are ballistic and composed of a measure-zero set of momenta. The hybridization of an extensive number of momenta most likely creates extensive degenerate zero energy states, causing a finite DOS. And indeed, we witness numerically [see Fig. 5.1(b)] that the unfreezing transition in the momentum-space wavefunction

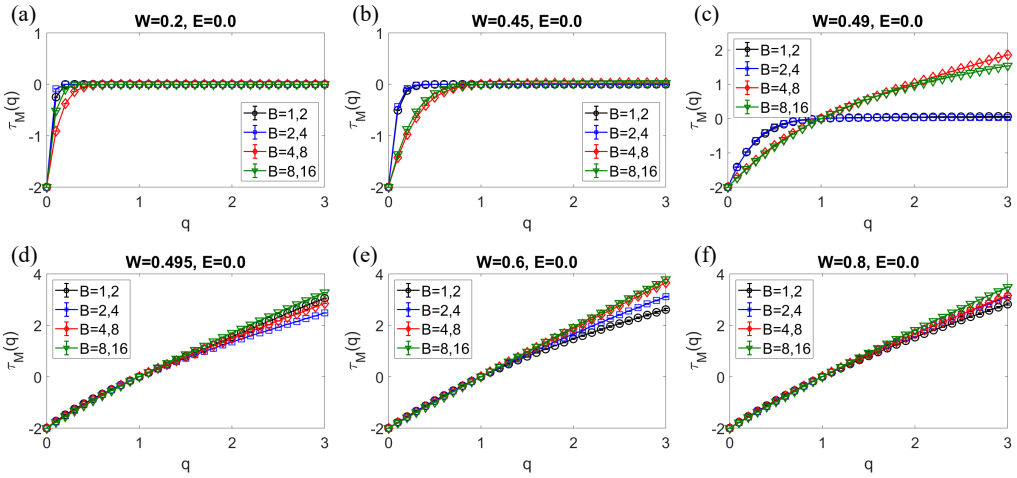

Figure 5.10: Multifractal spectrum of the zero-energy momentum-space wavefunction with different W for $L = 144$. Each $\tau_M(q)$ is obtained via numerical extrapolation of two different values of the binning size B. Each data is averaged over 100 realizations. (a)-(b) All the $\tau_M(q)$ spectra show freezing behavior. (c) $\tau_M(q)$ spectra extracted from larger binning sizes ($B = 4, 8$ and $B = 8, 16$) start to show unfreezing behavior. While the spectra from $B = 1, 2$ and $B = 2, 4$ are still frozen. This is very close to the critical value of W. (d)-(f) All the $\tau_M(q)$ spectra show unfreezing, weakly multifractal behavior.

coincides with the semimetal to metal transition in the DOS.

To study the momentum-space wavefunction quantitatively, we first compute the second momentum-space IPR $\mathcal{I}_M(q = 2, B = 1, N = L)$ [given by Eq. (5.8)] for different system sizes ($L = 55, 89, 233$). In Fig. 5.7, the IPR with $q = 2$ in different system sizes are essentially L-independent for $W < 0.49$. For $W > 0.49$, the IPR becomes size-dependent, an indication that the wave function is composed of an extensive number of momentum states. Similar results can be obtained for $L = 34, 144, 610$. Note that, while it looks like $W = 0.7$ is close to being localized in momentum space, this is not the case as we demonstrate in Fig. 5.9. For even numbers, the Dirac nodes gap out at order $L/2$ in perturbation theory, so while the trend of the IPR is the same as for odd numbers, it quantitatively differs. Correspondingly, we compute the $\tau_M(q)$ spectrum [37] for $L = 144$ by varying the binning size B in every realization as shown in Figs. 5.9 (b) and 5.10. This analysis directly answers if the wavefunctions are governed by well-localized peaks. For $W < 0.49$, the wavefunctions show freezing which is characterized by $\tau_M(q) = 0$ for all $q \geq 1$. We note that a single localized peak results in a spectrum

with $\tau_M(q) = 0$ for all $q > 0$. The frozen spectrum indicates that the dominating regions in the probability distribution of a wavefunction are characterized by a measure-zero set of peaks. For $W > 0.49$, the well-defined ballistic peaks are broadened with finite widths due to hybridization with the satellite peaks. We find that the $\tau_M(q)$ spectrum is weakly "multifractal." For instance, with $W = 0.495$, the $\tau_M(q) \approx 2(q-1) - 0.34q(q-1)$ for $|q| < 1$. These results are summarized in Fig. 5.10. The ballistic peaks are no longer sharply defined as their weights strongly depend on the binning size B. The location of the semimetal to metal transition obtained from the wavefunction diagnostic is in excellent agreement with the semimetal to metal transition in the DOS. As a comparison, we also plot the real-space wavefunctions with the associated parameters in Fig. 5.11. We also emphasize that the present transition is not related to the freezing transition [177, 178, 179, 180, 181, 168] in the context of highly random delocalized systems. Here, we simply use the multifractal analysis to explore the intricate structures in the momentum-space wavefunctions due to the QP hopping.

A theory for the chiral metal phase in terms of topological zero modes

For $W > W_c(Q)$, we have seen how the low-energy eigenstates delocalize in momentum space, which induces well-defined patterns in the real-space structure of the wavefunction (see Fig. 5.11). There are a few key features that are unique to this chiral model and were not observed for a QP potential in Ref. [7]. Firstly, the low-energy excitations minibandwidth has been substantially renormalized reducing it by a factor of $\sim 10^{-8}$, which is a much larger effect then we observed for a QP potential [7], see Fig. 5.6. Second, we do not find any reentrant semimetal phase, for the chiral model, once the system has undergone a transition to the metallic phase, it remains there. This suggests that the metallic phase in the chiral limit should have a unique description that relies on the chiral symmetry. In the following, we will show that the our model possesses a band of quasizero modes which are intimately linked to the chiral symmetry. These solutions to an effective Dirac equation are bound states due to a sign changing Dirac mass induced by the QP hopping. For $W < W_c(Q)$ these bound state solutions strongly overlap: They are not well-defined local eigenstates, therefore they hybridize with the

continuum of plane waves and hence do not play a role in the low-energy behavior. On the other hand for larger $W > W_c(Q)$, these zero mode bound states become sufficiently sharp to be stable. This produces a finite DOS at zero energy and a non-trivial structure in the wavefunction that agrees well with our numerical results in the metallic phase. Since it exists only due to the chiral symmetry (e.g. they do not occur in the QP potential model in Ref. [7]) we dub this phase the chiral metal.

To mathematically derive the above statements, we invoke a perturbative inclusion of the incommensurate modulation on top of a continuum model. In view of the stability of the semimetallic phase below the "magic-angle" semimetal-to-metal transition. Therefore, the physics near the center of the band may be treated in the continuum approximation leading to Dirac Hamiltonians subjected to certain background "Higgs" fields (i.e. a spatially dependent mass fields [182, 183]). We can derive such effective Hamiltonians, which take the form $H = \sum_{\pm} h_{\pm} \frac{\mathbf{1} \pm \tau_y}{2}$ with ($v_0 = 2t$)

$$h_{\pm} = v_0 \not{p} \lambda_z + V(x)\lambda_y \pm V(y)\lambda_x. \tag{5.14}$$

Here $\not{p} = p_x\sigma_x + p_y\sigma_y$ and the original basis in Eq. (2) has been rotated for convenience; to account for all four Dirac nodes, we require more sets of Pauli matrices, τ_μ works within blocks of the same helicities $(0,0)$ and (π,π) [or $(0,\pi)$ and $(\pi,0)$], while λ_μ connect these blocks. In this basis, the chiral symmetry is represented by $\{\sigma_z\lambda_z, H\} = 0$ and time reversal symmetry implies $H = \sigma_y\lambda_z H^T \sigma_y\lambda_z$. Both constrain the structure of the effective Hamiltonian. The dominant contributions for the model at $Q = 2\pi[2/(\sqrt{5}+1)]^2$ are

$$V(x) \;\; = \;\; V_1 \sin((\pi - Q)x) + V_4 \sin((4Q - 3\pi)x), \tag{5.15}$$

with $V_1 = 2W$, $V_4 = W^4/[t^3 \prod_{l=1}^{3}(2\sin(lQ))]$. Since, in the chiral model $\gamma_1 = \sigma_x\lambda_z, \gamma_2 = \sigma_y\lambda_z, \gamma_3 = \lambda_y, \gamma_4 = \lambda_x$ form a Clifford algebra, zero modes (as in other magic-angle systems, such as twisted bilayer graphene [184]) may be readily found analytically at the vortex like nodes of $(V(x), V(y))$. The zero modes of $h_{\pm}$ have the form

$$\Psi_{\pm}(\check{x}) = \mathcal{N} e^{-\sum_{i=1,4} \frac{2V_i}{v_0 q_i}[\sin^2(\frac{q_i x}{2})\lambda_x\sigma_x \mp \sin^2(\frac{q_i y}{2})\lambda_y\sigma_y]} \Phi_{\pm}, \tag{5.16}$$

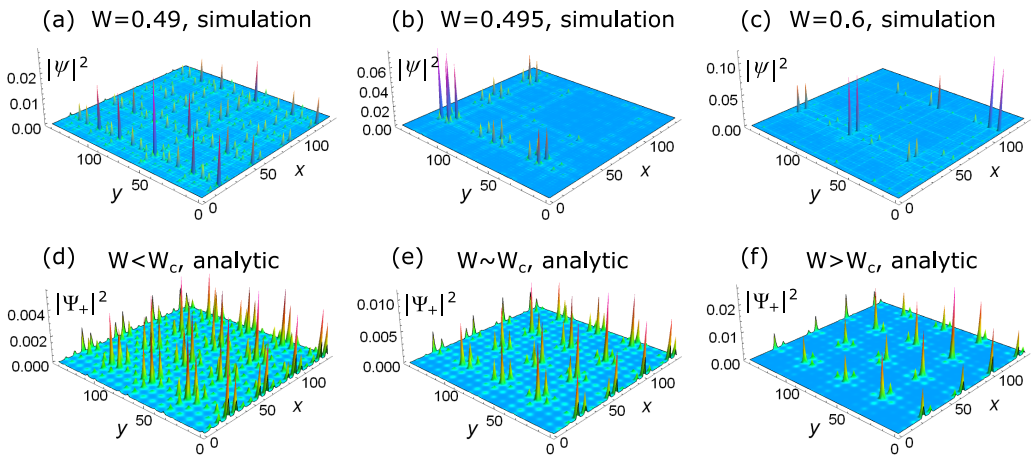

Figure 5.11: Probability distributions of zero-energy wavefunctions in real space with $L = 144$ and different values of W comparing the exact numerical calculations (top row) with the analytic results (bottom row) for the wavefunctions of the chiral metal, in Eq. (5.16). (a) and (d): The wavefunctions are plane waves. (b) and (e): The model is close to the critical point of the semimetal to metal transition and the wavefunction looks like a periodic array of localized peaks. (c) and (f): The wavefunctions are delocalized but possess intricate structure that agrees qualitatively well with the analytic prediction. The critical value obtained from numerics is close to $W = 0.49$. Despite the analytical treatment overestimating the position of the semimetal to metal transition by a factor of 2, it leads to qualitatively similar behavior near the transition. As a result for the analytic results we show $W = 0.83$ in (d), $W = 0.87$ in (e), and $W = 0.91$ in (f).

with $q_1 = \pi - Q$, $q_4 = 4Q - 3\pi$, $\Phi_+ = (1, 0, 0, 1)$, and $\Phi_- = (0, 1, 1, 0)$ such that the eigenvalues of $\sigma_x\lambda_x$ and $\mp\sigma_y\lambda_y$ are both 1. The solution of Eq. (5.16) is plotted in Fig. 5.11 along with the numerical solutions. These bound states are irregularly localized at distances set by $2\pi/q_{1,4}$ and their decay length is given by $\sqrt{v_0/(q_{1,4}V_{1,4})}$. Therefore, a simplest estimate (keeping only q_1 and V_1) suggests that bound states become stable for $W \gtrsim W_c^{(0\text{ modes})} \equiv 1/\sqrt{1 + \text{const.} \times (\pi - Q)^{-2}}$, in good agreement for Q close to π (apart from the numerical constants) with the W_c obtained of Eq. (5.13).

We conclude with three remarks: First, we repeat that this non-perturbative analysis is based on the continuum Dirac Hamiltonian which is clearly only justified for sufficiently low W and inapplicable deep in the metallic phase. Second, we highlight that the bound state picture explains the observation of the sparse real-space structure of the eigenstates for $W \gtrsim W_c$, see Fig. 5.11. Finally, in order to analyze the importance

of symmetries, we also applied the same method to a non-chiral model with a QP potential (from Ref. [7]) and to the model with complex hopping (not included in this thesis). In both cases additional mass terms appear in Eq. (5.14), which breaks the topologically protected depletion of the gap inside a vortex configuration of $[V(x), V(y)]$. As a consequence, topological bound state solutions are absent in these cases.

Real-space Anderson localization and structure of the mobility edges

Real-space Anderson localization in disordered systems of orthogonal and unitary chiral classes are special, because the zero energy state is robust against localization [43, 179, 185], and tend to form a line of critical fixed points between Anderson localized states at finite energy [36]. This model [1] is fundamentally distinct from its random counterpart because the QP hopping is, in some sense, infinitely correlated and generic localization at $E \neq 0$ no longer occurs. It is therefore non-trivial to determine the localization phase diagram in the present model at finite energies. To do so we compare the typical and average DOS [see Eq. (2.21)]. Anderson localized eigenstates necessarily have a typical DOS that goes to zero for increasing KPM expansion order (or system size), and we compare with the average DOS to differentiate between a hard gap (with no states) and localized states. We also use Lanczos diagonalization to examine the localization properties directly via wavefunctions.

As shown in Fig. 5.12, we find that the finite energy eigenstates are not localized for weak QP hopping strength. For QP hopping strengths beyond the semimetal to metal phase transition we find semimetal minibands develop at *finite energy* with a linearly vanishing DOS that is shifted away from $E = 0$ and the edges of the these minibands have Van Hove-like peaks in the average DOS. Interestingly, the typical DOS shows that these finite energy semimetal minibands are Anderson localized As a result, for a single value of W there can be various mobility edges in the system and the region separating localized and delocalized states does not monotonically vary as we tune W. Looking directly at wavefunctions, we confirm the non-monotonic localization behavior

[1] $L = 610$ is a large enough L to suppress this rounding at the expansion orders we consider here.

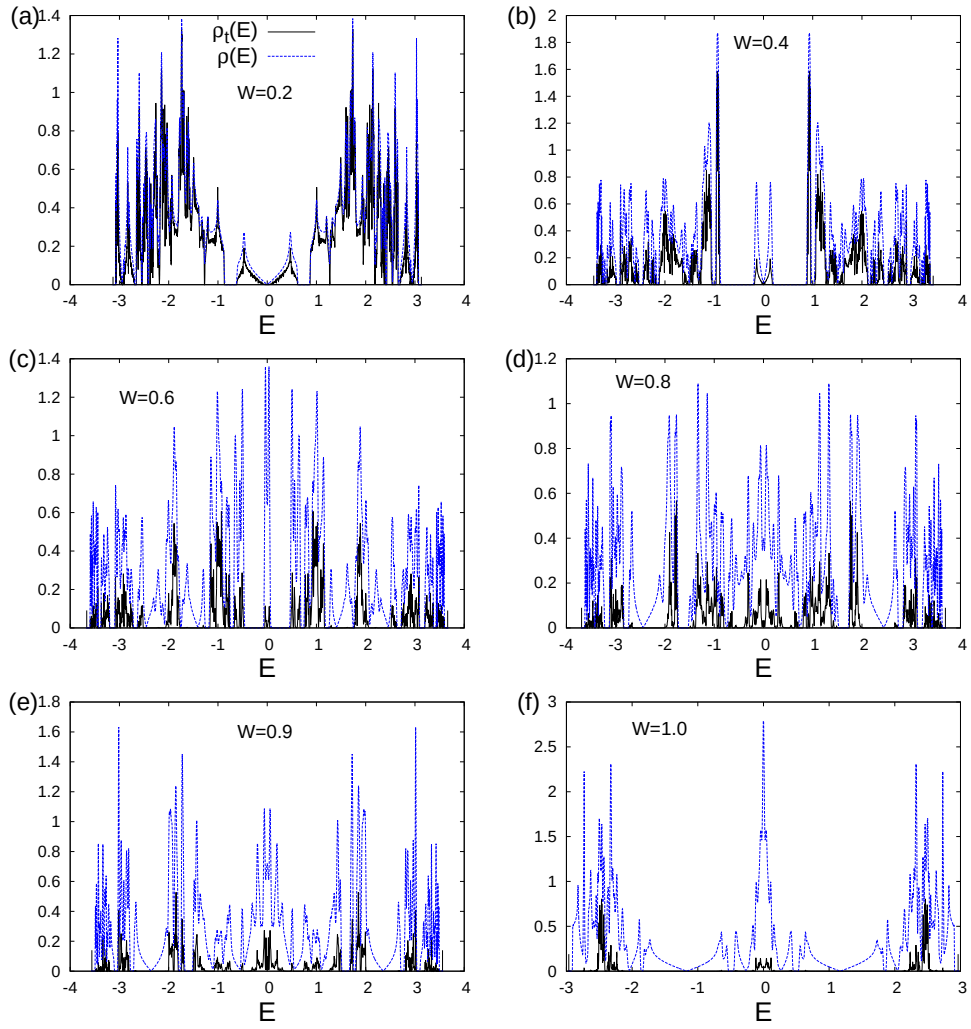

Figure 5.12: Localization properties obtained through the typical DOS. Typical DOS are in black solid lines, and average DOS are in blue dashed lines (to distinguish hard gaps and localized states) for $L = 144$ and $N_C = 2^{14}$ [(a) $W = 0.2$; (b) $W = 0.4$; (c)$W = 0.6$; (d) $W = 0.8$; (e) $W = 0.9$ and (f) $W = 1.0$].

and multiple mobility edges in Fig. 5.12. For example, wavefunctions for $W = 0.8$ and $L = 144$ at different energies are plotted in Fig. 5.13. The results clearly show the same non-monotonic localization properties as a function of energy and are consistent with the typical DOS diagnostics.

Upon increasing the QP hopping strength further, the number of localized states increases but even for pure QP hopping ($W = 1.0$) we still find a finite number of delocalized states. In particular, the low-energy states that contribute to the diverging DOS do not appear to localize.

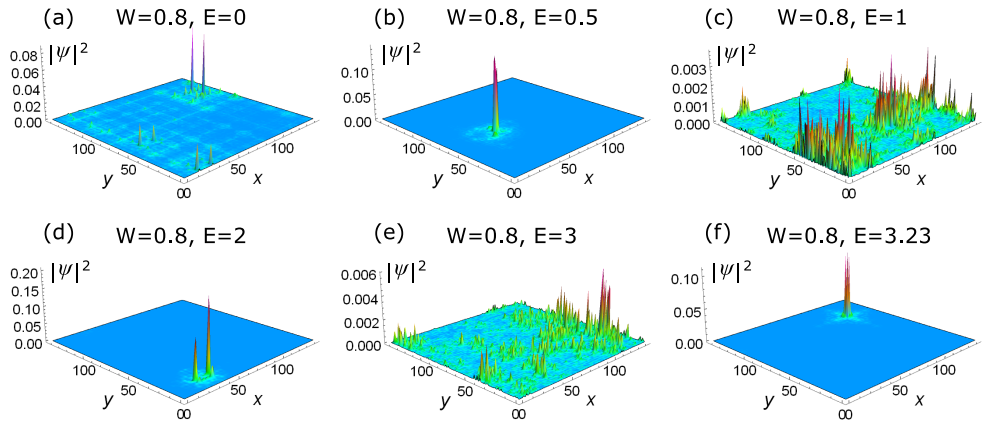

Figure 5.13: Real-space wavefunctions at various energies corresponding to $W = 0.8$ and $L = 144$. (a), (c), and (e) are delcoalized wavefunctions; (b), (d), and (f) are localized wavefunctions. This confirms the multiple mobility edges observed in the typical DOS in Fig. 5.12.

5.3.2 Strong quasiperiodic hopping

We now turn to the properties of the QP hopping model in the limit of large W, where our parametrization of the model gives a purely QP hopping model for $W = 1$, see Eq. (5.5). A striking feature of random chiral class models is the presence of a divergence in the low-energy DOS [43, 44, 179, 181, 37], but this behavior is strongly dependent on the type of model chosen. In random hopping models the precise form of this divergence is modified due to Griffith effects [179]. This is naturally a very interesting problem to compare with the QP hopping model since we know *a priori* it has no rare region effects. However, observing anything beyond just a power-law divergence is notoriously difficult numerically and therefore that is not our goal here. Instead, we aim to demonstrate the existence of a divergence and not necessarily pinpoint its precise analytic form beyond the leading power-law dependence.

Diverging low-energy density of states

Focusing on the pure QP limit $W = 1$, we compute the DOS using KPM on very large system sizes ($L = 987$) such that any low-energy divergence of the DOS is not affected by the mean level spacing on finite size systems. Any low-energy divergence in the DOS will be rounded out to due the extrinsic effects of finite system size and KPM

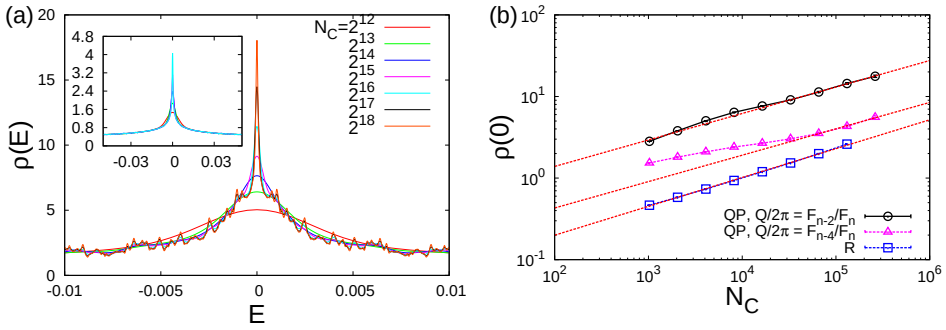

Figure 5.14: Divergence of the low-energy DOS for $W = 1$ (i.e. pure QP hopping). (a) N_C-dependence near zero energy for a very large system size $L = 987$ and $Q_L = 2\pi F_{n-2}/F_n$. (Inset) Similar results for the randomized version of the model (letting the phase be random at each site) with $L = 233$ for $N_C = 2^{12}, 2^{13}, 2^{14}$, $L = 377$ for $N_C = 2^{15}$ and $L = 610$ for $N_C = 2^{16}$, note that the divergence is similar between the two. (b) Divergence of the low-energy DOS for $W = 1$ in the pure QP limit comparing two different quasiperiodic wavevectors and the random (R) hopping model with the KPM expansion order that acts like a low-energy scale that rounds out the divergence of the DOS. Fits to the power law form are shown as red dashed lines.

expansion order. By going to $L = 987$ we are able to reach large enough system sizes so that all of the (artificial) rounding is due to the KPM expansion order i.e. a finite N_C [2]. We now reach one of our main results, as shown in Fig. 5.14, we find a clear divergence of the low-energy DOS in the pure QP hopping model (rounded by the finite KPM expansion order N_C). Since we are working at such large system sizes we can use the rounding of the divergence in the DOS by N_C to our advantage: in order to accurately compute the power-law divergence in the DOS $\rho(E) \sim 1/|E|^{x_{QP}}$, we use the fact that the KPM expansion order is related to an infrared energy scale $N_C \sim 1/\delta E$ that implies the ansatz

$$\rho(E = 0) \sim (N_C)^{x_{QP}}. \tag{5.17}$$

As shown in Fig. 5.14, we find that $x_{QP} \approx 0.32$ for $Q = 2\pi F_{n-2}/F_n$ and $Q = 2\pi F_{n-4}/F_n$, which is consistent with the divergence and value of x_{QP} being Q-independent for irrational Q. Thus, we conclude that randomness is not necessary to create a low-energy divergence in the DOS. Using $\rho(E) \sim |E|^{d/z-1}$ this leads to the estimate $z \approx 3$ for $W = 1$.

[2] The real hopping model in this work can be decomposed into two decoupled π-flux hopping models. It belongs to the chiral orthogonal class.

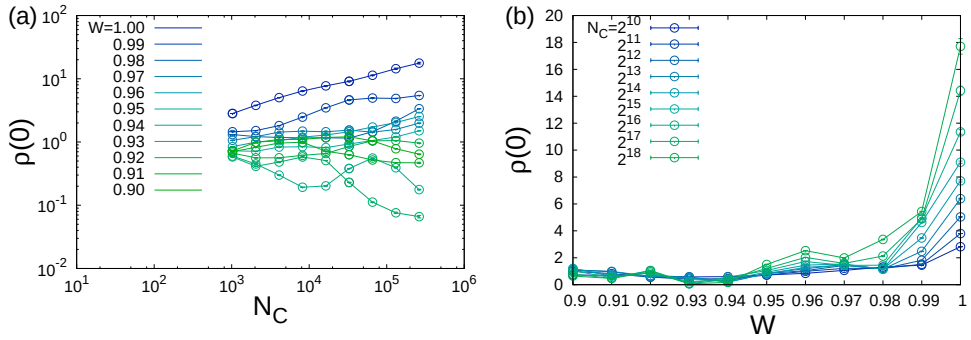

Figure 5.15: The onset of a divergence in the DOS at zero energy $\rho(0)$ versus (a) N_C and (b) W close to $W = 1$ and $L = 610$. We see a trend towards an increasing $\rho(0)$ for $W > 0.95$, but there is no clear sign of divergence in the data other then at $W = 1$.

It is interesting to compare this result with the corresponding randomized version of the model, which has phases that are random across each bond [i.e. the ϕ_ν in Eq. ((5.4)) are replaced by $\phi_\nu(\mathbf{r})$ and sampled between $(0, 2\pi)$ at each site]. We find the nature of the divergence of the DOS goes like $\rho(E = 0) \sim (N_C)^{x_R}$ with $x_R \approx 0.35$. Thus, we find that the low-energy divergence in the QP hopping model agrees well with that of the random model to within our numerical accuracy. Since these two problems share the same distribution of hopping strengths at each bond, with the distinction being that the phases (ϕ_ν) are correlated across the entire sample for the QP model. Note that this distribution is Q-independent and is given by the distribution of $\cos(x) + \cos(y)$ for $x, y \in [0, 2\pi]$, which is consistent with x_{QP} being Q-independent as we have already found. In this way, our results on x_{QP} and x_R implies that the nature of the low-energy divergence, is dictated by the distribution and not whether the models possess rare regions. We note that other numerical studies have also seen just a simple power-law divergence in related (but not equivalent) disordered models [179].

The low-energy divergence of the DOS for the pure QP limit of the model poses a natural question: is there a phase with a divergent low-energy DOS or is it only an isolated point as a function of W? As shown in Fig. 5.15, for KPM expansion orders up to $N_C = 2^{18}$ and $L = 610$ we do not find a clear sign of a divergence at $W < 1$ in the data for $\rho(0)$ versus N_C, but we do find that the DOS is showing trends to a divergence at the largest expansion orders for $W \gtrsim 0.95$. Thus, our data suggests that the point $W = 1$ is fundamentally distinct from the phases of the model with $W < 1$, i.e. any

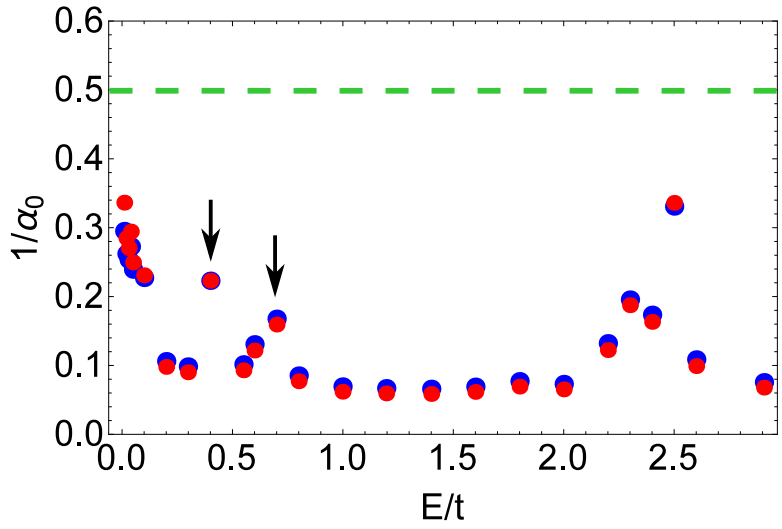

Figure 5.16: Inverse multifractal exponent α_0 as a function of energy for $W = 1$ and $L = 144$. The green dashed line indicate the plane wave value $1/\alpha_0 = 0.5$. Localized states in the thermodynamic limit give $1/\alpha_0 \to 0$. The results demonstrate non-monotonic dependence as a function of energy. Blue dots indicate the data extracting from $\psi(\mathbf{x})$ ($b = 1$); red dots correspond to the data extracting from binned wavefunctions with resolution length $b = 2$. The black arrows indicate the states consisted of double identical peaks. The corresponding typical DOS values are very small but non-zero in Fig. 5.12.

finite bare hopping ($t > 0$) appears to be sufficient to suppress this divergence. If we instead consider complex QP hopping matrix elements then the low-energy divergence goes away. As we discuss in Sec. 5.5, we attribute the divergence in the low-energy DOS to the hopping vanishing along lines in real space which induces an extensive number of zero modes.

Real-space wavefunctions at $W = 1$

Here, we focus on the pure QP hopping case ($W = 1$). As plotted in Fig. 5.12(f), both low ($|E| \ll 1$) and finite energy ($|E| \approx 2.2 - 2.5$) delocalized states still appear in the pure QP hopping limit. This is very different from the expectation from the disordered problem where all finite-energy states are localized. Therefore, it is important to confirm the detailed features of the finite-energy localized states.

We compute the multifractal exponent α_0 (Ref. [77], see Section 2.2.1) as an indicator of localization. For a uniformly distributed plane wave, $\alpha_0 = d = 2$. For a

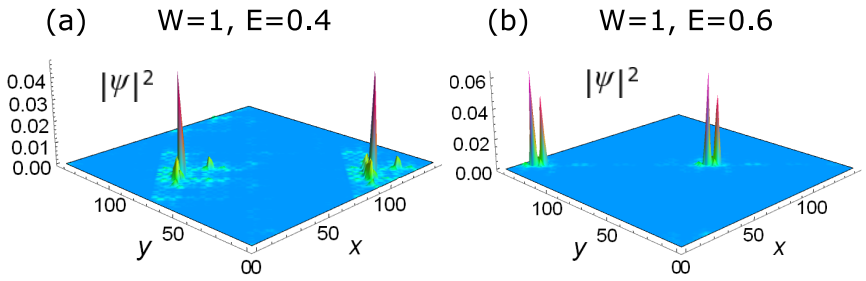

Figure 5.17: Real-space wavefunctions that show double peaks structure for $W = 1$ and certain finite energies [(a) $E = 0.4$; (b) $E = 0.6$]. These two wavefunctions correspond to the data in Fig. 5.16 indicated by the black arrows. They are not the conventional localized or frozen wavefunctions that are found in the disordered systems. Such an unconventional feature is probably due to the quasiperiodicity.

localized state, $\alpha_0 \to \infty$. As shown in Fig. 5.16, the values of α_0 show non-monotonic dependence as a function of energy. We found strongly multifractal delocalized states (intermediate α_0 values) in certain finite energies. Importantly, the low-energy states remain delocalized within every measure we have considered so far. In addition, we identify a few delocalized states within the region where the typical DOS is small but finite (near $E \approx 0.5$). Those finite energy wavefunctions consist of two similar peaks with arbitrary separation in $L = 144$ as shown in Fig. 5.17. We attribute this feature to the QP hopping rather than the (chiral) symmetry of the present model. Similar features are also presents for larger system sizes ($L = 610$), but the associated energy region becomes narrower. We can not conclude if such states are due to a finite-size effect in the current study.

We also study the low-energy wavefunctions in a fixed realization. The low-energy wavefunctions are strongly multifractal for $L = 144$ and $L = 610$. We compute the two-wavefunction correlation $C(E)$ [given by Eq. (5.9)] to quantify the degrees of probability amplitude overlap. The numerical results of $L = 144$ with $W = 1$ and $W = 0.99$ ($W/t \approx 7$) are plotted in Fig. 5.18. The finite overlap of the wavefunctions with adjacent energies signals the metallic rather than localized behavior and is consistent with our intuitive argument about the hybridizing subregion states. Remarkably, the pure QP hopping ($W = 1$) limit gives a power-law behavior, $C(E) \sim E^{-\mu}$, where $\mu \approx 0.48$ for $L = 144$. In the disordered problems with a power-law low-energy DOS, the exponent

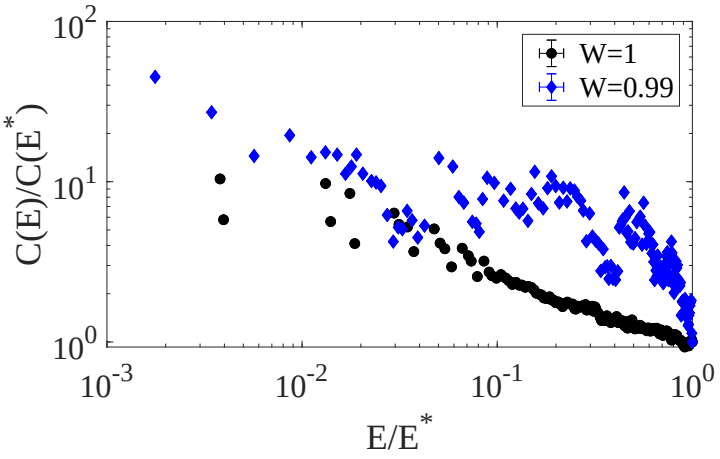

Figure 5.18: Two-wavefunction correlation [given by Eq. (5.9) with $E_0 \approx 0$] as a function of energy (E). We take 300 lowest positive energy states of $L = 144$ per realization and compute the probability overlap of two wavefunctions in the same realization. The data is averaged over 400 realizations. $E^* = 0.01$ for $W = 0.99$; $E^* = 0.0025$ for $W = 1$. We rescale all the data points with the rightmost point. In the pure QP hopping limit ($W = 1$), the two wavefunction correlation shows a clear power law scaling. For $W = 0.99$, the low-energy wavefunctions lose clear power law overlapping features.

μ is given by $\mu = [d - \tau_R(2)]/z$. In the QP hopping model, we are not aware of any scaling argument that supports such a relation. If we assume $\mu = [d - \tau_R(2)]/z$ and compute the $\tau_R(2)$ numerically, the dynamic exponent extracted this way is $z^* \approx 2$, different from the dynamic exponent from low-energy DOS. The discrepancy might come from (a) the sampled energies are not low enough in $C(E)$ or (b) the relation $\mu = [d - \tau_R(2)]/z$ does not hold in this QP hopping model.

The presence of power law correlations in the wavefunctions implies a multifractal enhancement of the interactions [170, 171, 172, 173]. Unlike the for plane wave states, these multifractal wavefunctions have an intricate spatial probability distribution. The existence of correlations in energy indicates that the probability distributions of wavefunctions at adjacent energies have significant overlaps. Therefore, we expect this potentially produces an enhancement of correlated effects for certain types of four-fermion interactions. In disordered systems, the multifractal enhancement of interactions is related to the wavefunction multifractality directly due to quantum-critical scaling. The relevance of the four-fermion interaction (U) is determined by [173] $dU/dl = x_1 - x_2^{(U)}$, where $x_1 = d - z$ is the local DOS exponent and $x_2^{(U)}$ is the scaling dimension of the

four fermion operator. In the clean case, the relevance is determined by x_1 alone since $x_2^{(U)} = 2x_1$. For disorder systems, $x_2^{(U)} \geq x_2$ where $x_2 = \tau_R(2) - 2(1 - x_1)$ is the scaling exponent for the second moment of the local DOS operator after the disorder average has been performed. Nevertheless, it is not currently clear if one can apply the above results to the present QP hopping model at $W = 1$; if we do, they imply a strong multifractal enhancement of some short-range interactions (e.g., the density-density interaction).

On the other hand, we do not observe power law correlation in our finite size data for $W = 0.99$. This indicates that the power law correlation is a special feature in the pure QP hopping limit. More quantitative tests (e.g., much larger system sizes) are required to pin down the precise mechanism.

Wavepacket Dynamics

Lastly, we now study the wavepacket dynamics in the QP hopping model using an expansion of the time evolution operator in terms of Chebyshev polynomials. We are interested in the spread of the wavepacket $\langle \delta r(t)^2 \rangle$ in the long-time limit, see Eq. (5.11). We initialize the state in an up-spin state localized to one lattice site. Then, we use Eq. (5.12) to extract estimates of an averaged dynamic exponent $\tilde{z}$ via $\langle \delta r(t)^2 \rangle \sim t^{2/\tilde{z}}$ as shown in Fig. 5.19 for the largest system size $L = 987$ considered. Despite the wave packet dynamics not being energy resolved, for moderate QP strength when a mobility edge is present in the spectrum, the localized states will not contribute and therefore the long-time limit of the wavepacket spreading probes contributions to transport from the "quickest" parts of the spectrum. Thus, in the limit of a large QP potential wavepackets are a good way to probe dynamical transport properties, despite not being energy resolved.

As shown in Fig. 5.19 we do not see any clearly diffusive regime in the model (consistent with other QP studies in two-dimensions [86, 7]). Instead $2/\tilde{z}$ smoothly decreases from 2 (for ballistic transport) as a function of the QP hopping strength and the transport looks super-diffusive $1 < \tilde{z} < 2$ and $2/\tilde{z}$ passes through 1 at $W \approx 0.95$. For $W > 0.95$ we find $\tilde{z} > 2$ and the transport appears sub-diffusive, approaching $\tilde{z} \approx 4$

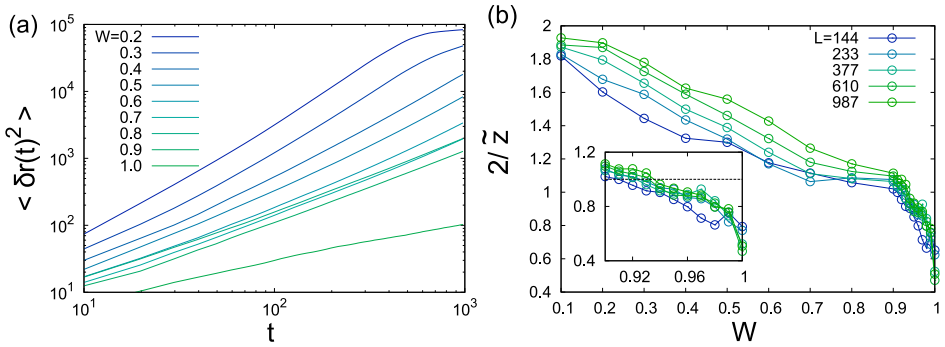

Figure 5.19: Wave packet dynamics, we initialize the wavefunction to be localized to a single site and evolve it under H. (a) Spread of the wavepacket as a function of time t on a log-log scale with $L = 987$ and $N_C = 2^{13}$ we never see a clear diffusive phase ($z = 2$). (b) Extracted dynamic exponent z from $\langle \delta r(t)^2 \rangle \sim t^{2/\tilde{z}}$ (inset) zoom in near $W = 1$ with a dashed line to mark diffusion $2/\tilde{z} = 1$. Note that the wave packet dynamics is not sensitive to the semimetal to metal transition at $E = 0$.

in the pure QP hopping limit.

It is an interesting finding that for the low-energy DOS to diverge requires $z > 2$, and our current estimate for $\tilde{z}$ from the wavepackets yields $\tilde{z} > 2$ for $W \gtrsim 0.95$. However, the DOS does not appear to have any divergence in this regime (see Fig. 5.15), which suggests that this feature is due to $\tilde{z}$ not being energy resolved. From this perspective, we contrast this estimate of z with that of the divergence in the DOS. From the power law divergence at $W = 1$ we estimate from the DOS $z \approx 3$, which is close but does not completely match the wave packet estimate ($\tilde{z} \approx 4$). However, this is not entirely surprising since the wave packet estimate gets contributions from states across the spectrum at finite energies (which possess both finite-energy delocalized and localized states as shown in Fig. 5.12), whereas the DOS is energy resolved and only probes the states near $E = 0$. The presence of finite-energy localized states will slow down the energy averaged transport and give an enhanced value of $\tilde{z}$. These results suggest that the energy averaged transport properties are sub-diffusive over a range of W, while the low-energy states only develop sub-diffusion at $W = 1$.

5.4 Experimental Realization

In this section we present a way to realize Eq. (5.1) in a cold atomic setup and discuss how to probe the phase diagram. In addition, we also briefly discuss how the model in Eq. (5.1) can be implemented using metamaterials.

We closely follow Ref. [121], where two-dimensional spin-orbit coupling in ultracold atomic bosonic systems was proposed and experimentally tested. The continuum version of Eq. (5.1) has the following form (we consider 2 internal degrees of freedom per atom)

$$H = \frac{\hat{p}^2}{2m} + V_{\text{latt}}(\check{x}) + \mathcal{M}_x(\check{x})\sigma_x + \mathcal{M}_y(\check{x})\sigma_y. \tag{5.18}$$

The limit of interest is a deep optical potential $V_{\text{latt}}(\check{x})$, in which spin preserving hopping is suppressed. However, an appropriately designed $\mathcal{M}_{x,y}(\check{x})$ assists spin flip hopping in a certain direction and generates the Hamiltonian of interest.

To realize Eq. (5.18), we follow the recent implementation of two-dimensional SOC in Ref. [121]. However, in contrast to that work, we tune the angle of incidence of the Raman beam and detune the system sufficiently strongly such that the Raman laser (called $E_{2x,z}$ in Ref. [121]) has a wavelength $2\pi/k_2$ which differs from twice the lattice constant $2\pi/k_0$. Then, tuning the optical path such that $\delta\varphi_L = \pi/2$ and $\varphi_L = 0$, we find that $\mathcal{M}_x \propto [\cos(k_0 x)\cos(k_2 y) - \cos(k_0 y)\sin(k_2 x)]$ (and analogously for $x \leftrightarrow y$). For k_0 and k_2 incommensurate, spin-flip hopping acquires a QP modulation, which in the tight binding limit leads to a Hamiltonian akin to Eq. (5.1).

In such a setup, experimental verification of the semimetal to metal transition (where the kinetic energy is quenched, i.e. the "magic-angle" effect) as well as a probe of the divergent DOS at $W = 1$ may be achieved using radiofrequency spectroscopy [186]. Within such an experiment, the magic-angle effect of quenched kinetic energy can be observed by means of momentum resolved radiofrequency spectroscopy. As a complementary approach, band mapping techniques [187, 188], allow one to reconstruct the miniband structure experimentally.

Alternatively, metamaterial setups can also realize our model with current experimental techniques. For example, using an array of connected electrical resonators with a

suitable choice of the intrinsic frequency and connecting capacitance, one can construct a circuit equivalent to the tight-binding model we have studied here and the overall absorption spectrum is analogous to the DOS [53, 189] and thus allows one to probe the semimetal-to-metal transition we have explored here. The spatial distribution of the eigenmodes of resonance can also verify our results regarding localization. Besides resonators, photonic [190] and phononic [191] systems are also nicely tunable and we also expect that they can be used to engineer the Hamiltonian in Eq (5.1) in a majority of the parameter space.

5.5 Discussion and Conclusion

We have analyzed the properties of a two-dimensional Dirac semimetal with quasiperiodicity that respects chiral symmetry. The quasiperiodicity takes the form of a QP hopping on a tight-binding model. As shown in Fig. 5.1(a), the low-energy states demonstrates a semimetal phase with Dirac cones in the band structure, a chiral metal phase with non-trivial real space structure in the wavefunctions, as well as the pure QP hopping limit $W = 1$ [see the paramaterization of t in Eq. (5.5)], which is critical exhibiting sub-diffusive dynamics. A clear demonstration of the semimetal to metal EPT, in the DOS [see Eq. (2.1)] and the inverse participation ratio (IPR) in momentum space [see Eq. (5.8)], is shown in Fig. 5.1(b). The momentum-space IPR (indicating a delocalization in the momentum basis) vanishes in a continuous fashion concomitantly with the onset of the zero-energy DOS, which demonstrates the nature of this phase transition in the structure of the eigenstates and eigenvalues, respectively. In Fig. 5.1(c) we show the diverging DOS in the pure QP hopping limit and we find that the low-energy eigenstates in this regime exhibit quantum-critical Chalker scaling.

First, we demonstrate the stability of the two-dimensional semimetal phase to QP hopping. We find that the QP hopping introduces gaps at finite energy that create a low-energy semimetal miniband that retains the scaling $\rho(E) \sim |E|$. The semimetal phase persists until a critical, Q-dependent, potential strength W_c where a semimetal to metal transition takes place. At this transition the Dirac velocity vanishes in a universal

fashion and the low-energy bands become flat, which should strongly enhance correlation effects and has been dubbed magic-angle transitions in analogy to twisted bilayer graphene at the magic-angle [55, 54]. Concomitantly, the single-particle wavefunctions delocalize in momentum space. Interestingly, we find that the velocity vanishes with a critical exponent that is in excellent agreement with models that have a QP potential and are lacking chiral symmetry. While these results suggest that the chiral symmetry does not play a role in the critical properties of the semimetal to metal transition, they do have a strong effect on the structure of the phase diagram and the minibandwidth renormalization (being about 4 orders of magnitude smaller then for a QP potential [7]). For example, we find that the metallic phase does not undergo an additional transition back to a reentrant semimetal phase, which occurs in a wide multitude of other models [7]. In the metallic phase, we find that the low-energy eigenstates are weakly multifractal in momentum space and wavepacket dynamics are super-diffusive over a large region of the phase diagram ($W < 0.95$). Using the chiral symmetry of the model, we characterize this transition and the formation of the low-energy DOS as a band of topological zero modes that form due to bound zero-energy states that arise from a sign-changing Dirac mass [182, 183]. If we consider values of Q that are commensurate but are close to the irrational values we have investigated here, then the single particle phase transition will be rounded into a cross over, which will result in a small but non-vanishing velocity and the momentum-space wavefunctions that do not truly delocalize.

We also investigate the effects of strong quasiperiodicity and therefore determine the real-space Anderson localization properties of this model. We demonstrate that the model exhibits a sequence of real space Anderson localization-delocalization transitions as a function of energy and thus the system hosts multiple mobility edges. Interestingly, the low-energy eigenstates evade exponential localization and appear to remain critical even for maximal QP hopping strength ($W = 1$). These results are markedly distinct from disordered systems, where all the finite-energy eigenstates would be localized for the models with real and complex random hopping terms. We verify this non-trivial

structure of the phase diagram characterizing real space localization by using a combination of typical density of states and wavefunction analysis.

In the pure QP hopping limit ($W = 1$), the system exhibits a diverging DOS at zero energy, see Fig. 5.1(c). We provide evidence that this power-law divergence is universal, for irrational Q. The low-energy states that make up this divergence are not exponentially localized, and instead appear strongly multifractal, i.e. critical. Using wavepacket dynamics we have shown that the majority of the chiral metal phase is super-diffusive and crosses over to sub-diffusion near $W \approx 0.95$. These results are consistent with that the low-energy states are not localized. The slow sub-diffusive wavepacket dynamics gives a dynamical exponent $z \approx 3$. In addition, we find power-law scaling as a function of energy for almost two decades in the two-wavefunction correlation [see Eq. (5.9)] (in the $W = 1$ limit). This provides strong numerical evidence of Chalker scaling without randomness [165, 166]. Interestingly, we find Chalker scaling does not clearly hold in the limit of the pure complex quasiperiodic hopping (not shown), demonstrating that the strong correlations between wavefunctions seem to rely on the low-energy diverging DOS in the limit of real quasiperiodic hopping.

One remaining important question is to understand the origin of the diverging low-energy DOS for $W = 1$. We provide evidence that this is a result of local sub regions with an imbalance $N_A \neq N_B$ of sublattice sites. This induces a pile up of an extensive number of zero modes due to the QP hopping elements vanishing along certain lines in real space. In Fig. 5.20 we plot the configuration of hopping matrix elements in the pure QP hopping model ($W = 1$) and strong QP hopping ($W = 0.9$). The pure QP hopping case shows nearly zero hopping lines which effectively cut the system into many subsystems. Those nearly zero lines roughly track the zeros of the QP hopping, which are obtained by solving $\cos(2\pi Q_L x^* + \phi_x) + \cos(2\pi Q_L y^* + \phi_y) = 0$ for x^* and y^*. It is apparent that there are several virtually disconnected subregions in which $N_A - N_B \neq 0$. Those are an imperative origin of zero modes by means of a poor-man's index theorem (rectangular matrices have a non-zero kernel)[192, 193]. To add additional support to this picture we have also studied a model with complex QP hopping amplitudes. This model is chosen to have no lines of vanishing hopping strength as in Fig. 5.20, since

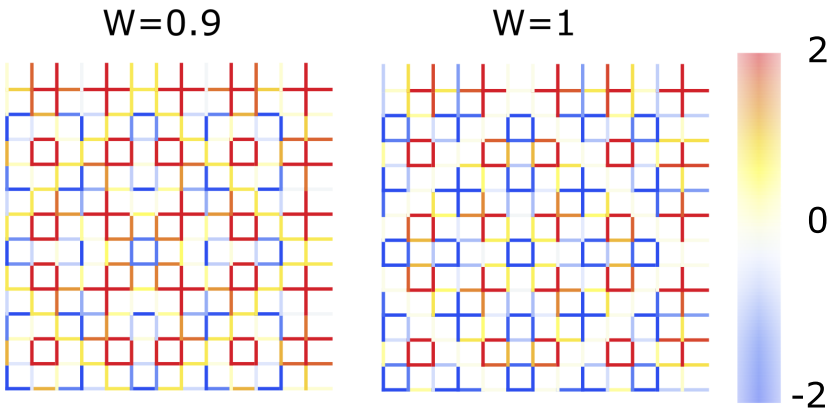

Figure 5.20: The hopping configurations of QP hopping models with $L = 13$. (Right) The hopping configuration of the QP hopping model with $W = 1$. The QP pattern generates nearly zero lines of bonds which effectively separate the system into many subsystems. (Left) The hopping configuration of the QP hopping model with $W = 0.9$. The system is typically well connected as a whole.

the bonds' norms can now never vanish. Interestingly, we also find that (not shown) the complex QP hopping model has no diverging DOS for pure complex hopping. In addition, we also find that this model does not exhibit Chalker scaling. These results lend support to the above argument but are not conclusive and therefore we leave the question of the origin of the pile up of zero energy states at $W = 1$ to future work.

Lastly, our work demonstrates two separate routes to inducing strong correlations in quasiperiodic semimetals. The first is due to magic-angle transitions, where the Dirac cone velocity vanishes at an EPT. The second route is due to Chalker scaling in the limit of pure QP hopping. The presence of power-law correlations in the wavefunctions potentially implies a multifractal enhancement of the interactions [170, 171, 172, 173]. Our work provides a clear cut example of how this can occur in the absence of randomness.

5.6 Appendix: Quadrupole topological insulator at commensurate limits of the model

As we already discussed in the main text, for $Q = \pi$, the model in Eq. (5.1) is a quadrupole topological insulator [162]. In this case, the model can be separated into two copies of decoupled π flux model by alternating spin. For each copy, four lattice

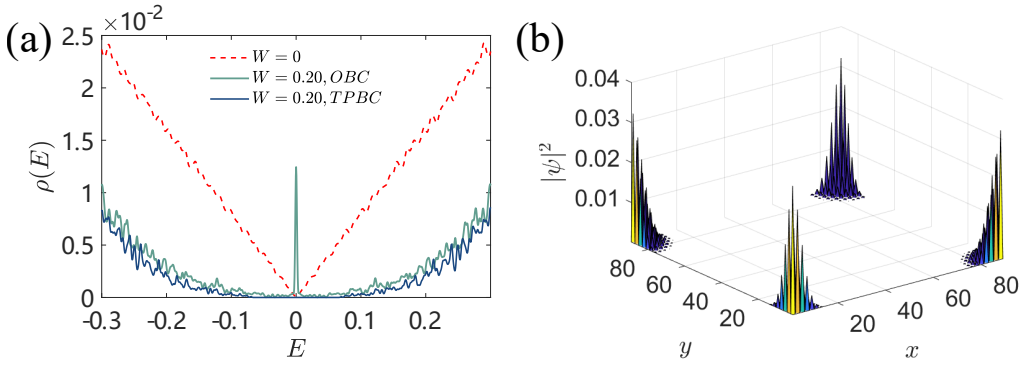

Figure 5.21: (a) Density of state by energy, with $Q_L = \pi$, in twisted periodic boundary condition (TPBC) and open boundary condition (OBC). Both boundary conditions show bulk gap, while OBC allows the topological corner states. The system size is $L = 144$, and $Q_L = 2\pi(72/L)$. $N_C = 8192$ for KPM calculations. (b) real space wave function at $Q_L = \pi$ and $W = 0.4$. System size is $L = 89$.

sites on the corners of a plaquette form a unit cell when $Q = \pi$. We label them from the left-bottom corner as $|1\uparrow\rangle$, $|3\downarrow\rangle$, $|4\uparrow\rangle$ and $|2\downarrow\rangle$ counterclockwise (and opposite spin labels for the other copy). The Bloch Hamiltonian is given by $h(\mathbf{k}) = W(\cos(k_x)\tau_x\sigma_0 - \sin(k_x)\tau_y\sigma_x - \cos(k_y)\tau_y\sigma_y - \sin(k_y)\tau_y\sigma_x) + E_0(\mathbf{k})\tau_z\sigma_0$, where σ, τ are Pauli matrices that act on the degrees of freedom within a unit cell, with identical/opposite spin respectively. The dispersion with $W = 0$ is $E_0(\mathbf{k}) = \pm 2t\sqrt{\sin k_x^2 + \sin k_y^2}$.

For $W > 0$, we see a hard gap near $E = 0$. When L is odd with twisted periodic boundary condition, or L is even with open boundary condition, a small peak is seen at $E = 0$ [Fig. 5.21(a)]. When L is even and taking closed boundary condition, the corner state do not show up. The corner states survive twisted periodic boundary condition when L is odd because the unit cell has size 2×2, and hence a strip of half unit cells opens the boundary. The peak includes two states, independent of what L is chosen to calculate the DOS, indicating a topological nature of such a peak. The wavefunction data shown in Fig. 5.21 (b) also indicates that the system is in a quadrupole TI phase since the zero-energy wavefunction concentrates near the corners.

Acknowledgment

I am indebted to included this work in my dissertation, as it has been the fruit of great collaboration with YZ.Chou, E.J.Konig, J.H.Wilson, and J.H.Pixley.

We thank Sarang Gopalakrishnan, David Huse, Alexander Mirlin, Rahul Nandkishore, and Zhentao Wang for useful discussions. In particular, we thank Matthew Foster for suggesting to us to look into Chalker scaling as well as for numerous insightful discussions.

Chapter 6

Flat Topological Bands and Eigenstate Criticality in a Quasiperiodic Insulator

6.1 Introduction

So far, the previous chapters solely focused on the behavior of semimetals. Now we shift gear to look at a model of topological insulators (TI), applying similar ideas. As we have discussed in Chapter 1, models of TI may often be tightly related to semimetals. For 2D TI, the chiral boundary state can be thought of as an 1D model of semimetal. Meanwhile, for models of 2D topological insulators controlled by a parameter (which will be called topological mass, to be clarified later), the phase boundary between topologically distinct insulating phases are semimetals. The existence of semimetal is guaranteed on the phase space of models of topological insulators because the topology can only change when different bands touch – and that is when semimetal shows up.

The existence of a point on the one-parameter phase diagram that manifests semimetal provides a natural path to expand the finding of previous chapters into topological insulator. In this chapter, we attempt to apply the same quasiperiodic (QP) potential as in the perfect spin-orbit coupling (SOC) model in Chapter 3 to a model of 2D topological insulator, the Bernevig-Hughes-Zhang(BHZ) model. From the semimetal phase boundary hosting a Dirac semimetal, we can first verify that the same universal physics, the "magic-angle" transition is valid here. Analytical method will allow as to have some basic understanding of the expected phase diagram with very weak quasiperiodicity. Then we move away from the semimetallic line and the weak quasiperiodicity regime in the two-parameter phase diagram and explore extensively the rich phase diagram created by the interplay between quasiperiodicity and topology, taking advantage of the numerical methods discussed in Chapter 2.

The particular interest of such generalization to topological insulator is connected to the pursuit for topological flat bands to host topological strong correlated phases. The phenomena from the interplay of topology and strong correlations has been generally fascinating, with the fractional quantum Hall effect [194] serving as the quintessential example. Conventionally, the magnetic field induces topology in the electronic many-body wavefunction; however, Berry curvature of the band structure is sufficient to induce topological single-particle wavefunctions that can survive the presence of interactions (see Ref. [195] for a review). Despite strong numerical evidence of fractional Chern and $\mathbb{Z}_2$ insulators [196, 197, 198, 199, 200, 201], identifying a clear experimental route to the many-body analog of the fractional quantum Hall effect without a magnetic field remains challenging. Research in this direction has aimed to identify lattices with flat topological bands that quench the kinetic energy, promoting strong correlations [202, 203, 204, 205, 206, 207, 94].

Recent work on twisted graphene heterostructures opened up new platforms to study strongly correlated physics, including correlated insulators [55], superconductivity [54, 97], and Chern insulators [208, 209, 210]. Proposals for realizing flat topological bands in these systems have followed [211, 212, 213, 114, 214, 215, 216, 217, 218]. Meanwhile, as clearly shown in Chapter 3 and 5, quasiperiodicity can emulate the incommensurate effect of the twist, which brings extreme downfolding of the Brillouin zone, can open gaps and quench the kinetic energy by flattening bands, and leads to new phases and critical eigenstates. Such idea of emulating the twist can help us in understanding the theory for fractional Chern and $\mathbb{Z}_2$ insulators in incommensurate systems and how eigenstate criticality plays a role, by providing a simple model to theoretically study and experimentally realize as we demonstrate in this chapter. The notion of flat band engineering with incommensuration has broad applicability outside twisted heterostructures, including ultra-cold atomic gases [219, 120, 121] and metamaterials [220, 221, 53, 222].

In this chapter, we study a minimal model for a two-dimensional topological insulator with a quasiperiodic potential to find a controllable route to create flat topological bands and induce quantum phase transitions beyond the Landau-Ginzburg paradigm,

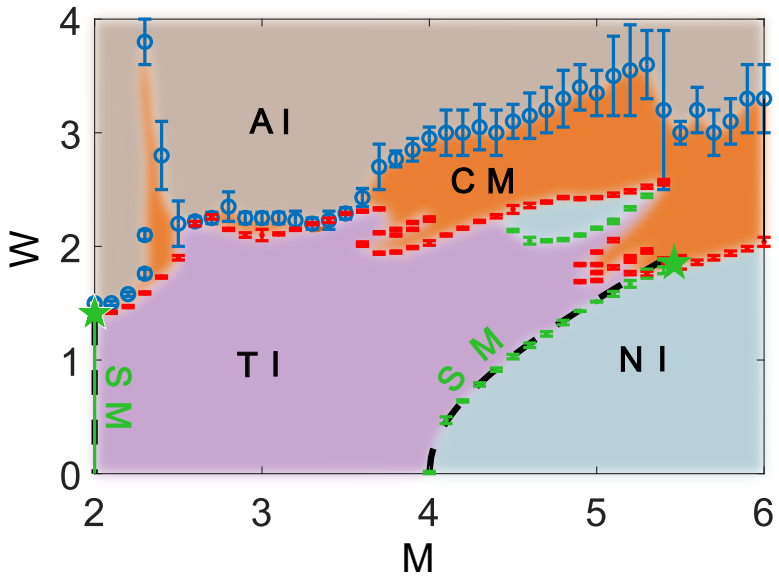

Figure 6.1: **Phase Diagram** of the BHZ model in Eq. (6.1) at the band center with topological mass M and quasiperiodic potential strength W. There are five illustrated phases: topological (TI), normal (NI), and Anderson (AI) insulators, Dirac semimetal (SM), and critical metal (CM). The green and red data points use the density of states in Eq. (6.3) to locate the transitions between TI and NI. Among them, the green data points and the green vertical line at $M = 2$ are SMs, terminated at magic-angle transitions (see Sec. 6.5) at the green stars. The black dashed lines are the perturbative prediction for the SM lines (e.g. Eq. (6.23)). The blue circles use transport [Eq. (6.2)] to determine the CM to AI boundary.

as there is no spontaneous symmetry breaking involved. These transitions represent a universality class beyond the Altland-Zirnbauer classification of random matrices for disordered systems [40, 223]. Using analytic and numeric techniques, we find an intricate phase diagram, as shown in Fig. 6.1. Particularly, quasiperiodicity creates practically flat topological bands near where finite-energy states exhibit criticality. At the transition between topological and trivial insulators, the system realizes a magic-angle semimetal with features previously studied in Chapter 3. We further characterize the critical properties of the various eigenstate transitions, understanding them as localization and delocalization transitions in momentum- or real-space bases. Importantly, these transitions and phases could be directly realized in twisted bilayer graphene that is close to aligned with a hexagonal boron nitride substrate [224, 225, 226].

6.2 Model

To describe a two-dimensional topological insulator, we use the Bernevig-Hughes-Zhang (BHZ) model [12] with a 2D quasiperiodic potential. The square-lattice Hamiltonian (with sites $\mathbf{r}$) is block diagonal

$$\hat{H} = \sum_{\mathbf{r},\mathbf{r}'} c^\dagger_{\mathbf{r}'} \begin{pmatrix} h_{\mathbf{r}'\mathbf{r}} & 0 \\ 0 & h^*_{\mathbf{r}'\mathbf{r}} \end{pmatrix} c_{\mathbf{r}} + \sum_{\mathbf{r}} c^\dagger_{\mathbf{r}} V_{QP}(\mathbf{r}) c_{\mathbf{r}}, \tag{6.1}$$

where $c_{\mathbf{r}}$ are four-component annihilation operators and $V_{QP}(\mathbf{r}) = W \sum_{\mu=x,y} \cos(Q r_\mu + \phi_\mu)$ is the quasiperiodic potential (QP) with amplitude W, wavevector Q, and random phase ϕ_μ; $h_{\mathbf{r}'\mathbf{r}}$ is a two-by-two matrix describing one block of the BHZ model (h^*, its complex conjugate). The nonzero elements of h are $h_{\mathbf{rr}} = (M - 2t)\sigma_z$ and $h_{\mathbf{r},\mathbf{r}+\hat{\mu}} = h^\dagger_{\mathbf{r},\mathbf{r}-\hat{\mu}} = \frac{1}{2}t(-i\sigma_\mu + \sigma_z)$ for $\mu = x, y$ with Pauli matrices σ_μ. Topological mass M and the hopping $t = 1$ set the energy scale. Most analyses are done on the two-by-two matrix since time-reversal symmetry relates each block, and $V_{QP}(\mathbf{r})$ does not couple blocks. To reduce finite-size effects, we average over twisted boundary conditions implemented with $t \to te^{i\tilde{\theta}_\mu/L}$ for a twist $\tilde{\theta}_\mu$ in the μ-direction randomly sampled from $[0, 2\pi)$. The model is invariant under $M \to 4 - M$, so we focus on $M \geq 2$. For $2 < M < 4$, the band structure (i.e., $W = 0$) is topological with a quantized spin Hall effect $\mathcal{Q} = \sigma^+_{xy} - \sigma^-_{xy}$ where $\sigma^\pm_{xy}$ are Hall conductivities for the blocks defined by h and h^* respectively. The superscript $\pm$ will be dropped as we focus on the h block only. At $M = 2$ [$M = 4$], the model is a Dirac semimetal with Dirac points at $\mathbf{X} = (\pi, 0)$ and $\mathbf{Y} = (0, \pi)$ [$\mathbf{M} = (\pi, \pi)$] with velocity $v_0 = t$.

Quasiperiodicity is encoded in Q, which in the thermodynamic limit we define as $Q/(2\pi) = (2/(\sqrt{5}+1))^2$. For simulations, we take rational approximates such that $Q \approx Q_L = 2\pi F_{n-2}/F_n$, where F_n is the nth Fibonacci number, and the system size is $L = F_n$. We also briefly explore other values of Q, which demonstrate qualitatively similar phase diagram but are worth further study.

6.3 Methods

We investigate the phase diagram and phase transitions with spectral observables and eigenstates. Despite the methods are largely similar to the other chapters in this dissertation and are explained in Chapter 2, it is worth some extra discussion, especially pertaining to the topology under quasiperiodicity. Because the model in Eq. (6.1) with quasiperiodicity lacks translational symmetry, we need to treat the entire $L \times L$ system as a supercell, where the thermodynamic limit is $L \to \infty$. At finite L, we define an effective band structure that is downfolded into a mini Brillouin zone (mBZ) of size $2\pi/L \times 2\pi/L$.

We utilize twisted boundary condition both to help converging numerical calculation of spectral quantities and to help studying the dispersion and band structures, probing into the mini Brillouin zone. The twisted boundary condition we implemented, $t_\mu \to t_\mu e^{i\theta_\mu/L}$, effectively shifts momentum $\mathbf{k}$ by $\boldsymbol{\theta}/L$. Without a quasiperiodic potential, this corresponds to a trivial folding of the original energy dispersion $E(\mathbf{k})$ such that $E_n(\boldsymbol{\theta}) = E(2\pi n/L + \boldsymbol{\theta}/L)$ for band n in the Brillouin zone defined by the supercell of size $L \times L$. In other words, $\boldsymbol{\theta}/L$ is the momentum in the mini-Brillouin zone of the superlattice made of $L \times L$ supercells.

We apply the kernel polynomial method (KPM, see Chapter 2) to compute spectral quantities and Lanczos or exact diagonalization to compute eigenstate properties. While the KPM and Lanczos work for larger L than exact diagonalization, KPM introduces broadening to the data controlled by polynomial expansion cutoff N_c [4] and Lanczos limited to a small range of the spectrum.

To distinguish trivial, topological, and Anderson insulator phases, we calculate the conductivity tensor defined through Kubo formula [64] as elaborated in 2.5.

$$\sigma_{\alpha\beta} = \frac{2e^2\hbar}{L^2}\int f(\epsilon)d\epsilon \,\mathrm{Im}\,\mathrm{Tr}\left[\!\!\left[v_\alpha \frac{dG^-}{d\epsilon} v_\beta \delta(\epsilon - H)\right]\!\!\right] \tag{6.2}$$

where f is the zero-temperature Fermi function with Fermi energy E_f, and G^- is the retarded Green's function. Importantly, the average for $[\![\cdots]\!]$ is over phases in the QP (ϕ_μ) and twists ($\tilde{\theta}_\mu$) in the boundary condition. To determine phase boundaries and transition properties, we compute the density of states (DOS) which reflects band gaps

and the low energy behavior of the semimetallic phase. The DOS at energy E is

$$\rho(E) = \frac{1}{N_H}\left[\!\!\left[\sum_i \delta(E - E_i) \right]\!\!\right] \tag{6.3}$$

where $N_H = 2L^2$ is the size of the single particle Hilbert space, and E_i denotes the energy eigenvalues. The gap centered at zero energy Δ is estimated with the KPM via the DOS satisfying $\rho(E) < 0.001$ and with shift-invert Lanczos about $E = 0$. Along the semimetal lines the low-energy DOS goes like $\rho(E) \sim \tilde{v}^{-2}|E|$, where $\tilde{v}$ is the renormalized velocity of the Dirac cones that we calculate through the scaling with N_c.

For wavefunctions, we compute the inverse participation ratios (IPRs) in real and momentum space to discern localized, extended or critical states. The IPR in a basis indexed by $\boldsymbol{\alpha}$ is (see Section 2.2.1 for details)

$$\mathcal{I}_\alpha(E) = \sum_{\boldsymbol{\alpha}} \left[\!\!\left[|\langle \boldsymbol{\alpha}|\psi_E\rangle|^4 \right]\!\!\right] \tag{6.4}$$

using normalized wave functions in the momentum space ($\boldsymbol{\alpha} = \mathbf{k}$) or real space ($\boldsymbol{\alpha} = \mathbf{r}$) basis. For systems localized in basis α, $\mathcal{I}_\alpha$ is L-independent; for delocalized systems, it goes like $\mathcal{I}_\alpha \sim 1/L^2$. At a localization transition [227, 37] $\mathcal{I}_\alpha \sim 1/L^\gamma$ where $0 < \gamma < 2$ is the fractal dimension (D_2); γ is extracted from the finite size effect when calculating $\mathcal{I}_\alpha$ at various system sizes.

To study band flatness and topology of the effective band-structure in the mBZ, we calculate the wavefunction $|\psi_{E_n}(\boldsymbol{\theta})\rangle$, where $\boldsymbol{\theta}$ is the crystal momentum of the $L \times L$ super-cell (via the twist in the boundary condition as $\boldsymbol{\theta} = \tilde{\boldsymbol{\theta}}/L$) and E_n is the energy of the nth band labelled in ascending order. The bandwidth is then defined as $w_n = \max|E_n(\boldsymbol{\theta}) - E_n(\boldsymbol{\theta}')|_{\boldsymbol{\theta},\boldsymbol{\theta}'}$ and the direct band gap is $\Delta_n = E_{n+1}(\boldsymbol{\theta}) - E_n(\boldsymbol{\theta})$. The flatness ratio, which measures a band's flatness and its isolation from the neighboring bands is defined following [207] as

$$f_n = \min\{\Delta_n, \Delta_{n-1}\}/w_n. \tag{6.5}$$

The Berry curvature $\Omega_n(\boldsymbol{\theta})$ and Chern number C_n can be determined via momentum-space plaquettes defined by the four momenta $\boldsymbol{\theta} \to \boldsymbol{\theta}_1 \to \boldsymbol{\theta}_2 \to \boldsymbol{\theta}_3 \to \boldsymbol{\theta}$ [1] and they can

[1] All plaquettes must be chosen with the same orientation.

be calculated following [228]

$$\Omega_n(\boldsymbol{\theta}) = \mathrm{Im}\ln\frac{U_n(\boldsymbol{\theta},\boldsymbol{\theta}_1)U_n(\boldsymbol{\theta}_1,\boldsymbol{\theta}_2)}{U_n(\boldsymbol{\theta},\boldsymbol{\theta}_3)U_n(\boldsymbol{\theta}_3,\boldsymbol{\theta}_2)},\ C_n = \frac{1}{2\pi}\sum_{\boldsymbol{\theta}}\Omega_n(\boldsymbol{\theta}) \tag{6.6}$$

where $U_n(\boldsymbol{\theta}_a,\boldsymbol{\theta}_b) = \langle\psi_n(\boldsymbol{\theta}_a)|\psi_n(\boldsymbol{\theta}_b)\rangle/|\langle\psi_n(\boldsymbol{\theta}_a)|\psi_n(\boldsymbol{\theta}_b)\rangle|$ and the sum to obtain C_n is over the mBZ $[0, 2\pi/L)^2$. Lastly, we use machine learning of the wavefunctions to provide an efficient survey of a large parameter space (in W, M, and E) as an additional validation of the main phase diagram.

6.4 Phase Diagram

: Using diagrammatic perturbation theory and numerical calculations with the KPM and Lanczos we obtain the phase diagrams shown in Fig. 6.1. There are five phases pictured: topological insulator (TI), normal insulator (NI), critical metal (CM), Anderson insulator (AI), and lines of Dirac semimetals (SM) between TI and NI phases. Both band-insulating and SM phases are stable to weak quasiperiodicity. Finite band gaps and quantized (zero) spin Hall conductivity describe the TI (NI) phase, calculated using the KPM method with Eq. (6.2). Low-energy scaling of the DOS $\rho(E) \sim \tilde{v}^{-2}|E|$ captures the SM phases (marked with green data points). Other boundaries between gapped and finite DOS at $E = 0$ are marked with red data points. These DOS results trace the phase boundaries between TI and NI (green) and between TI and CM (red). The AI phase has a finite DOS but zero conductivity and localized wave functions (i.e., real space IPR that is L-independent), with the phase boundary marked by blue circles with error bars. The structure revealed is Q-dependent and reminiscent of other studies of insulating phases perturbed by quasiperiodicity [229].

Upon increasing W, for $M \lesssim 4$ and $M \gtrsim 5$ we traverse the phases TI/NI $\to$ CM $\to$ AI. However, more complicated cuts are possible between $M = 4.5$ and $M = 5.3$, where quasiperiodicity drives trivial phases topological (for $4 < M \lesssim 5.0$) and into-and-out-of metallic and topological phases at zero-energy. An example is shown in Fig. 6.2(b) for $M = 4.9$, where increasing W leads to the phases NI $\to$ SM $\to$ TI $\to$ CM $\to$ TI $\to$ SM $\to$ NI $\to$ CM $\to$ AI.

The physics on the SM lines emanating from $M = 2$ or $M = 4$ at $W = 0$ agrees

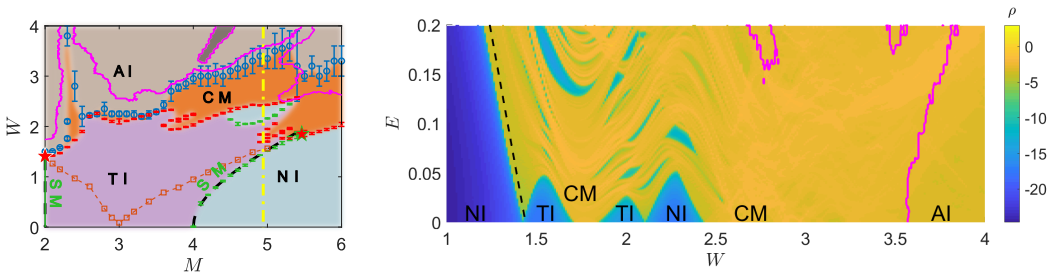

Figure 6.2: (a) Full phase diagram with all measures used to diagonose phases and transitions. The magenta line shows the boundary between delocalized or critical phase and localized phase at zero energy, as indicated by the neural net model. The dark region, roughly extending from $M = 4$, $W = 3$ to $M = 4.5$, $W = 4$ is indicated as critical phase by the neural net model, but not identified by any other observables. The dashed orange line inside the TI phase shows where the size of the gap centered at $E = 0$ is maximals and thus starts to significantly deviate from perturbation theory. (b) A cut of the phase diagram in energy space represented by the yellow line in (a). Notice the multiple phase transitions, all driven by quasiperiodicity (W) and the higher energy metallic nature. The pink curve represents the boundary to machine-learned, localized eigenstates.

with the universal features found in Ref. [7] and reveals magic-angle transitions marked by green stars in Fig. 6.1(a). Concentrating on $M = 2$, the semimetal is stable with a velocity (calculated from the DOS) that vanishes like $\tilde{v} \sim (W_c(M = 2) - W)^{\beta/2}$ where $W_c(M = 2) = 1.42 \pm 0.02$ and $\beta = 2 \pm 0.3$, which is close to the universal value $\beta \approx 2$ obtained in other models and symmetry classes (see Chapter 3 and 5). A CM phase is found as well as a localization transition at $W_A(M = 2) = 1.50 \pm 0.03$.

6.4.1 Machine Learning the localization transition

In the present model, we found it challenging to pinpoint the Anderson localization transition using conductivity and the inverse participation ratio due to a large number of critical states that can appear localized by some metrics but not others. Therefore, we have supplemented this analysis with a machine learning classification of the single particle wavefunctions, utilizing a neural network model.

The problem that we want the neural network to solve is to distinguish localized wavefunctions from extended ones. This task can be thought of as a mapping from the space of all wavefunctions to a binary result of localized or extended. Using a set of wavefunctions labelled in advance, we can train the neural network to capture the

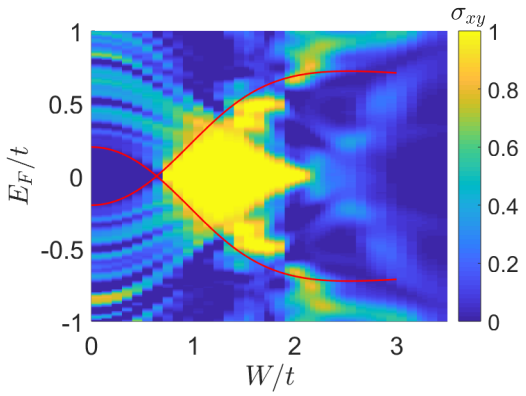

Figure 6.3: **Finite energy topological phase diagram**. The Hall conductivity σ_{xy} at various Fermi energies E_F and quasiperiodicity W. The red lines are the perturbation theory prediction of gap size.

relation between wavefunction data and the prediction of a localized phase. Once the training is finished, we can use the neural network model to classify a much larger dataset of wavefunctions, and map out a detailed phase diagram.

In this problem, we find a simple version of ConvNet [230] easily applicable. The wavefunction classification task is somewhat analogous to figuring out whether the image includes a dog or cat, which is a classical application of ConvNet models. The ConvNet architecture makes use of a convolution operation prior to applying the nonlinear functions. The convolution operations effectively scrambles but preserves the information at various locations of the input data, and hence makes the model "translational invariant", i.e. the location of the feature does not affect the output. Such translational invariance allows the neural net model to treat critical and/or localized structures at different locations in the same way.

The neural network methods of machine learning usually suffer from over-fitting that harms the predictive power of the model. Simple and conventional methods against over-fitting including adding regularization terms, use of drop-off layers [231] and so on. These methods are practically efficient and sufficient for our purpose.

A summary of the architecture we have used with a convolutional neural network and drop-off layers is shown in Fig. 6.4. The result is not sensitive to different choices of model hyper-parameters. The robustness across different setups is likely because the localization feature is prominent and less ambiguous as opposed to typical computer

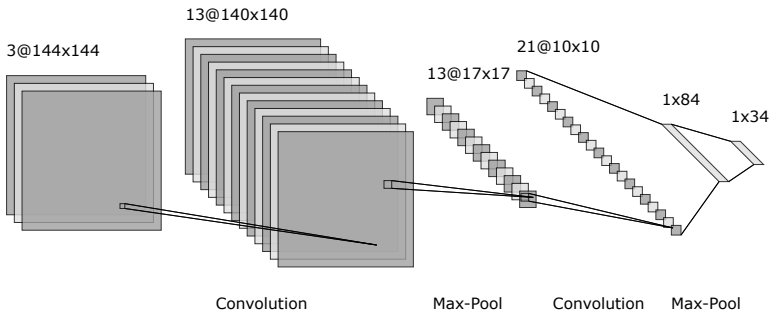

Figure 6.4: **Schematic diagram of the neural network structure used for localization detection**. For convolution layers, we apply a convolution operation over a small window to get a data point in the next layer. Max-Pool layer simply takes the maximum of each window to reduce the model size. We also add batch-normalization and dropout layers before and after Max-Pool, but they are not shown here as they do not alter the overall architecture.

vision tasks.

What remains crucial is the labelling of training set. The training set is constructed in two different ways:

1. We look at the images to judge whether each wavefunction is clearly localized or not. The cases in which we are unsure are discarded from the training set. To minimize the affect of systematic bias caused in labelling the training set, we go through wavefunctions at several runs where each set is drawn randomly from the entire collection of wavefunctions and shuffled. Hence, the mislabelling can be considered as a random variation that is independent from the features that do not affect decision boundaries.

2. We choose $W > 6$ for localized wavefunction examples, and sample $W = 0$ at various values of M for extended wavefunctions.

The training set of method 2 does not include any of the critical wavefunctions in the CM phase. As a result, the ConvNet model identifies the critical phase as localized, producing a phase boundary in line with SM/TI to CM transition. This result can also be replicated using the training set from method 1 if we only include extended and fully localized wavefunctions. However, with method 1 we can instead label a dataset such that the non-localized label *includes* critical wavefunctions to provide an interesting

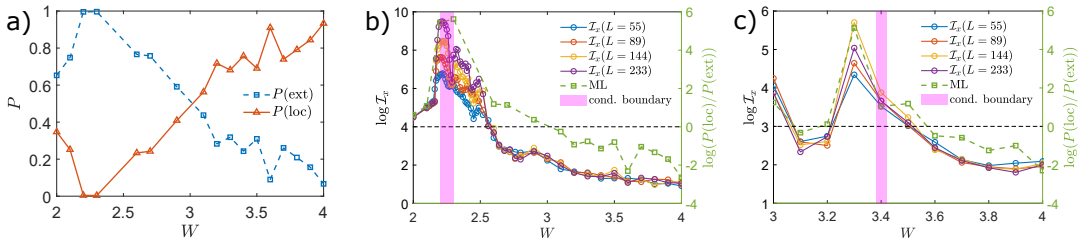

Figure 6.5: **Comparing the IPR with the machine learning outcome**. (a) Shows an example of the neural network output for $M = 2.7$, given as the probability of a state being localized [P(loc)] or extended [P(ext)]. The summarized results are shown for $M = 2.7$ (b) and $M = 4.9$ (c), with comparison against KPM and IPR results. The difference between the two probabilities measures how confidently the model can distinguish localized or extended. Also shown in the figure with the magenta strips is the phase boundary determined by the conductivity, which indicates a transition near $W = 2.25$ for $M = 2.7$, and $W = 3.4$ for $M = 4.9$. Although the three different methods match quite well for $M = 4.9$, for $M = 2.7$ the IPR shows strongly critical behavior up until $W = 2.5$, well after the conductivity appears to vanish. Such critical behavior is detected by the neural net model. For W between 2.3 and 2.5 the IPR shows a strong L dependence and the neural net model predicts an extended phase with high confidence. For a range of W larger than 2.5, the IPR shows a weak L dependence across different system sizes, while in the neural net model P(loc) and P(ext) are quite close to each other.

complement to the KPM results and is hence included in the main results of Figure 6.1, which we overlaid in Figure 6.2(a).

The phase boundary obtained from machine learning between localized and non-localized wavefunctions roughly traces the CM-AI phase boundary provided by the conductivity computed with the KPM for M between 3.8 and 5.4, but it provides a slightly different boundary elsewhere. For $M < 3.8$, the machine learning result labels regions as critical that have a conductivity that looks localized (i.e. σ_{xx} is vanishing with increasing N_c). We further investigate the nature of this region using the inverse participation ratio (IPR) in real and momentum space bases, see Fig. 6.5. The IPR in this region shows critical behavior that transits into a localized phase at a point that is hard to accurately determine. The machine learning result provides a conservative estimate of where the criticality ends and localization sets in.

In summary, our use of the machine learning method in the present context is to provide an additional measure of the non-trivial phase boundaries that have a lot of structure. We then use conventional methods (conductivity and the IPR) to validate

the physical nature of the phase boundaries.

6.5 Magic-angle transition

The boundary between topologically distinct insulating phases is semimetal in the case without quasiperiodicity. In the BHZ model, the semimetal at $M = 2$ exstend to a line of semimetal for a range of W until it undergoes a magic-angle transition much similar to the discussion in Chapter 3. Also, the perturbation theory in previous section shows that the topological mass is not renormalized from $M = 2, W = 0$, making the semimetal phase a straight line in the $M-W$ phase diagram. As quasiperiodic potential increases, the semimetal stays stable with a renormalized velocity (calculated from the DOS) that vanishes like $\tilde{v} \sim (W_c(M = 2) - W)^{\beta/2}$ where $W_c(M = 2) = 1.42 \pm 0.02$ and $\beta = 2 \pm 0.3$. This is demonstrated in Fig. 6.6(a) where $\tilde{v}$ vanishes when $\rho(0)$ rises.

Additionally, the wave functions are localized in momentum space when $W < W_c(M = 2)$, and delocalized in momentum space when $W > W_c(M = 2)$ (as indicated in Fig. 6.6(b) by $\mathcal{I}_k$ being L-independent and $\mathcal{I}_k \sim 1/L^2$, respectively). When the real space IPR is L-independent and the resistivity increases with L and N_c, there is a localization transition with $W_A(M = 2) = 1.50 \pm 0.03$, indicating a small but finite CM phase.

6.6 TI-to-CM transition

To analyze topological transitions that are forbidden in disorder systems we use numerics to capture the full, nonperturbative transition to the CM phase located at $W_c(M)$. Near the transition, the correlation length diverges as $\xi \sim |W - W_c|^{-\nu}$ while scale invariance implies that the gap $\Delta \sim \xi^{-z}$; therefore the gap vanishes like $\Delta \sim |W - W_c|^{\nu z}$. Through the KPM calculation of DOS and Lanczos calculation of lowest energy states, we find $\nu z \approx 1$ for each M value we have considered, see Fig. 6.7(a).

These exponents indicate a unique universality class driven by quasiperiodicity distinct from random systems. Since our system breaks up into two blocks, each in the same symmetry class as the quantum Hall effect (i.e., class A), random disorder does not

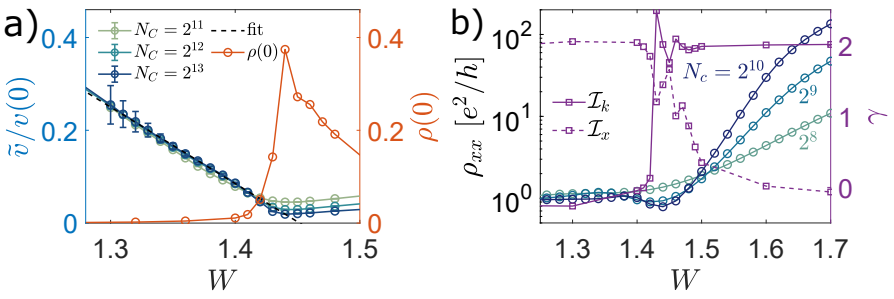

Figure 6.6: **The magic-angle transition for the semimetal line $M = 2$.** (a) Renormalized velocity $v/v(0)$ and the resulting finite density of states $\rho(0)$ at the transition, extracted from $\rho(E)$ that is calculated using KPM method with system size $L = 144$, Chebyshev cutoff $N_c = 2^{15}$. (b) These plots indicate the appearance of a critical metallic phase $1.4 \lesssim W \lesssim 1.5$ inferred from both the resistivity ρ_{xx} and the scaling of the momentum- and real-space IPRs. ρ_{xx} is calculated using Kubo formula with KPM method. The L-dependence of the IPRs is fitted from lowest energy eigenstates obtained using Lanczos method for $L = 89$, $L = 144$, and $L = 233$ to a power law form $\mathcal{I}_\alpha \sim 1/L^{\gamma_\alpha}$, and γ_α is shown as the right vertical axis.

allow for a metallic phase [37, 223, 232]. Therefore, topological phase transitions driven by quasiperiodicity host unique universality classes beyond the ten Altland-Zirnbauer random matrix classes [40].

When gap closes at $W_c(M)$, the conductivity at $E = 0$ becomes finite, and the Hall conductivity is no longer quantized, indicating the onset of the CM phase. As seen in Fig. 6.7(b), the Hall conductivity drops, and σ_{xx} peaks at the transition, remaining finite for the duration of the CM. The transition does not involve any symmetry breaking; it occurs when the topological gap closes and σ_{xy} is no longer quantized. For larger values of W, we find a transition into an Anderson insulating phase [37, 36] with exponentially localized wavefunctions in real space and a vanishing σ_{xx}.

6.6.1 Critical Exponents at the topological insulator to metal phase transition

The critical exponents at the TI-to-CM phase transition is extracted from the gap size. Here we demonstrate this process in more detail. The Δ is calculated using Lanczos here, as we focus on a very small range of parameters, making Lanczos more efficient than KPM.

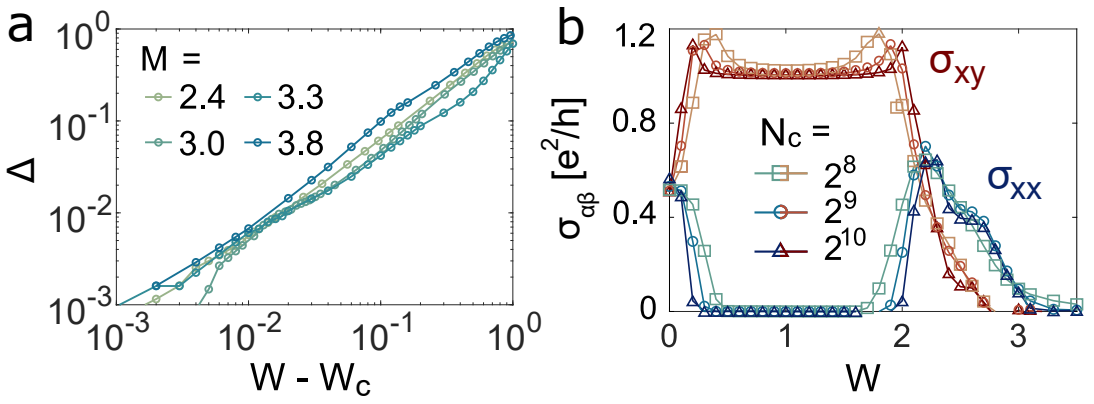

Figure 6.7: **Demonstration of the TI-to-CM transition.** (a) Tracking the density of states computed with the KPM in Eq. (2.1), we see the (hard) band gap closes as a power law $\Delta = (W_c(M) - W)^{\nu z}$ and find $\nu z \approx 1$ at the TI-to-CM transition across each value of M. (b) Shows the conductivity computed with the KPM in Eq. (6.2) as a function of quasiperiodic strength W for $M = 4.0$. The Hall conductivity σ_{xy} saturates to a finite value in the TI phase, but for $W_c(M = 4) \approx 2 \lesssim W \lesssim 3$ the longitudinal conductivity becomes finite and the Hall part is suppressed. The system is localized when $W \gtrsim 3$. Note that the feature near $W = 0$ is due to $M = 4$ being a SM. We stress that this metallic phase and therefore this transition does not exist in the presence of randomness.

We first estimate the critical quasiperiodic strength W_c from the density of states data. Near the estimated W_c, we consider a range of W_c and fit $\log(\Delta)$ over $\log(W_c - W)$, see Fig. 6.12(d). Then we identify the range of W that $\log \Delta$ is linear to $\log(W_c - W)$ and use least square fit. The best W_c is picked according to the goodness of linear fit, here quantified with root mean square error of the fit, see Fig. 6.12(e). The slope of the best fit is then νz, where $\Delta \sim (W_c - W)^{\nu z}$. For some cases this critical exponent is difficult to determine accurately because of the very fine phase diagram structure. For a few fixed M cuts including $M = 2.4$, $M = 3.0$, $M = 3.3$ and $M = 3.8$, we find νz near 1.0. To be precise, for $M = 2.4$ we have $\nu z = 1.06 \pm 0.1$; for $M = 3.0$, $\nu z = 1.00 \pm 0.1$; for $M = 3.3$, $\nu z = 0.95 \pm 0.2$; for $M = 3.8$, $\nu z = 1.13 \pm 0.15$

6.7 Criticality and flat topological bands

At small W, the insulating band gap [computed via the DOS in Eq. (6.3)] increases for some values of M but decreases for larger W, which is beyond the perturbative theory in Eq. (6.23). This non-monotonicity (whose onset is mapped in Fig. 6.13) coincides

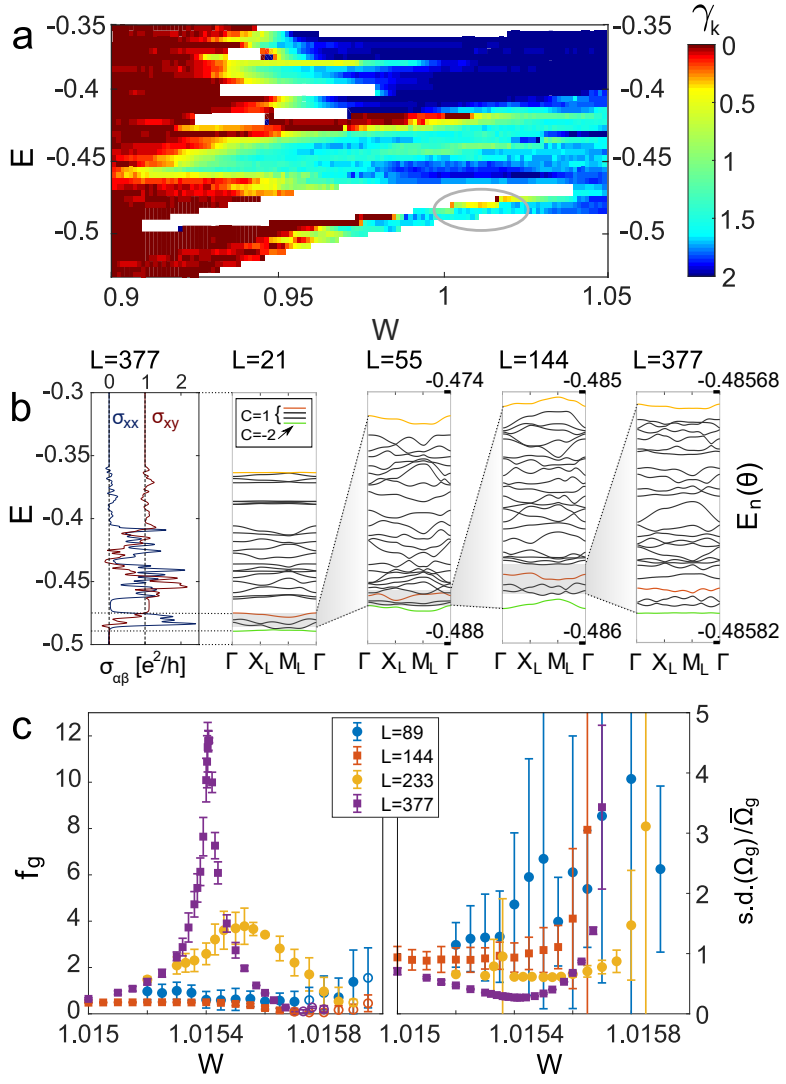

Figure 6.8: **Flat Chern bands and eigenstate criticality.** (a) Color plot of the momentum-space IPR system-size scaling. The value of γ_k is given by the color. The lowest energy states (and narrowest set of states) has a Chern number of 1. The white regions are hard gaps. (b; left) the conductivity calculated from Eq. 6.2 with $L = 377$ and cutoff $N_c = 2^{14}$. (b; right) Dispersion relation $E_n(\boldsymbol{\theta})$ along a representative cut in the mBZ for a sequence of $L = F_n$ with even n, for $W = 1.0154$. For each L, the green band carries Chern number -2, the first 4 bands (from green to cyan) sum to Chern number 1, and the 25 bands pictured in each plot sum to Chern number 1 (for $L = 55$, the pattern appears to hold but the lowest bands do not have a well-defined gap). (c) the flatness ratio f_g (left) and the normalized standard deviation of Berry curvature Ω_g across the folded Brillouin zone (right) of the first band above $E = -0.5$, for various L values. The filled markers (•) indicate topological bands while empty markers (○) indicate trivial bands (excluded in the right). The squares (■) and circles (•) correspond to $L = F_n$ such that n is odd and even, respectively.

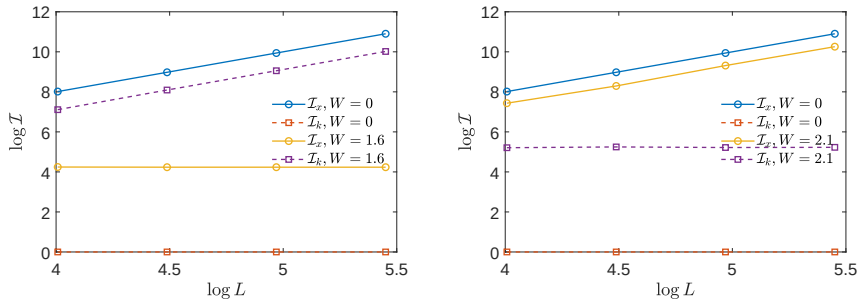

Figure 6.9: ***L* dependence of the IPR** Here we demonstrate two examples of how we determine γ_α for IPR data in the basis $\alpha = x, k$, where $I_\alpha \sim L^{-\gamma_\alpha}$, for $M = 2.7$ (a) and $M = 3.3$ (b). We take a linear fit for $\log I_k$ or $\log I_x$ over $\log L$, then the slope of the fit estimates γ.

with the onset of criticality in the finite energy states (i.e. a mobility edge) near the edge of the gap centered about $E = 0$ (e.g. in Fig. 6.8 this corresonds to the states near $E \approx -0.5$ for $W \approx 1$). Due to the interplay of topology, criticality, and quasiperiodicity several physically interesting effects occur near the gap maximum. This is demonstrated in Fig. 6.8 for $M = 4.0$ as a representative cut of the phase diagram in Fig. 6.1 that we now explore in more detail.

It can be seen from Fig. 6.8(a) that the states [2] near $E \approx -0.5$ narrow around $W \approx 1$ and are well isolated from other states by hard gaps. Additionally, by calculating σ_{xy}, Fig. 6.8(b) (left most panel) shows this collection of bands has total Chern number equal to 1, independent of L. Meanwhile, these states become critical, as measured by the IPR in momentum and position space ($1/\mathcal{I}_\alpha \approx L^{\gamma_\alpha}$). To consistently assess the behavior of the IPR, we calculate the IPR in both real and momentum space bases for each combination of parameters at $L = 55$, 89, 144 and 233. Then we fit the log of the IPR $\log(\mathcal{I})$ vs $\log L$ to extract the slope for an estimation of γ. We demonstrate some examples of such fitting in Fig. 6.9. Aggregating the IPR data for various W at an energy window we have Fig. 6.8(a) where color shows γ_k When $0 < \gamma_\alpha < 2$, the system is delocalized in both bases ($\alpha = x, k$).

Interestingly, we observe a self-similarity in these critical bands; the sequence of decreasing energy windows shown in Fig. 6.8(b) have the same Chern number as we

[2] By downfolding this collection of states originated from a band at a given L

increase the super-cell size. When $M = 4$ and $W = 1.01541$ the relevant energy window $E \in [-0.49, -0.47]$ has $(F_{n-5})^2$ states for a system size $L = F_n$. When we can identify the lowest band [depicted by the green line in Fig. 6.8(b)] in this energy window the value of its Chern number follows the self similar sequence of $C = -2$ for $L = F_{2n}$ and $C = 1$ for $L = F_{2n-1}$ (in each case examined).

The flatness of the lowest (green) band is apparent in the dispersion in the mBZ in Fig. 6.8(b) as well as by its large effective mass(Sec. 6.7.1. By computing the flatness ratio (of the green band) f_g and Berry curvature Ω_g (in Eqs. (6.5) and (6.6), respectively) our data also demonstrates that larger L leads to flatter, isolated topological bands in the mBZ at some optimal W. As shown in Fig. 6.8(b and c left) for increasing L the peak in f_g sharpens concomitantly with the development of critical eigenstates [Fig. 6.8(a)] as the Chern bands in the mBZ occur at an increasingly fine energy scale. At the W with maximal f_g, we also see a reduction in the fluctuation in Berry curvature Ω_g (of the green band), probed via its standard deviation divided by the mean across the mBZ, Fig. 6.8(c,right). Precisely, the normalized standard deviation of Berry curvature is

$$\frac{\text{s.d.}(\Omega_n)}{\bar{\Omega}_n} \equiv \frac{\sqrt{\sum_{\boldsymbol{\theta}} \Omega_n(\boldsymbol{\theta})^2 - \left(\sum_{\boldsymbol{\theta}} \Omega_n(\boldsymbol{\theta})\right)^2}}{\sum_{\boldsymbol{\theta}} \Omega_n(\boldsymbol{\theta})} \tag{6.7}$$

The reduction of fluctuations of Ω_g for increasing L suggest that the model could host a fractional Chern insulating state in the presence of interactions [233, 234]; however, it is possible that an incommensurate charge density wave state could be stabilized instead (see Fig. 6.10 for Berry curvature profiles in the mBZ).

6.7.1 Effective mass

One additional measure of band flatness to consider is the effective mass of the lowest band. We define an effective mass m^* by the expansion of the energy dispersion about its minimum $E(\mathbf{q}) = E(0) + \frac{1}{2m^*}\mathbf{q}^2 + \cdots$. Numerically, m^* can be obtained through a quadratic fitting of $E_n(\boldsymbol{\theta})$ near $\boldsymbol{\theta} = \mathbf{0}$, where the n indexes the first, folded band above $E = 0$ (Fig. 6.11(a), for example). The effective mass can also be obtained, perturbatively, from the pole of the Green function $E_{\text{eff}}(\mathbf{q}) = \pm(\tilde{M} + \mathbf{q}^2/2m^*)$ where

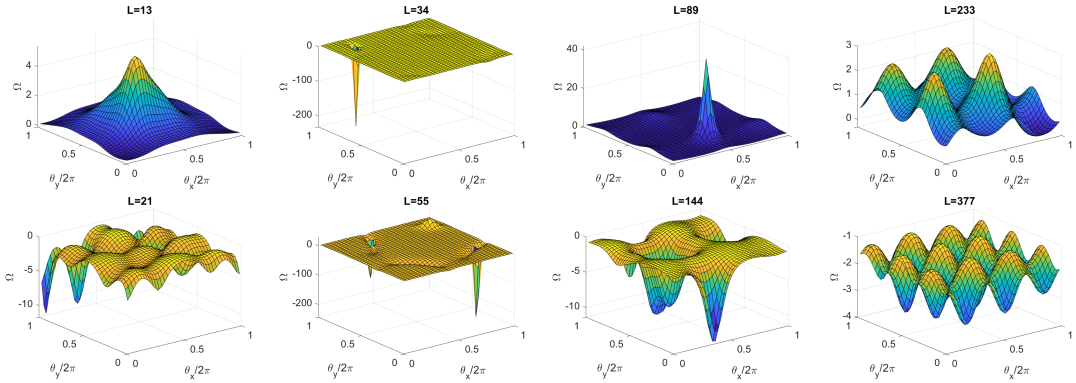

Figure 6.10: **Berry curvatures**. The Berry curvature of of the first band above the hard gap near $E = -0.5$. The samples shown are at $W = 1.01541$, $M = 4$ and $L = 377$, i.e. at its peak flatness (see Fig. 6.8). The first row are system sizes in the sequence of $L = F_n$ with odd n, and the second row for even n. For $L = 55$ and $L = 89$, Berry curvature have clear peaks; while larger L's see flatter Berry curvature.

$m^* = \tilde{M}/(2\tilde{v}^2)$. At fourth-order, $m^* \sim 10^5(1/t)$ at $W = 3t$, indicating that the QP is flattening the topological bands; our numerics (the blue solid line in Fig. 6.11(b)) show this effect is even more drastic [Fig. 6.11(b)].

6.7.2 Edge states

For finite size calculation, (twisted) periodic boundary conditions eliminate all edge contribution and keep only the bulk. With open boundary conditions, the edge states can be observed, but we no longer have access to any $\boldsymbol{\theta} \neq \mathbf{0}$. Here, we use twisted boundary conditions only in the x-direction but open boundary conditions along the y-direction, so that we can see the dispersion of the edge states as we vary θ_x, as clearly demonstrated in Fig. 6.11(c).

6.8 Conclusion

In a simple model of a two-dimensional topological insulator, we demonstrated that the inclusion of quasiperiodicity induces flat bands, eigenstate criticality, and a phase diagram full of structure. The eigenstates go through several Anderson-like transitions (delocalizing in momentum space before localizing in real space), which leads to critical eigenstates in a metallic phase. Meanwhile, we see the onset of flat topological bands

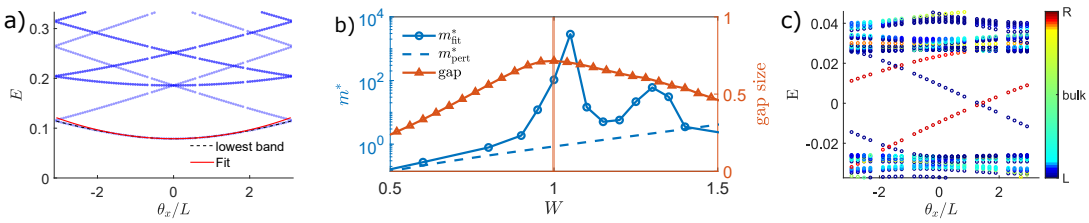

Figure 6.11: **Twist Dispersions**. (a) Using the twist dispersion to obtain the effective mass m^*. The red curve is the quadratic fitting result to estimate m^*. The figure shows an example for $M = 4.0$, $W = 0.4$. (b) The effective mass obtained from fitting twist dispersion ($m^*_{\rm fit}$) and from perturbation theory ($m^*_{\rm pert}$), compared with gap size. The vertical line marks the W where we scrutinize flat topological bands. (c) Twist dispersion with open boundary conditions in the y direction and twisted boundary conditions in the x direction. The color corresponds to the location of the eigenstates along the y axis. The red and dark blue states in the bulk gap are the edge states.

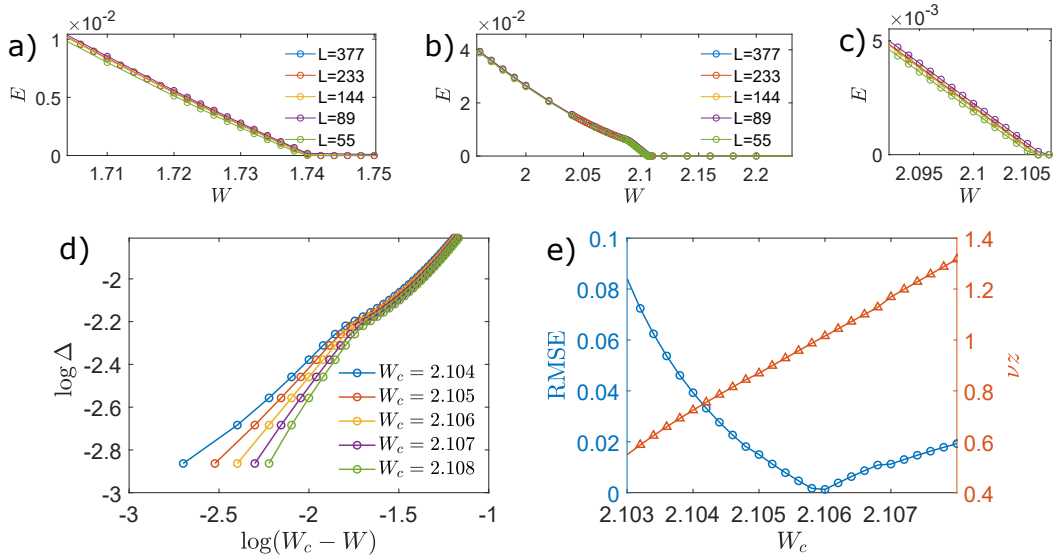

Figure 6.12: **Vanishing of the spectral gap.** The gap size as a function of W for $M = 2.4$ (a) and $M = 3.0$ (b) with various system sizes L. (c) is a more zoomed in view of the $M = 3.0$ cut near the transition. In the second row, we show an example of how the combination of critical exponents νz is extracted from the spectral gap data. For a range of choices of W_c, we fit $\log \Delta$ against $\log(W_c - W)$ in the range when $W_c - W$ is under 0.015 and $\Delta > 0.001$ with a straight line. This data is shown in (d). Then we find the point where the root mean square error (RMSE) as shown in (e) of the linear fit is smallest as our best estimation of W_c, where the slope is then νz. For these results, our best estimate of $\nu z = 1.0 \pm 0.1$, with $W_c = 2.106 \pm 0.001$.

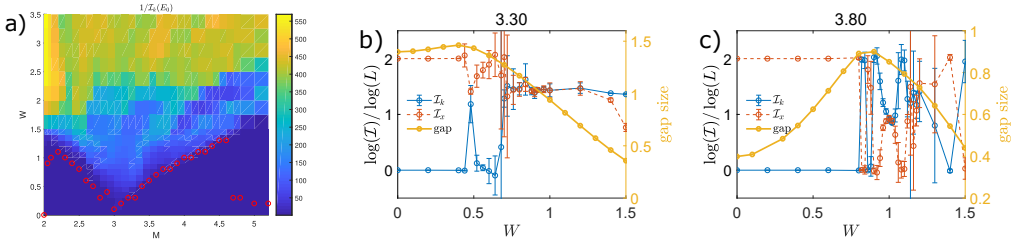

Figure 6.13: **Properties of the IPR.** (a) Phase diagram of the momentum space IPR of the lowest eigenstates. The red circles mark where the gap size $\Delta(W)$ changes its trend from increasing to decreasing as determined by the location of the maximum in $\Delta'(W)$. The cuts $M = 3.3$ (b) and $M = 3.8$ (c) show the non-trivial L dependence of the IPR in both real and momentum space start to dramatically change when $\Delta(W)$ begins to turn downward.

within the TI phase concomitant with critical high energy eigenstates. Our results go beyond twisted heterostructures and allows for cold atom labs and metamaterial labs (both of which have already realized 2D TIs [53, 222, 220, 221, 219, 120, 121]) to emulate similar physics.

6.9 Appendix: Perturbation theory

For smaller values of W, we shall use perturbation theory to estimate the location of the NI-to-TI and SM-to-CM transitions. Perturbation theory can also help determining the trend of topological mass, whose discrepancy from numerical results can serve as a proxy for determining the onset of the regime dominated by non-perturbative effect.

We begin by considering the single-particle Green function

$$\hat{G}_0(\omega) = [\omega - h_0(\omega)]^{-1}, \quad \hat{G}(\omega) = [\omega - h_0(\omega) + V]^{-1} \tag{6.8}$$

and use Dyson's equation

$$G(\mathbf{k}, \omega)^{-1} = \omega - h_0(\mathbf{k}) - \Sigma(\mathbf{k}, \omega) \tag{6.9}$$

where $\Sigma(\mathbf{k}, \omega)$ is the self-energy at momentum $\mathbf{k}$ including all $G_0(\mathbf{k}, \omega)$ irreducible diagrams. Close to the SM phase near $M = M_1 \equiv 2$ or $M = M_2 \equiv 4$, we express the Hamiltonian in the low-energy limit around the corresponding Dirac node $\mathbf{K}$ as $h_0(\mathbf{K} + \mathbf{q}) = v\mathbf{q} \cdot \boldsymbol{\sigma} + (M - M_i)\sigma_z$ and similarly expand the self-energy to obtain $\Sigma(\boldsymbol{k} = \boldsymbol{K} + \boldsymbol{q}, \omega) = \omega\Sigma_E\sigma_0 + \Sigma_p \boldsymbol{q} \cdot \boldsymbol{\sigma} + \Sigma_z\sigma_z$ (where σ_0 is the 2-by-2 identity matrix and

the $\sigma_{x,y,z}$ are the Pauli matrices). We define the quasiparticle residue Z, the renormalized topological mass $\tilde{M}$. and renormalized velocity $\tilde{v}$ such that the resulting Green function in the low-energy limit has the form

$$G(\mathbf{k} = \mathbf{K} + \mathbf{q}, \omega) = \frac{Z}{\omega - \tilde{v}\mathbf{q} \cdot \boldsymbol{\sigma} - \tilde{M}\sigma_z}. \tag{6.10}$$

Then using Σ_E, Σ_z and Σ_p from $\Sigma(\mathbf{k}, \omega)$ we can express Z, $\tilde{M}$ and $\tilde{v}$ as:

$$\begin{aligned} Z^{-1} &= 1 - \Sigma_E, & (6.11)\\ \tilde{M} - M_i &= (M - M_i + \Sigma_z)Z^{-1}, & (6.12)\\ \tilde{v} &= v(1 + \Sigma_p/v)Z^{-1}, & (6.13) \end{aligned}$$

To calculate $\Sigma(\mathbf{k}, \omega)$, we treat $V_{QP}(\mathbf{r})$ perturbatively. In momentum space, V is a delta function connecting $\mathbf{k}$ to $\mathbf{k} \pm Q\hat{x}$ and $\mathbf{k} \pm Q\hat{y}$. Hence, at second order the self energy is

$$\Sigma^{(2)}(\mathbf{k}, \omega) = (W/2)^2 \sum_{\pm, \hat{\mu} = \{\hat{x}, \hat{y}\}} \frac{1}{\omega - h_0(\mathbf{k} \pm Q\hat{\mu})}. \tag{6.14}$$

Near $M = 4$, $\mathbf{k} = \mathbf{M} + \mathbf{q}$ with $\mathbf{M} = (\pi, \pi)$, this yields

$$\begin{aligned} \Sigma_E^{(2)} &= -\frac{W^2}{D_2}, & (6.15)\\ \Sigma_p^{(2)} &= \frac{W^2}{2}\frac{(4 - M)^2(1 + \cos Q)}{D_2^2}v, & (6.16)\\ \Sigma_z^{(2)} &= W^2\frac{(4 - M) + (\cos Q - 1)}{D_2}, & (6.17) \end{aligned}$$

where $D_2 = (4 - M)^2 + 2(3 - M)(\cos Q - 1)$ is the common denominator that is always positive for $M > 3$. Observe that the numerator of $\Sigma_z^{(2)}$ is also always negative for $M > 4$, and $\Sigma_E^{(2)}$ is always negative. Hence $\tilde{M}$ is renormalized to be smaller as W increases, predicting a critical W where $\tilde{M}(W) = 4$ where TI to CM transition occurs. On the other hand, the direction of velocity renormalization is not obvious from the second-order perturbation theory, and indeed we can only predict the velocity to be renormalized to 0 at fourth-order perturbation theory. This is indicative of scattering off a single Dirac cone, where due to spin selection rules it requires a larger momentum exchange to induce intranode scattering.

The fourth-order perturbation theory includes all of the diagrams that connect the Dirac node to points in the Brillouin zone that are $2Q$ Manhattan distance apart and then back. The fourth order contributions to $\Sigma(\mathbf{k},\omega)$ are

$$\Sigma_E^{(4)} = \frac{W^4}{4}(-15M^4+166M^3+(-36M^2+206M-295)\cos(3Q)-732M^2+$$
$$(2M(M(24M-221)+697)-1497)\cos(Q)+(2M(M(13M-115)+356)-770)\cos(2Q)+$$
$$6(M-3)\cos(4Q)+1522M-1260)/D_4 \quad (6.18)$$

$$\Sigma_z^{(4)} = \frac{W^4}{8}(-10M^5+138M^4-806M^3+2509M^2+$$
$$(2M(2M(M(11M-134)+622)-2615)+4212)\cos(Q)+$$
$$2(M(M(3M(3M-37)+538)-1208)+1048)\cos(2Q)+$$
$$2(451-6M(M(3M-26)+76))\cos(3Q)+$$
$$5(M-3)(3M-8)\cos(4Q)-2(M-3)\cos(5Q)-4155M+2904)/D_4 \quad (6.19)$$

where D_4 is the common denominator

$$D_4 = (-2(M-3)\cos(Q)+(M-6)M+10)^2(-4(M-2)\cos(Q)+$$
$$(M-4)M+\cos(2Q)+7)(-2(M-3)\cos(2Q)+(M-6)M+10) \quad (6.20)$$

With the fourth-order correction, we find that the perturbation theory agrees very well with the numerical results, as well as Figs. 6.1 and 6.3. However, fourth order perturbation theory for the velocity renormalization only qualitatively predicts the magic-angle transition where $\tilde{v}=0$, but at a much larger W than indicated by numerical results. It is natural to expect that this is due to the single node nature of the bandstructure at $\mathbf{M}=(\pi,\pi)$ (all of the scattering is intranode). We anticipate a better prediction of magic angle transition may be achievable only at even higher orders of perturbation theory.

Using exactly the same procedure we can consider the case of M near 2, which is the SM line that divides the two TI regions with opposite sign in the quantum spin Hall effect. From a symmetry point of view it is not surprising that the $M=2$ SM line is W-independent. This is indeed the case from the perturbation theory, as up to

fourth order we have $\Sigma_z^{(2)} = 0$ and $\tilde{M} = M = 2$, hence there is no topological mass renormalization. That means starting from such a SM phase, quasiperiodicity is not driving it out of SM due to curvature in the phase boundary. At second order the velocity only reduces but does not go to zero and the renormalization of $\tilde{v}$ is only due to the quasiparticle residue $\Sigma_E^{(2)} = -\csc(Q/2)^2$, while $\Sigma_p^{(2)} = 0$. This can be understood as follows, at $M = 2$ the two Dirac cones are at $\mathbf{X} = (\pi, 0)$ and $\mathbf{Y} = (0, \pi)$ and being separated by 2π Manhattan distance in momentum space, second order perturbation theory will not be able to induce internode scattering. Whereas, at fourth order the two Dirac cones can be connected by $2Q$ hops in the Brillioun zone. Thus, only fourth order perturbation will be able to predict a vanishing velocity and a magic-angle transition. In line with this reasoning, the renormalized velocity $\tilde{v}$ up to fourth order is

$$\tilde{v} = (v + \Sigma_p^{(2)} + \Sigma_p^{(4)})/Z \tag{6.21}$$

Here $\Sigma_p^{(2)}$ vanishes, and the fourth order term

$$\Sigma_p^{(4)} = \frac{W^4}{16^2}(1 + 4\cos(Q))\csc(Q/2)^4 v \tag{6.22}$$

is negative only when $Q > \cos^{-1}(1/4) \approx 1.82$. Only in this regime does the perturbation theory predict a magic-angle transition. For example, at $Q = 2\pi F_{n-2}/F_n$, it predicts $\tilde{v}$ to vanish at $W_c^{(4)} = 4\sin(Q/2)(-1 - 4\cos Q)^{-1/4} \approx 3.16$. This fourth order perturbative result $W_c^{(4)}$ is an overestimate of the true critical W_c, and thus a more accurate prediction will require higher order perturbation theory. For smaller Q such as $Q = 2\pi F_{n-3}/F_n$, the velocity can never reach 0 at fourth order in perturbation theory. Hence, the magic-angle transition is an even higher order effect than that of $Q = 2\pi F_{n-2}/F_n$. In other words, the reduction of the value of Q requires higher order in perturbation (more Q "hops") to capture internode scattering.

These phase transitions can be assessed in this regime (i.e. near $M = 4$) by computing the renormalized mass $\tilde{M}$ and velocity $\tilde{v}$. We obtain up to second order in W

$$\tilde{M} - 4 = \frac{\left[(M-4) + W^2 \frac{(4-M)+(\cos Q - 1)}{(4-M)^2 + 2(3-M)(\cos Q - 1)}\right]}{1 + W^2/((4-M)^2 + 2(3-M)(\cos Q - 1))}. \tag{6.23}$$

By solving for $\tilde{M} = 4$, we obtain the phase boundary between insulating phases, illustrated by the black dotted line in Fig. 6.1(a) (at fourth-order in W), which is in

excellent agreement with the numerics. The curvature to this line demonstrates that quasiperiodicity can drive a topological phase transition NI-to-TI, which is the deterministic analog of the disordered topological Anderson insulator [235, 236]. For $M = 2$, there is no renormalization of $\tilde{M}$. Using numerics to access higher M and W, when $M \gtrsim 5.4$, the NI transitions into the CM. The magic-angle transition (i.e., SM-to-CM) is obtained by solving $\tilde{v} \to 0$ on the line $\tilde{M} = 4$.

Besides determining topological phase boundary by solving $\tilde{M} = 0$, the perturbation theory also determines gap size Δ as function of W when W is sufficiently small. Not surprisingly, the prediction of $\Delta(W)$ fails after some finite W. This is when the lowest band is mixing with other minibands nearby in energy due to the quasiperiodic potential. When such deviation between perturbation theory and numerical result of gap size happens (i.e. when Δ begin to decrease with W), IPR of the lowest energy state changes dramatically at the same W as shown in Fig. 6.13.

Acknowledgement

This chapter is based on collaborative work with Justin Wilson and Jed Pixley. We thank Yafis Barlas, Elio König, and Jie Wang for useful discussions.

Chapter 7

Rare region effect in 3D TI phase transition

7.1 Introduction

The previous chapter focused on the effect of quasiperiodicity on a model of a 2D topological insulator. We now turn to the case of a 3D topological insulator with disorder.

Unlike the case of 2D semimetals (SM), the fate of 3D topological SM under disorder does not have a consensus answer. The perturbative renormalization group predicts that for dimensions $d > 2$, the quantum critical point exists between semimetal and diffusive metal [237] – in another word, semimetal can withstand some finite disorder as far as perturbation theory can tell. The stability against weak disorder was assumed also by various numerical calculations[238]. However, more careful treatment of numerics that incorporates non-perturbative effect has revealed that arbitrarily small disorders can destabilize Weyl semimetals (WSM) and the quantum critical point between WSM phase and diffusive metal phase a avoided one[46].

The studies mentioned above have focused on stand-alone WSM models. An interesting question to ask is that whether the WSM living on the phase boundary between topological insulator phases destabilizes with the disorder. Superficially, the fact that the WSM has a context as topological phase boundary provides some extra perseverance against disorder, as the topological insulator phases on both sides of the WSM can hold up to disorder. The assumption of a stable semimetal has been assumed by previous theoretical works [34, 35]. On the other hand, the non-perturbative rare-region effect may still destabilize the WSM phase boundary as in the case of Ref. [46]. To answer this question, careful numerical treatment is needed.

This theoretically intriguing and debated problem is also experimentally important, especially as experimentalists have tried hunting for Weyl semimetals. The expectation is that tuning a parameter that controls the topological phase (the topological mass M, to be defined below) always pass through the semimetal phase. Experimental attempts include $BiTl(S_{1-\delta}Se_{\delta})_2$ for example [47] where the parameter δ determines the topological mass and can be controlled by doping.

However, the expectation implicitly assumed that the topological and trivial insulator phases, in a two-parameter phase diagram of M and disorder W, have the common boundary of finite length. The precise description of the SM phase under disorder can provide important insight for the experiments, whether it justifies or disproves the implicit assumption.

In this chapter, we will use a combination of numerical methods to investigate the phase boundary between TI and weak TI phases of a 3D model of topological insulator that is a generalization of the 2D Bernevig-Hughes-Zhang (BHZ) model. The phase boundary is perturbatively expected to be an SM until a quantum critical point(QCP).

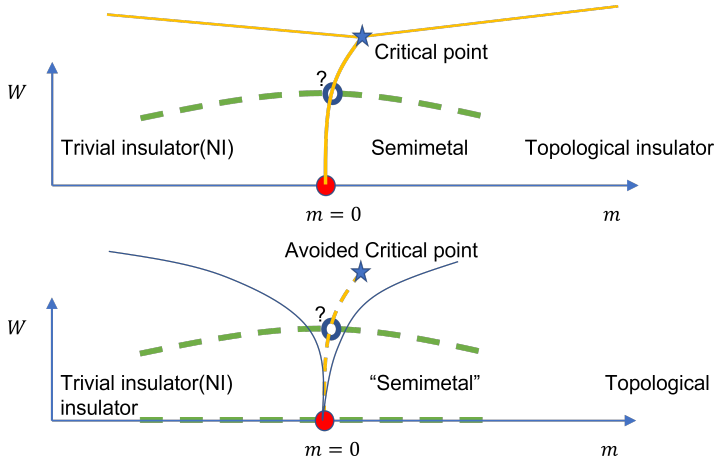

Figure 7.1: Schematics of the two candidate scenarios of phase transition between topologically distinct insulator phases in the presence of disorder. The question we address chapter is whether the phase transition along the green dash line is TI-SM-NI or TI-Metal-NI.

7.2 Model

We consider the 3D generalization of the BHZ model that has been studied by many [34, 35] to understand the topological insulator in presence of disorder. We define the model as a lattice for convenience in adding random potential that is spatially uncorrelated.

$$H = \sum_{\vec{r}} \sum_{\mu=x,y,z} \left[\frac{it}{2} c^{\dagger}_{\vec{r}+\mu} \alpha_\mu c_{\vec{r}} - \frac{m_2}{2} c^{\dagger}_{\vec{r}+\mu} \beta c_{\vec{r}} + h.c. \right] + (m_0 + 3m_2) \sum_{\vec{r}} c^{\dagger}_{\vec{r}} \beta c_{\vec{r}} \tag{7.1}$$

where α_μ and β are Dirac matrices defined using Pauli matrices σ_μ as

$$\beta = \begin{bmatrix} I & 0 \\ 0 & -I \end{bmatrix}, \alpha_\mu = \begin{bmatrix} 0 & \sigma_\mu \\ \sigma_\mu & 0 \end{bmatrix} \tag{7.2}$$

We fix $t = 1$ for convenience. The topology of the model is controlled by the ratio between $m0$ and $m2$. We define the ratio $M = m_0/m_2$ for convenience, and topological invariant $\mathcal{Q}$ is a function of M. Before we introduce disorder, The model is in the topological insulator phase for $M > -2$ and $M < 0$, and a weak topological insulator phase for $-4 < M < -2$. Otherwise, the topology is trivial. The band structure is shown in Figure 7.2. A topological phase transition happens only when the bands touch.

The disorder is included as a random potential that is independently sampled at each lattice site of the model. We use Gaussian distribution with standard deviation W which is a natural choice that is close to the experiment. Previous work has used uniform distribution within $[-W, W]$ [34, 35]. The specific choice of disorder does not change the physics, but Gaussian disorder is easier to study rare region effects.

7.3 Methods

The KPM method provides a convenient survey for the density of states and conductivity/conductance across various levels of Fermi energy. In addition, the result of KPM can be formulated to conveniently capture the basis-independent fluctuation of the conductivity, which helps determine the phase transition as mean or typical conductivity is difficult to calculate.

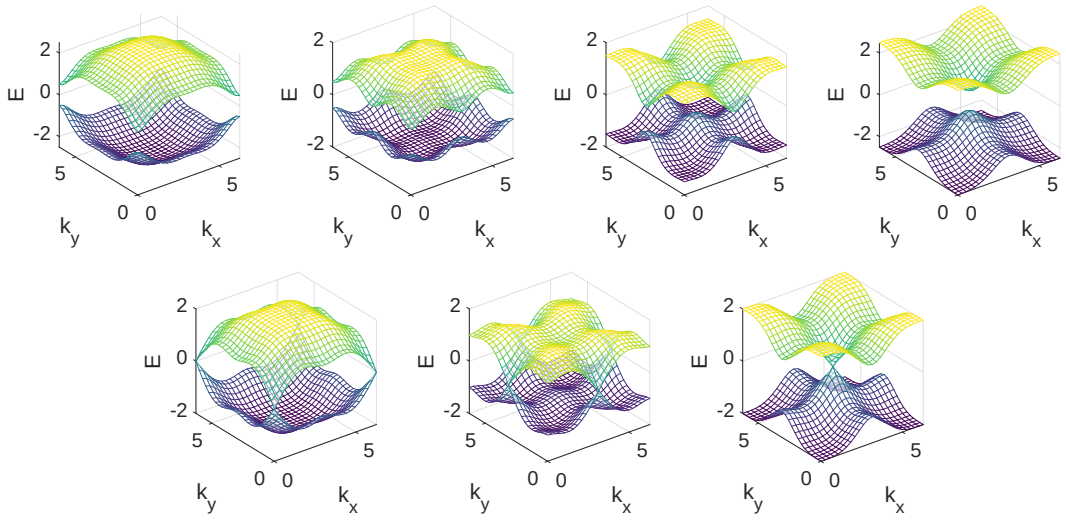

Figure 7.2: The clean band structure of the 3D topological insulator model we consider. The plots are a cut of $k_z = 0$. From left to right correspond to $M = 1, 0, -1, -2, -3, -4, -5$. The panels in the first row are in NI, TI, weak TI, NI phases and those in the second row are all in the SM phase. Notice that $M = 0$ and $M = 4$ has one band touching point but $M = 2$ has two.

On the other hand, using the Lanczos method we can calculate wavefunction. Specifically, we use the method of square-and-shift to calculate the lowest energy eigenstates. The criticality measures similar to Chapter 5 then follow from the eigenstates data. The multifractal analysis provides a well-validated approach to determine the phase boundaries from crossings with scaling by systems size L.

7.4 Phase Diagram

We present the phase diagram acquired by considering the density of the state at zero Fermi energy (Fig.7.3). $\rho(0)$ as small as $\sim 1/N_C^3$ represents the insulator region, where $\rho(0)$ is dominated by the far-tail of Jackson Kernel (See Chapter 2). For semimetal or destabilized semimetal phases, $\rho(0)$ is at the order of $1/N_C^2$ because the WSM phase has density of state scaling $\rho(E) \sim |E|^2$. The metallic phase is characterized by larger $\rho(0) \sim O(1)$ regardless of N_C. With a $N_C = 2048$, the color map of $\rho(0)$ visually presents the insulating and metallic phases, as well as their boundaries.

We also provide a zoomed-in phase diagram from conductivity at zero Fermi energy (Fig.7.3 bottom). The conductivity is more costly to compute and is hence only mapped

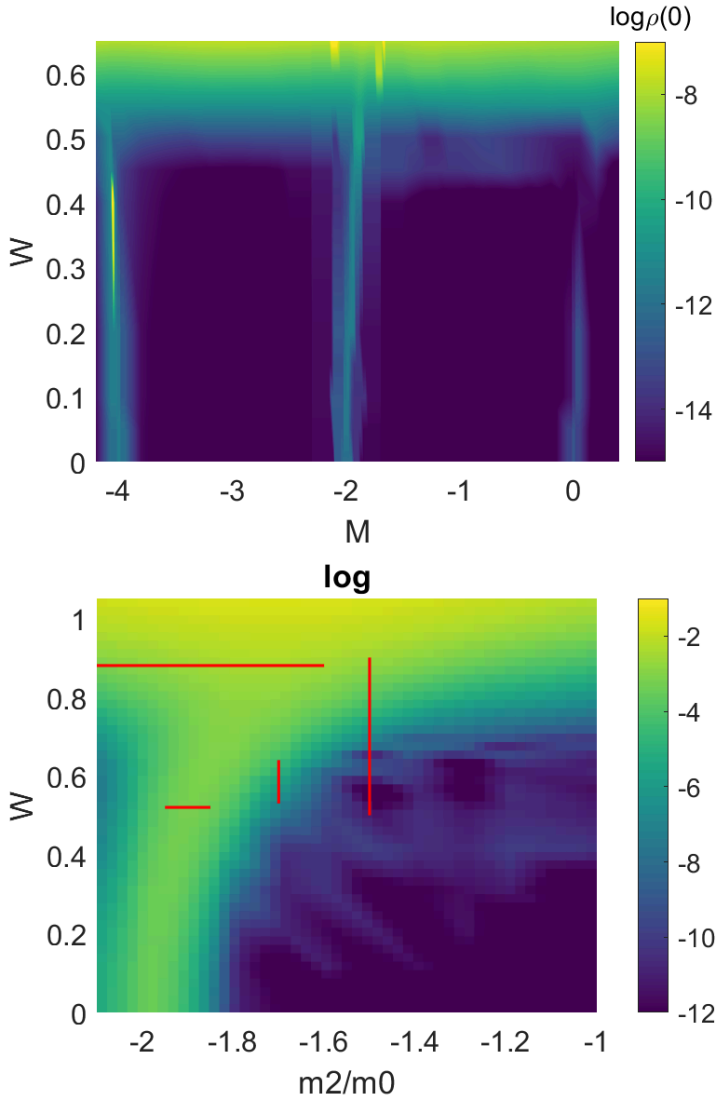

Figure 7.3: The phase diagram as mapping of $\log \rho(W, M, E = 0)$ (top) and $\log \sigma(W, M, E = 0)$ for a smaller range of parameters(bottom), marked with cuts that will be scrutinized in some detail. The DOS result is calculated with $N_C = 2048$ and $L = 151$. The light strips correspond to the SM and metallic phases.

for a small region. Although the phase diagrams have limited resolution (with only $N_C = 512$), they hint at the important feature that the insulator-metal transition follows the second scenario in Fig. 7.1. The WSM line that would have existed if there were not any rare-region effect is broadened into a critical fan.

However, we must keep in mind that the phase diagram in Fig. 7.3 can only be taken as a coarse indicator of the phase, unless even larger scale calculation is carried out to improve the resolution until fully saturated. For the next few sections, we will resort to a detailed calculation of several cuts guided by the tentative phase diagram to understand the phase transitions.

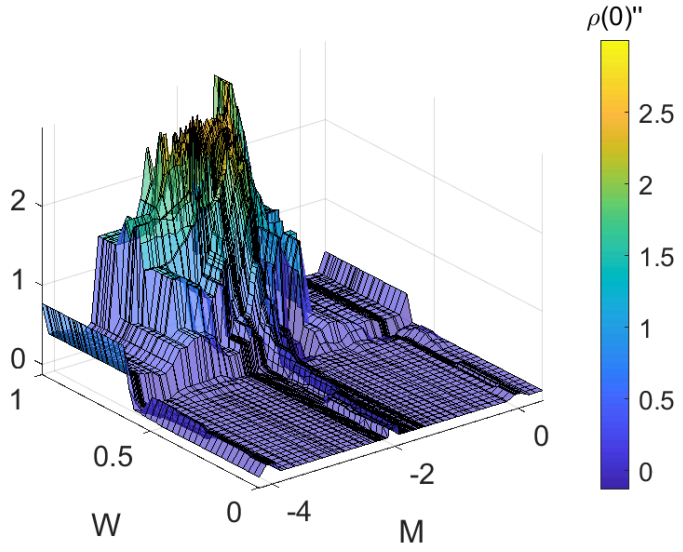

Figure 7.4: The landscape of $\rho''(W, M, E = 0)$ for a larger range of parameters. The calculation is done with $N_C = 2560$ and $L = 151$. A peak exists, marking the location of the avoided quantum critical points.

7.5 Avoided criticality

One feature discovered in Ref. [46] is the avoided quantum critical point in semimetal (that does not have a topological context) with the disorder. The criticality, being avoided, loses the analytical property but retains its critical behavior away from $E = 0$.

In another word, if the quantum criticality predicted by perturbative theory were not avoided, the density of states $\rho(E)$ would be non-analytic at the transition. Expanding near $E = 0$, we have $\rho(E) = \rho(0)+1/2\rho(0)''E^2$. Non-analytic behavior would be seen as

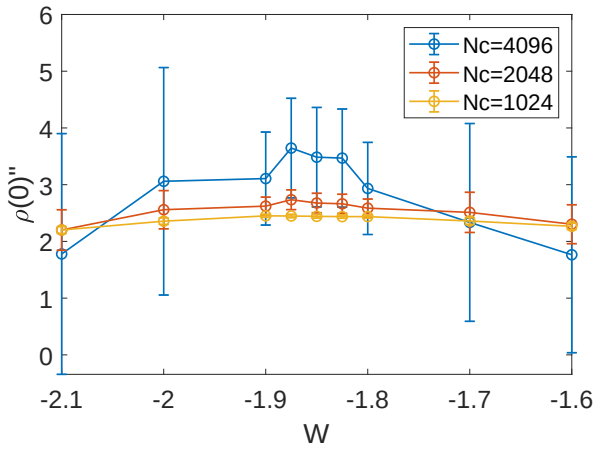

Figure 7.5: The second derivative of the density of states as a function of Fermi energy, at $E_f = 0$. As N_c increases, the peak stays within the same order of magnitude.

$\rho(0)$ being discontinuous in (M, W), or as $\rho''(0)$ with a singularity at certain (W_c, W_c).

From Fig. 7.4 we can clearly see the critical point – no matter avoided or not – occurs near $W_{QCP} = 0.88 \pm 0.05$ and $M_{QCP} = -1.8 \pm 0.1$. If the quantum critical point were not avoided, the WSM phase boundary would have been stable up to W_{QCP}. However, from the figure, it can be visually identified that a metallic region of a finite range of M has developed at a much smaller W. The finite metallic region will be shown more concretely in the next section.

To clearly demonstrate the avoided QCP being analytical and is not a result of finite size effect, we shall utilize the scaling of $\rho(0)''$ in N_c, the energy resolution (Fig. 7.5). As $N_c \to \infty$ the second derivative $\rho(0)''$ grows slowly into a finite peak (in sharp contrast to, for example, the orders of magnitude steep peak in the magic-angle transition in Chapter 5), indicating the quantum critical point is avoided.

7.6 Insulator to Metal phase transition and the mobility edge

We use both multifractal finite-size-scaling (MFSS)[239] as the primary tool to study the insulator to Metal phase transition and mobility edge for a few cuts across the phase boundaries indicated by the phase diagrams. In addition, we will discuss in the appendix the KPM calculation of conductivity[64] that shows the strong fluctuation near the phase transition.

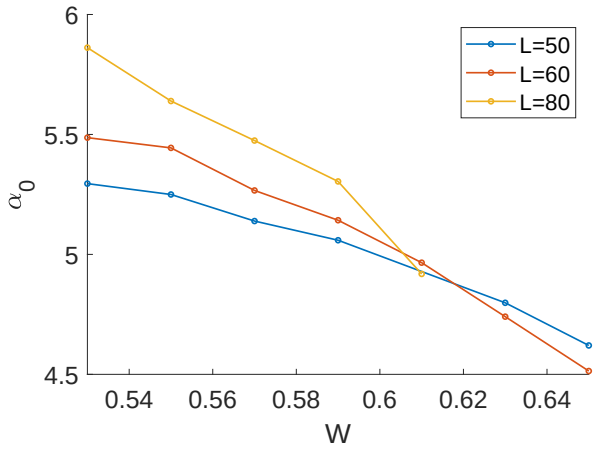

Figure 7.6: The crossing of α_0 as lattice size L varies. The critical W_C can be estimated from the figure as $W_C = 0.6 \pm 0.02$ for $M = -1.7$. Notice the drifting toward lower W_C as L increases, making our estimation more likely to be an overestimate.

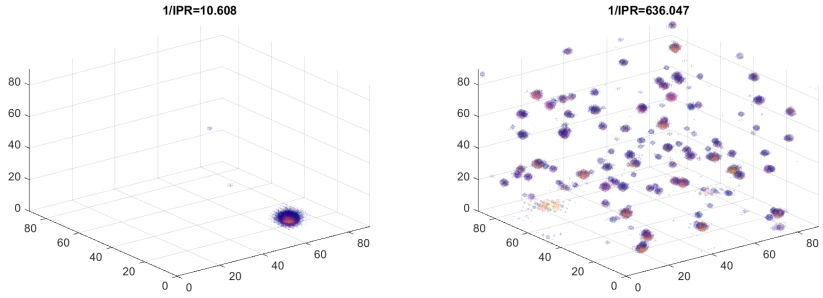

Figure 7.7: Plots of 3D $|\psi(x, y, z)|^2$ for a case of insulating phase close to transition ($M = -1.5$, $W = 0.54$, left) and in metallic phase ($M = -1.5$, $W = 0.69$, right). The size of dots represent $|\psi|^2$ that is below 0.001; and color represent those above 0.001.

7.6.1 Multifractal finite-size-scaling

The phase transition from insulator to metallic phase can be visually seen from the wavefunctions. In Fig. 7.7 we visualize examples of wavefunctions, one in the insulating phase and the other in the metallic phase. In the insulating phase the state is highly localized at one peak; and post-transition the wavefunction is more widespread. An interesting feature to observe from the wavefunctions is that some of the high-probability regions are confined to a thin but wide volume that almost looks like 2D. These are likely occurring at some domain wall.

To quantify the change of the wavefunctions, we study observables derived from the multifractal spectra. The multifractality of the wavefunctions is an important feature

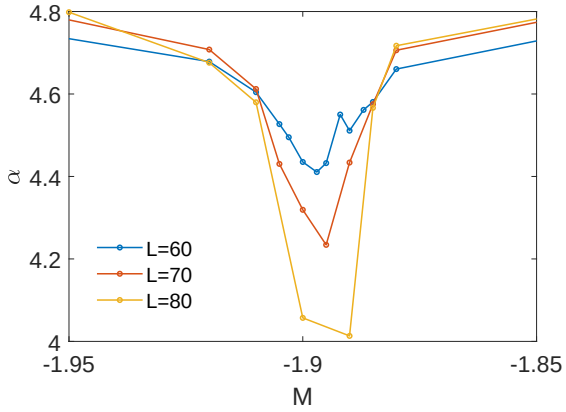

Figure 7.8: The crossing of $\alpha_0(M)$ for various L at fixed disorder $W = 0.52$. The finite range of M where α_0 approaches toward $\alpha_0 = d = 3$ as L increase is the metallic region that the semimetallic line develops into.

of the Anderson transition[37]. Following [239], we consider generalized singularity strengths

$$\tilde{\alpha}_q \equiv d\tilde{\tau}_q/dq \tag{7.3}$$

where $\tilde{\tau}_q$ is the generalized mass exponent

$$\tilde{\tau}_q(W, \lambda) = \ln\langle \mathcal{I}_q \rangle / \ln \lambda \tag{7.4}$$

where $\mathcal{I}_q$ is the generalized inverse participation ratio (IPR), and $1/\lambda$ is the size of the coarse-grained lattice when we box the L^3 lattice into l^3 cubes. The tilde in the above two equations emphasizes that the quantities, originally intended for the study at a critical point only, are extended to finite λ and W away from critical W_C. The tilde is dropped when the implication is clear.

We consider $\lambda = 0.1$ and even L's, so as to minimize the contribution from states in the band. A finite energy window of $0.001t$ is chosen to aggregate α_q. For computational considerations, we pick $q = 0$ such that α_q is expected to diverge for the insulating phase and approach $d = 3$ for the metallic phase. When the system is critical, $d < \alpha_q < 2d$ is expected. Hence, as L various a crossing would show up. For L ranging $[50, 80]$, a clear crossing shows up (Fig. 7.6) from which we can estimate the critical W_C. For $W < W_C$, α_0 increases with L signaling an insulating phase; and $W > W_C$ we see $\alpha_0 \to d = 3$.

Similarly, we can determine the mobility edge that is the localization-delocalization

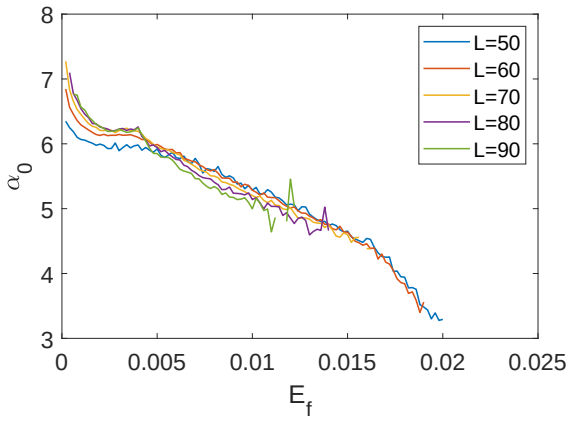

Figure 7.9: The mobility edge for $M = 1.5$, $W = 0.59$ is at 0.005 ± 0.001 where the curves for different L crosses.

transition at fixed W and M, but varying Fermi energy E. $\alpha_q(E)$ demonstrates a crossing at the mobility edge (Fig. 7.9) where the zero energy state is still insulating, while outside the mobility edge the system is metallic. As W increases, the mobility edge moves toward $E = 0$ at $W = W_C$ (data available upon request).

7.7 The stability of Weyl semimetal

To directly see the destabilized WSM for an arbitrary small disorder, we shall look into the spectral observables along the putative semimetal line. We consider both the density of states as similar to previous studies, [35] as well as the transport calculation at a size not previously considered in similar studies. In particular, to reach numerically stable results the necessary system size is much larger for transport properties. For the density of states, we consider lattice of size ranging from 80^3 to 120^3, while for conductivity we consider lattice of 150^3 and 200^3 sites. We take expansion order N_C as a handle for energy resolution. As we increase L and N_C, we have a range of parameters W that the density of state $\rho(E_f = 0)$ and $\sigma(E_f = 0)$ saturate to varying finite-size effects. The results are shown in Fig. 7.10 for density of states and Fig. 7.11 for DC conductivity. For both of the two observables, larger L and N_C saturate toward

$$\rho(E_f = 0) \sim e^{-a/W^2} \tag{7.5}$$

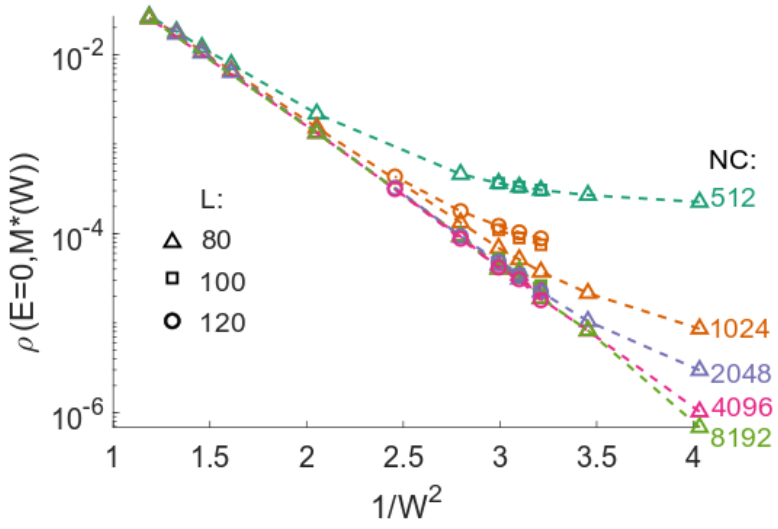

Figure 7.10: The DOS at $E = 0$ along the line that SM would have existed if it were stable. As L and N_C increases, the relation between $\log \rho$ and $1/W^2$ saturates to be linear.

and

$$\sigma(E_f = 0) \sim e^{-b/W^2} \tag{7.6}$$

where a and b are constants. Hence, as W decreases, both DOS and DC conductivity are suppressed very fast(hence the finite value can be easily overlooked and be identified as stable semimetals); however, for arbitrarily small $W > 0$ we have strictly $\rho(E_F = 0) > 0$ and $\sigma(E_f = 0) > 0$, indicating the non-existence of a stable semimetal line.

7.8 Conclusion and outlook

In this chapter, we provided evidence that the WSM phase boundary between topologically distinct insulator phases is destabilized by an arbitrarily small disorder. Instead, on the $W - M$ phase diagram, the WSM line is broadened into a fan of diffusive metal. The quantum critical point predicted by perturbation theory does not exist but becomes an avoided one. The destabilized semimetal and avoided quantum criticality indicates the putative Weyl semimetal line between topological insulators in fact resembles a finite region of metallic phase, which naturally explains the existence of a wide critical regime when tuning the topological insulator towards trivial insulator.

With the convenient numerical method, one feasible task is to map out a detailed

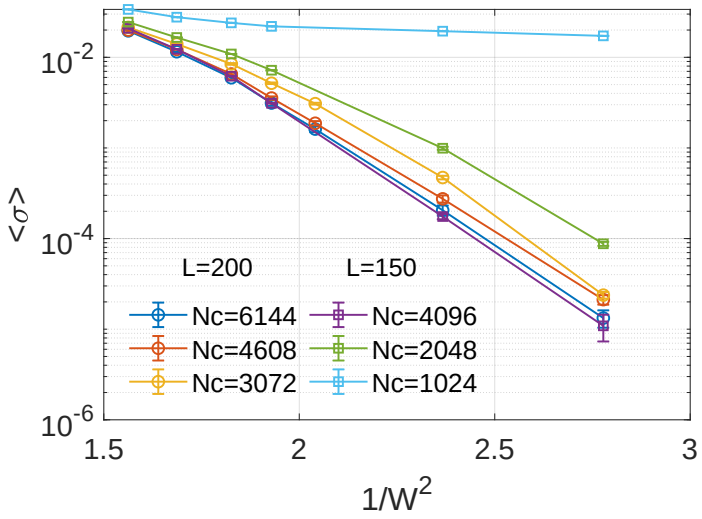

Figure 7.11: The conductivity at $E = 0$ along the putative SM line. As N_C and L increase, the linear relation between $\log \sigma$ and $1/W^2$ emerges.

phase diagram with conductivity. Such a phase diagram may reveal more detail of the phase transitions, as opposed to the guide of sight phase boundaries in early works regarding the topological insulator with the disorder (for example, Ref. [34]). Moreover, with the wave function methods, we can accurately determine the phase boundary between the insulating and diffusive metal phases. An accurate phase boundary can quantitatively show the range of parameter that experiences criticality.

The same method can even be applied with a more realistic model (similar to the work we do in Ref. [20]) to calculate the phase diagram of tunable topological insulators such as $BiTl(S_{1-\delta}Se_{\delta})_2$ to validate with observation results on the putative Weyl semimetal phase line.

7.9 Appendix: Conductance fluctuation at the TI to metal transition

The calculation of average conductivity is only plausible in the metallic phase, as a consequence of the universal conductance fluctuation (UCF) that penetrates into the critical point [240]. When conductance vanishes, the fluctuation of conductance does not vanish and even demonstrates $\langle (\delta g)^n \rangle \propto e^{n^2/\langle g \rangle}$ scaling. Hence, near the transition, the distribution of conductance becomes extremely broad with a log-normal tail. For

a log-normal distribution, accurate estimation of statistical parameters requires prior knowledge of the distribution itself. However, the precise mathematical form of the distribution is not known, while we know the distribution is neither strictly log-normal nor Gaussian. The broad distribution is shown in Figure. 7.12.

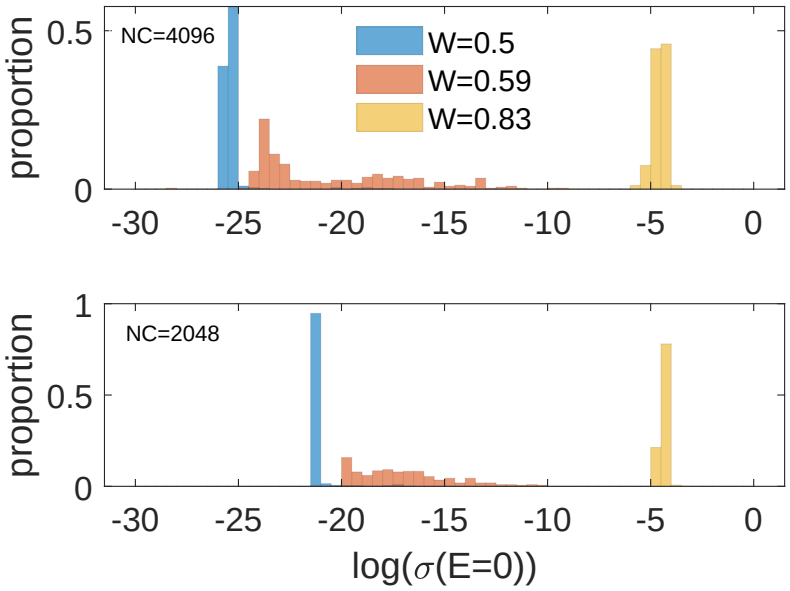

Figure 7.12: Histogram of KPM estimated sample conductance. The horizontal axis is log-scaled, highlighting the extremely broad distribution near the transition. In contrast, the metallic phase sees smaller fluctuation. The fluctuation increases with larger N_C.

As a substitution of mean conductivity as a scaling variable, it has been conventional [240] to use typical value (geometric mean) instead. However, even with typical conductance g_{typ}, it is not particularly efficient for KPM. The intrinsic broad distribution and small average falls exactly into the condition discussed in Section 2.5, where the stochastic trace estimation that backs the efficiency of the KPM method bears no advantage over exact trace. In addition, the tail of the distribution of the stochastic estimator of g can significantly extend to negative values for some of the samples, prohibiting the application of geometric mean across sample conductance. Statistically, it is common to use robust estimators to remediate (such as median, the median of means, the trimmed sample mean, and many more[241, 242]), but the robust estimators come at the price of neglecting the effect of far tails – which is against our goal of

understanding the contribution of rare region effects.

To tackle the situation, we take advantage of the random-vector fluctuation of KPM discussed in Section 2.5 to directly estimate the second moment of conductance,

$$\mu_2'[g] =< g^2 > / < g >^2 \tag{7.7}$$

whose numerator can be acquired directly from the standard deviation across random-vectors of each sample calculated in KPM. There is no need to use robust statistics for $< g^2 >$ because it is naturally positive definite; and robust estimation is applied to the denominator $< g >^2$ for which we only need a scale. Here for simplicity, we will just use median.

Figure. 7.13 shows the normalized second moment as a function of W along a cut of $M = -1.5$. The second-moment peak to several orders of magnitude is larger than the mean, which provides a crude estimate of the location of the transition. As lattice size in the calculation increases, the peak moves towards the left, similar to what we observe in the wave-function calculation. Hence the estimation of W_c is an upper bound – the metallic phase can only be larger in the phase diagram than we estimated.

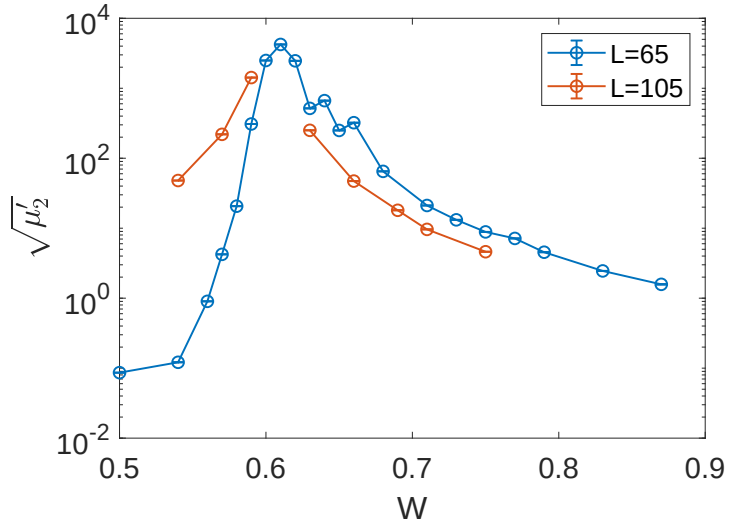

Figure 7.13: The normalized but not centralized second moment for a cut of $M = -1.5$, varying W. The peak marks the broadest distribution of conductance which estimates the critical W_c for metal-insulator transition. As L increases, the estimation of transition drifts to lower W_c, hence we shall only quote an upper bound of the transition.

Acknowledgements

The research in this chapter is done in collaboration with Justin Wilson and Jed Pixley.

Chapter 8

Conclusion

In this dissertation, we extensively studied the effect of quasiperiodicity and disorder in the context of topological phases of matter with a focus on phase transition and criticality. We applied an extensive set of tools to study the thermodynamic limit of lattice models whose translational symmetry is broken. With the KPM method, (iterative) exact diagonalization, multi-fractal analysis, machine learning, and so on, we numerically studied the effects of quasiperiodicity and disorder that are intrinsically non-perturbative. While most methods are not previously unseen, by pushing the boundary of optimization and utilizing the latest computational resources and paradigms, we largely extended the boundary of what we can calculate – and more importantly, what we can *easily* calculate. The easiness of computation allowed us to produce detailed phase diagrams for all models we studied (as opposed to guide-of-sight lines) and helped with many of our discoveries.

Applying the methods, we studied the quasiperiodic semimetals that we take as the prototype of the universal magic-angle semimetals including the famous twisted bilayer graphenes. We characterize the magic-angle transition as semimetal to metal transition as velocity is renormalized down to zero, which happens as a universal novel quantum phase transition that is deeply related to the incommensurability introduced by quasiperiodic modulation. Based on the model we studied, we proposed new routes to host magic-angle physics. We also extensively studied the same base model but with quasiperiodic modulation that preserves chirality. In the chiral model, we characterized the eigenstate phase transition through both the density of state and wave-function measures. The similarity and difference between the chiral and non-chiral models mark

the importance of the classification of quasiperiodicity-driven phase transition analogous to the classification of disorder-driven Anderson transition.

To connect our work with the ongoing experiments on twisted bilayer graphenes, we studied a special type of disorder that can show up in twisted bilayer graphene systems and find that the velocity of the Dirac cone is robust to disorder, whereas the other features of the miniband are rather sensitive to randomness in the twist angle.

For topological insulators, we extensively investigated the 2D BHZ model with the presence of quasiperiodicity, which is a natural generalization of magic-angle semimetals, to uncover an eigenstate criticality that coincides with the proliferate of flat topological bands. The rich phase diagram that we mapped out show a multitude of phase transition that can consecutively occur by varying strength of quasiperiodicity. We also demonstrated that the topological phase transition driven by quasiperiodicity does not follow any known symmetry classes.

Lastly, we studied a 3D topological insulator model with the disorder, focusing on the effect of the rare-region effect in the context of topologically protected phases. We find that any disorder destabilizes the Weyl semimetal that resides at the boundary between topological insulator phases. The WSM line is turned into a metallic phase that spans a finite area on the phase diagram, and the perturbatively anticipated quantum critical point between WSM and diffusive metal is turned into an avoided quantum critical point.

Bibliography

[1] Edward Witten. Three lectures on topological phases of matter. *La Rivista del Nuovo Cimento*, 39(7):313–370, 2016.

[2] Rafi Bistritzer and Allan H MacDonald. Moiré bands in twisted double-layer graphene. *Proc. Natl. Acad. Sci. U.S.A.*, 108(30):12233–12237, 2011.

[3] Grigory Tarnopolsky, Alex Jura Kruchkov, and Ashvin Vishwanath. Origin of magic angles in twisted bilayer graphene. *Phys. Rev. Lett.*, 122:106405, Mar 2019.

[4] Alexander Weiße, Gerhard Wellein, Andreas Alvermann, and Holger Fehske. The kernel polynomial method. *Reviews of modern physics*, 78(1):275, 2006.

[5] Nguyen N. T. Nam and Mikito Koshino. Lattice relaxation and energy band modulation in twisted bilayer graphene. *Phys. Rev. B*, 96:075311, Aug 2017.

[6] Stephen Carr, Shiang Fang, Ziyan Zhu, and Efthimios Kaxiras. Exact continuum model for low-energy electronic states of twisted bilayer graphene. *Phys. Rev. Research*, 1:013001, Aug 2019.

[7] Yixing Fu, EJ König, JH Wilson, Yang-Zhi Chou, and JH Pixley. Magic-angle semimetals. *arXiv preprint arXiv:1809.04604*, 2018.

[8] K v Klitzing, Gerhard Dorda, and Michael Pepper. New method for high-accuracy determination of the fine-structure constant based on quantized hall resistance. *Physical Review Letters*, 45(6):494, 1980.

[9] Daniel C Tsui, Horst L Stormer, and Arthur C Gossard. Two-dimensional magnetotransport in the extreme quantum limit. *Physical Review Letters*, 48(22):1559, 1982.

[10] F Duncan M Haldane. Model for a quantum hall effect without landau levels: Condensed-matter realization of the" parity anomaly". *Physical review letters*, 61(18):2015, 1988.

[11] Charles L Kane and Eugene J Mele. Z 2 topological order and the quantum spin hall effect. *Physical review letters*, 95(14):146802, 2005.

[12] B Andrei Bernevig, Taylor L Hughes, and Shou-Cheng Zhang. Quantum spin hall effect and topological phase transition in hgte quantum wells. *science*, 314(5806):1757–1761, 2006.

[13] Frank Schindler, Ashley M Cook, Maia G Vergniory, Zhijun Wang, Stuart SP Parkin, B Andrei Bernevig, and Titus Neupert. Higher-order topological insulators. *Science advances*, 4(6):eaat0346, 2018.

[14] NP Armitage, EJ Mele, and Ashvin Vishwanath. Weyl and dirac semimetals in three-dimensional solids. *Reviews of Modern Physics*, 90(1):015001, 2018.

[15] Binghai Yan and Claudia Felser. Topological materials: Weyl semimetals. *Annual Review of Condensed Matter Physics*, 8:337–354, 2017.

[16] Philip W Anderson. Absence of diffusion in certain random lattices. *Physical review*, 109(5):1492, 1958.

[17] Justin H Wilson, Yixing Fu, S Das Sarma, and JH Pixley. Disorder in twisted bilayer graphene. *arXiv preprint arXiv:1908.02753*, 2019.

[18] Yang-Zhi Chou, Yixing Fu, Justin H Wilson, EJ König, and JH Pixley. Magic-angle semimetals with chiral symmetry. *arXiv preprint arXiv:1908.09837*, 2019.

[19] Liang Wu, Fangdi Wen, Yixing Fu, Justin H Wilson, Xiaoran Liu, Yujun Zhang, Denis M Vasiukov, Mikhail S Kareev, JH Pixley, and Jak Chakhalian. Berry phase manipulation in ultrathin srruo 3 films. *Physical Review B*, 102(22):220406, 2020.

[20] Xiaoran Liu, Shiang Fang, Yixing Fu, Wenbo Ge, Mikhail Kareev, Jong-Woo Kim, Yongseong Choi, Evguenia Karapetrova, Qinghua Zhang, Lin Gu, et al. A

magnetic weyl semimetallic phase in thin films of eu _2 ir _2 o _7. *arXiv preprint arXiv:2106.04062*, 2021.

[21] Alexey A Soluyanov, Dominik Gresch, Zhijun Wang, QuanSheng Wu, Matthias Troyer, Xi Dai, and B Andrei Bernevig. Type-ii weyl semimetals. *Nature*, 527(7579):495–498, 2015.

[22] Holger Bech Nielsen and Masao Ninomiya. No-go theorum for regularizing chiral fermions. Technical report, Science Research Council, 1981.

[23] M Zahid Hasan, Su-Yang Xu, Ilya Belopolski, and Shin-Ming Huang. Discovery of weyl fermion semimetals and topological fermi arc states. *Annual Review of Condensed Matter Physics*, 8:289–309, 2017.

[24] M Gärttner, SV Syzranov, AM Rey, V Gurarie, and L Radzihovsky. Disorder-driven transition in a chain with power-law hopping. *Phys. Rev. B*, 92(4):041406, 2015.

[25] Sergey V Syzranov and Leo Radzihovsky. High-dimensional disorder-driven phenomena in weyl semimetals, semiconductors, and related systems. *Annual Review of Condensed Matter Physics*, 9:35–58, 2018.

[26] Kostya S Novoselov, Andre K Geim, Sergei V Morozov, De-eng Jiang, Yanshui Zhang, Sergey V Dubonos, Irina V Grigorieva, and Alexandr A Firsov. Electric field effect in atomically thin carbon films. *science*, 306(5696):666–669, 2004.

[27] Xiao-Liang Qi, Yong-Shi Wu, and Shou-Cheng Zhang. Topological quantization of the spin hall effect in two-dimensional paramagnetic semiconductors. *Physical Review B*, 74(8):085308, 2006.

[28] Markus König, Steffen Wiedmann, Christoph Brüne, Andreas Roth, Hartmut Buhmann, Laurens W Molenkamp, Xiao-Liang Qi, and Shou-Cheng Zhang. Quantum spin hall insulator state in hgte quantum wells. *Science*, 318(5851):766–770, 2007.

[29] Louk Rademaker and Marco Gibertini. Gate-tunable imbalanced kane-mele model in encapsulated bilayer jacutingaite. *Physical Review Materials*, 5(4):044201, 2021.

[30] Antimo Marrazzo, Marco Gibertini, Davide Campi, Nicolas Mounet, and Nicola Marzari. Prediction of a large-gap and switchable kane-mele quantum spin hall insulator. *Physical review letters*, 120(11):117701, 2018.

[31] Haijun Zhang, Chao-Xing Liu, Xiao-Liang Qi, Xi Dai, Zhong Fang, and Shou-Cheng Zhang. Topological insulators in bi 2 se 3, bi 2 te 3 and sb 2 te 3 with a single dirac cone on the surface. *Nature physics*, 5(6):438–442, 2009.

[32] YL Chen, James G Analytis, J-H Chu, ZK Liu, S-K Mo, Xiao-Liang Qi, HJ Zhang, DH Lu, Xi Dai, Zhong Fang, et al. Experimental realization of a three-dimensional topological insulator, bi2te3. *science*, 325(5937):178–181, 2009.

[33] David Hsieh, Yuqi Xia, L Wray, Dong Qian, Arijeet Pal, JH Dil, J Osterwalder, F Meier, G Bihlmayer, CL Kane, et al. Observation of unconventional quantum spin textures in topological insulators. *Science*, 323(5916):919–922, 2009.

[34] Koji Kobayashi, Tomi Ohtsuki, and Ken-Ichiro Imura. Disordered weak and strong topological insulators. *Physical review letters*, 110(23):236803, 2013.

[35] Koji Kobayashi, Tomi Ohtsuki, Ken-Ichiro Imura, and Igor F Herbut. Density of states scaling at the semimetal to metal transition in three dimensional topological insulators. *Physical review letters*, 112(1):016402, 2014.

[36] Elihu Abrahams, PW Anderson, DC Licciardello, and TV Ramakrishnan. Scaling theory of localization: Absence of quantum diffusion in two dimensions. *Physical Review Letters*, 42(10):673, 1979.

[37] Ferdinand Evers and Alexander D. Mirlin. Anderson transitions. *Rev. Mod. Phys.*, 80:1355–1417, Oct 2008.

[38] Elihu Abrahams. *50 years of Anderson Localization*, volume 24. world scientific, 2010.

[39] S Bogdanovich, Myriam P Sarachik, and RN Bhatt. Scaling of the conductivity with temperature and uniaxial stress in si: B at the metal-insulator transition. *Physical review letters*, 82(1):137, 1999.

[40] Alexander Altland and Martin R Zirnbauer. Nonstandard symmetry classes in mesoscopic normal-superconducting hybrid structures. *Physical Review B*, 55(2):1142, 1997.

[41] Eugene P Wigner. On the statistical distribution of the widths and spacings of nuclear resonance levels. In *Mathematical Proceedings of the Cambridge Philosophical Society*, volume 47, pages 790–798. Cambridge University Press, 1951.

[42] Freeman J Dyson. Statistical theory of the energy levels of complex systems. i. *Journal of Mathematical Physics*, 3(1):140–156, 1962.

[43] Renate Gade and Franz Wegner. The n = 0 replica limit of u(n) and u(n)so(n) models. *Nucl. Phys. B*, 360(2â3):213 – 218, 1991.

[44] Renate Gade. Anderson localization for sublattice models. *Nucl. Phys. B*, 398(3):499 – 515, 1993.

[45] IM Lifshitz. The energy spectrum of disordered systems. *Advances in Physics*, 13(52):483–536, 1964.

[46] JH Pixley, David A Huse, and S Das Sarma. Rare-region-induced avoided quantum criticality in disordered three-dimensional dirac and weyl semimetals. *Physical Review X*, 6(2):021042, 2016.

[47] Su-Yang Xu, Y Xia, LA Wray, S Jia, F Meier, JH Dil, J Osterwalder, B Slomski, A Bansil, H Lin, et al. Topological phase transition and texture inversion in a tunable topological insulator. *Science*, 332(6029):560–564, 2011.

[48] Serge Aubry and Gilles André. Analyticity breaking and anderson localization in incommensurate lattices. *Ann. Israel Phys. Soc*, 3(133):18, 1980.

[49] Philip George Harper. Single band motion of conduction electrons in a uniform magnetic field. *Proceedings of the Physical Society. Section A*, 68(10):874, 1955.

[50] Giacomo Roati, Chiara D'Errico, Leonardo Fallani, Marco Fattori, Chiara Fort, Matteo Zaccanti, Giovanni Modugno, Michele Modugno, and Massimo Inguscio. Anderson localization of a non-interacting bose–einstein condensate. *Nature*, 453(7197):895, 2008.

[51] Michael Schreiber, Sean S. Hodgman, Pranjal Bordia, Henrik P. Lüschen, Mark H. Fischer, Ronen Vosk, Ehud Altman, Ulrich Schneider, and Immanuel Bloch. Observation of many-body localization of interacting fermions in a quasirandom optical lattice. *Science*, 349(6250):842–845, August 2015.

[52] J. Smith, A. Lee, P. Richerme, B. Neyenhuis, P. W. Hess, P. Hauke, M. Heyl, D. A. Huse, and C. Monroe. Many-body localization in a quantum simulator with programmable random disorder. *Nat. Phys.*, 12(10):907–911, October 2016.

[53] Christopher W Peterson, Wladimir A Benalcazar, Taylor L Hughes, and Gaurav Bahl. A quantized microwave quadrupole insulator with topologically protected corner states. *Nature*, 555(7696):346, 2018.

[54] Yuan Cao, Valla Fatemi, Shiang Fang, Kenji Watanabe, Takashi Taniguchi, Efthimios Kaxiras, and Pablo Jarillo-Herrero. Unconventional superconductivity in magic-angle graphene superlattices. *Nature*, 556(7699):43–50, 2018.

[55] Yuan Cao, Valla Fatemi, Ahmet Demir, Shiang Fang, Spencer L Tomarken, Jason Y Luo, Javier D Sanchez-Yamagishi, Kenji Watanabe, Takashi Taniguchi, Efthimios Kaxiras, et al. Correlated insulator behaviour at half-filling in magic-angle graphene superlattices. *Nature*, 556(7699):80, 2018.

[56] Dov Levine and Paul Joseph Steinhardt. Quasicrystals: a new class of ordered structures. *Physical review letters*, 53(26):2477, 1984.

[57] Dan Shechtman, Ilan Blech, Denis Gratias, and John W Cahn. Metallic phase with long-range orientational order and no translational symmetry. *Physical review letters*, 53(20):1951, 1984.

[58] Roger Penrose. Pentaplexity a class of non-periodic tilings of the plane. *The mathematical intelligencer*, 2(1):32–37, 1979.

[59] Huaqing Huang and Feng Liu. Theory of spin bott index for quantum spin hall states in nonperiodic systems. *Physical Review B*, 98(12):125130, 2018.

[60] Yaacov E Kraus, Yoav Lahini, Zohar Ringel, Mor Verbin, and Oded Zilberberg. Topological states and adiabatic pumping in quasicrystals. *Physical review letters*, 109(10):106402, 2012.

[61] Ion C Fulga, Dmitry I Pikulin, and Terry A Loring. Aperiodic weak topological superconductors. *Physical review letters*, 116(25):257002, 2016.

[62] Yaacov E Kraus and Oded Zilberberg. Topological equivalence between the fibonacci quasicrystal and the harper model. *Physical review letters*, 109(11):116404, 2012.

[63] David A Drabold and Otto F Sankey. Maximum entropy approach for linear scaling in the electronic structure problem. *Physical review letters*, 70(23):3631, 1993.

[64] Jose H. García, Lucian Covaci, and Tatiana G. Rappoport. Real-space calculation of the conductivity tensor for disordered topological matter. *Phys. Rev. Lett.*, 114:116602, Mar 2015.

[65] S M João and J M Viana Parente Lopes. Basis-independent spectral methods for non-linear optical response in arbitrary tight-binding models. *Journal of Physics: Condensed Matter*, 32(12):125901, dec 2019.

[66] G. B. Ventura, D. J. Passos, J. M. B. Lopes dos Santos, J. M. Viana Parente Lopes, and N. M. R. Peres. Gauge covariances and nonlinear optical responses. *Phys. Rev. B*, 96:035431, Jul 2017.

[67] Daniel E. Parker, Takahiro Morimoto, Joseph Orenstein, and Joel E. Moore. Diagrammatic approach to nonlinear optical response with application to weyl semimetals. *Phys. Rev. B*, 99:045121, Jan 2019.

[68] J. Skilling. *Maximum Entropy and Bayesian Methods*. Fundamental Theories of Physics. Springer Netherlands, 1988.

[69] Michael F Hutchinson. A stochastic estimator of the trace of the influence matrix for laplacian smoothing splines. *Communications in Statistics-Simulation and Computation*, 18(3):1059–1076, 1989.

[70] Cornelius Lanczos. An iteration method for the solution of the eigenvalue problem of linear differential and integral operators. 1950.

[71] Sanjeev Arora, Elad Hazan, and Satyen Kale. Fast algorithms for approximate semidefinite programming using the multiplicative weights update method. In *46th Annual IEEE Symposium on Foundations of Computer Science (FOCS'05)*, pages 339–348. IEEE, 2005.

[72] Richard B Lehoucq, Danny C Sorensen, and Chao Yang. *ARPACK users' guide: solution of large-scale eigenvalue problems with implicitly restarted Arnoldi methods*. SIAM, 1998.

[73] Jeff Bezanson, Alan Edelman, Stefan Karpinski, and Viral B Shah. Julia: A fresh approach to numerical computing. *SIAM review*, 59(1):65–98, 2017.

[74] Alan George and Esmond Ng. On the complexity of sparse qr and lu factorization of finite-element matrices. *SIAM journal on scientific and statistical computing*, 9(5):849–861, 1988.

[75] Bodo Huckestein. Scaling theory of the integer quantum hall effect. *Rev. Mod. Phys.*, 67:357–396, Apr 1995.

[76] Claudio de C. Chamon, Christopher Mudry, and Xiao-Gang Wen. Localization in two dimensions, gaussian field theories, and multifractality. *Phys. Rev. Lett.*, 77:4194–4197, Nov 1996.

[77] Ashvin Chhabra and Roderick V. Jensen. Direct determination of the f(α) singularity spectrum. *Phys. Rev. Lett.*, 62:1327–1330, Mar 1989.

[78] Tomoki Ohtsuki and Tomi Ohtsuki. Deep learning the quantum phase transitions in random two-dimensional electron systems. *Journal of the Physical Society of Japan*, 85(12):123706, 2016.

[79] Juan Carrasquilla and Roger G Melko. Machine learning phases of matter. *Nature Physics*, 13(5):431–434, 2017.

[80] Pierre Baldi, Peter Sadowski, and Daniel Whiteson. Searching for exotic particles in high-energy physics with deep learning. *Nature communications*, 5:4308, 2014.

[81] Igor Sfiligoi, Daniel C Bradley, Burt Holzman, Parag Mhashilkar, Sanjay Padhi, and Frank Wurthwein. The pilot way to grid resources using glideinwms. In *2009 WRI World Congress on Computer Science and Information Engineering*, volume 2 of *2*, pages 428–432, 2009.

[82] François Chollet et al. Keras. https://keras.io, 2015.

[83] Andrea Damascelli, Zahid Hussain, and Zhi-Xun Shen. Angle-resolved photoemission studies of the cuprate superconductors. *Reviews of modern physics*, 75(2):473, 2003.

[84] Jerry Tersoff and DR Hamann. Theory and application for the scanning tunneling microscope. *Physical review letters*, 50(25):1998, 1983.

[85] Edsger W. Dijkstra and DIJKSTRA EW. Information streams sharing a finite buffer. 1972.

[86] Trithep Devakul and David A Huse. Anderson localization transitions with and without random potentials. *Phys. Rev. B*, 96(21):214201, 2017.

[87] JH Pixley, Justin H Wilson, David A Huse, and Sarang Gopalakrishnan. Weyl semimetal to metal phase transitions driven by quasiperiodic potentials. *Physical review letters*, 120(20):207604, 2018.

[88] Su-Yang Xu et al. Topological phase transition and texture inversion in a tunable topological insulator. *Science*, 332(6029):560–564, April 2011.

[89] Netanel H Lindner, Gil Refael, and Victor Galitski. Floquet topological insulator in semiconductor quantum wells. *Nat. Phys.*, 7(6):490–495, 2011.

[90] AA Burkov and Leon Balents. Weyl semimetal in a topological insulator multilayer. *Phys. Rev. Lett.*, 107(12):127205, 2011.

[91] Ilya Belopolski et al. A novel artificial condensed matter lattice and a new platform for one-dimensional topological phases. *Sci. Adv.*, 3(3):e1501692, 2017.

[92] Jean Dalibard, Fabrice Gerbier, Gediminas Juzeliūnas, and Patrik Öhberg. Colloquium: Artificial gauge potentials for neutral atoms. *Rev. Mod. Phys.*, 83:1523–1543, Nov 2011.

[93] Monika Aidelsburger, Sylvain Nascimbene, and Nathan Goldman. Artificial gauge fields in materials and engineered systems. *C R Phys*, 19(6):394–432, 2018.

[94] Ching Hua Lee, Stefan Imhof, Christian Berger, Florian Bayer, Johannes Brehm, Laurens W Molenkamp, Tobias Kiessling, and Ronny Thomale. Topolectrical circuits. *Commun. Phys.*, 1(1):39, 2018.

[95] Tomoki Ozawa, Hannah M. Price, Alberto Amo, Nathan Goldman, Mohammad Hafezi, Ling Lu, Mikael C. Rechtsman, David Schuster, Jonathan Simon, Oded Zilberberg, and Iacopo Carusotto. Topological photonics. *Rev. Mod. Phys.*, 91:015006, Mar 2019.

[96] Guorui Chen, Lili Jiang, Shuang Wu, Bosai Lyu, Hongyuan Li, Bheema Lingam Chittari, Kenji Watanabe, Takashi Taniguchi, Zhiwen Shi, Jeil Jung, et al. Evidence of a gate-tunable Mott insulator in a trilayer graphene moiré superlattice. *Nat. Phys.*, 15(3):237–241, 2019.

[97] Matthew Yankowitz, Shaowen Chen, Hryhoriy Polshyn, Yuxuan Zhang, K Watanabe, T Taniguchi, David Graf, Andrea F Young, and Cory R Dean. Tuning superconductivity in twisted bilayer graphene. *Science*, 363(6431):1059–1064, 2019.

[98] Justin C. W. Song, Andrey V. Shytov, and Leonid S. Levitov. Electron interactions and gap opening in graphene superlattices. *Phys. Rev. Lett.*, 111:266801, Dec 2013.

[99] Kyounghwan Kim, Ashley DaSilva, Shengqiang Huang, Babak Fallahazad, Stefano Larentis, Takashi Taniguchi, Kenji Watanabe, Brian J LeRoy, Allan H MacDonald, and Emanuel Tutuc. Tunable moiré bands and strong correlations in small-twist-angle bilayer graphene. *Proc. Natl. Acad. Sci. U.S.A.*, 114:3364–3369, 2017.

[100] Fengcheng Wu, Timothy Lovorn, Emanuel Tutuc, and A. H. MacDonald. Hubbard model physics in transition metal dichalcogenide moiré bands. *Phys. Rev. Lett.*, 121:026402, Jul 2018.

[101] G Trambly de Laissardiere, Didier Mayou, and Laurence Magaud. Localization of Dirac electrons in rotated graphene bilayers. *Nano Lett.*, 10(3):804–808, 2010.

[102] JMB Lopes dos Santos, NMR Peres, and AH Castro Neto. Continuum model of the twisted graphene bilayer. *Phys. Rev. B*, 86(15):155449, 2012.

[103] P. San-Jose, J. González, and F. Guinea. Non-abelian gauge potentials in graphene bilayers. *Phys. Rev. Lett.*, 108:216802, May 2012.

[104] Guohong Li, A Luican, JMB Lopes Dos Santos, AH Castro Neto, A Reina, J Kong, and EY Andrei. Observation of Van Hove singularities in twisted graphene layers. *Nat. Phys.*, 6(2):109–113, 2010.

[105] I. Brihuega, P. Mallet, H. González-Herrero, G. Trambly de Laissardière, M. M. Ugeda, L. Magaud, J. M. Gómez-Rodríguez, F. Ynduráin, and J.-Y. Veuillen. Unraveling the intrinsic and robust nature of van Hove singularities in twisted bilayer graphene by scanning tunneling microscopy and theoretical analysis. *Phys. Rev. Lett.*, 109:196802, Nov 2012.

[106] Youngwook Kim, Patrick Herlinger, Pilkyung Moon, Mikito Koshino, Takashi Taniguchi, Kenji Watanabe, and Jurgen H Smet. Charge inversion and topological

phase transition at a twist angle induced van Hove singularity of bilayer graphene. *Nano Lett.*, 16(8):5053–5059, 2016.

[107] Bikash Padhi, Chandan Setty, and Philip W Phillips. Doped twisted bilayer graphene near magic angles: Proximity to Wigner crystallization, not Mott insulation. *Nano Lett.*, 18(10):6175–6180, 2018.

[108] Hoi Chun Po, Liujun Zou, Ashvin Vishwanath, and T. Senthil. Origin of Mott insulating behavior and superconductivity in twisted bilayer graphene. *Phys. Rev. X*, 8:031089, Sep 2018.

[109] Noah F. Q. Yuan and Liang Fu. Model for the metal-insulator transition in graphene superlattices and beyond. *Phys. Rev. B*, 98:045103, Jul 2018.

[110] Jian Kang and Oskar Vafek. Symmetry, maximally localized wannier states, and a low-energy model for twisted bilayer graphene narrow bands. *Phys. Rev. X*, 8:031088, Sep 2018.

[111] Cenke Xu and Leon Balents. Topological superconductivity in twisted multilayer graphene. *Phys. Rev. Lett.*, 121:087001, Aug 2018.

[112] Biao Lian, Zhijun Wang, and B. Andrei Bernevig. Twisted bilayer graphene: A phonon-driven superconductor. *Phys. Rev. Lett.*, 122:257002, Jun 2019.

[113] J. F. Dodaro, S. A. Kivelson, Y. Schattner, X. Q. Sun, and C. Wang. Phases of a phenomenological model of twisted bilayer graphene. *Phys. Rev. B*, 98:075154, Aug 2018.

[114] Tobias MR Wolf, Oded Zilberberg, Ivan Levkivskyi, and Gianni Blatter. Substrate-induced topological minibands in graphene. *Physical Review B*, 98(12):125408, 2018.

[115] C. Janot. *Quasicrystals: A Primer*. Monographs on the physics and chemistry of materials. OUP Oxford, 2012.

[116] J. H. Pixley, Justin H. Wilson, David A. Huse, and Sarang Gopalakrishnan. Weyl semimetal to metal phase transitions driven by quasiperiodic potentials. *Phys. Rev. Lett.*, 120:207604, May 2018.

[117] Leticia Tarruell, Daniel Greif, Thomas Uehlinger, Gregor Jotzu, and Tilman Esslinger. Creating, moving and merging dirac points with a fermi gas in a tunable honeycomb lattice. *Nature*, 483(7389):302, 2012.

[118] Gregor Jotzu, Michael Messer, Rémi Desbuquois, Martin Lebrat, Thomas Uehlinger, Daniel Greif, and Tilman Esslinger. Experimental realization of the topological Haldane model with ultracold fermions. *Nature*, 515(7526):237–240, 2014.

[119] M. Aidelsburger, M. Lohse, C. Schweizer, M. Atala, J. T. Barreiro, S. Nascimbène, N. R. Cooper, I. Bloch, and N. Goldman. Measuring the Chern number of Hofstadter bands with ultracold bosonic atoms. *Nat. Phys.*, 11:162–166, 12 2015.

[120] Lianghui Huang, Zengming Meng, Pengjun Wang, Peng Peng, Shao-Liang Zhang, Liangchao Chen, Donghao Li, Qi Zhou, and Jing Zhang. Experimental realization of two-dimensional synthetic spin–orbit coupling in ultracold fermi gases. *Nature Physics*, 12(6):540–544, 2016.

[121] Zhan Wu, Long Zhang, Wei Sun, Xiao-Tian Xu, Bao-Zong Wang, Si-Cong Ji, Youjin Deng, Shuai Chen, Xiong-Jun Liu, and Jian-Wei Pan. Realization of two-dimensional spin-orbit coupling for bose-einstein condensates. *Science*, 354(6308):83–88, 2016.

[122] Philip Richerme, Zhe-Xuan Gong, Aaron Lee, Crystal Senko, Jacob Smith, Michael Foss-Feig, Spyridon Michalakis, Alexey V Gorshkov, and Christopher Monroe. Non-local propagation of correlations in quantum systems with long-range interactions. *Nature*, 511(7508):198, 2014.

[123] Kai Sun, W. Vincent Liu, Andreas Hemmerich, and S. Das Sarma. Topological semimetal in a fermionic optical lattice. *Nat. Phys.*, 8:67–70, 11 2012.

[124] Jian-Hua Jiang. Tunable topological Weyl semimetal from simple-cubic lattices with staggered fluxes. *Phys. Rev. A*, 85:033640, Mar 2012.

[125] Tena Dubček, Colin J. Kennedy, Ling Lu, Wolfgang Ketterle, Marin Soljačić, and Hrvoje Buljan. Weyl points in three-dimensional optical lattices: Synthetic magnetic monopoles in momentum space. *Phys. Rev. Lett.*, 114:225301, Jun 2015.

[126] Christof Weitenberg, Manuel Endres, Jacob F. Sherson, Marc Cheneau, Peter Schauß, Takeshi Fukuhara, Immanuel Bloch, and Stefan Kuhr. Single-spin addressing in an atomic Mott insulator. *Nature*, 471(7338):319–324, March 2011.

[127] Hisashi Hiramoto and Mahito Kohmoto. Electronic spectral and wavefunction properties of one-dimensional quasiperiodic systems: a scaling approach. *Int. J. Mod. Phys. B*, 6(03n04):281–320, 1992.

[128] Nicola Marzari, Arash A. Mostofi, Jonathan R. Yates, Ivo Souza, and David Vanderbilt. Maximally localized wannier functions: Theory and applications. *Rev. Mod. Phys.*, 84:1419–1475, Oct 2012.

[129] Christian Brouder, Gianluca Panati, Matteo Calandra, Christophe Mourougane, and Nicola Marzari. Exponential localization of Wannier functions in insulators. *Phys. Rev. Lett.*, 98(4):046402, January 2007.

[130] Jennifer Cano, Barry Bradlyn, Zhijun Wang, L. Elcoro, M. G. Vergniory, C. Felser, M. I. Aroyo, and B. Andrei Bernevig. Topology of disconnected elementary band representations. *Phys. Rev. Lett.*, 120(26):266401, June 2018.

[131] Hoi Chun Po, Haruki Watanabe, and Ashvin Vishwanath. Fragile Topology and Wannier Obstructions. *Phys. Rev. Lett.*, 121(12):126402, September 2018.

[132] Mikael C. Rechtsman, Hyeong-Chai Jeong, Paul M. Chaikin, Salvatore Torquato, and Paul J. Steinhardt. Optimized structures for photonic quasicrystals. *Phys. Rev. Lett.*, 101:073902, Aug 2008.

[133] JP Gaebler, JT Stewart, TE Drake, DS Jin, A Perali, P Pieri, and GC Strinati.

Observation of pseudogap behaviour in a strongly interacting Fermi gas. *Nat. Phys.*, 6(8):569–573, 2010.

[134] Ulrich Schneider, Lucia Hackermüller, Jens Philipp Ronzheimer, Sebastian Will, Simon Braun, Thorsten Best, Immanuel Bloch, Eugene Demler, Stephan Mandt, David Rasch, and Achim Rosch. Fermionic transport and out-of-equilibrium dynamics in a homogeneous Hubbard model with ultracold atoms. *Nat. Phys.*, 8(3):213–218, March 2012.

[135] E. J. Mele. Commensuration and interlayer coherence in twisted bilayer graphene. *Phys. Rev. B*, 81:161405, Apr 2010.

[136] Antonello Scardicchio and Thimothée Thiery. Perturbation theory approaches to Anderson and many-body localization: some lecture notes. Preprint at https://arxiv.org/abs/1710.01234, 2017.

[137] Hridis K. Pal, Stephen Spitz, and Markus Kindermann. Emergent geometric frustration and flat band in moiré bilayer graphene. *Phys. Rev. Lett.*, 123:186402, Oct 2019.

[138] Wei Yao, Eryin Wang, Changhua Bao, Yiou Zhang, Kenan Zhang, Kejie Bao, Chun Kai Chan, Chaoyu Chen, Jose Avila, Maria C Asensio, et al. Quasicrystalline 30° twisted bilayer graphene as an incommensurate superlattice with strong interlayer coupling. *Proc. Natl. Acad. Sci. U.S.A.*, 115:6928–6933, 2018.

[139] Sung Joon Ahn et al. Dirac electrons in a dodecagonal graphene quasicrystal. *Science*, 361(6404):782–786, 2018.

[140] A González-Tudela and J Ignacio Cirac. Cold atoms in twisted-bilayer optical potentials. *Physical Review A*, 100(5):053604, 2019.

[141] Tymoteusz Salamon, Alessio Celi, Ravindra W. Chhajlany, Irénée Frérot, Maciej Lewenstein, Leticia Tarruell, and Debraj Rakshit. Simulating twistronics without a twist. *Phys. Rev. Lett.*, 125:030504, Jul 2020.

[142] Andre Konstantin Geim. Graphene: status and prospects. *Science*, 324(5934):1530–1534, 2009.

[143] Andre K Geim and Irina V Grigorieva. Van der waals heterostructures. *Nature*, 499(7459):419, 2013.

[144] S. Das Sarma, Shaffique Adam, E. H. Hwang, and Enrico Rossi. Electronic transport in two-dimensional graphene. *Rev. Mod. Phys.*, 83:407–470, May 2011.

[145] AA Zibrov, C Kometter, H Zhou, EM Spanton, T Taniguchi, K Watanabe, MP Zaletel, and AF Young. Tunable interacting composite fermion phases in a half-filled bilayer-graphene landau level. *Nature*, 549(7672):360, 2017.

[146] Xu Du, Ivan Skachko, Fabian Duerr, Adina Luican, and Eva Y Andrei. Fractional quantum hall effect and insulating phase of dirac electrons in graphene. *Nature*, 462(7270):192, 2009.

[147] Xiaobo Lu, Petr Stepanov, Wei Yang, Ming Xie, Mohammed Ali Aamir, Ipsita Das, Carles Urgell, Kenji Watanabe, Takashi Taniguchi, Guangyu Zhang, et al. Superconductors, orbital magnets, and correlated states in magic angle bilayer graphene. *arXiv preprint arXiv:1903.06513*, 2019.

[148] Kyounghwan Kim, Matthew Yankowitz, Babak Fallahazad, Sangwoo Kang, Hema CP Movva, Shengqiang Huang, Stefano Larentis, Chris M Corbet, Takashi Taniguchi, Kenji Watanabe, et al. van der waals heterostructures with high accuracy rotational alignment. *Nano letters*, 16(3):1989–1995, 2016.

[149] Dillon Wong, Yang Wang, Jeil Jung, Sergio Pezzini, Ashley M. DaSilva, Hsin-Zon Tsai, Han Sae Jung, Ramin Khajeh, Youngkyou Kim, Juwon Lee, Salman Kahn, Sajjad Tollabimazraehno, Haider Rasool, Kenji Watanabe, Takashi Taniguchi, Alex Zettl, Shaffique Adam, Allan H. MacDonald, and Michael F. Crommie. Local spectroscopy of moir\'e-induced electronic structure in gate-tunable twisted bilayer graphene. *Phys. Rev. B*, 92(15):155409, October 2015.

[150] Alexander Kerelsky, Leo McGilly, Dante M. Kennes, Lede Xian, Matthew Yankowitz, Shaowen Chen, K. Watanabe, T. Taniguchi, James Hone, Cory Dean, Angel Rubio, and Abhay N. Pasupathy. Magic Angle Spectroscopy. *arXiv:1812.08776 [cond-mat]*, December 2018. arXiv: 1812.08776.

[151] Youngjoon Choi, Jeannette Kemmer, Yang Peng, Alex Thomson, Harpreet Arora, Robert Polski, Yiran Zhang, Hechen Ren, Jason Alicea, Gil Refael, Felix von Oppen, Kenji Watanabe, Takashi Taniguchi, and Stevan Nadj-Perge. Imaging Electronic Correlations in Twisted Bilayer Graphene near the Magic Angle. *arXiv:1901.02997 [cond-mat]*, January 2019. arXiv: 1901.02997.

[152] Yuhang Jiang, Xinyuan Lai, Kenji Watanabe, Takashi Taniguchi, Kristjan Haule, Jinhai Mao, and Eva Y. Andrei. Charge-order and broken rotational symmetry in magic angle twisted bilayer graphene. *Nature*, pages 1–8, July 2019.

[153] Yonglong Xie, Biao Lian, Berthold Jäck, Xiaomeng Liu, Cheng-Li Chiu, Kenji Watanabe, Takashi Taniguchi, B. Andrei Bernevig, and Ali Yazdani. Spectroscopic signatures of many-body correlations in magic-angle twisted bilayer graphene. *Nature*, 572(7767):101–105, August 2019.

[154] J. M. B. Lopes dos Santos, N. M. R. Peres, and A. H. Castro Neto. Graphene bilayer with a twist: Electronic structure. *Phys. Rev. Lett.*, 99:256802, Dec 2007.

[155] Pilkyung Moon and Mikito Koshino. Energy spectrum and quantum Hall effect in twisted bilayer graphene. *Phys. Rev. B*, 85(19):195458, May 2012.

[156] Zhen Bi, Noah F. Q. Yuan, and Liang Fu. Designing Flat Band by Strain. *arXiv:1902.10146 [cond-mat]*, February 2019. arXiv: 1902.10146.

[157] A. H. Castro Neto, F. Guinea, N. M. R. Peres, K. S. Novoselov, and A. K. Geim. The electronic properties of graphene. *Rev. Mod. Phys.*, 81(1):109–162, January 2009.

[158] Xianqing Lin and David Tománek. Minimum model for the electronic structure

of twisted bilayer graphene and related structures. *Phys. Rev. B*, 98:081410, Aug 2018.

[159] Wei Yao, Eryin Wang, Changhua Bao, Yiou Zhang, Kenan Zhang, Kejie Bao, Chun Kai Chan, Chaoyu Chen, Jose Avila, Maria C Asensio, et al. Quasicrystalline 30° twisted bilayer graphene as an incommensurate superlattice with strong interlayer coupling. *Proc. Natl. Acad. Sci.*, 115(27):6928–6933, 2018.

[160] Xianqing Lin, Dan Liu, and David Tománek. Shear instability in twisted bilayer graphene. *Phys. Rev. B*, 98:195432, Nov 2018.

[161] A. Luican, Guohong Li, A. Reina, J. Kong, R. R. Nair, K. S. Novoselov, A. K. Geim, and E. Y. Andrei. Single-layer behavior and its breakdown in twisted graphene layers. *Phys. Rev. Lett.*, 106:126802, Mar 2011.

[162] Wladimir A Benalcazar, B Andrei Bernevig, and Taylor L Hughes. Quantized electric multipole insulators. *Science*, 357(6346):61–66, 2017.

[163] Moon Jip Park, Youngkuk Kim, Gil Young Cho, and SungBin Lee. Higher-order topological insulator in twisted bilayer graphene. *Phys. Rev. Lett.*, 123:216803, Nov 2019.

[164] Holger Fehske, Ralf Schneider, and Alexander Weiße. *Computational many-particle physics*, volume 739. Springer, 2007.

[165] J. T. Chalker and G. J. Daniell. Scaling, diffusion, and the integer quantized hall effect. *Phys. Rev. Lett.*, 61:593–596, Aug 1988.

[166] J.T. Chalker. Scaling and eigenfunction correlations near a mobility edge. *Physica A: Statistical Mechanics and its Applications*, 167(1):253 – 258, 1990.

[167] E. Cuevas and V. E. Kravtsov. Two-eigenfunction correlation in a multifractal metal and insulator. *Phys. Rev. B*, 76:235119, Dec 2007.

[168] Yang-Zhi Chou and Matthew S. Foster. Chalker scaling, level repulsion, and

conformal invariance in critically delocalized quantum matter: Disordered topological superconductors and artificial graphene. *Phys. Rev. B*, 89:165136, Apr 2014.

[169] Yan V. Fyodorov and Alexander D. Mirlin. Strong eigenfunction correlations near the anderson-localization transition. *Phys. Rev. B*, 55:R16001–R16004, Jun 1997.

[170] M. V. Feigel'man, L. B. Ioffe, V. E. Kravtsov, and E. A. Yuzbashyan. Eigenfunction fractality and pseudogap state near the superconductor-insulator transition. *Phys. Rev. Lett.*, 98:027001, Jan 2007.

[171] Matthew S. Foster and Emil A. Yuzbashyan. Interaction-mediated surface-state instability in disordered three-dimensional topological superconductors with spin su(2) symmetry. *Phys. Rev. Lett.*, 109:246801, Dec 2012.

[172] I. S. Burmistrov, I. V. Gornyi, and A. D. Mirlin. Enhancement of the critical temperature of superconductors by anderson localization. *Phys. Rev. Lett.*, 108:017002, Jan 2012.

[173] Matthew S. Foster, Hong-Yi Xie, and Yang-Zhi Chou. Topological protection, disorder, and interactions: Survival at the surface of three-dimensional topological superconductors. *Phys. Rev. B*, 89:155140, Apr 2014.

[174] I. L. Aleiner and K. B. Efetov. Effect of disorder on transport in graphene. *Phys. Rev. Lett.*, 97:236801, Dec 2006.

[175] Alexander Altland. Low-energy theory of disordered graphene. *Phys. Rev. Lett.*, 97:236802, Dec 2006.

[176] Andreas W. W. Ludwig, Matthew P. A. Fisher, R. Shankar, and G. Grinstein. Integer quantum hall transition: An alternative approach and exact results. *Phys. Rev. B*, 50:7526–7552, Sep 1994.

[177] Horacio E. Castillo, Claudio de C. Chamon, Eduardo Fradkin, Paul M. Goldbart,

and Christopher Mudry. Exact calculation of multifractal exponents of the critical wave function of dirac fermions in a random magnetic field. *Phys. Rev. B*, 56:10668–10677, Oct 1997.

[178] David Carpentier and Pierre Le Doussal. Glass transition of a particle in a random potential, front selection in nonlinear renormalization group, and entropic phenomena in liouville and sinh-gordon models. *Phys. Rev. E*, 63:026110, Jan 2001.

[179] Olexei Motrunich, Kedar Damle, and David A. Huse. Particle-hole symmetric localization in two dimensions. *Phys. Rev. B*, 65:064206, Jan 2002.

[180] Baruch Horovitz and Pierre Le Doussal. Freezing transitions and the density of states of two-dimensional random dirac hamiltonians. *Phys. Rev. B*, 65:125323, Mar 2002.

[181] C. Mudry, S. Ryu, and A. Furusaki. Density of states for the π-flux state with bipartite real random hopping only: A weak disorder approach. *Phys. Rev. B*, 67:064202, Feb 2003.

[182] R. Jackiw and C. Rebbi. Solitons with fermion number $\frac{1}{2}$. *Phys. Rev. D*, 13:3398–3409, Jun 1976.

[183] R Jackiw and Paolo Rossi. Zero modes of the vortex-fermion system. *Nuclear Physics B*, 190(4):681–691, 1981.

[184] Long Zhang. Lowest-energy moiré band formed by dirac zero modes in twisted bilayer graphene. *Science Bulletin*, 64(8):495–498, 2019.

[185] E. J. König, P. M. Ostrovsky, I. V. Protopopov, and A. D. Mirlin. Metal-insulator transition in two-dimensional random fermion systems of chiral symmetry classes. *Phys. Rev. B*, 85:195130, May 2012.

[186] Qijin Chen, Yan He, Chih-Chun Chien, and K Levin. Theory of radio frequency spectroscopy experiments in ultracold fermi gases and their relation to photoemission in the cuprates. *Reports on Progress in Physics*, 72(12):122501, 2009.

[187] Markus Greiner, Immanuel Bloch, Olaf Mandel, Theodor W Hänsch, and Tilman Esslinger. Exploring phase coherence in a 2d lattice of bose-einstein condensates. *Physical Review Letters*, 87(16):160405, 2001.

[188] Michael Köhl, Henning Moritz, Thilo Stöferle, Kenneth Günter, and Tilman Esslinger. Fermionic atoms in a three dimensional optical lattice: Observing fermi surfaces, dynamics, and interactions. *Phys. Rev. Lett.*, 94:080403, Mar 2005.

[189] Alicia J Kollár, Mattias Fitzpatrick, and Andrew A Houck. Hyperbolic lattices in circuit quantum electrodynamics. *Nature*, 571(7763):45, 2019.

[190] Alexander B Khanikaev and Gennady Shvets. Two-dimensional topological photonics. *Nature Photonics*, 11(12):763, 2017.

[191] Lisa M Nash, Dustin Kleckner, Alismari Read, Vincenzo Vitelli, Ari M Turner, and William TM Irvine. Topological mechanics of gyroscopic metamaterials. *Proceedings of the National Academy of Sciences*, 112(47):14495–14500, 2015.

[192] M Inui, SA Trugman, and Elihu Abrahams. Unusual properties of midband states in systems with off-diagonal disorder. *Physical Review B*, 49(5):3190, 1994.

[193] Norman Weik, Johannes Schindler, Soumya Bera, Gemma C Solomon, and Ferdinand Evers. Graphene with vacancies: Supernumerary zero modes. *Physical Review B*, 94(6):064204, 2016.

[194] Horst L Stormer, Daniel C Tsui, and Arthur C Gossard. The fractional quantum hall effect. *Reviews of Modern Physics*, 71(2):S298, 1999.

[195] Joseph Maciejko and Gregory A Fiete. Fractionalized topological insulators. *Nature Physics*, 11(5):385–388, 2015.

[196] Nicolas Regnault and B Andrei Bernevig. Fractional chern insulator. *Physical Review X*, 1(2):021014, 2011.

[197] Zhao Liu, Emil J Bergholtz, Heng Fan, and Andreas M Läuchli. Fractional chern insulators in topological flat bands with higher chern number. *Physical review letters*, 109(18):186805, 2012.

[198] Fenner Harper, Steven H Simon, and Rahul Roy. Perturbative approach to flat chern bands in the hofstadter model. *Physical Review B*, 90(7):075104, 2014.

[199] Miguel A Bandres, Mikael C Rechtsman, and Mordechai Segev. Topological photonic quasicrystals: Fractal topological spectrum and protected transport. *Physical Review X*, 6(1):011016, 2016.

[200] Joseph Maciejko, Xiao-Liang Qi, Andreas Karch, and Shou-Cheng Zhang. Fractional topological insulators in three dimensions. *Physical review letters*, 105(24):246809, 2010.

[201] Brian Swingle, Maissam Barkeshli, John McGreevy, and Todadri Senthil. Correlated topological insulators and the fractional magnetoelectric effect. *Physical Review B*, 83(19):195139, 2011.

[202] Emil J Bergholtz and Zhao Liu. Topological flat band models and fractional chern insulators. *International Journal of Modern Physics B*, 27(24):1330017, 2013.

[203] Siddharth A Parameswaran, Rahul Roy, and Shivaji L Sondhi. Fractional quantum hall physics in topological flat bands. *arXiv preprint arXiv:1302.6606*, 2013.

[204] Yi-Fei Wang, Hong Yao, Chang-De Gong, and DN Sheng. Fractional quantum hall effect in topological flat bands with chern number two. *Physical Review B*, 86(20):201101, 2012.

[205] Shuo Yang, Zheng-Cheng Gu, Kai Sun, and S Das Sarma. Topological flat band models with arbitrary chern numbers. *Physical Review B*, 86(24):241112, 2012.

[206] Tero T Heikkilä, Nikolai Borisovich Kopnin, and Grigorii Efimovich Volovik. Flat bands in topological media. *JETP letters*, 94(3):233, 2011.

[207] Ching Hua Lee, Daniel P Arovas, and Ronny Thomale. Band flatness optimization through complex analysis. *Physical Review B*, 93(15):155155, 2016.

[208] Aaron L Sharpe, Eli J Fox, Arthur W Barnard, Joe Finney, Kenji Watanabe,

Takashi Taniguchi, MA Kastner, and David Goldhaber-Gordon. Emergent ferromagnetism near three-quarters filling in twisted bilayer graphene. *Science*, 365(6453):605–608, 2019.

[209] Jed H Pixley and Eva Y Andrei. Ferromagnetism in magic-angle graphene. *Science*, 365(6453):543–543, 2019.

[210] H Polshyn, J Zhu, MA Kumar, Y Zhang, F Yang, CL Tschirhart, M Serlin, K Watanabe, T Taniguchi, AH MacDonald, et al. Electrical switching of magnetic order in an orbital chern insulator. *Nature*, 588(7836):66–70, 2020.

[211] Ya-Hui Zhang, Dan Mao, Yuan Cao, Pablo Jarillo-Herrero, and T Senthil. Nearly flat chern bands in moiré superlattices. *Physical Review B*, 99(7):075127, 2019.

[212] Bheema Lingam Chittari, Guorui Chen, Yuanbo Zhang, Feng Wang, and Jeil Jung. Gate-tunable topological flat bands in trilayer graphene boron-nitride moiré superlattices. *Physical review letters*, 122(1):016401, 2019.

[213] Fengcheng Wu. Topological chiral superconductivity with spontaneous vortices and supercurrent in twisted bilayer graphene. *Physical Review B*, 99(19):195114, 2019.

[214] Qingjun Tong, Hongyi Yu, Qizhong Zhu, Yong Wang, Xiaodong Xu, and Wang Yao. Topological mosaics in moiré superlattices of van der waals heterobilayers. *Nature Physics*, 13(4):356–362, 2017.

[215] Pablo San-Jose, A Gutiérrez-Rubio, Mauricio Sturla, and Francisco Guinea. Electronic structure of spontaneously strained graphene on hexagonal boron nitride. *Physical Review B*, 90(11):115152, 2014.

[216] Biao Lian, Zhaochen Liu, Yuanbo Zhang, and Jing Wang. Flat chern band from twisted bilayer mnbi _2 te _4. *arXiv preprint arXiv:1908.02581*, 2019.

[217] Patrick J Ledwith, Grigory Tarnopolsky, Eslam Khalaf, and Ashvin Vishwanath. Fractional chern insulator states in twisted bilayer graphene: An analytical approach. *arXiv preprint arXiv:1912.09634*, 2019.

[218] Zhida Song, Zhijun Wang, Wujun Shi, Gang Li, Chen Fang, and B Andrei Bernevig. All magic angles in twisted bilayer graphene are topological. *Physical review letters*, 123(3):036401, 2019.

[219] Colin J Kennedy, Georgios A Siviloglou, Hirokazu Miyake, William Cody Burton, and Wolfgang Ketterle. Spin-orbit coupling and quantum spin hall effect for neutral atoms without spin flips. *Physical review letters*, 111(22):225301, 2013.

[220] Roman Süsstrunk and Sebastian D Huber. Observation of phononic helical edge states in a mechanical topological insulator. *Science*, 349(6243):47–50, 2015.

[221] Eran Lustig, Steffen Weimann, Yonatan Plotnik, Yaakov Lumer, Miguel A Bandres, Alexander Szameit, and Mordechai Segev. Photonic topological insulator in synthetic dimensions. *Nature*, 567(7748):356, 2019.

[222] Stefan Imhof, Christian Berger, Florian Bayer, Johannes Brehm, Laurens W Molenkamp, Tobias Kiessling, Frank Schindler, Ching Hua Lee, Martin Greiter, Titus Neupert, and Ronny Thomale. Topolectrical-circuit realization of topological corner modes. *Nature Physics*, 14(9):925–929, 2018.

[223] Ai Yamakage, Kentaro Nomura, Ken-Ichiro Imura, and Yoshio Kuramoto. Criticality of the metal–topological insulator transition driven by disorder. *Physical Review B*, 87(20):205141, 2013.

[224] Dan Mao and Senthil Todadri. Quasiperiodicity, band topology, and moir\'e graphene. *arXiv preprint arXiv:2011.06034*, 2020.

[225] Tommaso Cea, Pierre A. Pantaleón, and Francisco Guinea. Band structure of twisted bilayer graphene on hexagonal boron nitride. *Phys. Rev. B*, 102:155136, Oct 2020.

[226] Jingtian Shi, Jihang Zhu, and A. H. MacDonald. Moiré commensurability and the quantum anomalous hall effect in twisted bilayer graphene on hexagonal boron nitride. *Phys. Rev. B*, 103:075122, Feb 2021.

[227] Alexander D Mirlin. Statistics of energy levels and eigenfunctions in disordered systems. *Physics Reports*, 326(5-6):259–382, 2000.

[228] Takahiro Fukui, Yasuhiro Hatsugai, and Hiroshi Suzuki. Chern numbers in discretized brillouin zone: efficient method of computing (spin) hall conductances. *Journal of the Physical Society of Japan*, 74(6):1674–1677, 2005.

[229] Guillaume Roux, T Barthel, IP McCulloch, Corinna Kollath, U Schollwöck, and Thierry Giamarchi. Quasiperiodic bose-hubbard model and localization in one-dimensional cold atomic gases. *Physical Review A*, 78(2):023628, 2008.

[230] Alex Krizhevsky, Ilya Sutskever, and Geoffrey E Hinton. Imagenet classification with deep convolutional neural networks. In *Advances in neural information processing systems*, pages 1097–1105, 2012.

[231] Geoffrey E Hinton, Nitish Srivastava, Alex Krizhevsky, Ilya Sutskever, and Ruslan R Salakhutdinov. Improving neural networks by preventing co-adaptation of feature detectors. *arXiv preprint arXiv:1207.0580*, 2012.

[232] Chui-Zhen Chen, Haiwen Liu, Hua Jiang, Qing-feng Sun, Ziqiang Wang, and XC Xie. Tunable anderson metal-insulator transition in quantum spin-hall insulators. *Physical Review B*, 91(21):214202, 2015.

[233] SA Parameswaran, R Roy, and Shivaji L Sondhi. Fractional chern insulators and the w_∞ algebra. *Physical Review B*, 85(24):241308, 2012.

[234] Martin Claassen, Ching Hua Lee, Ronny Thomale, Xiao-Liang Qi, and Thomas P. Devereaux. Position-momentum duality and fractional quantum hall effect in chern insulators. *Phys. Rev. Lett.*, 114:236802, Jun 2015.

[235] CW Groth, M Wimmer, AR Akhmerov, J Tworzydło, and CWJ Beenakker. Theory of the topological anderson insulator. *Physical review letters*, 103(19):196805, 2009.

[236] Eric J Meier, Fangzhao Alex An, Alexandre Dauphin, Maria Maffei, Pietro

Massignan, Taylor L Hughes, and Bryce Gadway. Observation of the topological anderson insulator in disordered atomic wires. *Science*, 362(6417):929–933, 2018.

[237] Pallab Goswami and Sudip Chakravarty. Quantum criticality between topological and band insulators in 3+ 1 dimensions. *Physical review letters*, 107(19):196803, 2011.

[238] Soumya Bera, Jay D Sau, and Bitan Roy. Dirty weyl semimetals: Stability, phase transition, and quantum criticality. *Physical Review B*, 93(20):201302, 2016.

[239] Alberto Rodriguez, Louella J Vasquez, Keith Slevin, and Rudolf A Römer. Multifractal finite-size scaling and universality at the anderson transition. *Physical Review B*, 84(13):134209, 2011.

[240] Martin Janssen. Statistics and scaling in disordered mesoscopic electron systems. *Physics Reports*, 295(1-2):1–91, 1998.

[241] Paulo Orenstein. Robust mean estimation with the bayesian median of means. *arXiv preprint arXiv:1906.01204*, 2019.

[242] Frank R Hampel, Elvezio M Ronchetti, Peter J Rousseeuw, and Werner A Stahel. *Robust statistics: the approach based on influence functions*, volume 196. John Wiley & Sons, 2011.